

Reconstructing Past Depositional and
Diagenetic Processes through Quantitative
Stratigraphic Analysis of the Martian
Sedimentary Rock Record

Thesis by
Kathryn M. Stack

In Partial Fulfillment of the Requirements for the degree
of
Doctor of Philosophy



CALIFORNIA INSTITUTE OF TECHNOLOGY
Pasadena, California
2015
(Defended June 30, 2014)

© 2015
Kathryn M. Stack
All Rights Reserved

ACKNOWLEDGMENTS

First, I would like to thank my advisor John Grotzinger for six years of support and for setting an inspiring example as a scientist and a mission leader. I am very grateful to John for the opportunities he has given me and for just the right amount of independence—enough to challenge me, but not so much as to be constantly “setting myself on fire.” A special thanks to my “step-advisor” Ralph Milliken, who took me under his wing when I first arrived at Caltech and has continued to guide and encourage me during our 5-year long-distance advisor-advisee relationship. A heartfelt thank you to my academic advisor George Rossman, who has always been there to help me whether it was a small task in the laboratory or a troubling academic conundrum. I am so fortunate to have been the recipient of his expertise and genuine kindness while at Caltech. Thank you also to the rest of my committee, Mike Lamb and Bethany Ehlmann, who provided invaluable advice, helpful perspective, and some important checks and balances during TAC meetings. I would also like to thank the amazing scientists and engineers of the MSL team whom I have had the honor to work with during my time as a graduate student on the mission. Your encouragement and support has been life-changing.

The students, post-docs, and staff of the Grotzinger Group have had a big impact on my experience here at Caltech and I thank this special group of women (and a few men) for many good discussions, fun experiences, and some important lessons learned about group dynamics. I am also appreciative of the Ehlmann Group, who allowed me to participate in group meetings and gave me helpful feedback on several of the chapters in this thesis. Thank you to the amazing staff of the GPS Division, particularly Janice Grancich, Marcia Hudson, Dian Buchness, and Liz Miura Boyd. Your helpfulness, constant supply of snacks, and genuine interest in my life has helped me feel at home here at Caltech. Thanks also to my officemates Claire Thomas, Ajay Limaye, and Kristin Bergmann, who were so much a part of my day-to-day experience as a grad student.

Finally, the biggest thanks goes to my family: my husband Jason, my parents Gary and Maria, my brother Matthew, and Cubbie the beagle. Their love, guidance, encouragement, and wagging tail (applies only to Cubbie) have kept me going throughout this endeavor.

ABSTRACT

High-resolution orbital and in-situ observations acquired of the Martian surface during the past two decades provide the opportunity to study the rock record of Mars at an unprecedented level of detail. This dissertation consists of four studies whose common goal is to establish new standards for the quantitative analysis of visible and near-infrared data from the surface of Mars. Through the compilation of global image inventories, application of stratigraphic and sedimentologic statistical methods, and use of laboratory analogs, this dissertation provides insight into the history of past depositional and diagenetic processes on Mars. The first study presents a global inventory of stratified deposits observed in images from the High Resolution Image Science Experiment (HiRISE) camera onboard the Mars Reconnaissance Orbiter. This work uses the widespread coverage of high-resolution orbital images to make global-scale observations about the processes controlling sediment transport and deposition on Mars. The next chapter presents a study of bed thickness distributions in Martian sedimentary deposits, showing how statistical methods can be used to establish quantitative criteria for evaluating the depositional history of stratified deposits observed in orbital images. The third study tests the ability of spectral mixing models to obtain quantitative mineral abundances from near-infrared reflectance spectra of clay and sulfate mixtures in the laboratory for application to the analysis of orbital spectra of sedimentary deposits on Mars. The final study employs a statistical analysis of the size, shape, and distribution of nodules observed by the Mars Science Laboratory Curiosity rover team in the Sheepbed mudstone at Yellowknife Bay in Gale crater. This analysis is used to evaluate hypotheses for nodule formation and to gain insight into the diagenetic history of an ancient habitable environment on Mars.

TABLE OF CONTENTS

Acknowledgments	iii
Abstract	iv
Table of Contents	v
List of Tables and Figures	ix
Acronyms	xii

Chapter 1:

Introduction	1
1.1 A Golden Age of Mars Exploration	1
1.2 The Sedimentary Rock Record of Mars	3
1.3 Dissertation Summary	4
1.4 Data and Methods	5
<i>1.4.1 Spacecraft Instrument Data</i>	5
1.4.1.1 Mars Orbiter Laser Altimeter (MOLA)	5
1.4.1.2 Thermal Emission Imaging System (THEMIS)	6
1.4.1.3 High Resolution Imaging Science Experiment (HiRISE)	7
1.4.1.4 Mars Science Laboratory (MSL) Curiosity Rover	8
<i>1.4.2 Software</i>	9
1.4.2.1 ArcGIS	9
1.4.2.2 MATLAB	10
<i>1.4.3 Laboratory Instruments</i>	10
1.4.3.1 Fourier Transform Infrared Spectrometer (FTIR)	10

Chapter 2:

Global distribution of stratified rocks on Mars	12
Abstract	12
2.1 Introduction	13
2.2 Data and Methods	16
<i>2.2.1 Data</i>	16
<i>2.2.2 Image Classification</i>	17
<i>2.2.3 Spatial Analysis</i>	19
2.3 Results	20
<i>2.3.1 Global Distribution of Stratified Rocks</i>	20
<i>2.3.2 Geomorphic Setting of Stratified Rocks</i>	21
<i>2.3.3 Basin Fill Versus Unconfined Stratified Deposits</i>	23
<i>2.3.4 Glacial/Periglacial Deposits</i>	24
2.4 Discussion	25
<i>2.4.1 Global Distribution and Comparison to Previous Studies</i>	25
<i>2.4.2 Implications for the Martian Sediment and Hydrological Cycles</i>	27
<i>2.4.3 Global-Scale Depositional Processes on Mars</i>	30
2.5 Conclusions	35

Chapter 3:

Bed thickness distributions on Mars: An orbital perspective	57
Abstract	57
3.1 Introduction	58
3.2 Background	61
3.2.1 <i>Statistical Analysis of Bed Thickness on Earth</i>	61
3.2.1.1 Lognormal Distributions	62
3.2.1.2 Exponential Distributions	62
3.2.1.3 Power-Law Distributions	64
3.3 Methods	66
3.3.1 <i>Identifying Beds from Orbit on Mars</i>	66
3.3.2 <i>Orbital Data</i>	66
3.3.3 <i>Measuring Bed Thickness</i>	68
3.3.3.1 Measured Sections	68
3.3.3.2 Bed Orientation	70
3.3.3.3 Correction for True Thickness	71
3.3.3.4 Error of Bed Thickness Measurements	72
3.3.4 <i>Statistical Methods</i>	73
3.4 Results	75
3.4.1 <i>Holden Crater</i>	75
3.4.1.1 Bed Thickness Statistics	75
3.4.1.2 Trends in Thickness versus Stratigraphic Position	76
3.4.1.3 Bed Thickness Distributions	77
3.4.1.4 Log-Log Plots	79
3.4.2 <i>Plateau West of Juventae Chasma</i>	79
3.4.2.1 Bed Thickness Statistics	79
3.4.2.2 Trends in Thickness versus Stratigraphic Position	80
3.4.2.3 Bed Thickness Distributions	81
3.4.2.4 Log-Log Plots	82
3.4.3 <i>Gale Crater</i>	82
3.4.3.1 Bed Thickness Statistics	82
3.4.3.2 Trends in Thickness versus Stratigraphic Position	83
3.4.3.3 Bed Thickness Distributions	84
3.4.3.4 Log-Log Plots	85
3.4.4 <i>Additional Sections</i>	85
3.4.4.1 Bed Thickness Statistics	85
3.4.4.2 Trends in Thickness versus Stratigraphic Position	86
3.4.4.3 Bed Thickness Distributions	87
3.4.4.4 Log-Log Plots	88
3.5 Discussion	88
3.5.1 <i>Bed Thickness on Mars</i>	88
3.5.2 <i>Stratigraphic and Statistical Trends in Bed Thickness</i>	89
3.5.2.1 Thinning and Thickening Trends	89
3.5.2.2 Statistical Distribution of Bed Thickness	93
3.5.2.3 Power-Law Behavior of Bed Thickness Frequency	96
3.5.3 <i>Building a Global Inventory of Bed Thickness Distributions on Mars</i>	97
3.5.4 <i>Challenges of Bed Thickness Analysis</i>	98
3.6 Conclusions	102
Notation	104

Chapter 4:

Modeling near-infrared reflectance spectra of clay and sulfate mixtures and implications for Mars	128
Abstract	128
4.1 Introduction	129
4.2 Spectral Mixing Models	134
4.3 Materials and Methods	139
4.3.1 <i>Laboratory Measurements</i>	139
4.3.2 <i>Analysis of Band Depths and Band Minima</i>	140
4.3.3 <i>Linear (Checkerboard) and Nonlinear (Intimate) Spectral Unmixing</i>	141
4.3.4 <i>Modeling Mass Fraction</i>	143
4.4 Results	145
4.4.1 <i>Spectral Observations</i>	145
4.4.2 <i>Full Wavelength Range (1.25-2.6 μm) Model Results</i>	148
4.4.2.1 Measured Versus Modeled Spectra	148
4.4.2.2 Measured and Optimized Particle Diameter Ratios	149
4.4.2.3 Modeled Mass Fractions	150
4.4.2.3.1 <i>Mass Fractions Modeled with Measured Mean and Mode Diameter Ratios</i>	150
4.4.2.3.2 <i>Mass Fractions Modeled with Optimized Particle Diameter Ratio</i>	151
4.4.2.4 <i>Relative Uncertainty of Model Fits</i>	152
4.4.3 <i>Partial Wavelength Range (2.1-2.6 μm) Model Results</i>	153
4.5 Discussion	155
4.5.1 <i>Implications of Measured and Modeled Particle Size</i>	156
4.5.2 <i>Checkerboard Versus Intimate Mixing Models</i>	161
4.5.3 <i>Relevance for Quantifying Hydrated Minerals on Mars</i>	163
4.6 Conclusions	166
Notation	169

Chapter 5:

Diagenetic origin of nodules in the Sheepbed member, Yellowknife Bay formation, Gale crater, Mars	196
Abstract	196
5.1 Introduction	197
5.2 Data and Methods	199
5.2.1 <i>Nodule Classification and Nomenclature</i>	199
5.2.2 <i>MAHLI</i>	200
5.2.3 <i>Mastcam</i>	202
5.2.4 <i>APXS</i>	204
5.2.5 <i>ChemCam</i>	204
5.3 Shape and Size Distributions	205
5.3.1 <i>Solid Nodules</i>	205
5.3.2 <i>Hollow Nodules</i>	206
5.3.3 <i>Filled Nodules</i>	209
5.3.4 <i>Statistical Testing</i>	210
5.3.5 <i>Summary</i>	210

5.4 Spatial Distribution.....	211
5.4.1 <i>Lateral Distribution</i>	211
5.4.1.1 John Klein Drill Site.....	211
5.4.1.2 Cumberland Drill Site	212
5.4.1.3 Raised Ridges and Nodules.....	214
5.4.2 Vertical Distribution.....	214
5.4.2.1 Selwyn	215
5.4.2.2 Yellowknife Bay Egress.....	216
5.4.3 <i>Summary</i>	216
5.5 Chemical Composition of the Sheepbed Nodules	217
5.5.1 <i>APXS</i>	217
5.5.2 <i>ChemCam</i>	218
5.5.3 <i>Summary of Geochemical Results</i>	218
5.6 Discussion.....	220
5.6.1 <i>Petrogenesis of Sheepbed Nodules</i>	220
5.6.2 <i>Controls on Nodules Shape and Size</i>	223
5.6.3 <i>Controls on Nodule Spacing</i>	225
5.6.4 <i>Growth of Solid Nodules</i>	226
5.6.5 <i>Growth of Hollow Nodules</i>	228
5.6.6 <i>Timing of Concretions Formation</i>	233
5.6.7 <i>Nodules on Mars: Gale Crater vs. Meridiani Planum</i>	234
5.6.8 <i>Concretions and the Preservation of Martian Organics</i>	237
5.7 Conclusions.....	238
Notation.....	240
References.....	266
Appendix A:	
Auxiliary Material for Chapter 3.....	299
Introduction	299
Error Analysis.....	300
Appendix B:	
Auxiliary Material for Chapter 5.....	312
Introduction	312
Mastcam Image List	314

LIST OF TABLES AND FIGURES

Chapter 2:	<i>Page</i>
Table 2.1: Summary of Previous Regional and Global Studies	37
Table 2.2: Number of Crater Wall Versus Crater Fill/Mound Deposits	38
Figure Captions.....	39
Figure 2.1: Classification scheme.....	43
Figure 2.2: Example crater, canyon, and channel fill and mound deposits	44
Figure 2.3: Example crater, canyon, and channel wall and uplift deposits	45
Figure 2.4: Example intercrater plains deposits	46
Figure 2.5: Example “other” deposits	47
Figure 2.6: Example glacial/periglacial deposits	48
Figure 2.7: Reference maps	49
Figure 2.8: Global distributions of HiRISE image database and stratified images....	50
Figure 2.9: Geomorphic settings of stratified deposits	51
Figure 2.10: Mapped distribution of basin fill and unconfined bedrock deposits.....	52
Figure 2.11: Mapped distribution of basin fill and unconfined bedrock deposits by age	53
Figure 2.12: Bar plots of basin fill and unconfined bedrock deposits counts	54
Figure 2.13: Glacial/periglacial deposits	55
Figure 2.14: Map of global depositional processes.....	56
Chapter 3:	<i>Page</i>
Table 3.1: HiRISE DTMs and Orthoimages	105
Table 3.2: Study Sites	106
Table 3.3: Basic Bed Thickness Statistics	107
Table 3.4: Runs Test Significance Probability Values	108
Table 3.5: Lilliefors Probability Significance Values	109
Figure Captions.....	110
Figure 3.1: Representative distributions.....	115
Figure 3.2: Global reference map	116
Figure 3.3: Geomorphic context of study sites	116
Figure 3.4: Holden crater sections	117
Figure 3.5: Plateau west of Juventae sections	118
Figure 3.6: Gale crater sections	118
Figure 3.7: Additional sections.....	119
Figure 3.8: Bed orientation measurements.....	119
Figure 3.9: Holden bed thickness measurements.....	120
Figure 3.10: Plateau west of Juventae Chasma bed thickness measurements.....	121
Figure 3.11: Gale crater bed thickness measurements.....	122
Figure 3.12: Additional location bed thickness measurements	123
Figure 3.13: Histograms	124
Figure 3.14: Empirical and theoretical CDF plots	125
Figure 3.15: Log-log plots	126
Figure 3.16: Stratigraphy of a simple alluvial fan.....	127
Figure 3.17: Lilliefors test results.....	127

Chapter 4:	<i>Page</i>
Table 4.1: Constrained Model Coefficients	170
Table 4.2: Optimized Particle Diameter Ratios	171
Table 4.3: Modeled Mass Fractions Using Full Spectrum and Optimized Diameter Ratio	172
Table 4.4: Modeled Mass Fractions Using Partial Spectrum and Optimized Diameter Ratio	173
Figure Captions.....	174
Figure 4.1: Endmember photomicrographs and histograms.....	179
Figure 4.2: NIR diffuse reflectance spectra of all mixtures and endmembers	180
Figure 4.3: Reflectance band minima positions.....	181
Figure 4.4: Reflectance band depths	182
Figure 4.5: JCSS-3501 saponite and epsomite measured and modeled mixture spectra	183
Figure 4.6: SapCa-2 saponite and epsomite measured and modeled mixture spectra	183
Figure 4.7: NAu-2 nontronite and epsomite measured and modeled mixture spectra	184
Figure 4.8: SWa-1 nontronite and epsomite measured and modeled mixture spectra	184
Figure 4.9: SCa-3 montmorillonite and epsomite measured and modeled mixture spectra.....	185
Figure 4.10: SWy-2 montmorillonite and epsomite measured and modeled mixture spectra	185
Figure 4.11: Optimized particle diameter ratios for individual mixtures- full spectra	186
Figure 4.12: Modeled vs. measured mass fraction- full spectra, mean particle sizes	187
Figure 4.13: Modeled vs. measured mass fraction- full spectra, mode particle sizes	188
Figure 4.14: Modeled vs. measured mass fraction- full spectra, optimized particle sizes.....	189
Figure 4.15: Relative uncertainties- full spectra, optimized particle sizes	190
Figure 4.16: Optimized particle diameter ratios for individual mixtures- partial spectra	191
Figure 4.17: Modeled vs. measured mass fraction- partial spectra, mean particle sizes	192
Figure 4.18: Modeled vs. measured mass fraction- partial spectra, mode particle sizes	193
Figure 4.19: Modeled vs. measured mass fraction- partial spectra, optimized particle sizes	194
Figure 4.20: Relative uncertainties- partial spectra, optimized particle sizes	195
Chapter 5:	<i>Page</i>
Table 5.1: MAHLI Images Used to Measure Size, Shape, and Concentration of Nodules	241
Table 5.2: Nodule Size and Shape Statistics	242
Table 5.3: Wilcoxon Rank Sum Test Results	242
Table 5.4: Nearest Neighbor Statistics for Lateral Solid and Hollow/Filled Nodule Distributions	242

Table 5.5: ChemCam Comparison (wt. %) between Nodule-Rich vs. Nodule-Free Sheepbed	243
Figure Captions.....	244
Figure 5.1: Yellowknife Bay context image and stratigraphic column.....	250
Figure 5.2: MAHLI images of solid, hollow, and filled nodules	251
Figure 5.3: MAHLI targets from the Selwyn, John Klein, and Cumberland areas... <td>252</td>	252
Figure 5.4: Size frequency histograms.....	253
Figure 5.5: Plots of hollow nodule rim thickness versus hollow nodule interior void diameter	254
Figure 5.6: Navcam overhead projection showing mosaic footprints.....	255
Figure 5.7: Nodule distributions mapped in the John Klein drill site mosaic	256
Figure 5.8: Nodule distributions mapped in the Cumberland 1 mosaic	257
Figure 5.9: Nodule distributions mapped in the Cumberland 2 mosaic	258
Figure 5.10: Nodule distributions mapped in the Raised Ridges and Nodules mosaic	259
Figure 5.11: Boundary between upper and lower Sheepbed member.....	260
Figure 5.12: Nodule distributions mapped in the Selwyn mosaic	261
Figure 5.13: Nodule distributions mapped in the Yellowknife Bay Egress mosaic.....	262
Figure 5.14: APXS results	263
Figure 5.15: ChemCam results	264
Figure 5.16: Two models for hollow nodule and filled nodule formation	265

Appendix A:

Page

Table A1: Bed thickness orientation measurements	303
Table A2: 1 m orthoimage thinning and thickening results	310
Figure A1: Measured section topographic profiles	311

Appendix B:

Page

Figure B1: MAHLI image nodule traces	313
--	-----

ACRONYMNS

APXS. Alpha Particle X-Ray Spectrometer

CF. Cumulative Frequency

CFD. Cumulative Frequency Distribution

ChemCam. Chemistry and Camera

CheMin. Chemistry and Mineralogy

CRISM. Compact Reconnaissance Imaging Spectrometer

CTX. Context Camera

DTM. Digital Terrain Model

EP. Expected Precision

FTIR. Fourier Transform Infrared Spectrometer

GIS. Geographic Information System

GLM. Gale Lower Member

GMM. Gale Middle Member

GSD. Ground Sample Distance

GUM. Gale Upper Member

HiRISE. High Resolution Imaging Science Experiment

HRSC. High Resolution Stereo Camera

IR. Infrared

IRB. Infrared Red Blue-green

LIBS. Laser-Induced Breakdown Spectroscopy

MAHLI. Mars Hand Lens Imager

Mastcam. Mast Camera

MGS. Mars Global Surveyor

MLE. Maximum Likelihood Estimation

MOC. Mars Orbiter Camera

MOLA. Mars Orbiter Laser Altimeter

MSL. Mars Science Laboratory

Navcam. Navigation Camera

NIR. Near Infrared

OMEGA. Observatoire pour la Minéralogie, l’Eau, les Glaces et l’Activité

PIGWAD. Planetary Interative G.I.S.-on-the-Web Analyzable Database

RAM. Runs Against the Mean

RUD. Runs Up and Down

RMI. Remote Micro-Imager

RSM. Remote Sensing Mast

SAM. Sample Analysis at Mars

TES. Thermal Emission Spectrometer

THEMIS. Thermal Emission Imaging System

USGS. United States Geological Survey

WJ. West of Juventae Chasma

VNIR. Visible Near Infrared

C h a p t e r I

INTRODUCTION

1.1 A Golden Age of Mars Exploration

The past two decades have been a veritable golden age of Mars exploration due to the success of numerous unmanned orbital, landed, and rover missions. Instruments onboard these spacecraft have probed the atmosphere, surface, and interior of Mars, collecting myriad data sets that provide the opportunity to study Mars' geological history at a level of detail rivaled only by studies of the Earth and Moon. Prior to the phase of increased Mars exploration that began in the mid-1990s, the Mariner and Viking missions provided the first detailed view of the Martian surface. Mariner 9, the first spacecraft to go into orbit around another planet, returned images during the early 1970s of landforms representing a diversity of sedimentary, volcanic, glacial/periglacial, and impact-related processes that had once occurred on the Martian surface [Masursky, 1973]. Launched in 1975 to Utopia Planitia and Chryse Planitia, respectively, the Viking 1 and 2 missions each consisted of an orbiter and a lander. The Viking orbiters took more than 1,400 images of the surface of Mars while the landers carried out environmental and geophysical experiments and provided the first in-situ images of the Martian surface [Soffen, 1976; Arvidson *et al.*, 1989].

Heralding a new phase of Mars exploration were the 1996 launches of the Mars Global Surveyor (MGS) orbiter and Mars Pathfinder, a lander (Carl Sagan Memorial Station) and rover (Sojourner) sent to Ares Vallis [Golombek *et al.*, 1999]. Instruments

onboard MGS provided a global view of Mars' atmosphere, surface, and interior, and included a magnetometer, a gravity field experiment, the Mars Orbiter Camera (MOC), Mars Orbiter Laser Altimeter (MOLA), and the Thermal Emission Spectrometer (TES) [Albee *et al.*, 2001]. Mars Odyssey, a NASA orbiter launched in 2001, consisted of a gamma ray spectrometer, a radiation experiment, and the Thermal Emission Imaging System (THEMIS).

The Mars Exploration Rovers Spirit and Opportunity were launched in 2003 and landed on the surface of Mars in 2004 at Gusev crater and Meridiani Planum, respectively [Squyres *et al.*, 2003; Squyres *et al.*, 2004a, 2004b]. Spirit ceased communications and surface operations six years after landing, but Opportunity continues to operate on the surface of Mars today. The European Space Agency's first orbiter to another planet, the Mars Express orbiter, also launched in 2003 [Chicarro *et al.*, 2009]. The Mars Express payload consists of radio, atmospheric, and surface instruments including the High Resolution Stereo Camera (HRSC) and the Observatoire pour la Minéralogie, l'Eau, les Glaces et l'Activité, (OMEGA), a visible near-infrared (VNIR) imaging spectrometer. The Mars Reconnaissance Orbiter (MRO) was launched by NASA in 2005, and entered Mars orbit in 2006 [Zurek and Smrekar, 2007]. The payload of this orbiter includes the High Resolution Imaging Science Experiment (HiRISE), Compact Reconnaissance Imaging Spectrometer (CRISM), and Context Camera (CTX), as well as a radar probe, a radiometer, and a weather camera. Recent lander and rover missions to Mars include the Phoenix lander, launched in 2007 to the northern, midlatitude region of Vastitas Borealis [Smith *et al.*, 2009], and the Mars Science Laboratory (MSL) Curiosity rover which has been

exploring Gale crater since August of 2012 [Grotzinger *et al.*, 2012; Grotzinger *et al.*, 2014].

1.2 Sedimentary Rock Record of Mars

Images from Mariner 9 first revealed the existence of stratified deposits in the polar and mid-latitude regions of Mars [Murray *et al.*, 1972; Soderblom *et al.*, 1973; Cutts, 1973; Sharp, 1973], and results from the Viking lander [Arvidson *et al.*, 1989] and Pathfinder [Golombek *et al.*, 1999] suggested the past occurrence of aqueous sedimentary processes. Yet the widespread distribution of sedimentary rocks on Mars was not recognized until the start of the 21st century in a landmark paper by Malin and Edgett [2000]. Malin and Edgett [2000] used high-resolution MOC images onboard MGS to identify and map the distribution of sedimentary rocks on Mars, identifying a record of surface processes spanning several billion years.

Subsequent imaging over the past two decades by HRSC [Neukum *et al.*, 2004], MOC [Malin and Edgett, 2001], CTX, and HiRISE [McEwen *et al.*, 2010; Grotzinger and Milliken, 2012] shows these deposits occurring in diverse settings on Mars that represent eolian, fluvial, and possibly lacustrine depositional environments [Carr, 1996; Malin and Edgett, 2000; Squyres *et al.*, 2004b; Grotzinger *et al.*, 2011; Grotzinger and Milliken, 2012]. In addition, high-resolution mapping by visible and near-infrared orbital spectrometers has revealed a diversity of hydrated minerals including clays, sulfates, carbonates, and chlorides on the surface of Mars, suggesting a complex history of aqueous alteration and mineral precipitation in sedimentary environments [Poulet *et al.*, 2005;

Gendrin et al., 2005; Bibring et al., 2005, 2006; Mustard et al., 2008; Ehlmann et al., 2008; Osterloo et al., 2008; Murchie et al., 2009; Carter et al., 2013; Ehlmann and Edwards, 2014]. Recent in situ observations by the Mars Exploration Rovers Spirit and Opportunity [Squyres et al., 2004c; Grotzinger et al., 2005; Squyres et al., 2007; Arvidson et al., 2014] and by the Mars Science Laboratory Curiosity rover [Williams et al., 2013; Vaniman et al., 2014; McLennan et al., 2014; Ming et al., 2014; Grotzinger et al., 2014] have enabled outcrop-scale geological investigations of sedimentary rock record.

1.3 Dissertation Summary

With the advent of high resolution orbital and rover investigations of Mars described above, the study of Mars' sedimentary rock record can transition from an exploratory phase based primarily on qualitative observations to one in which quantitative analyses provide constraints on the evolution of depositional and diagenetic environments on Mars. The following chapters will illustrate how the synthesis of global data sets and the application of statistical methods to orbital, rover, and laboratory data can be used to advance our understanding of the Martian rock record.

A global inventory of stratified deposits on Mars is presented in Chapter 2. This global database is used with geologic maps employing relative crater age-dating techniques to better understand the diversity, global significance, and relative importance of various depositional processes through time and across the surface of Mars. Chapter 3 examines the statistical analysis of bed thickness; specifically, how these quantitative techniques can be adapted and applied to sedimentary strata on Mars while working within the constraints and

limitations of orbital data sets. This study explores ways in which orbital bed thickness measurements can provide an objective and quantitative approach for describing the depositional history of Martian stratified deposits. Chapter 4 presents a study of laboratory spectra of fine-grained mixtures of clay and sulfate minerals. This study assesses the ability of spectral mixing models to reproduce spectra of these mixtures and derive mineral abundances from mixture spectra. This study was undertaken in the laboratory, but its results are broadly applicable to the detection and quantification of hydrated minerals in sedimentary deposits on Mars. Chapter 5 presents a quantitative analysis of the size, shape, and spatial distribution of diagenetic nodules observed by the MSL Curiosity rover in Gale crater. Understanding the origin and distribution of nodules in the Sheepbed member is essential to reconstructing the diagenetic aqueous history of the Yellowknife Bay formation and assessing its potential habitability.

1.4 Data and Methods

1.4.1 *Spacecraft Instrument Data*

Data from the instruments described below are used in this dissertation.

1.4.1.1 Mars Orbiter Laser Altimeter (MOLA)

MOLA, one of five instruments onboard the MGS orbiter, collected altimetry data from the surface of Mars from 1996 to 2001. While in operation, MOLA created a global topographic map by sending infrared pulses at a rate of 10 Hertz and a spot size of 168 meters to the surface of Mars at an along track spacing of 300 meters [Smith *et al.*, 2001].

The altitude of the surface was measured by calculating the time elapsed between pulse emission from the instrument and signal return to the spacecraft's collection mirror after reflecting off the surface of Mars.

A MOLA topographic map created by Goddard Spaceflight Center at a resolution of 128 pixels per degree was used in Chapter 2 to identify the geomorphic setting of each stratified deposit identified in HiRISE images. This MOLA map was also used in Chapters 3 and 5 as a basemap for displaying the topographic setting of study sites. This map is available for download online at <http://webgis.wr.usgs.gov>, the United States Geological Survey (USGS) Planetary Interactive G.I.S.-on-the-Web Analyzable Database (PIGWAD).

1.4.1.2 Thermal Emission Imaging System (THEMIS)

The THEMIS camera was part of the payload onboard the Mars Odyssey orbiter which launched in April of 2001 and arrived at Mars in October of the same year. THEMIS images the surface of Mars with 5 visual bands at a resolution of 18 meters per pixel and with 10 infrared bands at a resolution of 100 meters per pixel to measure the thermal and compositional properties of the surface. A THEMIS Day IR basemap (100 meter per pixel resolution) produced by Arizona State University in 2010 is used in Chapters 2, 3, and 5 to display data, and is used together with the MOLA basemap to provide geomorphic context for observations and study sites. The most recent THEMIS Day IR mosaic basemap is available for download from the USGS PIGWAD at <http://webgis.usgs.gov>.

1.4.1.3 High Resolution Imaging Science Experiment (HiRISE)

The HiRISE camera onboard MRO is a three-mirror astigmatic reflecting telescope with a Cassegrain objective. Launched in 2005, HiRISE took its first image of the Martian surface in September 2006 at the highest level of detail ever achieved by an orbital camera. HiRISE images the surface of Mars at resolutions between 0.25-1.3 meters per pixel in red (panchromatic), blue-green (BG), and near infrared (NIR) wavelength bands, and can resolve objects on the order of 1 meter due to the high resolution and high signal-to-noise ratio achieved by the camera [McEwen *et al.*, 2007]. Since 2006, HiRISE has acquired nearly 30,000 images covering about 2% of the Martian surface.¹ HiRISE images of the same area on the surface taken at different look angles (stereo-pairs) can be used to make Digital Terrain Models (DTMs) with a post-spacing of 1-2 meters and vertical precision of tens of centimeters [Kirk *et al.*, 2008].

HiRISE images are used in Chapter 2 to identify and classify stratified deposits. In Chapter 3, HiRISE orthoimages and DTMs are used to measure bed thickness in stratified deposits. A HiRISE image is also used in Chapter 5 to display the location of MSL Curiosity rover targets. All HiRISE images used in this dissertation are available for download online from the Planetary Data System (PDS) at <https://pds.jpl.nasa.gov> or from the HiRISE website at <http://hirise.lpl.arizona.edu>. HiRISE DTMs used in this study are available for download from the HiRISE website at <http://hirise.lpl.arizona.edu/dtm>.

¹ Recent image coverage statistics were stated in a Smithsonian.com article by Magan Gambino titled, “This is Mars in Extremely High Resolution,” published online October 9, 2013, web.smithsonianjourneys.org.

1.4.1.4 Mars Science Laboratory (MSL) Curiosity Rover

The MSL mission to Gale crater launched in November of 2011 and successfully delivered the Curiosity rover to the surface of Mars in August of 2012. The payload of the Curiosity rover consists of a sophisticated suite of cameras, spectrometers, radiation detectors, and environmental and atmospheric sensors. Chapter 5 of this thesis presents new analysis of data from Mast Camera (Mastcam), Mars Hand Lens Imager (MAHLI), Alpha Particle X-Ray Spectrometer (APXS), and Chemistry and Camera (ChemCam) instrument, and uses images from the Navigation camera (Navcam) as a basemap. K. Stack performed the analysis of Mastcam and MAHLI data presented in Chapter 5; the APXS analysis was contributed by M. Schmidt and R. Lee and the ChemCam analysis was contributed by N. Mangold and M. Nakhon. K. Stack synthesized the results from all instruments.

The Navcam, Mastcam, and ChemCam instrument suites are located on the Curiosity Remote Sensing Mast (RSM). Navcam uses two 14.67 millimeter fixed-focal length lens cameras to provide stereo context images for traverse planning and image targeting with a 45 degree field of view and a pixel scale of 0.82 milliradians per pixel [Maki *et al.*, 2012]. Mastcam is composed of two multispectral cameras each with a different fixed focal length. The Mastcam-34 (M-34) camera has a 34 millimeter focal length and a 15 degree field of view, and the Mastcam-100 (M-100) camera has a 100 millimeter focal length and a 5.1 degree field of view [Grotzinger *et al.*, 2012]. ChemCam is a remote sensing instrument suite that employs Laser-Induced Breakdown Spectroscopy (LIBS) to measure the elemental composition of rock and soil samples located between

1.3-7 meters away from the rover mast [Maurice *et al.*, 2012; Wiens *et al.*, 2012]. The ChemCam laser has a spot size 0.35-0.55 millimeters in diameter and produces a plasma when interacting with a surface sample. The photon emission from this plasma can be used to detect major, minor, and trace elements with the ChemCam spectrometers. ChemCam also includes a Remote Micro-Imager (RMI) to provide context images with a 20 milliradian field of view and submillimeter pixel resolution.

Curiosity's MAHLI camera and APXS are mounted on the rover arm. MAHLI is a 2-megapixel focusable camera capable of imaging objects at working distances between 2.1 centimeters and infinity at a maximum resolution of ~14 micrometers [Edgett *et al.*, 2012]. At the minimum working distance, a MAHLI pixel is 14 by 14 micrometers and a full image measures 1600 by 1200 pixels. The APXS is mounted on the rover arm and uses a combination of X-ray fluorescence and particle-induced X-ray emission to measure the bulk chemical composition of rocks and soils [Campbell *et al.*, 2012].

1.4.2 Software

The data analysis presented in this dissertation was performed primarily with ArcGIS and MATLAB software packages. Excel, Adobe Illustrator, and ENVI were also used.

1.4.2.1 ArcGIS

Version 10.0 of Esri's ArcGIS geographic information system was used in Chapters 2, 3, and 5 to create global maps, measure bed thicknesses in orbital images, and to map the

distribution of nodules in rover images. The global stratified deposit database and geologic map shapefiles presented in Chapter 2 were plotted in ArcGIS on MOLA and THEMIS Mars 2000 equicylindrical projected basemaps. In Chapter 3, X , Y , and Z coordinates were extracted from HiRISE orthoimages and DTMs in ArcGIS to calculate bed orientation and bed thickness. In Chapter 5, the distribution and size of diagenetic nodules were mapped using Mastcam and MAHLI images loaded into ArcGIS. Spatial analyst tools provided in the software package were used to calculate the size and statistical distribution of the different nodule types.

1.4.2.2 MATLAB

All data plots (excluding maps produced in ArcGIS) presented in Chapters 3, 4, and 5 were created using MATLAB scripts written by K. Stack. The orientation of bedding planes measured in HiRISE images in Chapter 3 were calculated using a MATLAB script written by J. Metz [Metz, 2010] and modified by K. Stack and A. Hayes. Spectral unmixing was performed in Chapter 4 using a code written by R. Milliken and modified by K. Stack.

1.4.3 *Laboratory Instruments*

1.4.3.1 Fourier Transform Infrared Spectrometer (FTIR)

Near-infrared diffuse reflectance spectra of clay-sulfate powder mixtures described in Chapter 4 were acquired in the laboratory at Caltech under ambient conditions with a Nicolet Fourier transform infrared (FTIR) spectrometer. In Fourier transform spectroscopy a source of infrared energy is passed through an interferometer which uses a beam-splitter

to divide the incoming IR beam into two. One beam reflects off a flat mirror fixed in place while the other beam reflects off a mirror that moves relative to the beamsplitter. Once the beams reflect off their respective mirrors, they recombine to produce a signal called an interferogram. This signal is then reflected off the surface of the sample and passed on to the detector. A computer then uses a Fourier transform to convert the detected interferogram signal (intensity vs. time) into an absorption spectrum (intensity vs. optical path difference) scaled relative to a background spectrum. Analyzed data are in units of reflectance vs. wavelength.

GLOBAL DISTRIBUTION OF STRATIFIED ROCKS ON MARS

Abstract

This study examines more than 17,000 of the highest resolution images available of the Martian surface obtained by the Mars Reconnaissance Orbiter (MRO) High Resolution Imaging Science Experiment (HiRISE) to create a global inventory of stratified deposits on Mars. The utility of such an inventory is based on the concept that the geographical distribution and depositional setting of stratified rocks can be linked, even in a general way, to the processes and environments associated with their deposition and preservation. Also, the distribution of stratified deposits relative to terrains for which relative ages have been determined provides insight into when and for how long these processes and depositional environments persisted on the Martian surface. Stratified deposits occur predominantly in four geomorphic settings: impact craters, canyons, channels, and plains as either basin fill or unconfined stratified rocks. This study shows that stratified rocks are widespread across the surface of Mars in terrains of all ages, preserving a record of surface processes that spans nearly four billion years. The proportion of unconfined stratified rocks relative to basin-fill deposits is lower in the youngest Amazonian-aged terrains compared to older Noachian and Hesperian-aged terrains, a trend that is consistent with a decrease in sediment cycling and/or the strength of the near-surface hydrological cycle over time. This global inventory offers insight into the diversity, timing, and relative importance of depositional processes represented in the stratified Martian rock record and lays a foundation for future

stratigraphic correlations essential for refining and globally correlating a Martian geologic time scale.

2.1 Introduction

Stratification within the rock record represents a time series of depositional and erosional events in which rock volumes are bounded by surfaces of erosion or nondeposition [Blackwelder and Barrows, 1911; Wheeler, 1958, 1959; Sloss, 1963; Sadler, 1981; Christie-Blick and Driscoll, 1995]. Changes within these time series, whether related to the chemical, biological, or physical properties of the rocks, provide important insight into the evolution of depositional environments and processes on both local and global scales. The wealth of information recorded in stratified rocks also enables the correlation of spatially distinct deposits, a critical step in the development of a planet's geologic time scale [McLennan and Grotzinger, 2008; Grotzinger *et al.*, 2011; Grotzinger and Milliken, 2012].

Stratigraphy is most often associated with the study of the sedimentary rock record, particularly on Earth where 75% of the rocks exposed at the surface above sea level are sedimentary [Tarbuck *et al.*, 2004]. However, on Mars a variety of volcanic, glacial/periglacial, and impact processes also have the ability to produce stratification within the rock record. Therefore, a major goal of studying the stratified rock record of Mars is to better understand the relative importance and timing of these varied depositional processes throughout Mars' geologic history. The Martian rock record can also provide insight into the sediment cycling on Mars, including changes in sediment transport, supply,

and deposition through time, that are related to past climate, aqueous processes, and habitability of the Martian surface.

The widespread coverage of high-resolution images of the Martian surface now provides an opportunity to study the rock record of Mars at an unprecedented level of detail. Mariner 9 images returned during the early 1970s first revealed the existence of stratified deposits in the polar and mid-latitude regions of Mars, e.g. *Cutts* [1973], *Sharp* [1973]. It was nearly thirty more years before the widespread occurrence and global importance of sedimentary rocks on Mars was recognized by *Malin and Edgett* [2000] as a result of the high-resolution global imaging campaign of the Mars Global Surveyor (MGS) Mars Orbiter Camera (MOC) [*Malin and Edgett*, 2001]. Subsequent imaging over the past two decades has led to the discovery of a diversity of past surface processes, and images from MOC, High Resolution Stereo Camera (HRSC) [*Neukum et al.*, 2004], Context Imager (CTX), the High Resolution Imaging Science Experiment (HiRISE) [*McEwen et al.*, 2007], and in situ studies by rovers and landers [*Squyres et al.*, 2004a; *Grotzinger et al.*, 2005; *Jaumann et al.*, 2007; *Grotzinger et al.*, 2014] have provided abundant evidence for a myriad of past volcanic, impact, glacial/periglacial, and sedimentary processes occurring at the Martian surface.

A number of previous studies (summarized in Table 2.1) have used inventories of orbital observations on both local and global scales to study the origin and composition of deposits exposed at the present-day Mars surface. Those studies that focused on a global scale have generally employed lower resolution data sets than what is currently available today, i.e., *Edwards et al.* [2009] and *Bandfield et al.* [2013], or have focused on one

specific feature or class of features, i.e., *Williams* [2007] and *Caudill et al.* [2012]. Other studies employ the highest resolution image data available, but are focused on particular regions of Mars, i.e., *Quantin et al.* [2012] and *Salvatore and Christiansen* [2014]. Using an inventory of HiRISE images, *Grotzinger and Milliken* [2012] presented a global synthesis of inferred sedimentary deposits, and suggested an initial approach of recognizing “orbital facies,” defined by a limited range of distinctive attributes inherent to the strata themselves (Table 2.1). However, the *Grotzinger and Milliken* [2012] inventory goes no further than identifying several “type sections” representing each orbital facies. The global distribution and significance of each orbital facies is largely unknown. Applying the exact orbital facies of *Grotzinger and Milliken* [2012] on a global scale is difficult because analysis of VNIR spectral data is needed to identify several of their orbital facies, but the widespread classification of stratified rocks by geomorphic and depositional setting and terrain age is possible given the global coverage of high resolution topographic and image data sets.

Building specifically on the work of *Malin and Edgett* [2000] and *Grotzinger and Milliken* [2012], this study presents a comprehensive inventory of Martian stratified deposits using the highest resolution images available of the Martian surface. This inventory is classified by geomorphic and depositional setting, and compared with geologic maps employing relative crater age-dating with the goal of better understanding the diversity, global distribution, and relative importance of various depositional processes in contributing to the stratified rock record of Mars.

2.2 Data and Methods

2.2.1 Data

The HiRISE camera on-board the Mars Reconnaissance Orbiter (MRO) is a three-mirror astigmatic reflecting telescope with a Cassegrain objective that images the surface of Mars at scales between 0.25-1.3 meters per pixel [McEwen *et al.*, 2007]. HiRISE has three filters: red (panchromatic), blue-green (BG), and near infrared (NIR) wavelength bands, and can resolve objects on the order of 1 meter due to the high resolution and high signal-to-noise ratio achieved by the camera. Launched in 2005, MRO entered into Mars orbit in March of 2006, and HiRISE took its first image of the Martian surface in September 2006 at the highest level of detail ever achieved by an orbital camera. Since 2006, HiRISE has acquired nearly 30,000 images covering about 2% of the Martian surface.²

The HiRISE image database used in this study contains 17,073 HiRISE images acquired between September 2006-January 1, 2013 within the latitude range of 60 degrees north and south of the Martian equator. The polar and high latitude regions of Mars were excluded from this study because of the predominance of ice-related surface ‘mantling’ deposits and periglacial features in these regions of Mars that largely obscure bedrock outcrops [Milliken *et al.*, 2003; Head *et al.*, 2003; Edwards *et al.*, 2009]. The list of HiRISE images used here was obtained from the Planetary Data System (<https://pds.jpl.nasa.gov>) and organized according to latitude and longitude. Calibration images, dust-obscured images, and duplicate images, i.e., second image acquired as part of a stereo-pair or subsequent images identified explicitly by the HiRISE team as part of change detection

² Recent image coverage statistics were stated in a Smithsonian.com article by Magan Gambino titled, “This is Mars in Extremely High Resolution,” published online October 9, 2013, web.smithsonianjourneys.org.

monitoring campaigns, were excluded from the database. Not all duplicate images are listed as stereo pairs or change detection images, so some repeat images are present in the database, although an attempt was made to remove them when found. All HiRISE images in the database were viewed at full-resolution using links from the HiRISE website (<http://hirise.lpl.arizona.edu>), and the HiView application.

2.2.2 Image classification

The classification system used to compile the global database is illustrated in Figure 2.1. Each panchromatic image was first evaluated by visual inspection in the HiView application for evidence of rock deposits. Deposits were identified as indurated rock using the criteria of *Malin and Edgett* [2000], who used the presence of cliffs and escarpments, yardangs, faults and offsets, lack of blurring between beds of varying albedos, and paucity of windblown sand accumulations as evidence for induration. Stratification within the outcrops was identified by the presence of systematic alternations in brightness that were laterally traceable for ~10 meters or more, or by distinct shadowed, shelf-like topographic breaks in slope. If images contained a stratified deposit(s), the deposit(s) was then classified by geomorphic context using the location of the image footprint plotted on a Mars Orbital Laser Altimeter (MOLA) topographic basemap. The geomorphic context of each deposit was classified as crater interior, canyon/chasm/chaos/channel interior, intercrater plains, or as “other,” a category that includes crater ejecta, volcanic constructs, e.g., volcano scarps, flanks, or calderas, or miscellaneous features that fall outside of the main categories (Figures 2.2-2.6).

Deposits were also classified by setting within each broad geomorphic category (Figure 2.1). Basin fill deposits are those that appear to be topographically confined and include fills and mounds found within craters, canyons, chasms, and channels. Deposits that do not appear to be controlled by modern-day topography at the length-scale of individual crater or canyon basins are categorized as unconfined stratified rock and include wall and uplift deposits, plains deposits, and most examples within the “other” category. A designation of unconfined stratified rock does not mean that the deposits were never controlled by topography, rather it means that it is not possible to define this topographic control today. Also identified within the database are those stratified deposits suspected of being periglacial in origin due to the association of these deposits with dissected mantle terrain, i.e., *Mustard et al.* [2001] and *Milliken et al.* [2003], or the occurrence these deposits as concentric crater fills, lobate debris aprons, or lineated valley fills, e.g., *Squyres and Carr* [1986] and *Carr* [2001]. These deposits represent only those showing clear stratification in existing HiRISE coverage and are not meant to represent a comprehensive survey of all periglacial and viscous flow features on Mars, e.g., *Souness et al.* [2012].

Images that contain stratified deposits in more than one geomorphic context or depositional setting are book-kept multiple times within the database, once for each deposit setting or type found within the image. An example of this would be an image of an impact crater containing stratified wall exposures, a central uplift composed of steeply-dipping beds, and a layered interior mound. This image would be entered into the database three

times, once for each occurrence of a stratified rock exposure. These duplicate images are not counted towards the total number of images listed above, or presented in Figure 2.8.

2.2.3 Spatial Analysis

All images in the database (Figure 2.8a) and all images in the database containing stratified deposits (Figure 2.8c) were plotted on a THEMIS Day IR equicylindrical projection basemap as single points according to the center latitude and longitude of each image. Histograms (Figure 2.8e and 2.8f) and point densities (Figure 2.8b and 2.8d) were calculated from the database using the ArcGIS Spatial Analyst toolbox to assess the distribution of images and images containing stratified deposits across the surface of Mars, and to illustrate potential spatial sampling biases that may be inherent to the data set. Point densities were calculated in units of square degrees using a circular area around each point with a defined radius and map cell size of 1 degree.

In order to examine the distribution and setting of stratified deposits in terrains of different ages, the locations of identified stratified deposits were overlain on a geologic map of Noachian, Hesperian, and Amazonian-aged terrains compiled from Mars Global Geologic Map 1802ABC [Scott and Tanaka, 1986; Tanaka and Scott, 1987; Greeley and Guest, 1987] (Figure 2.7). The stratified deposit database was also grouped by geomorphic context and terrain age (Figure 2.9) and setting (basin fill vs. unconfined, Figures 2.10-2.12) and plotted on the geologic map to examine trends in the distribution, geomorphic setting, and deposit type in terrains of different age.

2.3 Results

2.3.1 *Global Distribution of Stratified Deposits*

Of the 17,073 HiRISE images examined in this study, 5,324 contain stratified rock in one or more geomorphic setting or deposit type (Figure 2.8). Counting images that have been double book-kept for the presence of stratified deposits in one or more settings, there are 5,781 unique stratified deposits observed in the HiRISE image inventory. Figures 2.8c and 2.8f show that stratified deposits occur ubiquitously throughout the latitude range from 60° N to 60° S, and are widespread over all longitudes. The histogram in Figure 2.8f shows a slight overall decrease in the number of images containing stratified deposits moving from the northern to southern hemispheres, but besides this weak trend there appears to be no clear latitudinal control on the distribution of stratified deposits that could not also be partially explained by the overall image distribution (Figure 2.8e), as described below.

Several regions show a particularly high density of images containing stratified deposits, including Valles Marineris, Meridiani Planum, Hellas basin, Aeolis Mensae, and the fretted terrains of Deuteronilus, Protonilus, Nilo Syrtis Mensae. Although stratified deposits are common and widespread in these regions, these areas of high concentration (Figure 2.8d) also coincide with the areas of highest image density (Figure 2.8b), suggesting that an image acquisition bias may be partly responsible for the density of images in this area. Histograms also show that latitude ranges containing a large number of images with stratified deposits also coincide with latitudes where the number of overall images taken is high. This is the case for the 0 to 20° S range, which includes the high density areas of Valles Marineris, Meridiani Planum, and Aeolis Mensae, as well as the 30-

40° S range, which includes images of stratified material in southern Terra Cimmeria and Terra Sirenum. In contrast, there is a disproportionate number of images in the 30-45° N range that contain stratified deposits relative to the overall number of images taken in this region. This suggests that the high concentration of images containing stratified deposits in the Deuteronilus, Protonilus, and Nilo Syrtis Mensae regions truly represents an abundance of stratified deposits present in this area that is not simply a reflection of an image acquisition bias in this area. Areas with a relatively low density of images containing stratified deposits include northern Terra Cimmeria and eastern Tyrrhenus Terra, Terra Sabaea, and northern Noachis Terra.

2.3.2 Geomorphic Setting of Stratified Deposits

Crater interiors are the most common and widespread settings in which stratified deposits are found on Mars (Figure 2.9b), and images containing stratified rocks in crater interiors occur at all latitude ranges. Plains deposits are the second most common setting for stratified deposits. These deposits are most prevalent in the northern hemisphere, and are concentrated around Valles Marineris, Meridiani Planum and western Arabia Terra, and near the dichotomy boundary in the fretted terrains of Deuteronilus, Protonilus, and Nilo Syrtis Mensae, Nili Fossae, and Aeolis Mensae. These fretted terrains contain an abundance of buttes and mesas; where these mesas form an interconnected network of valleys, they and any deposits between the mesas were identified as walls or fills in the canyon/chasm category, respectively. Where these deposits were isolated, and not clearly part of an interconnected network of mesas and buttes, they were identified as plains

deposits. Stratified plains deposits also occur throughout Elysium Planitia and the Tharsis region.

Canyon deposits are largely concentrated near the equator in Valles Marineris and in the northern hemisphere, particularly along the dichotomy boundary between the southern highlands and northern lowlands. Aside from areas of high density, canyon deposits are also observed to be fairly widespread throughout the Elysium Planitia and Tharsis regions, where layered lavas flows are frequently exposed in fissure and catena walls, both landforms tabulated in the canyon/chasm category. Aside from deposits north of Argyre Planitia, in the Uzboi-Margaritifer-Ladon system, and Niger and Dao Vallis in eastern Hellas Basin, canyon/chasm deposits are sparse below $\sim 15^{\circ}$ S. The “other” category of deposits, which includes volcanic constructs, crater ejecta, and odd features like the Acidalia mounds, are also largely limited to the northern lowlands.

As seen in Figure 2.9c, most of the stratified deposits found in craters are located in Noachian-aged terrains. This is not unexpected, as the oldest terrains on Mars are also the most heavily cratered. Accordingly, the percent of images containing stratified deposits in craters decreases systematically from Noachian (45%) to Hesperian (33%) to Amazonian-aged terrains (33%) (Figure 2.12). Canyon, chasm, and channel deposits are most often found in Hesperian-aged terrains (Figure 2.9c), and are concentrated around the Valles Marineris canyon system. Few images containing canyon or channel deposits are found in Noachian-aged terrains, consistent with the paucity of these deposits in the southern highlands of Mars. Plains deposits are found most commonly in the layered lavas that compose Amazonian-aged terrains, e.g., Tharsis region and Elysium Planitia, but also in

Noachian-aged terrains such as Meridiani Planum and in the plains north of Hellas basin. Very few of the “other” category of deposits are found in Noachian-age terrains, instead occurring nearly equally in terrains of Hesperian or Amazonian age. Again, this is not unexpected, as this category consists largely of volcanic constructs of Hesperian or Amazonian age and deposits associated with well-defined crater ejecta at the modern surface, where the latter is not likely to be preserved due to erosion for older Noachian craters.

2.3.3 Basin Fill versus Unconfined Stratified Deposits

The global distribution of basin fill deposits (fills and mounds) versus unconfined stratified deposits (wall, uplift, plains, and other deposits) is presented in Figures 2.10 and 2.11. In total, unconfined stratified deposits outnumber basin fill deposits (Figure 2.12b) and are widespread across the surface of Mars in terrains of all ages (Figure 2.10a and Figure 2.11a-2.11c). In contrast, basin fill deposits occur predominantly in the southern highlands in terrains of Noachian and Hesperian age, where they are fairly widespread (Figure 2.10b). In Amazonian-aged terrains, basin-fill deposits are localized to a few locations, including Valles Marineris, Dueteronilus, Protonilus, and Nilo Syrtis Mensae, and Elysium and Utopia Planitia. The plots in Figure 2.12 illustrate the changes in the global distribution and relative proportions of basin fill and unconfined stratified deposits in terrains of different age. The data exhibit an overall decrease in the percentage of basin fill deposits found in successively younger terrains (Figure 12a); 42% of all basin fill deposits are located in Noachian-aged terrains, 36% are found in Hesperian-aged regions,

and only 22% are found in Amazonian-aged terrains. In contrast, the percentage of unconfined stratified deposits, which consists predominantly of crater, canyon, and channel wall deposits, found in Noachian (30%), Hesperian (35%), and Amazonian (35%) terrains remains fairly constant (Figure 2.12a). The successive decrease in the proportion of basin fill deposits in younger terrains is also illustrated in Figure 2.12b, in which Noachian-aged terrains contain 40% basin fill deposits and 60% unconfined stratified deposits, while Amazonian terrains contain only 23% basin fill deposits and 77% unconfined stratified deposits.

2.3.4 Glacial/Periglacial Deposits

The distribution of all stratified deposits associated with dissected mantle terrain or viscous flow features, including concentric crater fills, lobate debris apron, or lineated valley fill, are presented in Figure 2.13. There is a clear latitudinal control on these deposits as they fall strictly between 30-60° bands N or S of the equator, with those deposits in the north outnumbering those in the south. The northern glacial/periglacial deposits occur in the northern lowlands and in high concentration at the dichotomy boundary within Dueteronilus and Nilo Syrtis Mensae. The southern deposits are sparsely distributed, with the only major concentration occurring within Hellas basin (Figure 2.6b).

2.4 Discussion

2.4.1 Global Distribution and Comparison to Previous Studies

The widespread occurrence of stratified deposits over the surface of Mars in terrains of all ages implies the preservation of a time series of discrete depositional events spanning nearly 4 billion years from the Noachian to Amazonian periods. The database compiled here shows that the stratified rock record of Mars is more extensively exposed than indicated by previous studies [*Malin and Edgett*, 2000; *Edwards et al.*, 2009; *Grotzinger and Milliken*, 2012] that took a similar global-scale approach. *Edwards et al.* [2009] used 100 meter per pixel THEMIS data to search for bedrock outcrops on the surface of Mars in crater and canyon walls, crater floors, and inter-crater plains, but stratification was not a required criterion for identification. Despite the stricter criteria for positive identifications used in this study, the lower resolution of THEMIS data and dust/sediment cover over much of the Martian surface above the equator prevented the identification of many of the outcrops included in this study's database. *Edwards et al.* [2009] described the relative paucity of bedrock outcrops observed on the surface of Mars in THEMIS data as indicative of global-scale crustal processing, presumably impact-related, capable of destroying most bedrock on Mars. However, the 0.25-0.50 meter per pixel resolution of HiRISE images permits the identification of small-scale outcrops even in the dustiest regions of Mars. Accordingly, this study finds stratified rock to be quite widespread on Mars, indicating that global-scale crustal processing need not be as prevalent as originally suggested by *Edwards et al.* [2009]. Indeed the presence of numerous stratified deposits in terrains of Noachian age indicates that information about

geological processes operating during early Martian history is preserved in the rock record, although the degree to which the observed strata simply represent impact-related processes remains unclear.

The global distribution of stratified deposits inventoried here is also much more widespread than that presented in *Malin and Edgett* [2000], although that mapping effort included only those deposits inferred to be sedimentary in origin based on criteria including induration, apparent fine grain-size, and the presence of repetitive bedding. Definitively quantifying grain-size is impossible even at the resolution of HiRISE, and repetitive bedding is difficult to define for thin deposits like those found in crater or canyon wall deposits. As a result, these distinctions were not made in this study's database, so the deposits identified herein include stratified deposits of sedimentary but also likely volcanic, glacial/periglacial, and impact origin. Additional work at a level of detail beyond the scope of this global database is likely needed to definitively distinguish sedimentary, volcanic, glacial/periglacial, or impact processes.

This study also finds stratified deposits to be more extensive than that of *Grotzinger and Milliken* [2012], who examined a smaller subset (~1/3) of the images included in the database presented here. *Grotzinger and Milliken* [2012] noted a concentration of stratified deposits near equatorial regions that is not observed in this larger database. The distribution of stratified deposits observed at higher latitudes observed in this study is more consistent with the identification of stratified deposits in high latitude regions also recognized by *Schon et al.* [2009]. Discrepancies between this study's database and that of *Grotzinger and Milliken*'s [2012] may be due to the smaller subset of images examined or the potential for

different criteria used to identify stratified deposits. Given the large number of images examined in the present study and their near-global distribution, the results presented here are a more accurate representation of the true global distribution of stratified deposits on Mars than previous studies based on more limited datasets.

2.4.2 Implications for the Martian Sediment and Hydrological Cycles

The inventory of basin fill versus unconfined stratified deposits presented in Figures 2.10-2.12 indicates basin filling materials are more commonly associated with the oldest Noachian-aged terrains relative to younger, Amazonian terrains in which unconfined stratified deposits are most prevalent. The following discussion will explore possible explanations for this observed trend, but first an important aspect of relative age dating on the surface of Mars must be considered.

Because in-situ absolute age dating techniques are not currently developed for widespread application on the surface of Mars, relative crater dating techniques [*Hartmann and Neukum, 2001*] are still the primary method of relative age dating on Mars. These techniques, which use the size and number of craters present on a surface to determine that surface's relative age, are relatively effective at determining regional-scale relative age relationships, but this method provides few age constraints on smaller-scale deposits, such as fills and mounds, found within craters or canyons. In other words, basin-fill deposits need not be the same relative age as the terrains in which they are currently located. For example, if a surface is found to be Noachian in age based on the number and size of craters found upon it, this Noachian "age" provides only an upper bound on the age of

deposits found within the craters of that surface. Therefore, basin-filling deposits observed in Noachian-aged terrains can only be robustly described as Noachian-aged or younger, while similar deposits found in Hesperian-aged terrains can only be constrained as Hesperian-aged or younger, unless specific cross-cutting relationships with other deposits of known relative age are observed or smaller-scale crater counts are attempted.

With this caveat considered, there is still a need to explain the apparent skew of basin fill deposits in older terrains observed in this database. One possibility is that basin filling deposits are preferentially found in older terrains simply because older terrains contain more topographic basins, i.e., craters in which deposits could accumulate. Although it is true that Hesperian and Amazonian-aged terrains are less heavily cratered than Noachian-aged terrains, the younger terrains do still contain craters, canyon and channel systems, as well as fossae, grabens, and catenas in close proximity to major volcanic centers, all of which could have served as depocenters for basin-filling sediments. In addition, the disparity between the number of images containing stratified crater wall deposits and the number containing fills and mounds (Table 2.2) suggests that within the areas covered by images in this database, crater wall deposits are more prevalent than crater fill/mound deposits for Hesperian and Amazonian-aged terrains. This disparity implies that there is a large proportion of crater basins (~50% for Amazonian-aged terrains, considering that some craters contain both wall and fill deposits) that could have been filled by stratified deposits, but are not. Since Hesperian and Amazonian-aged terrains tend to be lower in elevation than Noachian-aged terrains, one might expect sediment infill to be more likely in younger craters if sedimentation was steady and continuous through time. Instead,

there is an apparent bias of crater-filling deposits in higher elevation Noachian terrains. Therefore, the decreased availability of topographic basins in younger terrains on Mars is not a likely explanation for the skew of basin-filling deposits towards older terrains.

Alternatively, if the age of the basin-filling deposits is comparable to the age of the terrains in which they are located, the predominance of stratified basin-filling deposits in older terrains with successively fewer basin-filling deposits in Hesperian and Amazonian terrains, could be broadly representative of global-scale changes in the sediment cycle through time. *Grotzinger et al.* [2011] and *Grotzinger and Milliken* [2012] presented a conceptual model in which volcanic activity and the higher rate of impact cratering early in Mars' history resulted in an increased flux of sediment. In this model, a more active cycle of sediment production, erosion, and deposition during the Noachian and early Hesperian could have led to the fairly widespread deposition of stratified sedimentary deposits in the oldest craters and canyons. *Golombek and Bridges* [2000] and *Golombek et al.* [2006] also suggested a decrease in the Martian sediment cycle, using data from the Pathfinder and Mars Exploration Rover landing sites extrapolated to the entire planet to show a 4-6 fold decrease in erosion rates during the Hesperian and Amazonian periods compared to the late Noachian/early Hesperian. These studies proposed a largely conceptual model. The skew of basin fill deposits in older terrains observed in this study's global dataset can support this conceptual model with observations.

The predominance of stratified basin-filling deposits in older terrains could also represent the manifestation of a more active hydrological cycle during the late Noachian and early Hesperian when the ground water table was shallow enough to allow the

widespread lithification and cementation of basin-filling sedimentary deposits, i.e., *Andrews-Hanna et al.* [2010]. The transition to arid conditions during the Late Noachian [Andrews-Hanna and Lewis, 2011] associated with the loss of water and a deepening of the water table would have prevented the widespread preservation of stratified sedimentary deposits in younger terrains on Mars even if the sedimentary cycle had remained active into the Amazonian.

2.4.3 Global-Scale Depositional Processes on Mars

Conclusively distinguishing between sedimentary, volcanic, glacial/periglacial, and impact origins for Martian stratified deposits requires detailed observations at a scale not possible in even the highest resolution orbital images available. Making these distinctions can be challenging even with in situ observations from sophisticated rover payloads [Grotzinger et al., 2014]. In many cases, a synthesis of orbital and rover observations and geochemical and image data is needed to reconstruct the depositional history of a sequence of rocks. Yet one of the major reasons for creating a comprehensive inventory of stratified deposits was to gain insight into the processes responsible for the deposition of the Martian rock record. Examining the distribution of stratified deposits in specific geomorphic settings with respect to major volcanic centers, predicted pyroclastic deposits, and regions where glacial/periglacial processes occur (Figure 2.14), can provide some basic constraints on the relative importance of these processes in the development of Mars' rock record.

The widespread global distribution of stratified deposits on Mars, particularly unconfined stratified deposits exposed in crater and canyon wall outcrops, implicates

depositional processes operating on planet-wide scales. The location of major volcanic centers relative to the global distribution of stratified deposits (Figure 2.14) suggests that many of the stratified deposits in Amazonian-aged terrains, particularly those in the vicinity of these volcanic centers, can be explained by effusive lava flows. Examples of stratified lavas can be found in the global database, particularly in the layered scarps and flanks of the major Martian volcanoes, stratified lobes of lavas in plains in the Tharsis region and Elysium Planitia, and in the stratigraphy preserved in the walls of catenas, pit craters, and fissures in close proximity to these major volcanic centers (Figure 2.14). These findings are consistent with those of *Bandfield et al.* [2013], who find a predominance of blocky effusive lavas in younger, Amazonian-aged terrains. Pyroclastic volcanism, as proposed by *Kerber et al.* [2012] and *Bandfield et al.* [2013], may be more effective at widespread distribution of material over the surface of Mars. Isopach maps of predicted pyroclastic deposit thickness produced by *Kerber et al.* [2012] plotted together with this study's stratified deposit database (Figure 2.14) show that many stratified deposits fit within the predicted regions of thick pyroclastic deposition. Approximately 3000 stratified deposits are located in regions near major volcanic centers and in areas of predicted thick pyroclastic deposition (Figure 2.14), suggesting that ~50% of all observed stratified deposits could be reasonably explained by extrusive volcanic processes. However, as *Kerber et al.* noted and can be seen in Figure 2.14, models of pyroclastic accumulation and proximity to volcanic regions cannot fully explain the distribution of stratified deposits, including some of the most widespread and conspicuous deposits in Arabia Terra and Meridiani Planum.

Glacial/periglacial processes can partially explain the distribution of stratified deposits, particularly at latitude ranges greater than 30° N and S, where these processes are known to occur [Milliken *et al.*, 2003; Head *et al.*, 2003; Schon *et al.*, 2009]. Approximately 400 basin fill and intercrater plains deposits observed in the database are associated with glacial/periglacial features, but nearly half (43%) of the entire inventory of 5,777 stratified deposits is located between 30-60° N or S in regions known to host numerous glacier-like forms [Souness *et al.*, 2012]. Of course not all of the deposits observed in these latitude ranges exhibit evidence for glacial processes, but the predominance of stratified deposits in these regions suggests that low temperature processes are important, and perhaps underappreciated, contributors to the stratified rock record of Mars.

Quantifying the relative importance of sedimentary processes to the Martian rock record is particularly challenging because unique criteria for the identification of sedimentary rocks in orbital images have not been established. Furthermore, predicting the global distribution of sedimentary rocks is made difficult by the variety of processes that can produce and transport sedimentary materials on both local and global scales. However, the database presented here can provide some initial quantitative constraints on the relative importance of sedimentary processes. Of the 5,781 total stratified deposits observed in the HiRISE database, 1,856 are basin fill deposits. Basin fill deposits need not be sedimentary in origin, but their occurrence in defined topographic basins suggests the transport and deposition of material. Furthermore, examples in the database where stratified basin fills are suspected to be layered lava flows are rare. Rather, most basin fills are similar to the

examples presented in Figure 2.2a-2.2h and Figure 2.6, and are most likely formed by sedimentary, glacial/periglacial, or volcaniclastic processes. In addition approximately half of all observed intercrater plains (~700 deposits) and wall/uplift deposits (~1000) are located in regions with no nearby volcanic centers, where predicted pyroclastic accumulation is fairly low (Figure 2.14). The basin fill deposits together with the intercrater plains and wall/uplift deposits not located near major volcanic centers make up ~50% of the deposits observed in this study, and represent an initial estimate for the contribution of sedimentary processes, although the ~400 deposits of glacial/periglacial origin are also included in this value. As mentioned above, in situ observations are likely needed to make more conclusive process-based distinctions. Still, the widespread occurrence of basin-fill deposits, particularly in the oldest terrains of Mars, where predicted pyroclastic accumulations are low and evidence for glacial/periglacial processes is sparse, requires the likely widespread occurrence of eolian, fluvial, and/or lacustrine sedimentary processes.

In summary, sedimentary and periglacial/glacial processes account for at least half of the stratified rock record of Mars. The other half of the deposits observed in the database (primarily crater and canyon wall deposits in the unconfined basin classification) could be reasonably explained by extrusive volcanic processes. Periglacial/glacial processes may be important contributors to the occurrence of stratified deposits observed at latitudes above 30°. The role of impact processes as a producer and transporter of sediment remains unquantified, and additional work is needed to understand the relative importance of impact processes in relation to the processes described above.

In the absence of widely applicable absolute age dating techniques on Mars, high-resolution image data sets and spectral observations become the primary tools for correlating spatially distinct deposits. However, on a largely basaltic planet such as Mars, mineral assemblages need not uniquely reflect one particular depositional process or time period, and may only be applicable for stratigraphic correlations in the most general sense, i.e., *Bibring et al.*, [2006]. The global distribution of stratified deposits presented here can aid in identifying regions on Mars where orbital stratigraphic correlations may be most successful. For example, high-density areas of unconfined stratified deposits in terrains of similar age may allow successful correlations between spatially distinct crater and canyon wall deposits. Good candidates for this type of future analysis include Noachian-aged terrains in Terra Cimmeria, Terra Sirenum, Meridiani Planum, and Western Arabia Terra, Hesperian deposits in Valles Marineris, and Amazonian-aged terrains in Elysium, Utopia, and Deuteronilus Mensae.

The HiRISE database presented here provides a framework for more detailed stratigraphic correlations based primarily on physical characteristics observed in the rocks, but image-based stratigraphy has obvious limits, particularly concerning absolute age correlations. The future construction of an absolute geologic time scale for Mars will require geochronological studies carried out by rovers and landers at a local scale, i.e., *Farley et al.* [2014].

2.5 Conclusions

This study presents the most comprehensive and highest resolution database of stratified deposits yet compiled for Mars. This database shows that:

- (1) Stratified deposits occur globally on Mars throughout terrains of Noachian, Hesperian, and Amazonian age.
- (2) Stratified deposits are found most commonly in craters, but canyons/chasms, channels, and plains provide additional geomorphic settings in which stratified deposits occur.
- (3) Unconfined stratified deposits (crater walls, uplifts, plains deposits) occur ubiquitously on the surface of Mars and generally outnumber basin-filling deposits.
- (4) Basin-filling materials are slightly skewed towards Noachian-aged terrains. This trend is consistent with decreased activity of the sedimentary cycle over time, or a bias towards preservation of older basin-filling deposits.
- (5) Extrusive volcanic processes can reasonably explain about half of the stratified deposits observed at the surface of Mars today. Sedimentary and glacial/periglacial processes are likely responsible for producing the remaining stratified deposits presented here, and glacial/periglacial processes are particularly important at high latitudes. Still, eolian and/or aqueous sedimentation on regional scales is needed to fully explain the distribution of stratified deposits in mid-latitude regions.

(6) The global inventory presented here can be used to identify high-density areas of stratified rock where correlative stratigraphy can be attempted, but absolute age correlations require *in situ* geochronology.

TABLES

Table 2.1. Summary of Previous Regional and Global Studies

	Dataset	Image Resolution	Map Extent	Mapped Deposit(s)	Geomorphic Distinctions
<i>Malin and Edgett [2000]</i>	MOC	3-12 m	Global	All light, intermediate, dark-toned layered, massive, and thin mesa deposits inferred to be sedimentary in origin	Distinguished crater interiors, intercrater terrain, chaotic terrain, chasm interiors within paper text, but deposit settings were not mapped
<i>Milliken et al. [2003]</i>	MOC	3-12 m	Global (90 °N -90 °S)	Dissected terrain, viscous flow features, gullies	Gullies
<i>Williams [2007]</i>	MOC THEMIS IR THEMIS NIR	0.5-12 m 100 m 18-36 m	Global (57 °N -57 °S)	Raised curvilinear features	-
<i>Edwards et al. [2009]</i>	THEMIS Nighttime	100 m	Global (75 °N -75 °S)	All bedrock (high thermal inertia exposures)	Crater and canyon walls, crater floors, inter-crater plains
<i>Schon et al. (2009)</i>	HiRISE MOC	0.25-0.5 m 3-12 m	Southern hemisphere (25-50 °S)	Exposures of layering in association with sublimation pitting	-
<i>Tornabene et al. (2010)</i>	CTX HiRISE	~5 m 0.25-0.5 m	Global	Crater-exposed bedrock including mega breccias; central peaks; fractured bedrock; intact stratigraphy	Craters
<i>Ehlmann et al. [2011]; Ehlmann and Edwards [2014]</i>	CRISM Hyperspectral		Global	Aqueous mineral deposits (phylllosilicates, silica, chlorides, carbonates, sulfates)	-
<i>Caudill et al. [2012]</i>	HiRISE	0.25-0.5 m	Global (70 °N -70 °S)	Craters containing bedrock exposures; craters containing no bedrock exposures	Craters
				Layered and massive bedrock in crater central uplifts	Crater central uplifts
<i>Quantin et al. [2012]</i>	HiRISE CRISM Hyperspectral	0.25-0.5 m 18-36 m	Valles Marineris region (3-37 °N, 93-25 °W)	Massive or layered bedrock in craters	Craters
<i>Carter et al. [2013]</i>	CRISM Hyperspectral OMEGA	18m and 100-200 m 4.1 km- 350 m	Global	Hydrous minerals on Mars	
<i>Grotzinger and Milliken [2012]</i>	HiRISE MOC	0.25-0.5 m 3-12 m	Global (60 °N -60 °S)	All images containing stratified deposits All images containing image description "light-toned" or "layered"	Distinguished underfilled basins, overfilled craters, chasm and canyon systems, plains covering deposits, and very ancient strata within paper text, but deposit settings were not mapped
<i>Bandfield et al. [2013]</i>	THEMIS Nighttime	100m	Global	All bedrock (high thermal inertia exposures) after Edwards et al. (2009)	Distinguished Valles Marineris, channels and plains surfaces, craters, landing sites, and meteorites within paper text, but deposit types were not mapped
<i>Harrison et al. [2014]</i>	CTX	6 m	Global	Gullied landforms and their orientation	Gullies
<i>Salvatore and Christiansen [2014]</i>	HiRISE	0.25-0.5 m	Chryse and Acidalia Regions (20-50 °N, 310-360 °E)	Occurrences of a discrete stratified unit	Craters
THIS STUDY	HiRISE	0.25-0.5 m	Global (60 °N -60 °S)	All images containing stratified deposits	Craters (fill/mounds, walls, uplifts); Canyons/Chasms (fill/mounds, walls, uplifts); Channels (fill/mounds, walls); Plains; Other (crater ejecta; volcanic constructs, misc.); Periglacial/glacial deposits

Table 2.2. Number of Crater Wall versus Crater Fill/Mound Deposits

Terrain Age	# of Images Containing:	
	Crater Walls	Crater Fills/Mounds
Amazonian	408	213
Hesperian	535	354
Noachian	578	683

FIGURE CAPTIONS

Figure 2.1. Classification scheme applied to each image in the dataset.

Figure 2.2. Example basin fill deposits found in craters, canyons, and channels in HiRISE IRB color images (left) located on MOLA topography (right). (a) Terby crater, PSP_002216_1525, (b) Danielson crater, ESP_026626_1885, (c) Eberwalde crater, PSP_001336_1560, (d) Cross crater, ESP_016175_1495, (e) Ius Chasma, ESP_021552_1725, (f) Juventae Chasma, ESP_016712_1760, (g) Melas Chasma, ESP_012638_1700, (h) Nilo Syrtis Mensae, ESP_028509_2140, (i) Athabasca Vallis, ESP_027042_1895, (j) Shalbatana Vallis, ESP_030135_1830.

Figure 2.3. Crater, canyon/chasm, and channel wall and uplift deposits. HiRISE IRB color (left), MOLA topography (right). (a) Crater in Tempe Terra, ESP_012611_2170, (b) Unknown crater, ESP_016163_1395, (c) Martin crater, ESP_011952_1585, (d) Crater in Lunae Planum, ESP_017833_1975, (e) Mawrth Vallis, ESP_018530_2045, (f) Capri Chasma, ESP_018017_1680, (g) Lethe Vallis, PSP_007553_1845.

Figure 2.4. Example plains deposits. HiRISE IRB color (left), MOLA topography (right). (a) Juventae plains, PSP_003579_1755, (b) Melas Plains, ESP_011359_1695, (c) Sinus Meridiani, ESP_026995_1830, (d) Aeolis Planum, ESP_018102_1775.

Figure 2.5. Examples of volcanic constructs, crater ejecta, and miscellaneous other deposits. HiRISE IRB color image (left), MOLA topography (right). (a) Ceraunius Catena, PSP_007022_2175, (b) Olympus Mons scarp, ESP_013998_2035, (c) Olympus Mons caldera, PSP_007669_1980, (d) Ascraeus Mons caldera, ESP_026313_1910, (e) Layered ejecta of Kontum crater, ESP_028435_1480, (f) Layered ejecta of Toro crater, ESP_029867_1980, (g) Mound in Xanthe Dorsa, ESP_025822_2165.

Figure 2.6. Examples of glacial/periglacial deposits. HiRISE IRB color (left), MOLA topography (right). (a) Concentric crater fill in unknown crater, PSP_007022_2175, (b) Swirly layers in Hellas basin, ESP_025635_1395, (c) Valley fill in Mamers Vallis, ESP_013254_2115.

Figure 2.7. (a) MOLA elevation draped on THEMIS Day IR showing place names mentioned in this chapter. (b) Timescale showing approximate ages of Noachian, Hesperian, and Amazonian periods and geologic map of Noachian, Hesperian, and Amazonian aged terrains from Mars Global Geologic Map 1802ABC [Scott and Tanaka, 1986; Tanaka and Scott, 1987; Greeley and Guest, 1987].

Figure 2.8. (a) Entire database of HiRISE images used in this study. (b) Image density plotted on a THEMIS Day IR basemap. (c) All HiRISE images containing stratified deposits plotted on MOLA topography. (d) Density of images containing stratified deposits plotted on a THEMIS Day IR basemap. Note correlations between high density areas in

this map and the map in (b). (e) Latitude histogram plotted for all images in the database. (f) Latitude histogram plotted for all images containing stratified deposits.

Figure 2.9. (a) Images containing stratified deposits, color coded by geomorphic setting plotted on geologic map of Noachian, Hesperian, and Amazonian-aged terrains. (b) Histogram showing the number of images containing deposits in craters, canyon/chasms, channels, plains, and other. (c) Bar graph showing the percent of images within each geomorphic setting category within Noachian, Hesperian, and Amazonian terrains. Note that canyons/chasms and channels have been counted together in this graph.

Figure 2.10. (a) All unconfined stratified deposits plotted on geologic map of Noachian, Hesperian, and Amazonian-aged terrains. (b) All basin fill deposits. (c) Basin fill and unconfined stratified deposits plotted together.

Figure 2.11. (a) Images containing unconfined stratified deposits plotted on mapped Amazonian-aged terrains (left), images containing stratified basin fill deposits plotted on Amazonian-aged terrains (right), (b) Images containing unconfined stratified deposits plotted on mapped Hesperian-aged terrains (left), images containing stratified basin fill deposits plotted on Hesperian-aged terrains (right). (c) Images containing unconfined stratified deposits plotted on mapped Noachian-aged terrains (left), images containing stratified basin fill deposits plotted on Noachian-aged terrains (right).

Figure 2.12. (a) Bar graph showing the percent of images located in Noachian, Hesperian, or Amazonian aged terrains, grouped by setting type (basin fill or unconfined stratified deposits). (c) Bar graph showing percent of images that contain unconfined stratified or basin fill deposits, grouped by terrain age.

Figure 2.13. Distribution of images containing stratified deposits associated with glacial/periglacial landforms.

Figure 2.14. Database of images containing stratified deposits plotted in relation to major volcanic centers (red triangles), latitude ranges of glacial/periglacial process (blue bars), and isopach map of *Kerber et al.* [2012] showing the modeled thickness of pyroclastic deposit thickness if every major volcanic center erupted at the same time. Areas in close proximity to major volcanic centers with expected thick accumulations of pyroclastic deposits (after *Kerber et al.* [2012]) are outlined in red. These areas represent the major regions on Mars where stratified deposits of volcanic origin are likely to occur.

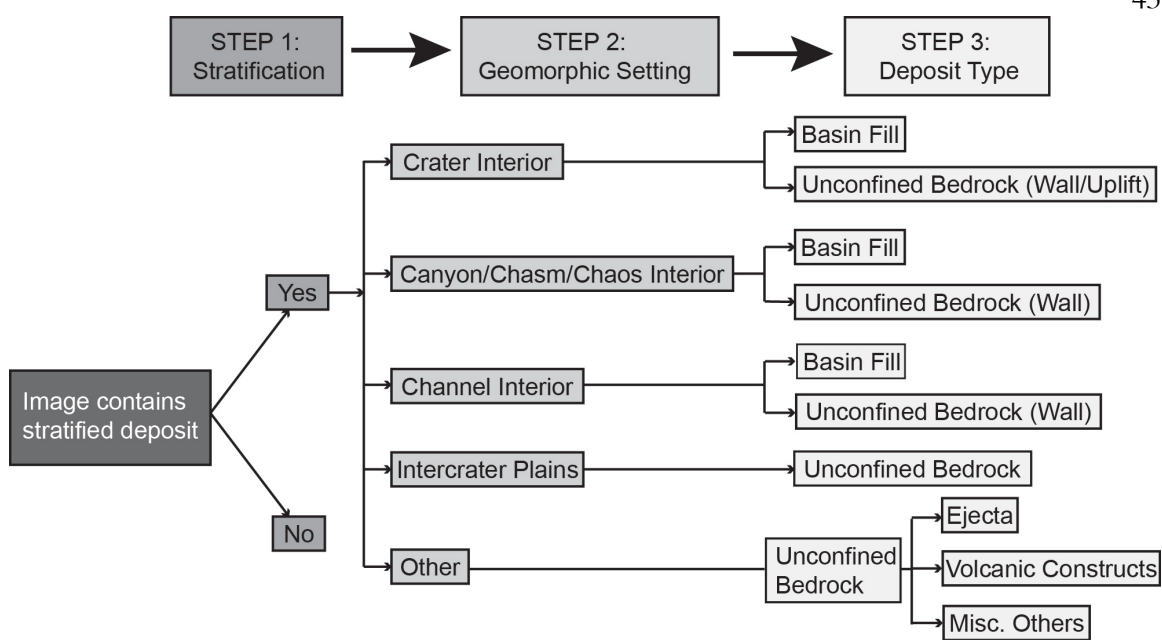
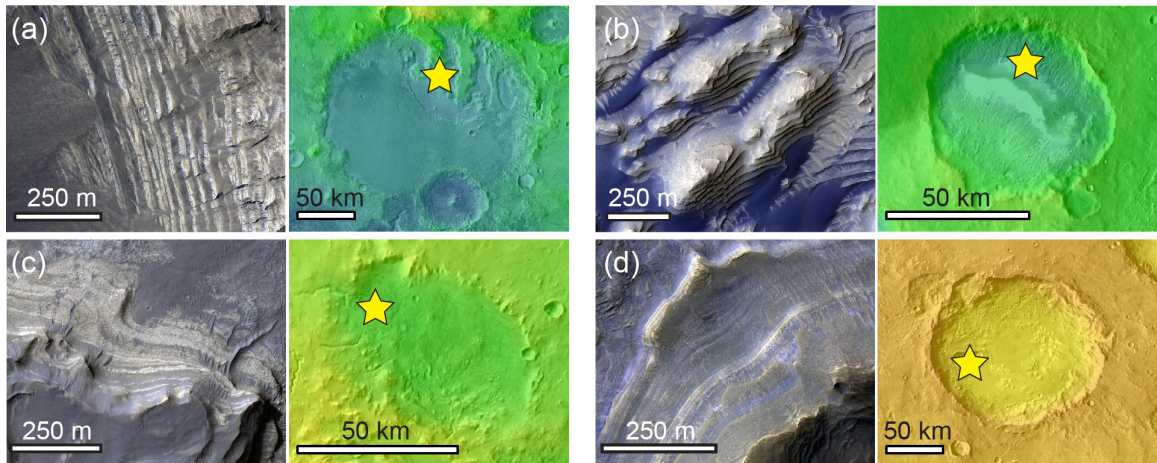
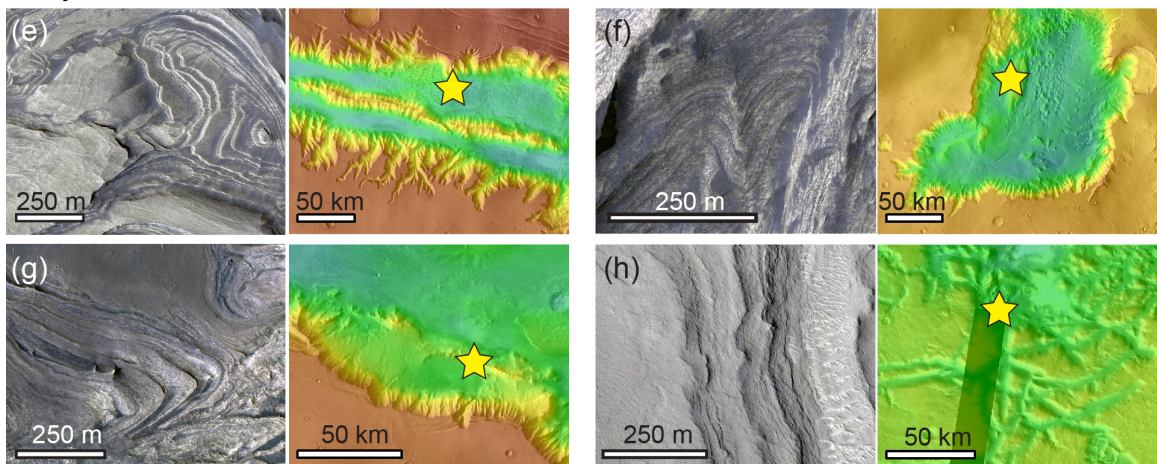


Figure 2.1

Crater Fills and Mounds



Canyon Fills and Mounds



Channel Fills and Mounds

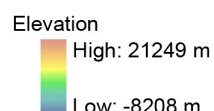
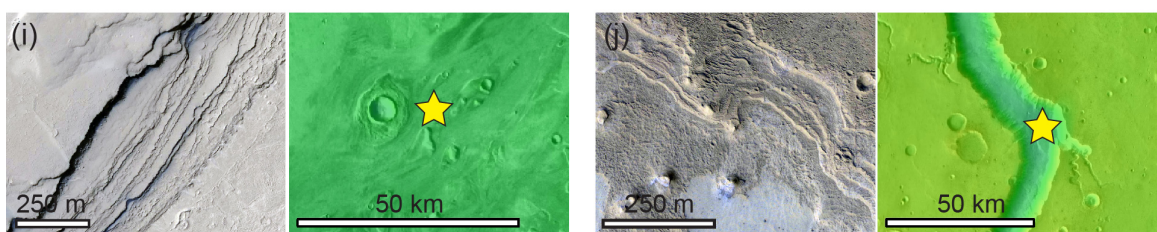
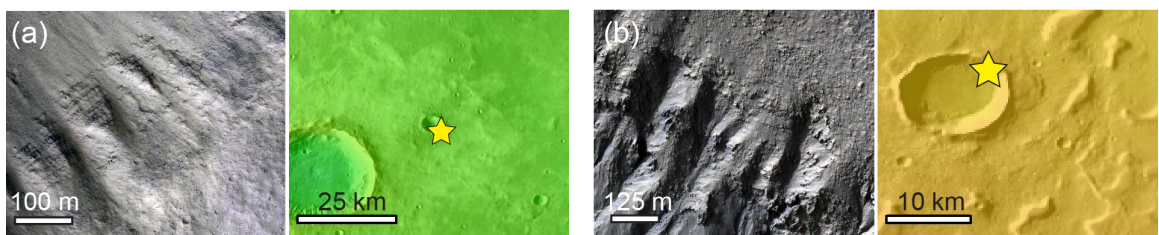
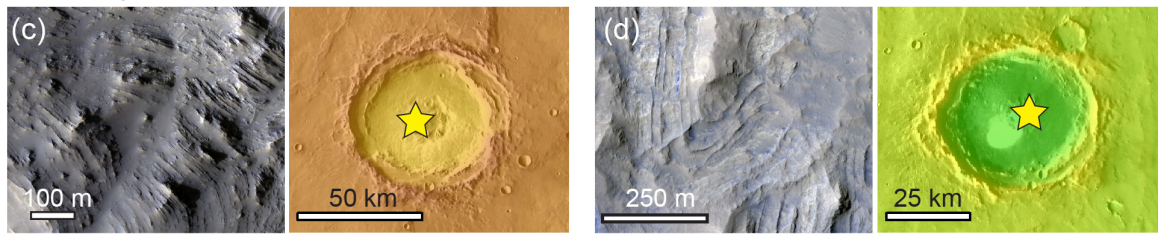


Figure 2.2

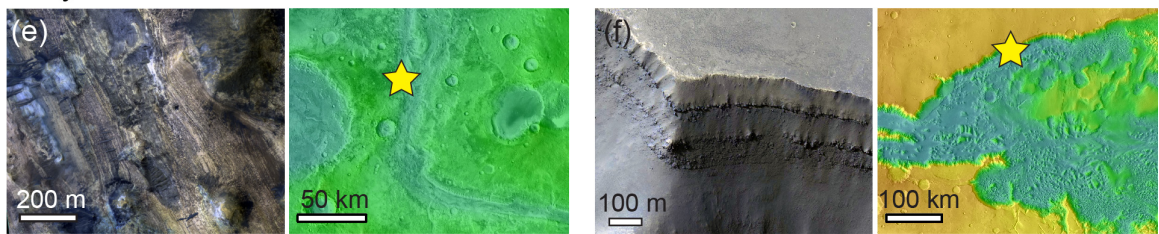
Crater Walls



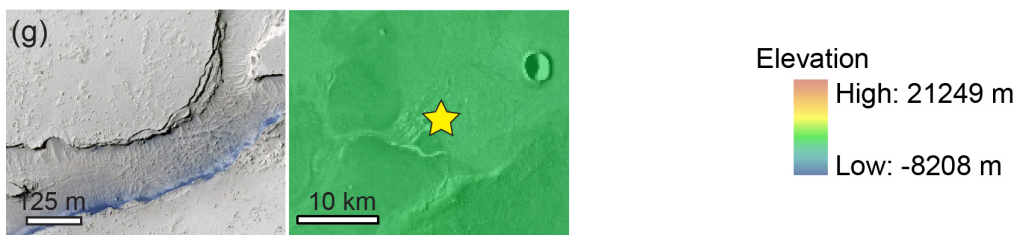
Crater Uplifts



Canyon/Chasm Walls



Channel Walls



Elevation

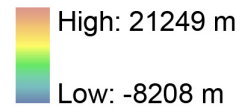


Figure 2.3

Intercrater Plains

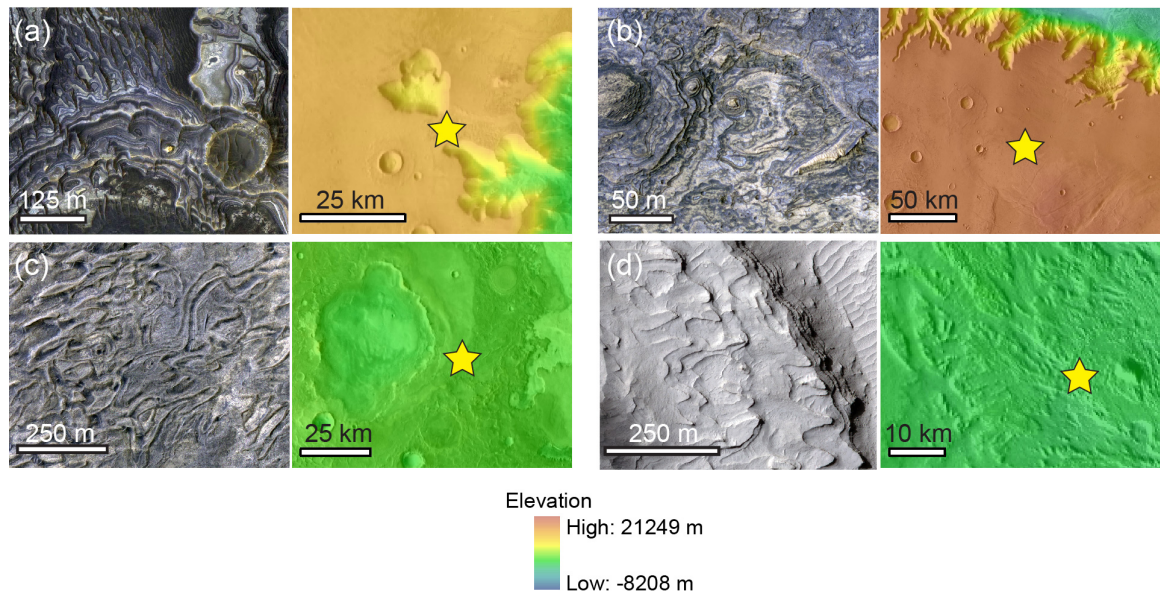
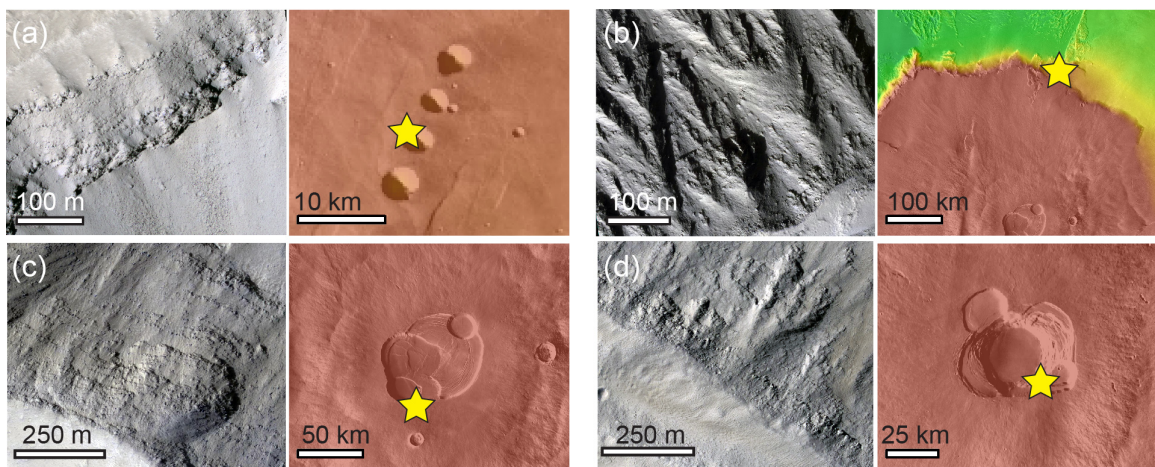
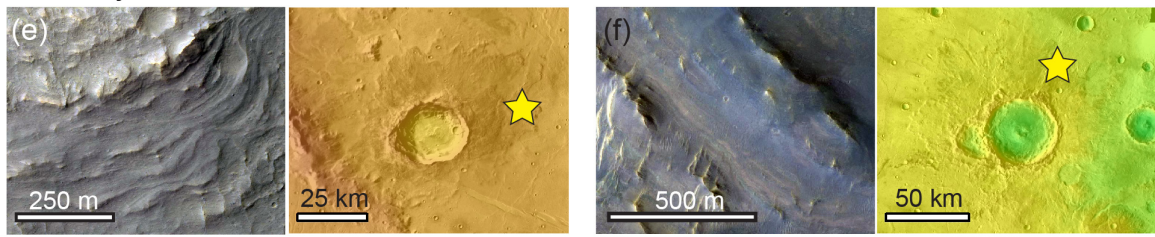


Figure 2.4

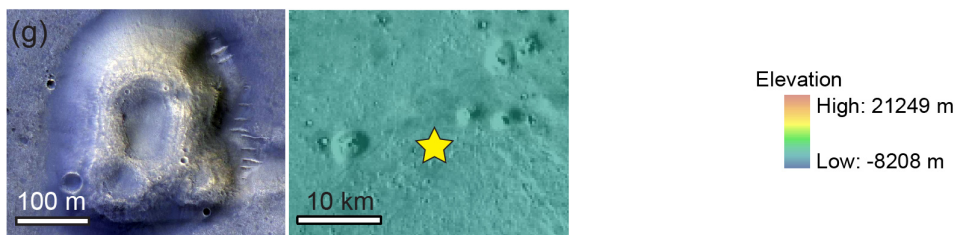
Volcanic Constructs



Crater Ejecta



Miscellaneous Other



Elevation
 High: 21249 m
 Low: -8208 m

Figure 2.5

Glacial/Periglacial Features

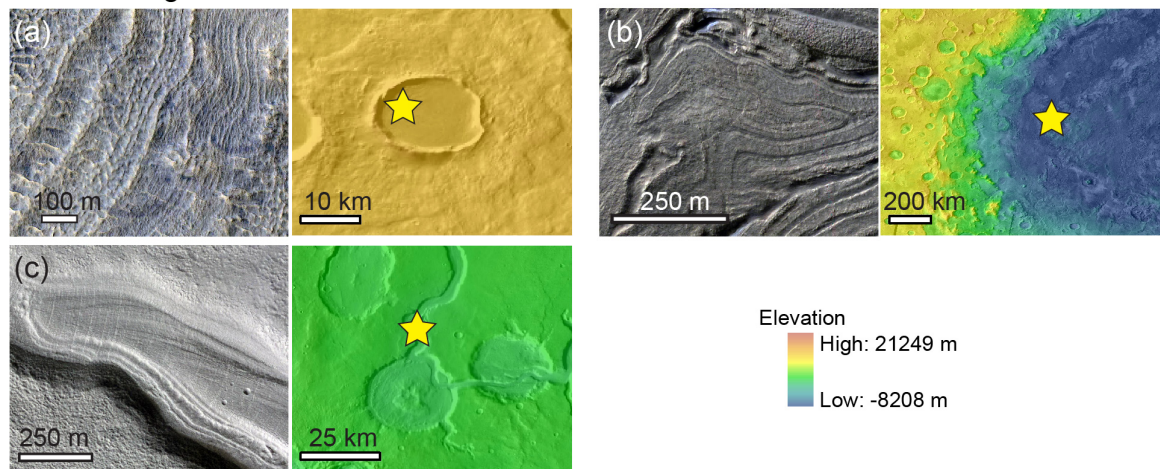


Figure 2.6

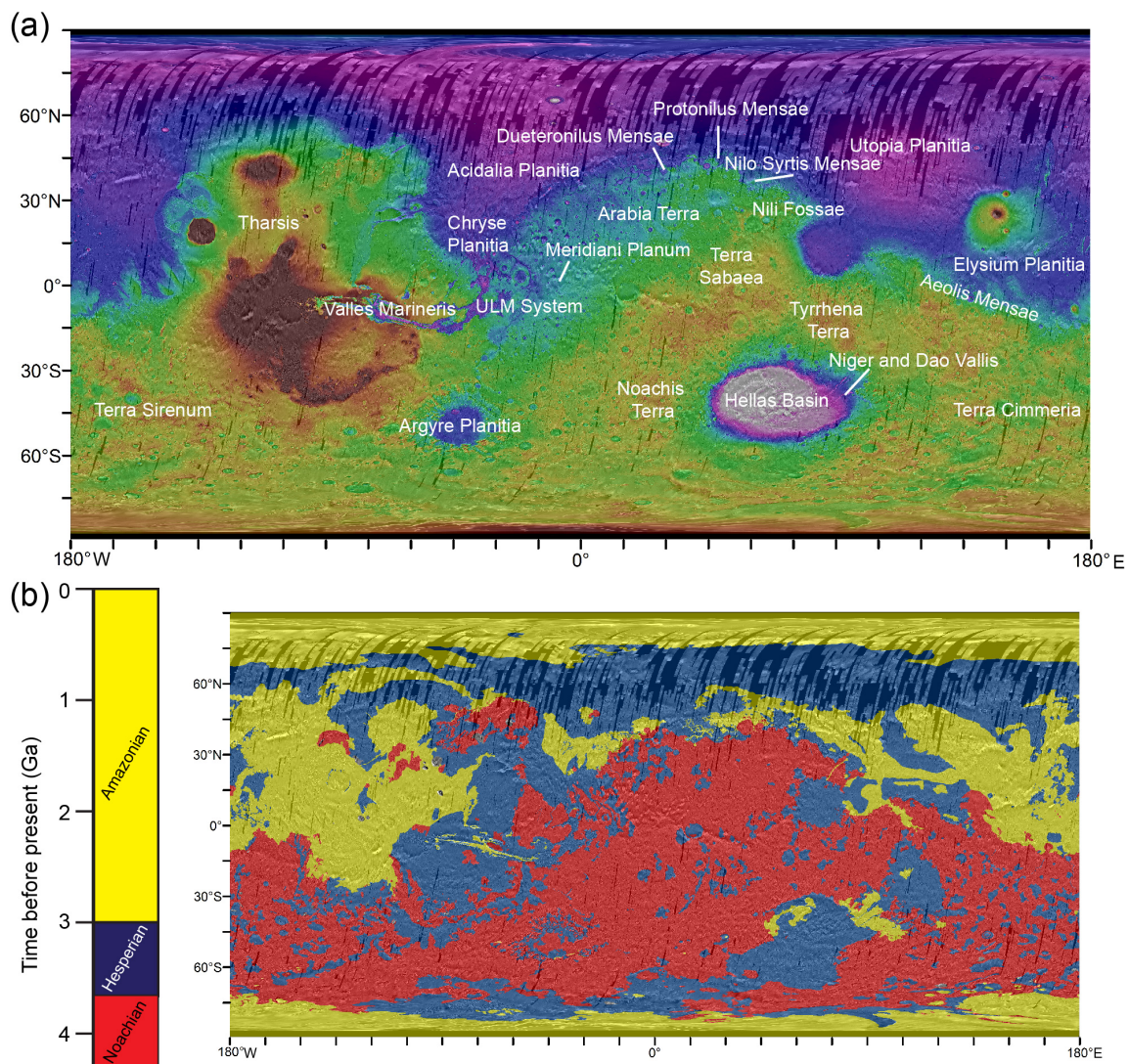


Figure 2.7

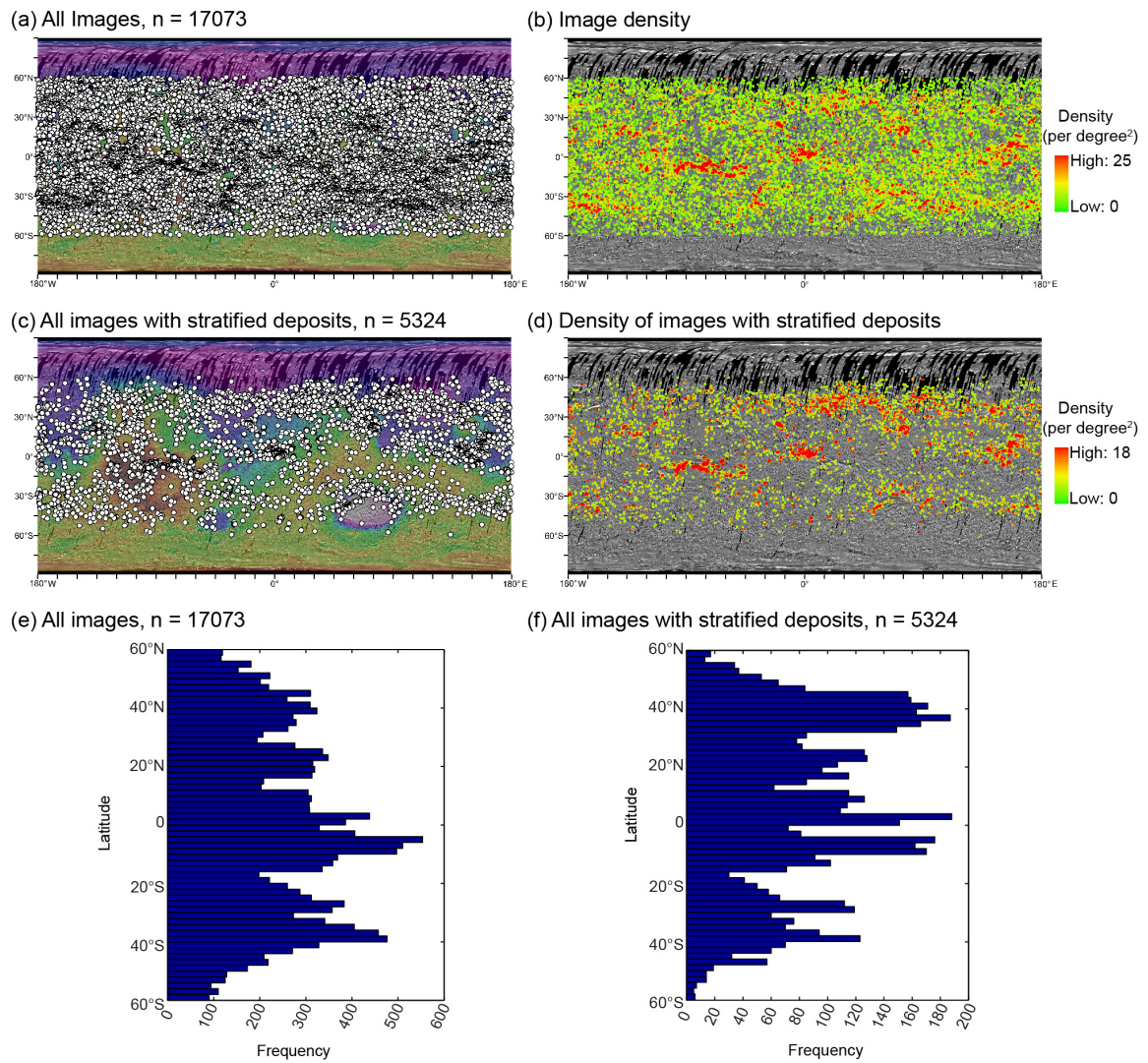


Figure 2.8

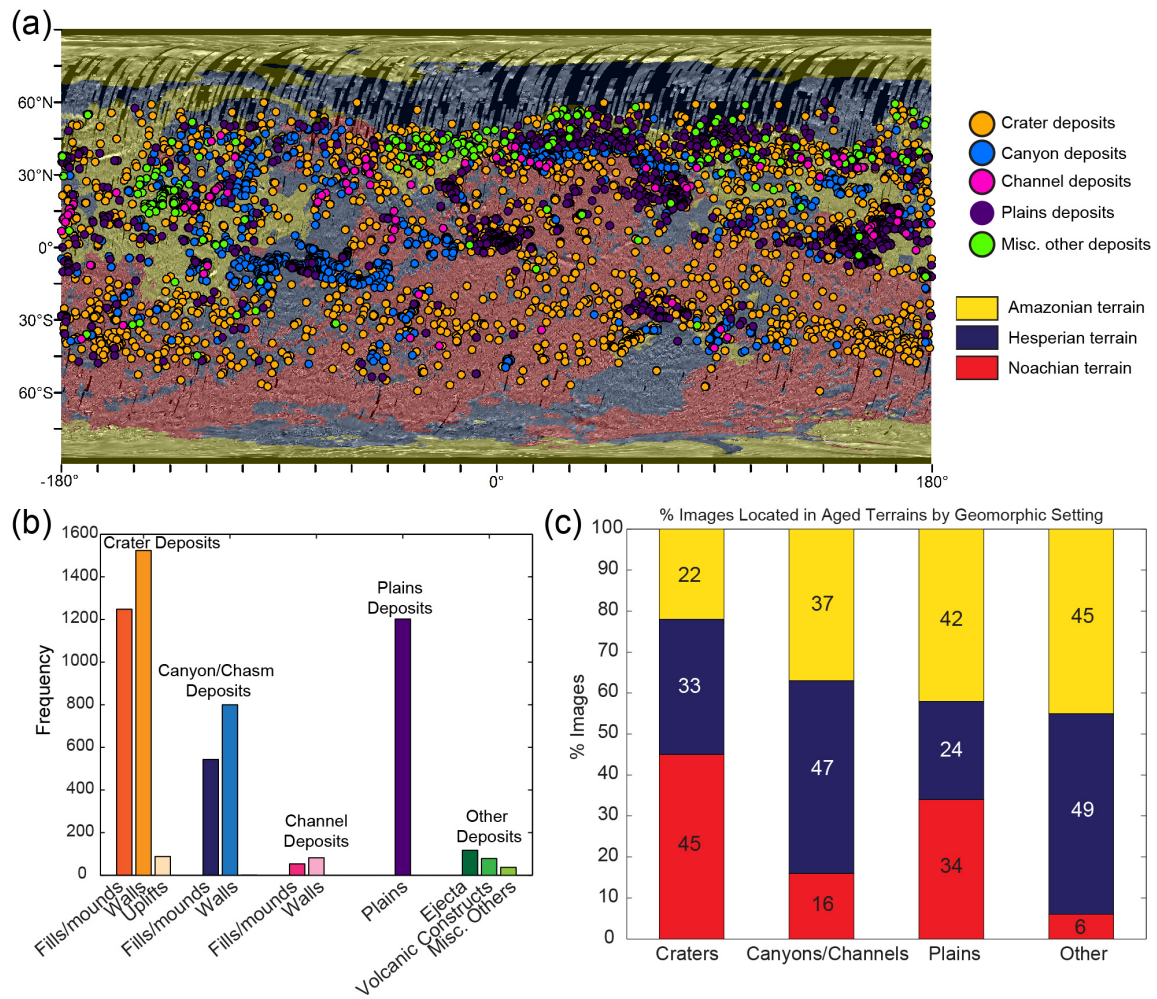


Figure 2.9

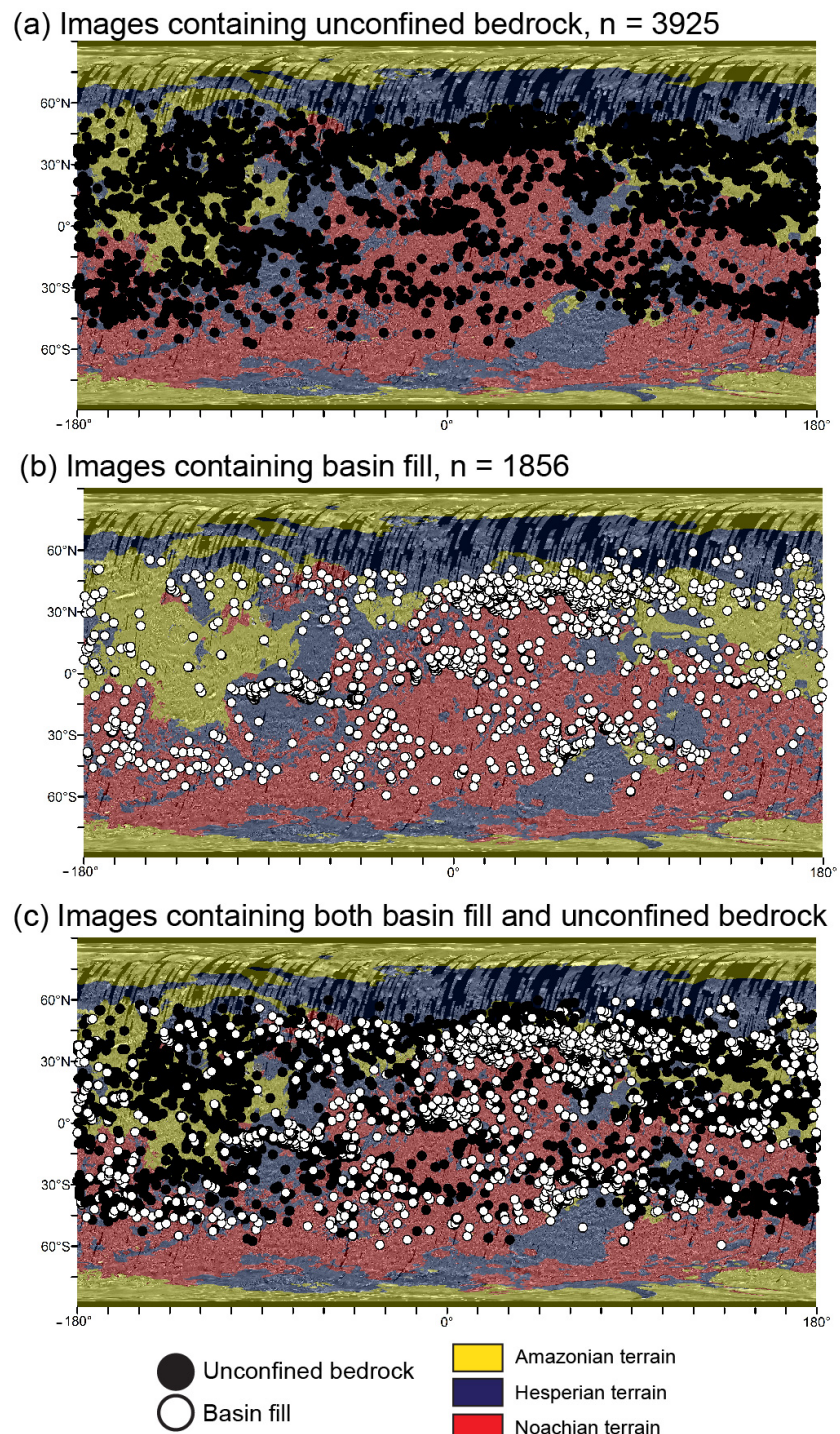


Figure 2.10

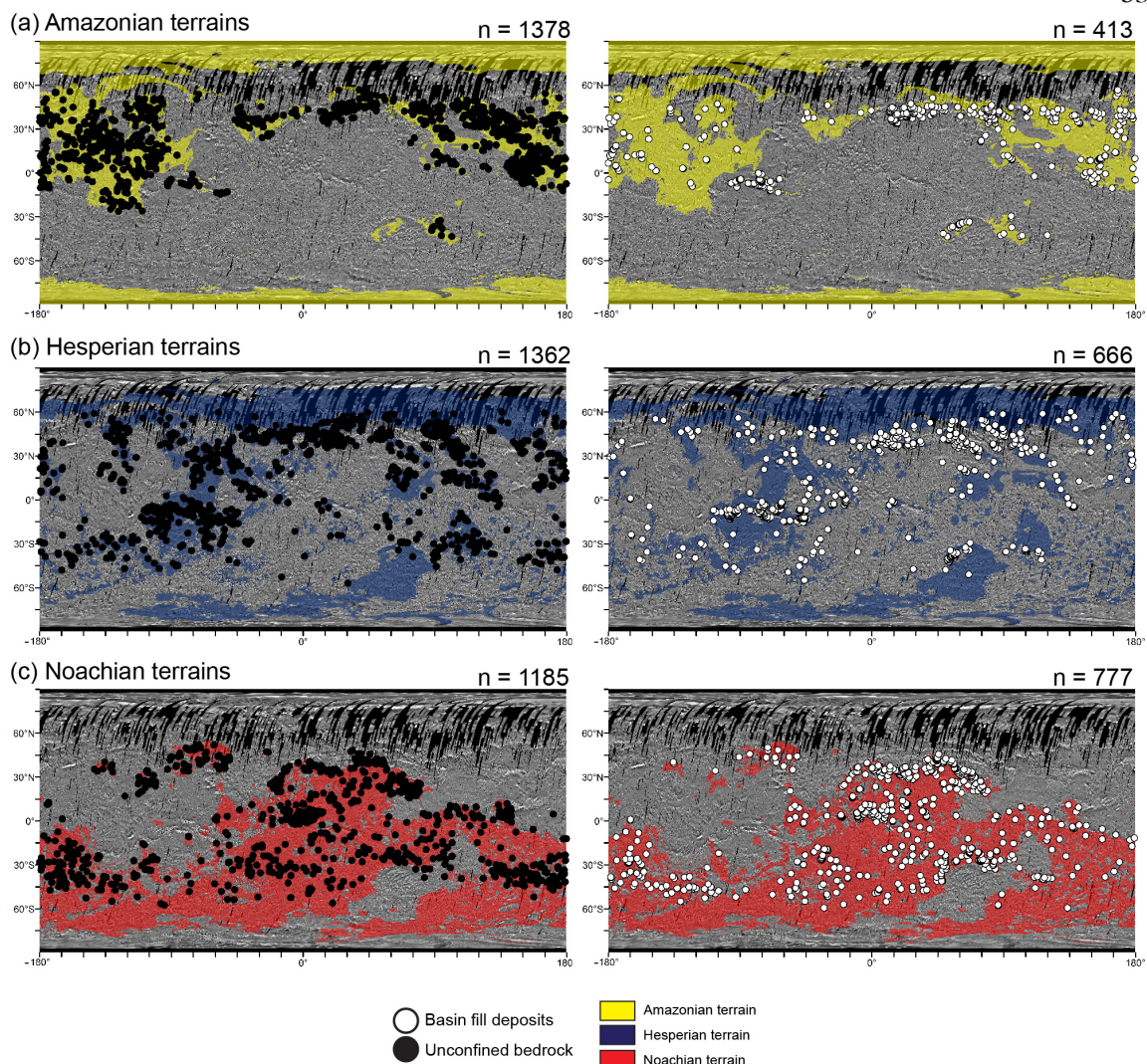


Figure 2.11

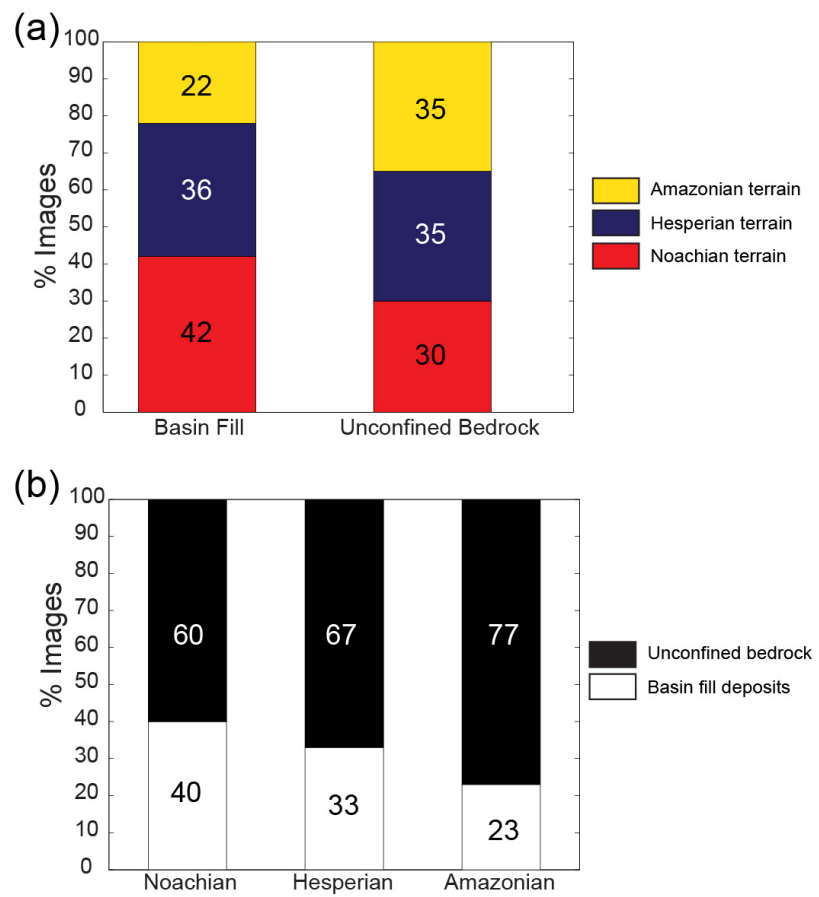


Figure 2.12

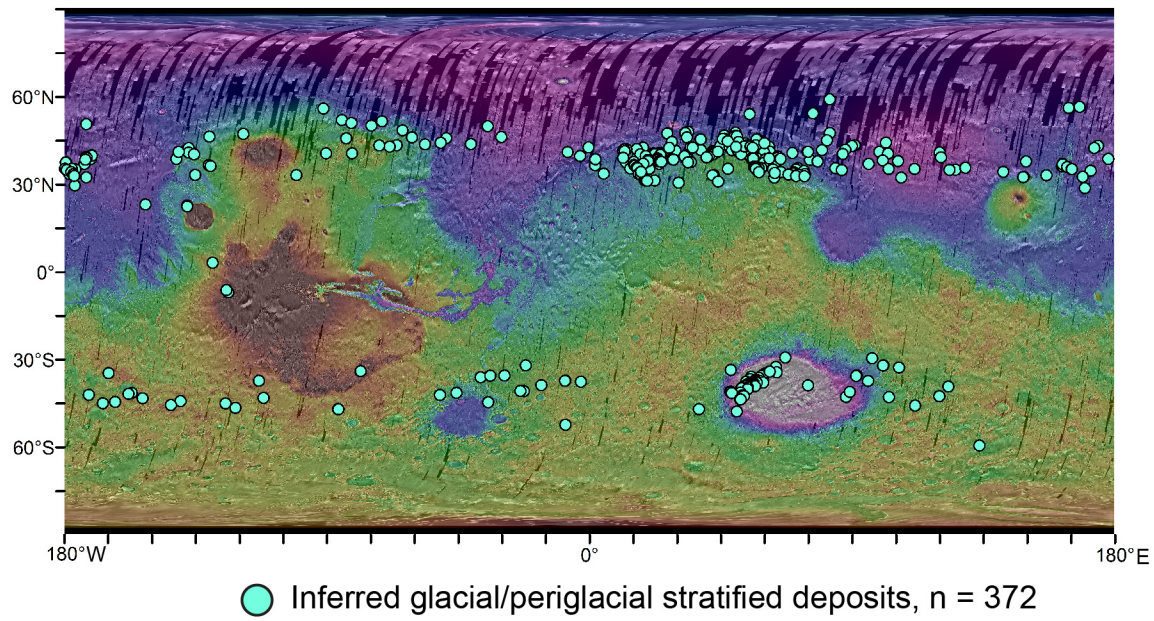


Figure 2.13

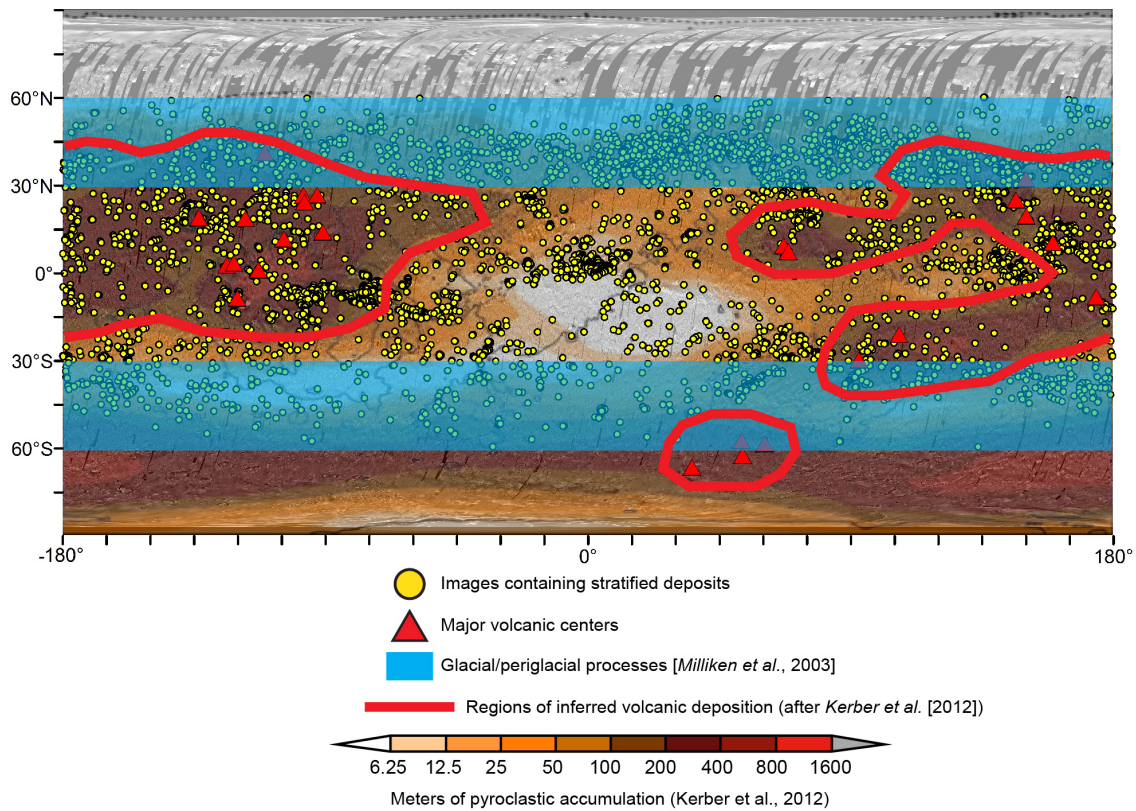


Figure 2.14

Chapter 3

BED THICKNESS DISTRIBUTIONS ON MARS: AN ORBITAL PERSPECTIVE

Originally published in:

Stack, K. M., J. P. Grotzinger, and R. E. Milliken (2013), Bed thickness distributions on Mars: An orbital perspective, *Journal of Geophysical Research- Planets*, 118, 1-27, doi:10.1002/jgre.20092.

Abstract

Studies on Earth show that sedimentary bed thickness and bed thickness distributions record information about the processes controlling sediment deposition. High-resolution digital terrain models (DTMs) such as those derived from the High Resolution Imaging Science Experiment (HiRISE) now provide the opportunity to quantify bed thickness properties on Mars over several orders of magnitude, down to the sub-meter scale. This study uses HiRISE DTMs and visible images to measure bed thickness distributions at 10 sites, with the aim of determining whether statistical techniques can provide useful criteria for distinguishing sedimentary depositional processes. Basic statistics including mean thickness and range are examined, as well as histograms, cumulative frequency plots, and log-log plots. Statistical tests are used to interrogate these deposits for thinning or thickening upward trends and the presence of normal, lognormal, and exponential distributions. Although there are caveats associated with these methods, the statistical analysis of bed thickness, coupled with morphologic and mineralogic interpretations, has the potential to be a powerful tool for characterizing and classifying

sedimentary rocks on Mars. In particular, bed thickness statistics are particularly well suited for examining changes in sediment supply and accommodation within Martian sedimentary sequences.

3.1 Introduction

In situ and remote observations of the Martian sedimentary record have shown that bedding is as fundamental a characteristic of sedimentary rocks on Mars as it is on Earth [Malin and Edgett, 2000; Grotzinger and Milliken, 2012]. Where primary, bedding generally represents a profound attribute of the stratigraphic record: the presence of hiatuses where time is represented by a surface rather than a volume of rock [Blackwelder and Barrows, 1911; Wheeler, 1958, 1959; Sloss, 1963; Sadler, 1981; Christie-Blick and Driscoll, 1995]. The thinnest beds have the potential to record individual sedimentation events, whereas thicker beds represent the amalgamation of strata that are related by composition (lithostratigraphic units) or time (sequences and cycles) [Mitchum and Vail, 1977]. Stratified deposits on Earth provide the principal archive of past surface processes and widespread stratified outcrops on Mars may hold similar promise [Tanaka, 1986; Malin and Edgett, 2000; Grotzinger and Milliken, 2012].

Mariner 9 images first revealed the existence of sedimentary, layered materials in both the polar [Murray *et al.* 1972; Soderblom *et al.* 1973; Cutts, 1973] and mid-latitude regions [Sharp, 1973] of Mars. The Viking mission [Snyder, 1979], High Resolution Stereo Camera (HRSC) data [Neukem *et al.*, 2004], and high-resolution images from Mars Orbiter Camera (MOC) [Malin and Edgett, 2001] and High Resolution Imaging Science

Experiment (HiRISE) [McEwen *et al.*, 2010; Grotzinger and Milliken, 2012] show these deposits to occur in diverse settings including impact craters, canyons, channels, and plateaus, reflecting sedimentary origins in eolian, fluvial, and possibly lacustrine environments [Scott and Tanaka, 1986; Luchitta *et al.*, 1992; Carr, 1996; Malin and Edgett, 2000; Edgett and Malin, 2002; Moore *et al.*, 2003; Squyres *et al.*, 2004; Grotzinger *et al.*, 2005; Jaumann *et al.*, 2007; Grotzinger *et al.*, 2011]. Recent in situ observations by the Mars Exploration Rovers Spirit and Opportunity [Squyres *et al.*, 2004; Grotzinger *et al.*, 2005; Squyres *et al.*, 2007] and by the Mars Science Laboratory Curiosity rover [Grotzinger *et al.*, 2012] have allowed outcrop-scale geological investigations of these past environments.

Numerous studies suggest a possible link between climate change, orbital parameters, and layered ice-rich deposits in the polar regions of Mars [Laskar *et al.*, 2002; Milkovich and Head, 2005; Fishbaugh *et al.*, 2010ab, Limaye *et al.*, 2012]. In contrast, few studies have attempted quantitative stratigraphic analysis of layering observed in what are likely sediment-dominated deposits [Lewis *et al.*, 2008; Lewis, 2009; Cadieux, 2011; Fueten *et al.*, 2011]. Lewis *et al.* [2008, 2010] identified rhythmic bedding in sedimentary deposits of Arabia Terra, Gale crater, Juventae Chasma, and the Medusa Fossae formation, suggesting that periodicity may be related to orbital forcing in the Milankovitch band. However, cyclic bedding is rare among putative sedimentary strata on Mars [Lewis *et al.*, 2010; Grotzinger and Milliken, 2012], and the search for periodicity is just one way bed thickness can be used to study the stratigraphic record. On Earth, the frequency distribution of sedimentary bed thickness has been related to depositional environment [Carlson and

Grotzinger, 2001; Talling, 2001] and process [Rothman *et al.*, 1994; Beattie and Dade, 1996]. Furthermore, systematic changes in bed thickness have been linked to basin-scale variations in sediment supply and accommodation [Fischer, 1964; Read and Goldhammer, 1988]. Despite the successful implementation of statistical bed thickness analyses on Earth and the recent ability to do so at the sub-meter scale on Mars, the potential to classify deposits and constrain depositional processes using bed thickness has been largely unexplored for Mars.

This study seeks to understand how the statistical analysis of bed thickness can be adapted and applied to sedimentary strata on Mars while working within the constraints and limitations of orbital data sets. Building upon the work of Lewis [2008, 2010], this study explores additional ways that bed thickness measurements can provide an objective and quantitative approach for describing and classifying Martian layered deposits. High-resolution images and DTMs are used to measure stratal thickness for ten spatially distinct Martian deposits that likely represent a variety of depositional settings, with a special focus on the deposits in Holden crater, Gale crater, and on the plateau west of Juventae Chasma. This study shows that bed thickness measurements, coupled with histograms, cumulative frequency distributions, and the results of statistical testing, can enhance understanding of the processes that control sediment transport and deposition on Mars. As additional HiRISE DTMs become publically available in future years, the methods presented here can provide a foundation for more detailed studies of sedimentary deposits whose depositional settings are well-constrained, providing even clearer insight into relationships between sedimentary process and bed thickness for Martian strata.

3.2 Background

3.2.1 Statistical Analysis of Bed Thickness on Earth

Statistical methods have been used to study the history of deposition in several sedimentary settings on Earth. The frequency distribution of turbidite bed thickness is thought to record information about initial sediment volume and source, flow rheology [Talling, 2001], lateral distribution and migration of facies [Carlson and Grotzinger, 2001], and intrinsic and extrinsic controls on depositional processes [Rothman *et al.*, 1994; Beattie and Dade, 1996; Chen and Hiscott, 1999]. Terrestrial turbidite frequency distributions are variable, showing truncated Gaussian, lognormal [Ricci Lucchi, 1969; Talling *et al.*, 2001], exponential [Drummond and Wilkinson, 1996], cumulative power-law [Carlson and Grotzinger, 2001], and segmented power-law [Rothman and Grotzinger, 1995; Sylvester, 2007] trends. Bed thickness distributions have also been studied for peritidal carbonates [Wilkinson *et al.*, 1997, 1999; Wilkinson and Drummond, 2004; Burgess, 2008], mixed carbonate-clastic deposits [Drummond and Wilkinson, 1996; Wilkinson and Drummond, 2004], debris flows [Rothman and Grotzinger, 1995], and fluvial deposits [Atkinson, 1962]. Still, the majority of studies have preferentially focused on turbidite and carbonate deposits to the extent that the understanding of bed thickness distributions on Earth is not balanced through all depositional environments.

Lognormal, exponential, and power-law statistical distributions are the most commonly observed trends in terrestrial sedimentary sequences (Figure 3.1), and are described in detail below.

3.2.1.1 Lognormal Distributions

A data set whose logarithm follows a normal distribution is lognormally distributed. Lognormal distributions arise when a variable is the product of a number of independent random variables rather than the addition of these variables, as for a normal distribution [Davis, 2002]. Lognormal distributions are common in geological data sets [Koch and Link, 1980], and sedimentary sequences on Earth commonly exhibit lognormal distributions [Hinnov and Goldhammer, 1991; Drummond and Wilkinson, 1996; Talling, 2001]. Atkinson [1962] attributed lognormal trends observed in fluvial sandstones, shales, and conglomerates to lognormally distributed time intervals between flood events and movements along faults. Talling [2001] suggested that the observed lognormal distribution of turbidite beds is a primary signal resulting from the multiplicative addition of several randomly distributed parameters such as flow duration, turbulence, and settling velocity, which are known to contribute to the thickness of any given turbidite bed. Despite the prevalence of lognormal distributions observed in sedimentary rocks, this distribution remains first and foremost an empirical explanation for the observed distribution of bed thickness. Alternatively, Drummond and Wilkinson [1996] explained lognormal trends as the result of sampling bias in which the thinnest beds of exponential distributions are missed during counting.

3.2.1.2 Exponential Distributions

The recurrence intervals of a Poissonian stream of events are approximated in the continuous limit by an exponential distribution. The presence of an exponential distribution

in a series of strata suggests the operation of a stochastic Poisson process where the deposition duration of a particular unit, which is assumed to be proportional to the unit thickness, is random and unrelated to the onset or duration of deposition of the next unit [Burgess, 2008]. Accordingly, an exponential frequency distribution of bed thickness takes the form

$$N(t) = ae^{-bt} \quad (3.1)$$

where N is the number of beds of thickness t , and a and b are constants.

Exponential thickness distributions have been observed in turbidite deposits and numerous ancient carbonate deposits [Wilkinson *et al.*, 1997, 1999; Burgess, 2008]. *Drummond and Wilkinson* [1996] suggested that both carbonate and clastic sedimentary sequences follow an exponential distribution where the number of thin beds is much greater than the number of thick beds, frequency decreases at a particular rate as thickness increases, and there is no modal thickness. The exponential model invokes a stochastic, memory-less stacking pattern at odds with deposition driven by cyclic or periodic forcing mechanisms [*Drummond and Wilkinson*, 1996; *Burgess*, 2008]. As a result, a stratigraphic sequence may only exhibit the effects of external forcing mechanisms, i.e., sea-level oscillations, on a multi-decameter scale [Wilkinson *et al.*, 1997, 1999; *Wilkinson and Drummond*, 2004; *Burgess*, 2008]. The exponential distribution of bed thickness is supported by the common occurrence of exponential processes in nature, and the likely unavoidable bias against thin beds that occurs when tabulating stratigraphic subdivisions

[*Drummond and Wilkinson, 1996*].

3.2.1.3 Power-Law Distributions

Scale-invariant power-law relationships can also describe the distribution of sedimentary bed thickness [*Rothman and Grotzinger, 1995; Awadallah et al., 2001; Carlson and Grotzinger, 2001*]. The equation for a power-law relationship takes the form

$$N(t) = ct^{-d} \quad (3.2)$$

where t is bed thickness, N is the number of beds of thickness t , c is a constant, and d is a constant scaling exponent given by the slope of the plot in $\log(N)$ versus $\log(t)$ space. For data sets exhibiting power-law scaling, the exponent d is related to depositional variations such as basin geometry or flow types [*Rothman et al., 1994; Rothman and Grotzinger, 1995*]. Numerous studies have documented power-law distributions of bed thicknesses in turbidite sequences, but the cause of this observed power-law trend is debated. *Rothman et al. [1994]* suggested that the distribution of turbidite bed thickness represents a self-organized system regulated by a complex non-linear diffusion equation that exhibits power-law scaling, while *Beattie and Dade [1996]* and *Awadallah et al. [2001]* favored turbidite deposition driven by the external forcing of earthquakes that follow Gutenberg-Richter scaling (another power law).

Following the assumption that bed thickness frequency follows a power law, systematic deviations from expected power law behavior have been interpreted to have

process significance. *Carlson and Grotzinger* [2001] linked deviations from power-law behavior to erosion, amalgamation, and channelization, thereby using bed thickness distributions to distinguish between proximal and distal facies within submarine fan deposits. *Carlson and Grotzinger* [2001] also showed that the process of bed amalgamation can create a lognormal distribution from a power-law distribution. If correct, this is a powerful concept suggesting that any given depositional system may behave as a filter capable of regulating bed thickness and, by implication, bed volumes [*Jerolmack and Paola*, 2010].

Alternatively, segmented power-laws have been invoked to describe deviations of natural bed thickness data from power-law behavior at very small or large thicknesses [*Rothman and Grotzinger*, 1995; *Malinverno*, 1997]. *Malinverno* [1997] suggested that bed thickness data should plot as a segmented power-law described by linear trends of different slope if there is a relationship between bed length and thickness that depends on bed volume.

Although a variety of distributions have been invoked to describe sedimentary bed thickness on Earth and the meaning of these distributions is actively debated, most studies agree that bed thickness distributions can provide meaningful insight into the magnitude, duration, and recurrence of depositional events. In some cases bed thickness distributions can even be linked directly to specific depositional environments. For these reasons, the statistical analysis of bed thickness is especially compelling on Mars, where the methods and data available to study sedimentary sequences are limited.

3.3 Methods

3.3.1 Identifying Beds from Orbit on Mars

This study defines a sedimentary bed as the thinnest recognizable unit observable in orthorectified HiRISE images. Generally, an individual bed is identified as an observable change in image brightness that is laterally continuous for tens of meters or more, or where a distinct shelf-like topographic expression is observed. Little else is known about the reason for stratification. It is important to consider that bedding likely exists at finer scales than is resolvable in HiRISE imagery. For example, in situ observations of bedding at the Opportunity landing site, i.e., *Grotzinger et al.* [2005], revealed stratification on a scale not observable in the orbital data. However, it is assumed that the sub-meter to meter-scale bedding observable in HiRISE images has sedimentary depositional significance, i.e., *Lang et al.*, 1987; *Sgavetti et al.*, 1995, meaning that it is not due to secondary processes such as diagenetic overprinting or metamorphism, including hydrothermal alteration. It is recognized, though, that if such processes produce boundaries parallel to true bedding, these boundaries will be indistinguishable from that bedding in orbital data.

3.3.2 Orbital Data

Table 3.1 lists the HiRISE DTMs used to measure bed thickness in this study. The U.S. Geological Survey generated DTMs according to the methods of *Kirk et al.* [2008]. The DTMs have grid spacings of 1 meter and absolute elevations tied to data acquired by the Mars Orbiter Laser Altimeter (MOLA; *Smith et al.* [2001]). The expected precision (*EP*) of the vertical elevation values extracted from the DTMs (Table 3.1) was calculated

using the equation of *Kirk et al.* [2008], which assumes 1/5 pixel correlations and takes into account the viewing geometry and resolution of the HiRISE imagery used to create the DTM,

$$EP = \rho \times GSD / (P/h) \quad (3.3)$$

where ρ is the pixel matching error assumed to be 1/5, GSD is the ground sample distance or the meter/pixel resolution of the more oblique image in the HiRISE stereo pair, and P/h is the ratio of parallax to height. For a narrow angle camera such as HiRISE this is equal to

$$P/h = |\tan(e_1) \pm \tan(e_2)| \quad (3.4)$$

where e_1 and e_2 are the emission angles of the HiRISE stereo pair, and the sign of the equation depends on whether the stereo pairs are viewing the target from the same side (-, roll angles are of the same sign) or opposite sides (+, roll angles are of opposite signs). For the DTMs listed in Table 3.1, the vertical precision is estimated to be between 0.07-0.35 meters, with all but two DTMs having vertical precision better than 0.20 meters.

HiRISE images orthorectified to the corresponding DTM [*Kirk et al.*, 2008] were used to measure bedding orientation and bed thickness. Beds were measured at each location using both the 25 centimeters per pixel and 1 meter per pixel orthoimages so that the effects of image resolution on bed thickness measurements and statistical results could be examined.

3.3.3 Measuring Bed Thickness

3.3.3.1 Measured Sections

Bed thickness was measured in Holden crater, on the plateau west of Juventae Chasma, in Gale crater, Argyre Planitia, Athabasca Valles, Becquerel crater, Candor Chasma, Cross crater, Danielson crater, and Eberswalde crater (Figures 3.2 and 3.3 and Table 3.2). Although the selection of study sites was determined by the availability of high-resolution DTMs produced by the U.S Geological Survey, the chosen sites fortuitously represent a variety of depositional settings and styles (Table 3.2).

Multiple, approximately correlative sections were measured in Holden crater, on the plateau west of Juventae Chasma, and in the lower strata of Mt. Sharp in Gale crater (Figures 3.4-3.6). In Holden crater bed thickness distributions were measured at ten continuous vertical sections in the interval identified by *Grant et al.* [2008] as the Lower unit and by *Pondrelli et al.* [2005] as Sed Unit 1. The measured sections in Holden crater were spaced along ~17 km of outcrop and arranged at increasing distance from the rim of the crater such that H1 is closest to the rim, H10 is furthest from the rim, and the remaining sections are located along a line between H1 and H10 (Figures 3.3i and 3.4). These sections were selected based on the quality of exposure and the vertical completeness of each section. Due to changes in illumination conditions caused by local changes in topography, it was difficult to correlate the individual Holden sections layer by layer, especially for those spaced farther apart. However, because the sections are all within or underlie the same alluvial fan system, they likely sample the same approximate stratigraphic interval.

The 10 sections measured on the plateau west of Juventae Chasma are spaced ~1 km

apart along a 10 km sinuous exposure exposed along the walls of a deep pit 20 km west of Juventae Chasma (Figures 3.3j and 3.5). WJ1 is the easternmost section; subsequent sections follow the trace of the outcrop to the northwest (Figure 3.5). It is possible to trace several beds throughout all of the sections, thus each section samples the same approximate stratigraphic interval.

Eight sections were measured at the base of Mt. Sharp in Gale crater (Figures 3.3h and 3.6). *Milliken et al.* [2010] identified three members within the Lower formation of Mt. Sharp, a lower member characterized by bright beds, a middle member containing dark-toned strata, and an upper member defined at its base by a dark, smooth marker bed. In this study, two sections were measured in the lower member, three sections in the middle member, and three sections measured in the upper member (Figure 3.6). The sections were chosen according to these stratigraphic boundaries so that changes in bed thickness could be examined laterally within the same stratigraphic interval and vertically through the stratigraphy of the Lower formation.

In addition to these three primary localities, bed thickness was also measured at seven other locations on Mars (Figures 3.3 and 3.7). Only one section (or two in the case of Candor) was measured at each of these additional locations. One section is located on the eastern flank of a north-south trending sinuous ridge located in the southern portion of the Argyre impact basin (Figures 3.3a and 3.7a). The Athabasca section is measured on the southeastern facing flank of a tear drop-shaped landform extending from a small impact crater within Athabasca Valles (Figures 3.3b and 3.7b). The section measured in Becquerel crater spans the rhythmic beds previously described by *Lewis et al.* [2008] and *Cadieux*

[2011], which are exposed in a small mound in the southern part of the crater (Figures 3.3c and 3.7c). Strata in the southwest region of Candor Chasma are extensively folded and faulted [Okubo and McEwen, 2007; Fueten *et al.* 2008; Metz *et al.*, 2010; Okubo, 2010], but the two sections measured here span a short sequence of undisrupted strata (Figures 3.3d, 3.7d and 3.7e). The measured section in Cross crater spans strata in a terrace that rings the inner rim of the crater (Figures 3.3e and 3.7f). The Danielson section spans a portion of layered fill within Danielson crater in Meridiani Planum (Figures 3.3f and 3.7g), while the section in Eberswalde crater measures layered strata exposed in an eroded scarp at the distal edge of a delta (Figures 3.3g and 3.7h).

3.3.3.2 Bed Orientation

The first step in calculating bed thickness was determining the three-dimensional orientation, or strike and dip, of bedding at each outcrop (Figure 3.8). X , Y , and Z coordinates, where X is the easting, Y is the northing, and Z is the elevation, were extracted from HiRISE DTMs along bedding planes in ArcGIS and fit to a plane using least squares multiple linear regression in MATLAB [Lewis *et al.*, 2008; Metz, 2010; Watters *et al.*, 2011] (Figure 3.8b and 3.8c). A Monte Carlo simulation of the random residual error in the elevation (Z coordinate) was performed to obtain the strike, dip, and estimates of error in strike and dip measurements for each bedding plane (Table A1). Multiple orientation measurements were made throughout each section and averaged to obtain one representative orientation measurement for each section (Table A1). If a significant change in orientation was observed within a section, the average strike and dip for each interval

was used.

Orientation measurements obtained from the plateau west of Juventae, Athabasca Valles, Eberswalde crater, and sections H1 and H10 in Holden crater showed shallow dips and inconsistent strike measurements with large errors (Table A1). Therefore, the beds at these locations were assumed to be approximately horizontal.

3.3.3.3 Correction for True Thickness

For each measured section, a topographic profile running perpendicular to the strike of the outcrop was extracted from the DTM (Figure 3.8b). The upper and lower boundaries of each bed along the topographic profile were identified by visual inspection of the HiRISE orthoimage using distinct changes in brightness and, when possible, the topographic expression of strata (Figure 3.8b). Considering the DTM as a continuous surface with interpolated values between the 1 m tiepoints, coordinates (X , Y , Z) of the upper and lower boundaries of each bed in the section were extracted from the DTM using bilinear interpolation in ArcGIS. The apparent thickness of each bed in the measured section was corrected following the procedure of *Groshong* [1999], taking into account the horizontal distance between the upper and lower boundary of the bed, the change in elevation between the boundaries of the bed, and the strike and dip for the section (Figure 3.8b and 3.8d). When the dip of the bed and the topographic slope are in the same direction, the true thickness is described by

$$t = |h \cos \alpha \sin \delta - v \cos \delta| \quad (3.5)$$

When the dip of the bed and the topographic slope are in opposite directions,

$$t = h \cos \alpha \sin \delta + v \cos \delta \quad (3.6)$$

where t is true thickness, h is the horizontal distance along the measured section line between the upper and lower bed boundaries, α is the angle between the measured section and the dip direction (Figure 3.8d), δ is the true dip, and v is the elevation difference between the upper and lower boundaries of each bed (Figure 3.8b). By applying these corrections to each bed in the measured section, a continuous series of true bed thicknesses from stratigraphic bottom to top was obtained (Figures 3.9-3.12).

3.3.3.4 Error of Bed Thickness Measurements

Absolute errors were calculated for each bed thickness measurement according to equation (A17), which propagates errors associated with the DTMs and bed orientation measurements through equations (3.5) and (3.6). One-sigma confidence limits for each strike and dip measurement were calculated via the methods of *Metz* [2010] and are reported in Table A1. By averaging strike and dip measurements at each location, errors of the average orientation measurement were greatly minimized. The DTM vertical precision (Table 3.1) was used to calculate the error of v , while the DTM horizontal resolution (1 m) was used to calculate the error of h . The complete derivation of error propagation for thickness measurements is included in Appendix A.

3.3.4 Statistical Methods

Changes in bed thickness with bed number (sequential beds numbered within the stratigraphic section from bottom to top) for each section are presented in Figures 3.9-3.12. These plots provide an objective way to track systematic changes in bed thickness throughout the section [Lowey, 1992]. Bed thickness data were analyzed for overall trends in thinning or thickening using several methods. First, thickness measurements were modeled as a function of stratigraphic position using linear regression. The observed significance probability, p , from a two-sided t-test was used to reject or fail to reject the null hypothesis that the slope of the model fit was zero. For $p < 0.05$, the null hypothesis was rejected, suggesting that the model slope was statistically significant and nonzero. These cases imply an overall thickening or thinning trend upsection.

Two varieties of runs tests were performed using MATLAB to verify whether successive increases or decreases in bed thickness throughout the sections were random [Davis, 2002]. The first test evaluates the null hypothesis that bed thickness values occur in random order and is based on the number of runs above or below the mean bed thickness for each section (RAM, runs about the mean). The second runs test interrogates the null hypothesis that the number of runs up or down is that expected from a random distribution of bed thicknesses (RUD, runs up down).

Bed thickness measurements were plotted in histograms where the frequency of bed thickness is normalized so that the total area in the histogram sums to 1 (Figure 3.13). This graphical representation provides an approximation of the probability distribution of bed thickness at each location. The number of bins was specified to be 15 for all sections. To

assess whether bed thickness distributions measured at each location followed the expected trend of a normal, lognormal, or exponential distribution, the empirical frequency of bed thickness was plotted together with theoretical distributions on normalized cumulative frequency (CF) plots (Figure 3.14). Maximum likelihood estimation (MLE) in MATLAB was used to estimate the parameters of normal, lognormal, and exponential distributions for each section using the measured thickness data. Estimated MLE parameters for the normal and lognormal distributions included the mean and standard deviation; for the exponential distribution the estimated parameter was the mean. The theoretical normal, lognormal, and exponential distributions were then plotted using these parameters (Figure 3.14).

A Lilliefors test was executed in MATLAB to determine whether empirical bed thickness measurements could be described by normal, lognormal, or exponential distributions. The Lilliefors test is a two-sided Kolmogorov-Smirnov test that does not require a fully specified null distribution [Lilliefors, 1967]. This test is suitable when parameters must be estimated from the data, as is the case for the bed thickness measurements here. The test statistic for the Lilliefors test is the same as that for the Kolmogorov-Smirnov test:

$$KS = \max_x |SCDF(x) - CDF(x)| \quad (3.8)$$

where $SCDF(x)$ is the empirical cumulative distribution function (CDF) measured from the sample and $CDF(x)$ is the CDF of a distribution with the same parameters, e.g., mean and standard deviation, as the sample. The Lilliefors test considers the maximum discrepancy

between the empirical CDF and the theoretical CDF, where the significance probability, p , is the probability of such an extreme discrepancy occurring by chance if the data followed the specified distribution. If the most extreme discrepancy has a probability of occurring at a significance probability <0.05 , the null hypothesis that the distribution is a good fit for the data was rejected. This analysis used the Lilliefors test because this test is valid for small sample sizes and does not require that data be grouped into arbitrary categories, as for the chi-squared goodness-of-fit test [Davis, 2002]. In addition, this test is valid for the location-scale family of probability distributions including normal, lognormal, and exponential distributions [Lilliefors, 1967, 1969].

To examine the possibility of power-law trends in the data, which may indicate a relationship with scale-invariant processes common in nature, thickness data were also plotted on log-log probability plots (Figure 3.15). If a data set exhibits power law behavior, it will plot as a linear function in log-log space.

3.4. Results

3.4.1 Holden Crater

3.4.1.1 Bed Thickness Statistics

Table 3.3 lists the total section thickness, total number of beds n , range of bed thickness, mean bed thickness μ , and standard deviation σ , measured with the 25 centimeter per pixel and 1 meter per pixel orthoimages for each section. Total thickness for Holden sections ranges between ~ 15 and 35 meters. The number of beds measured using the 25 centimeter per pixel orthoimages ranges from 41 beds (H5) to as many as 90 beds

(H9), and the mean bed thickness ranges from 0.26 meters (H2) to 0.51 meters (H1). Using the 1 meter per pixel orthoimages (Table 3.3), the number of beds is approximately half that measured with the 25 centimeter per pixel orthoimages, ranging from 23 beds (H5) to only 49 beds (H9). Mean bed thickness approximately doubles when beds were identified with the lower resolution orthoimages, ranging from 0.36 meters (H2) to 0.92 meters (H1). The maximum bed thickness measured with the 25 centimeter orthoimage was 1.62 meter (H3). In contrast, the thickest bed measured with the 1 meter orthoimage was almost three times that (4.51 m, H1).

Error bars estimated for Holden thickness measurements are strongly influenced by the vertical precision of the DTMs. H1 and H10 were measured using a DTM with a high vertical precision so the estimated error of these measurements is smaller compared to the error of measurements in H2-H9, which were measured using a DTM with a lower vertical precision (Table 3.1).

3.4.1.2 Trends in Thickness Versus Stratigraphic Position

Eight of ten Holden sections show no statistically significant thinning or thickening upward trends when beds were identified with the 25 centimeter per pixel orthoimage (Figure 3.9). Only H2 and H9 show trends, both thinning upwards, although the estimated error bars on individual measurements in these sections are large enough to cover nearly the full range of measured thicknesses (Figure 3.9). Using the 1 meter orthoimage, four of the ten sections show no thinning or thickening trends (H3-H5, H7), whereas four sections show thickening upwards trends and two thin upwards (Table A2).

Significance testing for RAM using the 25 centimeter per pixel orthoimage thickness data reveals that eight of the ten sections are consistent with non-random ordering of deviations above and below the mean (Table 3.4). In contrast, the null hypothesis for RUD cannot be rejected for any of the 25 centimeter per pixel orthoimage sections, suggesting that most sections are consistent with a random ordering. RAM and RUD results for the 1 m/pixel orthoimage sections are similar to those from the 25 centimeter per pixel sections. In summary, thickness trends based on the 25 centimeter per pixel orthoimages are most consistent with random variations in bed thickness that alternate frequently between high and low values, and suggest a lack of significant thinning or thickening upward trends in the Holden sections. Runs testing of the 1 meter per pixel thickness values are consistent with the 25 centimeter per pixel results, although the tests for thinning and thickening upward suggest several trends present in the 1 m/pixel data set that do not appear in the 25 centimeter per pixel data.

3.4.1.3 Bed Thickness Distributions

Histogram and CF plots for the 25 centimeter per pixel and 1 meter per pixel orthoimage results are qualitatively very similar, so only the 25 centimeter per pixel plots are discussed in detail. Histograms for Holden sections show that thickness frequency distributions are generally unimodal and positively skewed, although H5 is an exception (Figure 3.13). Sections H2 and H9 exhibit modes less than 40 centimeters, and only sections H1 and H10 exhibit modes greater than or equal to 40 centimeters. Holden sections, excluding H1, H6, and H10, show an offset between the mode and the mean

thickness, with the mode being less than mean bed thickness.

Holden CF plots show that bed thickness measurements are generally best described by lognomal CDFs (Figure 3.14). Theoretical exponential CDFs tend to overestimate the number of thin beds measured in the stratigraphic sequences and underestimate the frequency of thick beds. Sections H5-H8 offer good examples of this disparity. For H2 and H9 the theoretical lognormal and exponential CDFs offer comparable fits to bed thickness measurements. In general, the theoretical normal CDFs do not match well with the measured data, overestimating the number of thin beds and underestimating beds of intermediate thickness.

The Lilliefors test of normality for both the 25 centimeter per pixel and 1 meter per pixel data sets suggests that the normal distribution is a poor fit for the Holden sections. This result is consistent with CF plots in Figure 3.14. The null hypothesis is confidently rejected at a 95% significance level or higher for all 25 centimeter per pixel sections except H5. Lilliefors testing for lognormality reveals that the null hypothesis cannot be rejected at a 95% significance level for eight of the ten 25 centimeter per pixel Holden sections. Meanwhile, the null hypothesis for exponentiality is rejected at a 95% significance level or higher for all Holden sections, suggesting that this distribution is a poor fit to the data. Statistical testing of the 1 meter per pixel orthoimage bed thicknesses produces similar results to the 25 centimeter per pixel data, with most sections rejecting the null hypothesis for normal and exponential distributions, but failing to reject lognormality for nine of ten sections. These results suggest that bed thickness measurements for Holden sections are most consistent with lognormal distributions.

3.4.1.4 Log-log plots

Sections H3, H4, and H7 may come closest to a power law trend based on visual inspection of the plots in Figure 3.15, but thicknesses measured in Holden generally do not follow power-law behavior over the full range of the data set. The thinnest and thickest beds in the sections consistently deviate from a linear trend in the log-log plots. In some cases roll-over of bed thickness frequency is identified by a sharp break in slope, as in sections H2 and H9. Interestingly, Lillefors tests for H2 reject the normal, lognormal, and exponential distributions (Table 3.5), raising the possibility that this section may be most consistent with a modified power law. For other sections the drop-off in thin beds is more gradual, i.e., H1, H4, H5, and Lillefors testing shows that bed thicknesses are consistent with lognormal distributions.

3.4.2 Plateau West of Juventae

3.4.2.1 Bed Thickness Statistics

Sections measured on the plateau west of Juventae range between 30 and 70 meters in total thickness (Table 3.3). The 1 meter per pixel sections contain between 36 and 119 beds per section (Table 3.3), whereas 25 centimeter per pixel sections contain between one and two times as many beds, ranging from 83 beds in WJ7 to as many as 167 beds in WJ8. Mean bed thickness measured at this location using the 25 centimeter per pixel orthoimage ranges from ~30 centimeters (WJ8) to ~50 centimeters (WJ7), while mean bed thickness measured with 1 meter per pixel orthoimages is between ~50 centimeters (WJ3, WJ8) to more than 1 meter (WJ7). The number of beds and mean bed thickness differs between the

25 centimeter per pixel and 1 meter per pixel sections, but minimum and maximum bed thickness measured in the two data sets is similar. In fact, the maximum bed thickness measured with the 1 meter per pixel orthoimages is sometimes smaller than the corresponding maximum thickness measured with the 25 centimeter per pixel orthoimage, i.e., WJ1-WJ3.

3.4.2.2 Trends in Thickness Versus Stratigraphic Position

Six of ten sections on the plateau west of Juventae exhibit no statistically significant thinning or thickening upward trend when measured with the 25 centimeter per pixel orthoimage (Figure 3.10). Four sections show statistically significant thickening upward trends (WJ5, WJ6, WJ9, and WJ10). For sections where possible thickening trends have been identified, the estimated error bars are generally small enough that they do not span the full range of measured thicknesses. WJ9 and WJ10 may be the exceptions. The 1 meter per pixel results are similar to those obtained with the 25 centimeter per pixel data set (Table A2), with six of ten sections showing no thickening or thinning upwards trends, but with sections WJ3, WJ5, WJ6, and WJ8 all exhibiting thickening upwards trends.

Significance testing for RAM reveals that nine of ten sections on the plateau west of Juventae measured with the 25 centimeter per pixel orthoimage are consistent with a non-random ordering of deviations above or below mean thickness, suggesting frequent alternations between high and low values (Table 3.4). The 1 meter per pixel orthoimage results are similar, with the RAM null hypothesis failing to be rejected for only two sections (Table 3.4). RUD testing shows that only three of ten west Juventae plateau

sections are random for both the 25 centimeter per pixel and 1 meter per pixel orthoimage datasets, although of these two sections only WJ9 is common between the two datasets. These results indicate that sections on the plateau west of Juventae exhibit non-random bed thickness variations with stratigraphic position, with several sections thickening upwards.

3.4.2.3 Bed Thickness Distributions

The histogram and cumulative frequency plots for the 25 centimeter per pixel and 1 meter per pixel orthoimage results are qualitatively very similar, so only the 25 centimeter per pixel plots are discussed in detail. Histograms reveal a high frequency of thin beds present in the west Juventae plateau sections (Figure 3.13). The mode commonly occurs at the thinnest bed interval (as in sections WJ2, WJ4, WJ5, WJ6-WJ9) and histograms show an offset between the mean bed thickness and the mode, where modal bed thickness is thinner than mean thickness.

Theoretical lognormal and exponential CDFs match well the frequency of measured bed thickness (Figure 3.14). Exponential CDFs overestimate the number of thin beds present in several sections (WJ1, WJ9) and in some cases underestimate the frequency of intermediate thickness beds (WJ7-WJ9), but disparity in the quality of fits provided by lognormal and exponential CDFs is not obvious for these sections.

In contrast, normal CDFs consistently over-predict the frequency of thin beds and under-predict the number of intermediate thickness beds. This is consistent with the Lilliefors tests of normality, which suggest that the normal distribution is a poor fit for all of the 25 centimeter per pixel and 1 meter per pixel measured sections on the plateau west

of Juventae (Table 3.5). Of the ten sections measured here, the null hypothesis for lognormality is rejected at a 95% significance level or higher for half of the sections in both the 25 centimeter per pixel (WJ1, WJ3, WJ5, WJ8, WJ10) and 1 meter per pixel (WJ3, WJ5, WJ7, WJ8, WJ10) orthoimages. The null hypothesis for exponentiality is rejected at a 95% significance level or higher for seven of the sections measured with the 25 cm/pixel orthoimage, and for eight of ten sections measured with the 1 meter per pixel orthoimage. All three distributions are rejected for sections WJ3, WJ8, and WJ10 in both the 25 centimeter and 1 meter per pixel orthoimages, suggesting that a distribution other than those examined here may best explain bed thickness measurements.

3.4.2.4 Log-log plots

Sections on the plateau west of Juventae do not exhibit power law behavior over the full range of measured bed thickness values (Figure 3.15). Sections exhibit a gradual deviation from power law behavior for thin beds starting between 20-40 centimeters. The thickest beds measured in the sections also deviate from an expected power law trend.

3.4.3 *Gale Crater*

3.4.3.1 Bed Thickness Statistics

Total thickness for the sections measured in Gale crater ranges from 84 meters (GLM2) to more than 400 meters (GLM1) (Table 3.3). Using the 25 centimeter per pixel orthoimages, 300 and 86 beds were identified in sections GLM1 and GLM2, respectively. Half as many beds were tabulated for GLM1 using the 1 meter per pixel orthoimage, but

section GLM2 maintained 69 beds. The middle member sections, GMM1, GMM2, and GMM3, contain between 106-201 beds using the 25 centimeter per pixel dataset, but only 52-94 beds when measured with the 1 meter per pixel orthoimage. Mean bed thickness is greatest for GLM1 (1.29 meters with 25 centimeter pixel orthoimage, 2.57 meters with 1 meter per pixel) and decreases upsection with middle member 25 centimeter per pixel mean thickness ranging from ~0.66 centimeters to 1 meter. Upper member sections contain the smallest mean thickness between ~0.40 and 60 centimeters. Mean bed thickness decreases upsection using the lower resolution orthoimage as well, but with middle member mean thickness ranging from 1.61 to 1.96 meters and upper member thickness ranging from 0.86 centimeters to ~1 meter. Minimum measured bed thickness for all sections, whether measured with the 25 centimeter per pixel orthoimage or the 1 meter per pixel image, is <10 centimeter. However, maximum bed thickness varies between the sections, with the thickest beds measured in the lower member sections.

3.4.3.2 Trends in Thickness versus Stratigraphic Position

Five of eight Gale sections show statistically significant thinning or thickening upward trends when measured with 25 centimeter per pixel orthoimages (Figure 3.11). GLM1 and GUM2 show thinning upward trends, while GLM2, GUM1, and GUM3 show thickening trends. Using data extracted with the 1 m/pixel orthoimage (Table A2), 4 of 8 Gale sections show thinning or thickening upwards trends, with GLM2 and GUM2 thinning upwards and GMM1 and GUM3 thickening upwards.

Significance testing for RAM reveals that the null hypothesis of randomness is

rejected for all eight Gale sections measured with the 25 centimeter per pixel orthoimage, and for all but GMM2 measured with the 1 meter per pixel orthoimages (Table 3.4). Meanwhile, the RUD null hypothesis is rejected for only the two GLM sections and GUM2 using the 25 centimeter per pixel orthoimages. The remaining sections are consistent with a random distribution of thicknesses. Using the 1 meter per pixel orthoimage data and the RUD test, randomness is rejected for GLM2, GUM1, and GUM2. These results indicate that observed bed thickness variations may be non-uniform in Gale, even within a given member of the Lower formation. RAM tests show that bed thickness variations are non-random (Table 3.4), but some sections in a given member are consistent with thinning upward trends while other sections in that member are consistent with thickening upward trends.

3.4.3.3 Bed Thickness Distributions

Gale histograms show that bed thickness is positively skewed and beds most frequently fall into the thinnest histogram bins (Figure 3.13). Mean thickness is offset from modal thickness for all sections, with the mode being less than the mean thickness.

Both lognormal and exponential CDFs match reasonably well with the bed thickness measurements obtained from lower Mt. Sharp (Figure 3.14). Normal CDFs provide a poor match to the measured data, over-predicting the frequency of thin beds and under-predicting intermediate beds. Results of Lilliefors testing (Table 3.5) are generally consistent with the histograms and CF plots. The normal distribution is rejected for all eight Gale sections using both the 25 centimeter per pixel and 1 meter per pixel orthoimages.

Seven of eight Gale sections measured with the 25 centimeter per pixel orthoimage and five of the eight sections measured with the 1 meter per pixel orthoimage reject the lognormal null hypothesis. Exponentiality is rejected for only three of eight Gale sections measured with the 25 centimeter per pixel orthoimage (GLM1, GMM1, GUM2), and rejected for only GLM1 and GUM3 1 meter per pixel orthoimage sections. These results suggest that exponential distributions, rather than lognormal distributions, provide the best fit to the data.

3.4.3.4 Log-Log plots

Gale thickness distributions do not show power law behavior (Figure 3.15). Data sets experience gradual deviation of thin beds from the expected power law trend. The thickest beds also deviate from power law behavior, i.e., GMM1, GMM2, GMM3.

3.4.4 Additional Sections

3.4.4.1 Bed Thickness Statistics

Total section thickness at the other locations examined in this study ranges from ~50 meters (Athabasca) to nearly 1 kilometer (Danielson) (Table 3.3). The Becquerel and Danielson sections contain the most beds, 339 and 158, respectively, when measured with the 25 centimeter per pixel orthoimage. These same sections contain only 261 and 99 beds when measured with the 1 meter per pixel orthoimage. Mean bed thickness for the additional sections ranges between ~1 and 3 meters, although Danielson is an exception with a mean bed thickness of 5.41 meters. Mean bed thickness increases significantly for

several of the sections when using the 1 meter per pixel orthoimage. For example, mean bed thickness in Cross crater is 1.49 meter using the 25 centimeter per pixel orthoimage, but increases to nearly 5 meters with the 1 meter per pixel orthoimage. Mean bed thickness also increases in Danielson from ~5 meters to nearly 10 meters.

3.4.4.2 Trends in Thickness versus Stratigraphic Position

According to bed thickness measurements made with the 25 centimeter per pixel orthoimage, only Argyre, Becquerel, and Candor1 show statistically significant thinning or thickening trends, with Argyre thickening upwards and Becquerel and Candor1 thinning upwards (Figure 3.12). When using bed thickness measurements extracted from the 1 meter per pixel orthoimages, only Eberswalde shows a significant trend, thickening upwards (Table A2).

RAM significance testing of the 25 centimeter per pixel orthoimage sections reveals that all sections except Athabasca and Candor2 reject the null hypothesis of randomness about the mean (Table 3.4). In contrast, all but two 1 meter per pixel sections fail to reject the RAM null hypothesis. Testing for RUD shows that all sections, both 25 centimeter per pixel and 1 meter per pixel, fail to reject the null hypothesis except Becquerel. The RAM results are somewhat contradictory between the two datasets, making interpretation difficult, but it is clear that all sections but Becquerel are indistinguishable from a random distribution according to RUD testing.

3.4.4.3 Bed Thickness Distributions

Histograms for these sections show that the most frequent bed thickness generally falls within the smallest bin (Figure 3.13). Argyre is the exception to this, but the distribution is still unimodal and positively skewed. As with other sections examined in this study, the mean is generally thicker than the mode.

Cumulative frequency plots show that theoretical normal distributions do not provide a good fit to the data (Figure 3.14). Except for Argyre, the normal distribution overestimate the number of thin beds and underestimate the number of intermediate beds. Both exponential and lognormal distributions provide decent qualitative fits for the Athabasca, Becquerel, Candor, Cross, Danielson, and Eberswalde sections. The Argyre section appears to be better described by the exponential fit, as the lognormal distribution overestimates the number of thin beds and underestimates the number of thick beds.

Statistical testing helps to support these qualitative observations (Table 3.5). Normal distributions are not a good fit because almost all sections measured reject the null hypothesis of normality at a significance level of 95% or higher, regardless of which orthoimage was used. Lognormal distributions provide relatively good fits to the data, with only Becquerel, Candor2, and Danielson rejecting the lognormal null hypothesis. The results are nearly opposite when using the 1 meter per pixel data, with all sections rejecting the null hypothesis of lognormality except Athabasca and Cross craters. Tests for exponentiality show that Athabasca, Candor2, Cross, and Danielson 25 centimeter per pixel sections fail to reject the null hypothesis, while others clearly reject the null hypothesis (Argyre, Becquerel, Candor1, and Eberswalde). Most noteworthy in these results is

Becquerel, which is not consistent with any of the three distributions regardless of which orthoimage is used for analysis, and for which it has been suggested that bed thicknesses are rhythmic and normally distributed [Lewis *et al.*, 2008].

3.4.4.4 Log-Log Plots

Log-log plots show that none of these additional sections follow power law behavior over the full range of bed thickness values (Figure 3.15). Gentle rollover in the number of thin beds occurs between ~0.5 m and 1m for these sections, and thick beds also deviate from the expected linear trend.

3.5 Discussion

3.5.1 Bed Thickness on Mars

The simplest possible interpretation of bed thickness on Mars is that thickness represents a sediment volume and each bed records information about transport and dispersal during deposition. Thicker beds may signal larger sediment volumes and/or shorter dispersal length scales, whereas thin beds signal smaller sediment volumes and/or longer dispersal length scales. Therefore, bed thickness characteristics might help broadly bound the processes associated with accumulation of strata (transport, deposition, erosion) while providing additional criteria—similar to mineralogy, tone, or weathering pattern—for correlation of spatially distinct strata. Similarities in bed thickness properties between spatially distinct deposits may indicate that such strata have experienced similar depositional histories, whereas differences in bed thickness properties highlight locations

where very distinct processes or conditions may have persisted. This study presents some of the ways that bed thickness can be used to learn more about the history and formation of sedimentary deposits on Mars, as well as some of the caveats associated with such an analysis.

3.5.2 Stratigraphic and statistical trends in bed thickness

3.5.2.1 Thinning and thickening trends

In sedimentary basins on Earth, the deposition and accumulation of material is regulated by three main factors: sediment supply, base level, and rate of subsidence. In aqueous environments on Earth, the main role of tectonic subsidence in sediment deposition is in creating accommodation space and modulating base level. In the absence of tectonic controls it is unclear what role, if any, subsidence would play in controlling the deposition, accumulation, and erosion of sedimentary materials on Mars over long timescales. Therefore, it is assumed that subsidence is not a primary control on the formation of most Martian sedimentary deposits [Grotzinger and Milliken, 2012]. In the absence of tectonically controlled subsidence, accommodation space is likely to be modulated more directly by sediment supply. Thus even in the absence of subsidence, accommodation, sediment supply, and bed thickness likely vary—very generally—from proximal to distal along a single chronostratigraphic interval for certain depositional environments. For example, a simple alluvial fan system shows how these parameters vary systematically as a function of distance from the source (Figure 3.16). At the apex of the fan, fast moving flows deposit thick, coarse-grained beds. Decrease in flow

competence downdip results in an effective decrease in accommodation, and lower flow velocities lead to the deposition of thinner, finer-grained deposits.

At odds with this simple model for alluvial fan bed thickness, Holden sections show no systematic or statistically significant change in mean or maximum bed thickness, either increasing or decreasing, from H1 (located in a proximal setting closest to the expected sediment source) to H10 (a more distal location, farthest from the crater wall). This suggests that sediment supply, accommodation, and erosion rates were fairly constant over the area covered by these sections. Mean and maximum bed thickness also remain fairly constant over the area covered by WJ1-WJ10 on the plateau west of Juventae. The simplest interpretation of these observation is that the deposits in Holden crater and on the plateau west of Juventae Chasma represent fall-out deposits—lacustrine, volcanic ash, or dust—where the depositional mechanism(s) predict greater lateral continuity of bed thickness. This hypothesis would be consistent with the deposits in Holden crater being lacustrine, as was suggested by *Grant et al.*, [2008]. In addition, no clear trends in mean bed thickness are observed laterally between sections measured within the members of lower Mt. Sharp, suggesting that depositional conditions were also fairly consistent over this area of Gale crater at the member scale.

Lateral changes in bed thickness reveal depositional and erosional conditions at a single time interval, but vertical thickening or thinning trends within a section express changes in deposition and erosion over time. Thickening and thinning trends observed in sedimentary sequences can represent changes in accommodation space [*Fischer*, 1964; *Read and Goldhammer*, 1988]. In a simple model, thick beds are deposited when there is

ample space for material to deposit (increased accommodation); thin beds form when accommodation decreases [Read and Goldhammer, 1988]. After considering the results of significance testing and error analysis, it is clear that the 25 centimeter per pixel Holden sections show no significant increase or decrease in thickness vertically through the sections. The paucity of thinning or thickening trends in Holden may imply that sediment dispersal was uniform over time, occurring in an environment where suspended materials were advected over broad regions and settled out of suspension to form sheet deposits. This type of deposition might occur in subaqueous lacustrine (muds) or eolian settings (dust, ash) where suspended fines settle out during quiescent periods. The lack of thinning or thickening trends in this location suggests that changes in base level may not have significantly influenced the formation of bedding, perhaps due to constant sediment supply and lack of tectonic subsidence.

On the plateau west of Juventae, four of the ten 25 centimeter per pixel sections exhibit a thickening upward trend at a statistically significant level, indicating that this trend may be real. However, because it is unclear why the other six sections at this location show no trend at all, it is difficult to speculate on the meaning of this trend. Consistent thickening or thinning trends are also not observed within the lower and upper member sections of Gale crater (Figure 3.11). Despite being within the same member, GLM1 shows an overall thinning trend while GLM2 shows a thickening trend. Similarly, GUM1 and GUM3 show thickening trends while GUM2 shows a thinning trend. As these sections are separated by several kilometers, it is possible that these disparate trends record distinct depositional conditions within the crater, but an alternative explanation is

that these trends are due to variations in lighting, slope, or quality of exposed outcrop that induce apparent thinning and thickening. Trends within members at Gale crater are difficult to interpret and may be susceptible to image artifacts, but a systematic decrease in mean bed thickness upsection is observed in Gale crater over the Lower formation as a whole (Table 3.3). Mean bed thickness decreases from the lower to middle members, with the upper member sections exhibiting the thinnest mean thickness. The overall change in mean bed thickness between the members may suggest changes in sediment deposition and erosion rates through time on the member-scale, rather than at the scale of individual beds. Therefore, the results presented here suggest that the morphological member boundaries and compositional changes identified by *Milliken et al.* [2010] may have been accompanied by broad changes in sediment supply and/or accommodation space within Gale crater. While the process by which the strata in the lower formation of Mt. Sharp were deposited is still unknown, the morphological and mineralogical changes identified by *Milliken et al.* [2010], coupled with the systematic bed thickness changes identified here, can form the basis for depositional hypotheses testable in situ with the Curiosity rover [*Grotzinger et al.* 2012].

RAM testing in Holden crater, on the plateau west of Juventae, and in Gale crater reveals that bed thickness in these sections is not randomly distributed about the mean; rather thin and thick beds tend to alternate frequently within the section (Table 3.4). RUD testing shows that Holden and Gale middle and upper member sections are consistent with a random ordering of bed thicknesses. However, a majority of the sections measured on the plateau west of Juventae are not random according to RUD testing. RUD testing

uses the number of runs present in the section to determine whether or not an overall trend exists—too few runs suggests a trend and the null hypothesis of randomness is rejected. While this test is particularly sensitive to small-scale runs within the data that can obscure overall trends [Chen and Hiscott, 1999], the RUD results for the west plateau of Juventae are consistent with the overall thickening upward trends observed at this location. The testing performed here does not explain the specific mechanism responsible for the non-random distributions observed on the west plateau of Juventae, but the difference between west Juventae plateau results and those obtained in Holden and Gale may suggest that the process influencing deposition at Juventae is distinct from the other two study sites.

3.5.2.2 Statistical Distribution of Bed Thickness

Cumulative frequency plots (Figure 3.14) show that lognormal distributions consistently provide the best fits to bed thickness frequencies in Holden crater. The results of Lilliefors testing support this observation (Table 3.5), as eight of ten Holden sections are statistically indistinguishable from a lognormal distribution at a 95% or greater significance level. *Talling* [2001] suggests that a lognormal bed thickness distribution represents a multiplicative addition of randomly distributed flow and sediment parameters. However, physical models that explain exactly how those parameters would produce a lognormal bed thickness distribution in a sedimentary sequence remain elusive. The lognormal distributions observed in Holden may represent the multiplicative combination of primary depositional variables, but additional modeling beyond the scope of this paper is needed to

explore this possibility.

Modal thickness is often interpreted as a recurrent response to some extrabasinal or intrabasinal periodic forcing function, i.e., *Lewis et al.* [2008] and *Limaye et al.*, [2012]. If the lognormal distributions observed in Holden crater represent primary signals, the modal thickness between 20-60 centimeters observed in histograms may imply the recurrence of an as yet unknown process within the Holden depositional system that favored the formation of beds ~50 centimeters thick. Interestingly, Becquerel and Danielson, the two deposits previously identified as cyclic [*Lewis et al.*, 2008, *Andrews-Hanna and Lewis*, 2011], reject both the normal and lognormal distributions in this study. In apparent conflict with these results, *Lewis et al.* [2008] observed a normal distribution in Becquerel crater, suggesting that a quasi-periodic process controlled by orbital variations was responsible for observed ~4 meter thick beds. A closer examination of the Becquerel histogram (Figure 3.3) reveals a minor mode at ~3 meters, in addition to the most frequently populated bin <1 meter. A minor mode is also present in the Danielson histogram at ~10 meters. If a sampling bias is not responsible for the emergence of these modes, i.e., *Drummond and Wilkinson* [1996], they could be representative of the cyclic processes suggested by *Lewis et al.* [2008] and *Andrews-Hanna and Lewis* [2011]. It is important to note that this study's results show the majority of beds in Becquerel and Danielson to be thinner than these minor modes, indicating that a previously unrecognized small-scale non-cyclic process modulated deposition at these locations.

Another explanation for the lognormal distributions observed in the Martian sections is the modification of an input signal, such as a power law or exponential

distribution, due to filtering processes [Malinverno, 1997; Carlson and Grotzinger, 2001; Jerolmack and Paola, 2010] or sampling biases [Rothman *et al.*, 1994; Drummond and Wilkinson, 1996]. Unfortunately, without a priori information about the depositional context for most Martian deposits it is difficult, if not impossible, to distinguish the input distribution from the current distribution of bed thickness using only orbital measurements. Alternatively, Drummond and Wilkinson [1996] and Rothman *et al.* [1994] suggest that all lognormal bed thickness distributions are the result of a sampling bias that under-represents thin beds in what should be negative exponential trends. Given that bed thickness was measured using orthoimages with resolution limits of 25 centimeters per pixel and 1 meter per pixel, it is almost certain that beds exist at finer scales than can be measured here. For this reason, a sample bias cannot be rejected for either the 25 centimeter per pixel or 1 meter per pixel sections examined in this study.

Lognormal distributions are common in Holden crater, but lognormality is rejected for all but one section in the lower part of Mount Sharp in Gale crater and for five of the ten sections measured on the west Juventae plateau. Additionally, sections measured on the west plateau of Juventae and in Gale crater rarely exhibit modal thickness (Figure 3.13). Theoretical exponential distributions provide reasonable fits to the west Juventae plateau and Gale sections (Figure 3.14), and five of eight Gale sections measured with the 25 centimeter per pixel orthoimages fail to reject the exponential distribution. These results suggest that bed thickness distributions measured in Gale and on the west Juventae plateau may be more consistent with stochastic sediment accumulation. In contrast to the bed thicknesses observed in the Lower formation, the Upper formation of Mount Sharp exhibits

beds of very regular thickness [Lewis, 2009; Milliken *et al.*, 2010; Grotzinger and Milliken, 2012], suggesting the influence of external forces not present in the deposition of lower mound materials. Bed thickness measurements with the *Curiosity* rover will likely provide additional insight to the observations made here, allowing a direct comparison of bed thicknesses derived from orbital observations to rover-based observations of bed thickness measurements and actual depositional processes.

3.5.2.3 Power Law Behavior of Bed Thickness Frequency

The log-log plots in Figure 3.15 show that bed thickness frequency measured in Holden, on the plateau west of Juventae, and in Gale crater does not follow a power-law trend. The lack of power-law scaling in these deposits may rule out formation by sedimentary gravity flows or deposition controlled by other scale-invariant processes. However, power-law scaling for many terrestrial turbidite deposits is supported by the occurrence of numerous thin beds that would be close to or below the resolution of HiRISE data. Because the number of thin beds decreases for most sections just above the resolution of HiRISE images, it is difficult to exclude power-law behavior entirely.

The observed systematic change in power-law behavior with distance from the source in submarine fan deposits [Carlson and Grotzinger, 2001] suggests that characteristic modification of power-law behavior is linked to unique facies. Of all the sections measured in the study, those in Holden crater offer the best opportunity to observe systematic changes in power-law behavior with lateral facies variations because a sediment source (the crater wall) is known, and the sections are arranged at increasing distance away

from this source. However, systematic modification of power-law behavior is not observed from H1 to H10. This implies that the length scale of changes in fluvial/alluvial/lacustrine facies may be much longer than the length scale represented by the distance between H1 to H10. Alternatively, this may imply that some sediments in the measured beds were not sourced solely from the crater walls and may instead reflect alternative sources, e.g., evaporites, airfall deposits, volcanic ash, etc.

3.5.3 Building a global inventory of bed thickness distributions on Mars

In addition to the 28 total sections measured in Holden crater, on the plateau west of Juventae, and in Gale crater, sections were measured at seven other locations on Mars. Bed thickness statistics measured at different locations, even if it is only one or two sections, can be used to build a global inventory of quantitative stratification characteristics. As an example, Figure 3.17 summarizes the Lilliefors test results of this study. Lognormal distributions are not ubiquitous for the sections measured here, but they are the most common distribution observed. Normal distributions are generally not observed in the Mars sections measured here consistent with the observation of *Grotzinger and Milliken* [2012] that rhythmite deposits are rare on Mars. Exponential distributions are observed in Gale and at several other locations, but they appear to be less common than lognormal distributions.

While this study builds the foundation for a global inventory of bed thickness, only ten locations on the surface of Mars were analyzed. As a result, linking unique depositional environments with specific bed thickness distributions is difficult. However, there are a

number of ways depositional environments or mechanisms could be linked to unique bed thickness statistics in the future. For example, dozens of large alluvial fans have been identified in highland craters on Mars [Moore and Howard, 2005]. If DTMs were produced and bed thickness distributions measured for the dozens of observed alluvial fan deposits, trends in bed thickness could lead to the development of facies-specific criteria. These criteria would have the potential to distinguish alluvial deposits globally on Mars, particularly in outcrops where morphologic characteristics may be ambiguous, i.e., crater-filling mounds. Another example could be the systematic study of bed thickness distributions in the interior layered deposits of Valles Marineris, a number of which are known to contain sulfates [Gendrin *et al.*, 2005; Mangold *et al.*, 2008]. Comparison of bed thickness properties of these deposits to those observed in locations such as Danielson could provide an independent test as to whether these deposits have similar origins, as has been suggested based on mineralogical data [Arvidson *et al.*, 2005; Bibring *et al.*, 2007]. Future work could also include a systematic study of bed thickness statistics in deposits exhibiting distinct orbital mineralogy [Bibring *et al.*, 2006], comparing bed thickness in phyllosilicate-bearing deposits [Poulet *et al.* 2005; Bibring *et al.*, 2006] with those measured in sulfate-bearing terrains [Gendrin *et al.*, 2005].

3.5.4 Challenges of Bed Thickness Analysis

Although the analysis of bed thickness statistics and distributions holds much promise in helping to illuminate the depositional history of sedimentary rocks on Mars, there are numerous challenges associated with this type of analysis.

For many, if not most of the sedimentary deposits on Mars, there exists limited a priori knowledge of the processes, conditions, or forcing mechanisms that produced the changes in brightness that are identified as beds. It is generally assumed that bedding planes represent primary depositional surfaces [Grotzinger and Milliken, 2012], but there is considerable uncertainty about the expression of depositional versus diagenetic signals, intrinsic organization versus external forcing, and what length hiatus, if any, bed boundaries signify. However, it is this uncertainty that necessitates bed thickness analyses like those presented in this study. Unlike on Earth, where outcrops and rocks can be examined in the field and laboratory in great detail to fully test depositional hypotheses, studies on Mars are currently (and for the foreseeable future) forced to rely on satellite and the rare rover and lander observations. In this context, it is prudent to consider all observations that can be accurately measured and quantified in order to fully characterize depositional environments and processes on Mars. Even if bed thickness is a non-unique parameter and if the specific mechanisms that give rise to bedding are unknown, it still remains one of the few properties of Martian strata that can be quantified and approached from a statistical vantage point with existing orbital data. Bed thickness alone is likely not sufficient to uniquely determine a depositional environment, but it is an important characteristic of sedimentary strata that should be integrated with other observations when documenting and describing a stratigraphic section. Parameters such as mean bed thickness, range in thickness, and thickening/thinning upward trends are probably most useful when integrated with additional statistical, stratigraphic, and compositional analyses.

The resolution limits of orbital data pose a major challenge when attempting to

extract depositional information from bed thickness measurements on Mars. This study uses 25 centimeter per pixel orthophotos draped on 1 meter DTMs to identify and measure bed thickness, thereby requiring oversampling of the 1 meter DTM to obtain elevation values for the observed bed boundaries. By interpolating between tiepoints, it is possible to measure the thickness of very thin beds visible in the 25 centimeter per pixel orthoimages, but oversampling can result in very large relative errors in thickness. This is the case for many of the Holden thickness measurements (Figure 3.9) where the error of individual thickness measurements is dominated by the vertical precision of the DTM. Averaging individual thickness measurements for each section helps reduce the overall error and enables comparison between sections, but large errors make identification of trends within each section difficult. Additionally, beds whose thickness is at or near the resolution of orbital data are particularly susceptible to the effects of slope on DTM and orthoimage resolution. Sections measured in this study generally do not show significant changes in slope upsection (Figure A1, Athabasca, Danielson, and Candor1 sections are exceptions), so this effect is likely minimal here. It is acknowledged, however, that comparisons between very thinly-bedded sections with different slopes could be susceptible to this effect.

It is also possible that the beds identified in orbital images consist of thinner beds that are amalgamated or simply below the image resolution. In addition, the quality of outcrop exposure may affect the scale of observable bedding, as thinner beds can be obscured by dust or other surficial deposits. Disruption of an outcrop by post-depositional deformation, such as impact cratering, may also obscure beds in orbital images. These

factors may result in an under-representation of thin beds in the histograms, CF plots, and log-log plots presented here, affecting the ability to detect lateral or vertical thinning or thickening trends. The effects of resolution are most apparent in this study when comparing the 25 centimeter and 1 meter datasets. The main trends in runs testing and distribution fits are generally similar between the 25 centimeter and 1 meter data sets, but statistical testing of specific sections sometimes fails to produce the same results at both resolutions. Disparities in the thinning and thickening trends identified in Holden and on the west plateau of Juventae in the 25 centimeter per pixel and 1 meter per pixel data sets are examples of this (Figures 3.9 and 3.10 and Table A2). Therefore, it is important to consider that the techniques presented in this study can only interrogate bedding and depositional processes down to a scale defined by image resolution. Scales of deposition representing the thinnest beds and finest-scale processes simply cannot be studied with these methods.

In studies of turbidite bed thickness on Earth, it is usually possible to measure hundreds to thousands of beds. On Mars, the number of beds that can be measured in an outcrop is constrained by a number of factors including the extent and quality of outcrop exposure and the outcrop slope. A sample size of $n = 30$ typically separates large-sample statistics from small-sample statistics and below this size sampling uncertainties become important [Davis, 2002]. The number of beds measured in several of the sections presented here is just at or below the small-sample statistic boundary and is still significantly less than the number of beds measured in Earth studies. Additionally, when only one section is measured at a location it is difficult to determine whether the statistical results are truly representative of the deposit. Therefore, Martian deposits must contain a certain number of

beds, the more the better, to avoid small-sample statistical uncertainties, and it is prudent to measure as many sections as possible in a particular location.

Because of the uncertainties and limitations associated with using bed thickness to study sedimentary deposits on Mars, it is unrealistic to expect that thickness measurements and frequency distributions will reveal unique depositional mechanisms and environments for all sedimentary sequences. The application of bed thickness analysis on Earth has been limited largely to specific facies, mostly commonly deep-water turbidites and shallow marine carbonates. A statistically significant number of bed thickness distributions simply has not been compiled for enough sedimentary deposits on Earth, e.g., pyroclastic deposits, alluvial fans, fluvial systems, and evaporite sequences, to know if bed thickness alone can uniquely represent a particular depositional process or environment. Additional work is needed on both Earth and Mars to link specific statistical distributions, deviations from those distributions, and characteristic bed thickness to depositional processes and environments.

3.6 Conclusions

By necessity, previous studies of sedimentary deposits and environments on Mars have been grounded in qualitative geomorphologic observations. Although such observations are powerful, the hypotheses that derive from such observations must ultimately be tested by actual measurements or models. For the first time, high-resolution DTMs such as those derived from HiRISE images provide the opportunity to quantify bed thickness properties down to the sub-meter scale. This study highlights ways that statistical

techniques can enhance understanding of sedimentary depositional processes and environments on Mars. For example, relatively constant bed thickness observed in Holden crater and on the plains west of Juventae Chasma favors deposition by fall out processes common in lacustrine and airfall deposits. Meanwhile, the exponential distributions observed in the lower Mt. Sharp suggest stochastic deposition at odds with rhythmic trends observed higher up in the sequence at Gale crater. The Becquerel-Danielson analysis illustrates the usefulness of statistical bed thickness analysis in several ways. First, it allows for a quantitative comparison between two spatially distinct locations on Mars, highlighting similarities and differences between the two deposits beyond what is apparent from qualitative morphological observations. Additionally, the methods presented here provide insight into a small-scale aperiodic depositional process previously unrecognized in a region of Mars known for its cyclic sedimentation. Although the likely non-uniqueness of bed thickness distributions and the limitations imposed by the resolution of the data are acknowledged, the statistical analysis of bed thickness provides a more objective and quantitative approach to the characterization of Martian strata, while also aiding in the study of sedimentary depositional processes. This statistical approach can now be applied to the increasing number of layered deposits imaged on Mars, building a global inventory of quantitative stratigraphic properties.

Notation

- a scaling constant in exponential equation.
- α angle between the measured section and the dip direction, degrees.
- b scaling constant in exponential equation.
- c scaling constant in power law equation.
- d constant scaling exponent in power-law equation given by slope of the plot in $\log(N)$ versus $\log(t)$ space.
- δ dip of beds, degrees.
- e emission angle, angle between a line extending from the center of a HiRISE image to the spacecraft and a “normal” perpendicular to the planet’s surface, degrees.
- EP expected vertical precision of DTM.
- G rate parameter of an exponential distribution.
- GSD ground sample distance, meter/pixel resolution of the more oblique image in the HiRISE image pair, m.
- h horizontal distance along the measured section line between the upper and lower bed boundaries, m.
- H_0 null hypothesis.
- N number of beds in a section.
- N number of beds as a function of thickness t .
- ρ pixel matching error between a stereo pair.
- p significance probability.
- P parallax, degrees.
- σ standard deviation of bed thickness, m.
- t bed thickness, m.
- μ mean bed thickness, m.
- v elevation difference between upper and lower boundaries of each bed, m.

TABLES**Table 3.1 HIRISE DTMs and Orthoimages Used in This Study**

DTMs	Resolution of Stereo Pairs (m/pixel)	Emission Angles	Roll Angles of Stereo Pairs	Precision of elevations values in DEM (m)	Grid spacing of DTM	Resolution of Orthoimage (m/pixel)
DTEEC_019045_1530	0.263	9.4	8.877	0.09	1 m	25 cm, 1 m
_019322_1530_U01	0.278	21.6	-19.865			
DTEEC_002088_1530	0.265-0.530	12.2	11.406	0.24	1 m	25 cm, 1 m
_002154_1530_U01	0.528	11.1	-10.871			
DTEEC_015999_1535	0.269	14.9	13.941	0.09	1 m	25 cm, 1 m
_016276_1535_U01	0.266	14.9	-13.673			
DTEEC_003434_1755	0.262	1.1	1.003	0.17	1 m	25 cm, 1 m
_003579_1755_U01	0.274	17.9	16.629			
DTEEC_012551_1750	0.271	3.5	-3.158	0.09	1 m	25 cm, 1 m
_012841_1750_U01	0.301	27.7	25.598			
DTEEC_001488_1750	0.267	2.5	2.365	0.15	1 m	25 cm, 1 m
_001752_1750_U01	0.28	17.5	-16.165			
DTEEC_019698_1750	0.291	24.1	-22.115	0.07	1 m	25 cm, 1 m
_019988_1750_U01	0.278	14.7	13.722			
DTEEC_003816_1245	0.254	4.1	3.823	0.14	1 m	25 cm, 1 m
_004106_124_A01	0.275	23.6	21.868			
DTEEC_002661_1895	0.296	21.8	20.111	0.19	1 m	25 cm, 1 m
_003294_1895_U01	0.278	4.8	4.428			
DTEEC_001546_2015	0.284	2.8	2.474	0.35	1 m	25 cm, 1 m
_001955_2015_U01	0.287	6.4	-5.938			
DTEEC_001918_1735	0.285	23.9	22.048	0.12	1 m	25 cm, 1 m
_001984_1735_U01	0.262	0.8	-0.763			
DTEEC_010228_1490	0.258	8.1	-7.452	0.13	1 m	25 cm, 1 m
_016320_1490_A01	0.26	13.5	12.703			
DTEEC_002878_1880	0.279	9.3	8.587	0.18	1 m	25 cm, 1 m
_002733_1880_U01	0.278	7.6	-6.996			
DTEEC_019757_1560	0.262	8.2	7.746	0.11	1 m	25 cm, 1 m
_020034_1560_U01	0.272	17.8	-16.373			

Table 3.2 Study Sites

Study Site	Setting	Orbital Facies [Grotzinger and Milliken, 2012]	Selected References
Holden crater	Crater interior	Distributary Network	Pondrelli <i>et al.</i> [2005]; Grant <i>et al.</i> [2008]; Milliken and Bish [2010]; Grant <i>et al.</i> [2011]
W. Juventae Plateau	Interchasm/intercrater plains	Laterally Continuous Heterolithic Strata	Milliken <i>et al.</i> [2008]; Bishop <i>et al.</i> [2009]; Weitz <i>et al.</i> [2008, 2010]; LeDeit <i>et al.</i> [2010]
Gale crater	Crater interior	Laterally Continuous Sulfate Strata	Malin and Edgett [2000]; Anderson and Bell [2010]; Milliken <i>et al.</i> [2010]; Thomson <i>et al.</i> [2011]
Argyre Planitia	Impact basin interior	-	Howard [1981]; Parker <i>et al.</i> [1986]; Kargel and Strom [1992]; Hiesinger and Head [2002]; Banks <i>et al.</i> [2009]
Athabasca Valles	Outflow channel	-	Rice <i>et al.</i> [2003]; Burr [2003, 2005]; Leverington [2004]; Jaeger <i>et al.</i> [2007, 2010]
Becquerel crater	Crater interior	Rhythmite	Lewis <i>et al.</i> [2008]
Candor Chasma	Chasm	Laterally Continuous Sulfate Strata	Okubo and McEwen [2007]; Fueten <i>et al.</i> [2008]; Murchie <i>et al.</i> [2009]; Metz <i>et al.</i> [2010]; Okubo [2010]
Cross crater	Crater interior	Laterally Continuous Heterolithic Strata	Wray <i>et al.</i> [2011]
Danielson crater	Crater interior	Rhythmite/Laterally Continuous Sulfate Strata	Edgett and Malin [2002]; Edgett [2005]
Eberswalde crater	Crater interior	Distributary Network	Bhattacharya <i>et al.</i> [2005]; Lewis and Aharonson [2006]; Pondrelli <i>et al.</i> [2008]

Table 3.3 Basic Bed Thickness Statistics

25 cm/pixel							1 m/pixel						
Location	Outcrop Slope	Total Section Thickness (m)	n	μ (m)		Min t (m)	Max t (m)	Total Section Thickness		μ (m)	σ (m)	Min t (m)	Max t (m)
				μ (m)	σ (m)			(m)	n				
H1	0.19	34.0 \pm 1.1	67	0.51 \pm 0.02	0.32	0.17 \pm 0.13	1.59 \pm 0.13	34.9 \pm 0.8	38	0.92 \pm 0.02	0.79	0.19 \pm 0.13	4.51 \pm 0.13
H2	0.11	17.7 \pm 2.8	68	0.26 \pm 0.04	0.26	<0.10 \pm 0.34	1.41 \pm 0.34	16.0 \pm 2.3	45	0.36 \pm 0.05	0.30	<0.10 \pm 0.34	1.63 \pm 0.34
H3	0.15	20.3 \pm 2.9	72	0.28 \pm 0.02	0.20	0.10 \pm 0.34	1.62 \pm 0.34	23.3 \pm 2.0	35	0.67 \pm 0.06	0.48	0.20 \pm 0.34	2.30 \pm 0.34
H4	0.22	22.6 \pm 2.7	60	0.38 \pm 0.04	0.23	0.14 \pm 0.35	1.28 \pm 0.34	20.3 \pm 1.8	28	0.73 \pm 0.06	0.25	0.38 \pm 0.34	1.35 \pm 0.34
H5	0.34	16.7 \pm 2.2	41	0.41 \pm 0.05	0.16	0.15 \pm 0.34	0.79 \pm 0.34	19.7 \pm 1.6	23	0.86 \pm 0.07	0.28	0.51 \pm 0.34	1.59 \pm 0.34
H6	0.24	14.5 \pm 2.3	47	0.31 \pm 0.05	0.17	0.11 \pm 0.34	0.85 \pm 0.34	15.8 \pm 1.8	28	0.56 \pm 0.06	0.33	0.13 \pm 0.34	1.39 \pm 0.34
H7	0.25	24.8 \pm 2.7	64	0.39 \pm 0.04	0.22	<0.10 \pm 0.34	1.19 \pm 0.34	25.0 \pm 2.1	39	0.64 \pm 0.06	0.36	0.10 \pm 0.34	1.83 \pm 0.34
H8	0.28	21.7 \pm 2.4	50	0.43 \pm 0.05	0.17	0.2 \pm 0.34	0.93 \pm 0.34	25.5 \pm 1.9	32	0.80 \pm 0.06	0.58	0.34 \pm 0.34	3.57 \pm 0.34
H9	0.13	25.2 \pm 3.2	90	0.28 \pm 0.04	0.23	<0.10 \pm 0.34	1.27 \pm 0.34	25.3 \pm 2.4	49	0.52 \pm 0.05	0.36	<0.10 \pm 0.34	1.45 \pm 0.34
H10	0.16	32 \pm 1.2	86	0.37 \pm 0.01	0.23	<0.10 \pm 0.13	1.55 \pm 0.13	32.8 \pm 0.9	48	0.68 \pm 0.05	0.41	0.24 \pm 0.13	2.88 \pm 0.13
WJ1	0.20	38.3 \pm 2.3	88	0.44 \pm 0.03	0.43	<0.10 \pm 0.24	2.83 \pm 0.24	44.4 \pm 2.0	67	0.66 \pm 0.03	0.47	<0.10 \pm 0.24	2.77 \pm 0.24
WJ2	0.15	53.0 \pm 2.5	108	0.49 \pm 0.02	0.55	<0.10 \pm 0.24	3.02 \pm 0.24	53.5 \pm 2.2	83	0.64 \pm 0.03	0.51	<0.10 \pm 0.24	2.92 \pm 0.24
WJ3	0.16	55.7 \pm 2.7	129	0.43 \pm 0.02	0.43	<0.10 \pm 0.24	2.89 \pm 0.24	58.1 \pm 2.6	119	0.49 \pm 0.02	0.41	<0.10 \pm 0.24	2.60 \pm 0.24
WJ4	0.15	46.9 \pm 2.6	119	0.39 \pm 0.02	0.41	<0.10 \pm 0.24	2.91 \pm 0.24	47.4 \pm 2.2	85	0.56 \pm 0.02	0.50	<0.10 \pm 0.24	3.03 \pm 0.24
WJ5	0.16	58.9 \pm 2.9	143	0.41 \pm 0.02	0.42	<0.10 \pm 0.24	2.75 \pm 0.24	70.1 \pm 2.5	108	0.65 \pm 0.02	0.66	<0.10 \pm 0.24	4.15 \pm 0.24
WJ6	0.13	45.7 \pm 2.4	101	0.45 \pm 0.02	0.50	<0.10 \pm 0.24	3.03 \pm 0.24	48.4 \pm 1.8	58	0.83 \pm 0.03	0.77	<0.10 \pm 0.24	3.41 \pm 0.24
WJ7	0.12	42.0 \pm 2.2	83	0.51 \pm 0.03	0.64	<0.10 \pm 0.24	4.37 \pm 0.24	42.9 \pm 1.4	36	1.19 \pm 0.04	1.20	<0.10 \pm 0.24	5.49 \pm 0.24
WJ8	0.06	46.5 \pm 3.1	167	0.28 \pm 0.02	0.31	<0.10 \pm 0.24	2.99 \pm 0.24	45.3 \pm 2.3	89	0.51 \pm 0.03	0.49	<0.10 \pm 0.24	3.82 \pm 0.24
WJ9	0.19	30.0 \pm 2.3	95	0.32 \pm 0.02	0.26	<0.10 \pm 0.24	1.93 \pm 0.24	31.6 \pm 1.6	43	0.73 \pm 0.04	0.63	0.15 \pm 0.24	3.60 \pm 0.24
WJ10	0.10	45.8 \pm 2.7	127	0.36 \pm 0.02	0.30	<0.10 \pm 0.24	1.59 \pm 0.24	48.0 \pm 1.9	62	0.77 \pm 0.03	0.63	<0.10 \pm 0.24	2.90 \pm 0.24
GLM1	0.20	410.4 \pm 2.3	300	1.37 \pm 0.01	1.29	<0.10 \pm 0.13	13.9 \pm 0.20	403.4 \pm 1.7	157	2.57 \pm 0.01	2.36	<0.10 \pm 0.13	16.08 \pm 0.15
GLM2	0.22	83.8 \pm 2.1	86	0.97 \pm 0.02	0.92	<0.10 \pm 0.22	4.49 \pm 0.22	129.9 \pm 1.8	69	1.88 \pm 0.03	2.94	<0.10 \pm 0.22	19.05 \pm 0.26
GMM1	0.18	179.0 \pm 1.9	201	0.89 \pm 0.01	0.79	<0.10 \pm 0.14	4.71 \pm 0.16	179.1 \pm 1.3	94	1.91 \pm 0.01	1.58	<0.10 \pm 0.13	7.72 \pm 0.14
GMM2	0.17	108.8 \pm 2.2	106	1.03 \pm 0.02	1.12	<0.10 \pm 0.22	6.79 \pm 0.21	101.9 \pm 1.6	52	1.96 \pm 0.03	2.54	<0.10 \pm 0.22	15.55 \pm 0.23
GMM3	0.19	123.5 \pm 1.6	186	0.66 \pm 0.01	0.76	<0.10 \pm 0.13	5.25 \pm 0.13	128.9 \pm 1.1	80	1.61 \pm 0.01	1.66	<0.10 \pm 0.12	8.92 \pm 0.15
GUM1	0.11	247.2 \pm 3.4	638	0.39 \pm 0.01	0.45	<0.10 \pm 0.21	4.85 \pm 0.13	237.1 \pm 3.9	275	0.86 \pm 0.01	0.92	<0.10 \pm 0.44	7.44 \pm 0.14
GUM2	0.14	268.4 \pm 2.9	441	0.61 \pm 0.01	0.73	<0.10 \pm 0.12	6.49 \pm 0.49	258.1 \pm 2.9	275	0.94 \pm 0.01	1.10	<0.10 \pm 0.48	6.8 \pm 0.57
GUM3	0.13	246.0 \pm 2.5	521	0.47 \pm 0.00	0.52	<0.10 \pm 0.11	3.6 \pm 0.11	239.4 \pm 1.7	232	1.03 \pm 0.01	0.97	<0.10 \pm 0.12	5.04 \pm 0.12
Argyre	0.23	204.8 \pm 2.4	138	1.48 \pm 0.02	1.01	0.15 \pm 0.20	6.63 \pm 0.21	207.3 \pm 1.7	69	3.00 \pm 0.03	1.69	0.16 \pm 0.21	9.09 \pm 0.24
Athabasca	0.06	57.6 \pm 2.0	55	1.05 \pm 0.04	1.04	<0.10 \pm 0.27	4.91 \pm 0.27	46.2 \pm 1.5	32	1.45 \pm 0.05	1.48	<0.10 \pm 0.27	7.05 \pm 0.27
Becquerel	0.11	685.9 \pm 9.2	339	2.02 \pm 0.03	1.86	<0.10 \pm 0.5	7.93 \pm 0.5	702.2 \pm 8.0	261	2.69 \pm 0.03	2.08	<0.10 \pm 0.50	12.13 \pm 0.52
Candor1	0.04	98.6 \pm 1.7	96	1.03 \pm 0.02	1.37	<0.10 \pm 0.18	7.78 \pm 0.17	110.1 \pm 1.4	61	1.80 \pm 0.02	1.68	<0.10 \pm 0.18	7.16 \pm 0.21
Candor2	0.13	178.8 \pm 1.5	60	2.98 \pm 0.03	2.27	0.16 \pm 0.17	9.61 \pm 0.20	182.9 \pm 1.4	48	3.81 \pm 0.03	2.48	<0.10 \pm 0.17	8.18 \pm 0.25
Cross	0.28	159.0 \pm 2.0	107	1.49 \pm 0.02	1.65	<0.10 \pm 0.19	10.45 \pm 0.19	152.2 \pm 1.1	31	4.91 \pm 0.03	5.37	0.78 \pm 0.19	23.99 \pm 0.20
Danielson	0.04	855.0 \pm 6.6	158	5.41 \pm 0.04	4.98	<0.10 \pm 0.33	20.93 \pm 0.26	964.3 \pm 2.8	99	9.74 \pm 0.03	10.05	0.14 \pm 0.26	82.04 \pm 0.80
Eberswalde	0.12	90.6 \pm 1.6	98	0.92 \pm 0.02	1.69	<0.10 \pm 0.16	14.8 \pm 0.16	86.2 \pm 1.2	57	1.51 \pm 0.02	2.21	0.12 \pm 0.16	15.44 \pm 0.16

Table 3.4 Runs Test Significance Probability Values

Location	25 cm/pixel						1 m/pixel					
	RAM			RUD			RAM			RUD		
	<i>p</i> value	Rej ect	No. of run s	<i>p</i> value	Reje ct	No. of run s	<i>p</i> value	Rej ect	No. of run s	<i>p</i> value	Reje ct	No. of run s
H1	0.001	Yes	18	0.402	No	47	0.001	Yes	8	0.257	No	21
H2	0.000	Yes	12	0.382	No	37	0.006	Yes	14	0.045	Yes	23
H3	0.000	Yes	14	0.156	No	39	0.499	No	15	0.630	No	24
H4	0.000	Yes	15	0.796	No	41	0.014	Yes	8	0.049	Yes	13
H5	0.585	No	19	0.218	No	22	1.000	No	12	0.791	No	14
H6	0.007	Yes	15	0.860	No	30	0.017	Yes	8	0.394	No	16
H7	0.008	Yes	21	0.726	No	44	0.004	Yes	11	0.199	No	20
H8	0.000	Yes	12	0.600	No	33	0.050	Yes	10	0.214	No	17
H9	0.000	Yes	24	0.831	No	57	0.010	Yes	16	0.186	No	28
H10	0.788	No	39	0.177	No	50	0.010	Yes	15	0.448	No	29
WJ1	0.138	No	29	0.327	No	54	1.000	No	31	0.034	Yes	36
WJ2	0.000	Yes	20	0.563	No	68	0.012	Yes	29	0.023	Yes	44
WJ3	0.000	Yes	35	0.000	Yes	67	0.000	Yes	37	0.008	Yes	64
WJ4	0.002	Yes	41	0.002	Yes	62	0.000	Yes	22	0.276	No	51
WJ5	0.000	Yes	39	0.002	Yes	75	0.000	Yes	25	0.000	Yes	52
WJ6	0.000	Yes	16	0.010	Yes	52	0.000	Yes	12	0.225	No	34
WJ7	0.002	Yes	23	0.001	Yes	41	0.061	No	11	0.004	Yes	16
WJ8	0.000	Yes	56	0.002	Yes	89	0.010	Yes	32	0.024	Yes	49
WJ9	0.000	Yes	24	0.424	No	56	0.030	Yes	14	0.295	No	25
WJ10	0.000	Yes	35	0.033	Yes	70	0.040	Yes	21	0.035	Yes	33
GLM1	0.000	Yes	85	0.016	Yes	181	0.000	Yes	52	0.080	No	94
GLM2	0.000	Yes	25	0.000	Yes	40	0.001	Yes	20	0.003	Yes	35
GMM1	0.000	Yes	57	0.152	No	124	0.001	Yes	30	0.150	No	56
GMM2	0.018	Yes	36	0.373	No	66	0.494	No	19	0.778	No	35
GMM3	0.000	Yes	49	0.837	No	120	0.008	Yes	24	1.000	No	53
GUM1	0.000	Yes	169	0.517	No	411	0.000	Yes	77	0.007	Yes	161
GUM2	0.000	Yes	122	0.000	Yes	255	0.000	Yes	87	0.007	Yes	161
GUM3	0.000	Yes	139	0.215	No	330	0.000	Yes	71	0.111	No	143
Argyre	0.004	Yes	50	0.660	No	89	0.016	Yes	25	0.360	No	42
Athabasca	0.201	No	20	0.957	No	37	0.0771	No	10	0.515	No	19
Becquerel	0.000	Yes	56	0.008	Yes	202	1.26E-16	Yes	64	0.002	Yes	151
Candor1	0.008	Yes	31	0.177	No	57	0.0613	No	23	0.329	No	44
Candor2	0.088	No	23	0.796	No	41	0.3262	No	21	0.949	No	31
Cross	0.003	Yes	34	0.261	No	65	0.2403	No	9	0.948	No	21
Danielson	0.021	Yes	59	0.924	No	106	0.3918	No	54	0.968	No	66
Eberswalde	0.008	Yes	26	0.656	No	62	0.792	No	22	0.958	No	38

Table 3.5 Lilliefors Probability Significance Values

Location	p-values (Lilliefors)					
	25 cm/pixel			1 m/pixel		
	Normal	Lognormal	Exponential	Normal	Lognormal	Exponential
H1	<0.001	0.276	<0.001	<0.001	>0.500	0.004
H2	<0.001	<0.001	0.010	0.005	0.003	0.083
H3	<0.001	0.212	<0.001	<0.001	0.275	<0.001
H4	<0.001	0.065	<0.001	0.006	0.084	<0.001
H5	0.342	>0.500	<0.001	0.021	0.296	<0.001
H6	<0.001	0.059	<0.001	0.008	>0.500	<0.001
H7	<0.001	0.115	<0.001	0.371	0.229	<0.001
H8	<0.001	0.056	<0.001	<0.001	>0.500	<0.001
H9	<0.001	0.240	0.002	0.020	0.139	0.068
H10	<0.001	0.015	<0.001	0.001	0.357	<0.001
WJ1	<0.001	0.001	<0.001	<0.001	0.079	<0.001
WJ2	<0.001	0.086	0.003	<0.001	>0.500	<0.001
WJ3	<0.001	<0.001	0.001	<0.001	<0.001	0.004
WJ4	<0.001	0.136	0.004	<0.001	0.122	0.025
WJ5	<0.001	<0.001	0.052	<0.001	0.014	0.008
WJ6	<0.001	0.244	0.070	<0.001	0.438	>0.500
WJ7	<0.001	0.056	0.251	<0.001	0.003	0.180
WJ8	<0.001	<0.001	0.019	<0.001	<0.001	0.002
WJ9	<0.001	0.378	0.001	0.001	>0.500	0.015
WJ10	<0.001	<0.001	0.002	<0.001	0.005	<0.001
GLM1	<0.001	<0.001	<0.001	<0.001	0.086	<0.001
GLM2	<0.001	<0.001	0.261	<0.001	0.075	0.100
GMM1	<0.001	<0.001	<0.001	0.001	0.012	0.281
GMM2	<0.001	0.008	0.324	<0.001	0.405	0.063
GMM3	<0.001	0.078	0.401	<0.001	0.019	0.394
GUM1	<0.001	<0.001	0.062	0.001	<0.001	0.179
GUM2	<0.001	<0.001	0.008	<0.001	<0.001	0.084
GUM3	<0.001	<0.001	0.054	<0.001	0.008	0.024
Argyre	<0.001	>0.500	<0.001	0.065	0.048	<0.001
Athabasca	<0.001	>0.500	>0.500	<0.001	0.276	>0.500
Becquerel	<0.001	<0.001	0.017	<0.001	<0.001	<0.001
Candor1	<0.001	0.159	<0.001	0.003	0.006	>0.500
Candor2	<0.001	0.046	0.128	0.002	0.034	0.008
Cross	<0.001	0.262	>0.500	<0.001	0.111	0.047
Danielson	<0.001	0.012	0.429	<0.001	0.001	0.074
Eberswalde	<0.001	>0.500	<0.001	<0.001	0.015	0.027

FIGURE CAPTIONS

Figure 3.1. Representative exponential, lognormal, normal, and power-law cumulative bed thickness distributions plotted on a linear scale.

Figure 3.2. Reference map showing locations discussed in this chapter. Sites where multiple bed thickness distributions were measured are highlighted in red. Basemap is MOLA topography draped over a THEMIS Day IR mosaic.

Figure 3.3. Geomorphic context of deposits examined in this study. Stars indicate the location of measured sections on MOLA topography draped over a THEMIS Day IR mosaic. (a) Argyre Planitia: -55.2 N, 314.3 E. (b) Athabasca Valles: 9.6 N, 156.3 E. (c) Becquerel Crater: 21.4 N, 351.9 E. (d) Candor Chasma: -6.5 N, 283.1 E. (e) Cross Crater: -30.6 N, 202.2 E (f) Danielson crater: 8.12 N, 353.1 E. (g) Eberswalde Crater: -23.9 N, 326.5 E. (h) Gale Crater: -4.8 N, 137.4 E. (i) Holden Crater: -26.6 N, 325.2 E. (j) Plateau west of Juventae Chasma: -4.7 N, 296.4 E. Scale bar = 25 km.

Figure 3.4. (Left) Location of Holden sections H1-H10 plotted on CTX image P22_009696_1531_XI_26S034W_080821. (Right) Sections along which bed thickness were measured. H1: HiRISE ESP_019045_1530; H2-H9: PSP_002088_1530; H10: ESP_015999_1535. Blue traces indicate profiles along which coordinates were extracted for orientation measurements. Orientation measurements displayed in red represent average strike and dip for each section; measurements displayed in yellow are representative individual measurements for sections whose beds were assumed to be horizontal. All

individual orientation measurements are listed in Table A1. Scale bar for inset boxes = 50 m; contours = 5 m.

Figure 3.5. (Left) Location of the sections measured on the plateau west of Juventae Chasma. WJ1-WJ10: HiRISE PSP_003579_1755. Blue traces indicate profiles along which coordinates were extracted for orientation measurements. Orientation measurements displayed in yellow are representative individual measurements since beds were assumed to be horizontal. All individual orientation measurements are listed in Table A1. (Right) Profiles along which bed thickness was measured. Scale bar for inset boxes = 75 m; contours = 5 m.

Figure 3.6. (Left) Sections measured in lower Mt. Sharp, Gale crater on CTX P02_001752_1753_XI_04S222W_061210. Dotted line represents the contact between lower and middle members; black solid line traces the marker bed between the middle and upper members of the Lower formation. (Right) Profiles along which bed thicknesses were measured. GLM1, GMM1, GUM1: ESP_012551_1750; GLM2, GMM2: PSP_001488_1750; GMM3, GUM2, GUM3: ESP_019698_1750. Blue traces indicate profiles along which coordinates were extracted for orientation measurements. Orientation measurements displayed in red represent average strike and dip for each section. All individual orientation measurements are listed in Table A1. Scale bar = 500 m; contours = 10 m.

Figure 3.7. Profiles measured at (a) Argyre Planitia, PSP_003816_1245; (b) Athabasca Valles, PSP_002661_1895; (c) Becquerel Crater, PSP_001546_2015; (d) Candor1,

PSP_001918_1735; (e) Candor2, PSP_001918_1735; (f) Cross Crater, ESP_010228_1490; (g) Danielson crater, PSP_002878_1880; (h) Eberswalde Crater, ESP_019757_1560. Blue traces indicate profiles along which coordinates were extracted for orientation measurements. Orientation measurements displayed in red represent average strike and dip for each section; measurements displayed in yellow are representative individual measurements for sections whose beds were assumed to be horizontal. All individual orientation measurements are listed in Table A1. Scale bar = 500 m; contours = 5 m for Athabasca, Cross, and Eberswalde sections; contours = 10 m for Argyre, Becquerel, Candor1, Candor2, Danielson sections.

Figure 3.8. (a) Three dimensional perspective of sample outcrop (WJ4) from the plateau west of Juventae Chasma. (b) Schematic diagram showing the profile along which bed boundaries were measured (shown in red), points extracted along bedding plane used to measure the orientation of bedding (shown in blue), and variables used to calculate true bed thickness. (c) Schematic representation of bedding plane points fit to a plane. (d) Plan view of outcrop illustrating α , the angle between the measured profile and the dip direction.

Figure 3.9. Bed thickness displayed as a function of stratigraphic position for sections measured in Holden crater. Slope values (bed thickness/bed number) are displayed in red. For p less than 0.05, the null hypothesis is rejected and the section is assigned a thinning or thickening trend. Scale bar = 20 m.

Figure 3.10. Bed thickness displayed as a function of stratigraphic position for sections measured on the plateau west of Juventae Chasma. Slope values (bed thickness/bed

number) are displayed in red. For p less than 0.05, the null hypothesis is rejected and the section is assigned a thinning or thickening trend. Scale bar = 50 m.

Figure 3.11. Bed thickness displayed as a function of stratigraphic position for sections measured in Gale Crater. Slope values (bed thickness/bed number) are displayed in red. For p less than 0.05, the null hypothesis is rejected and the section is assigned a thinning or thickening trend. Scale bar = 100 m.

Figure 3.12. Bed thickness displayed as a function of stratigraphic position for sections measured in Argyre Planitia, Athabasca Valles, Becquerel crater, Candor crater, Cross crater, Eberswalde crater, and Danielson crater. Slope values (bed thickness/bed number) are displayed in red. For p less than 0.05, the null hypothesis is rejected and the section is assigned a thinning or thickening trend. Scale bar = 100 m.

Figure 3.13. Histograms of sections in Holden, west Juventae plateau, Gale, Argyre, Athabasca, Becquerel, Candor Chasma, Cross, Eberswalde, and Danielson. Histograms are normalized so that the total area sums to 1. Dashed line indicates the mean thickness, and n is the number of beds measured for each section.

Figure 3.14. Plots of empirical CDFs and theoretical exponential, lognormal, and normal CDFs for the bed thickness measured in Holden, west Juventae plateau, Gale, Argyre, Athabasca, Becquerel, Candor Chasma, Cross, Eberswalde, and Danielson.

Figure 3.15. Log-log plots displaying the proportion of bed thickness values greater than or equal to t for sections measured in Holden, west Juventae plateau, Gale, Argyre,

Athabasca, Becquerel, Candor Chasma, Cross, Eberswalde, and Danielson.

Figure 3.16. Stratigraphy of a simple alluvial fan modeled with STRATA [*Flemings and Grotzinger, 1996*], assuming constant flux of sediment and equal marine and non-marine diffusion constants. VE=250. Note change in thickness of time equivalent depositional sequences from the proximal location (a) to the median location (b) to the distal section (c).

Figure 3.17. Pie charts showing proportion of measured sections (measured on both 1 m and 25 cm orthoimages) for which the null hypothesis is rejected or failed to be rejected at a 95% significance level using the Lilliefors test.

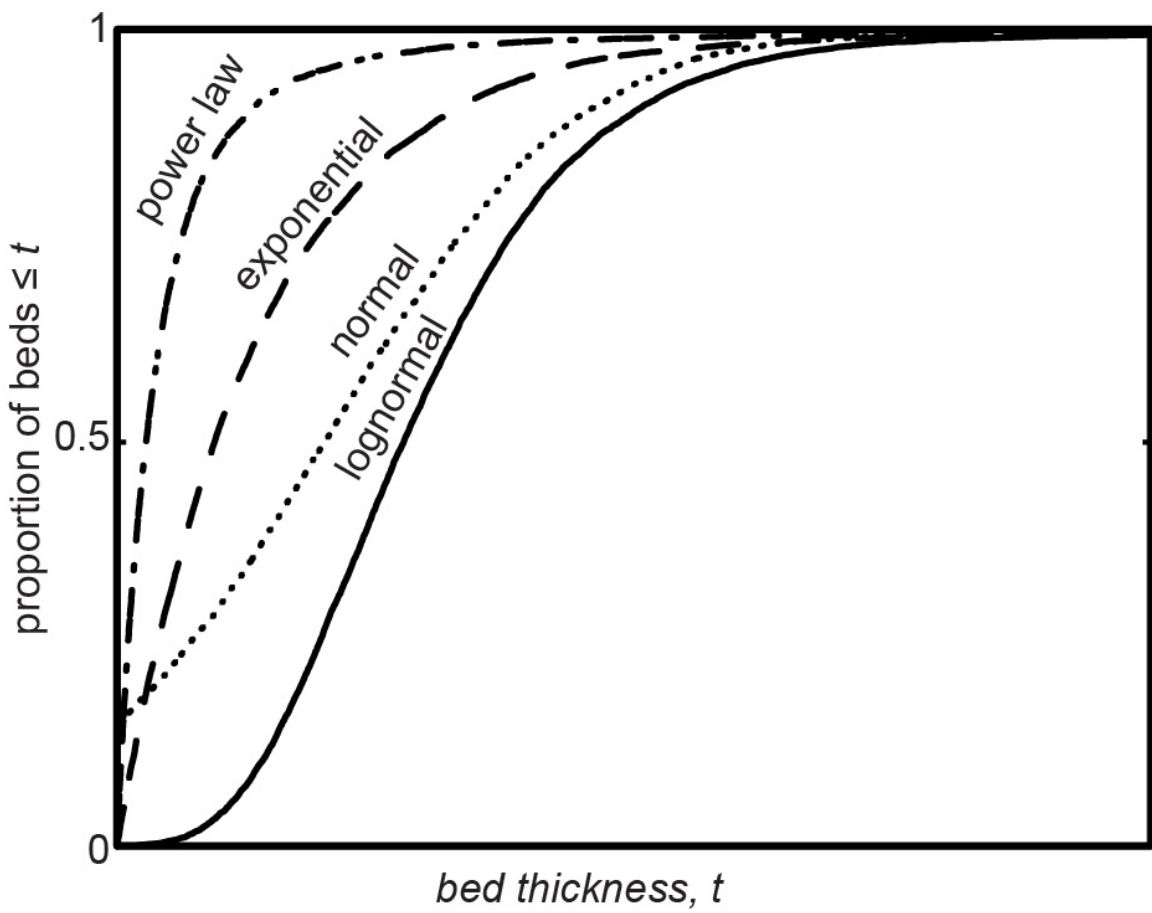


Figure 3.1

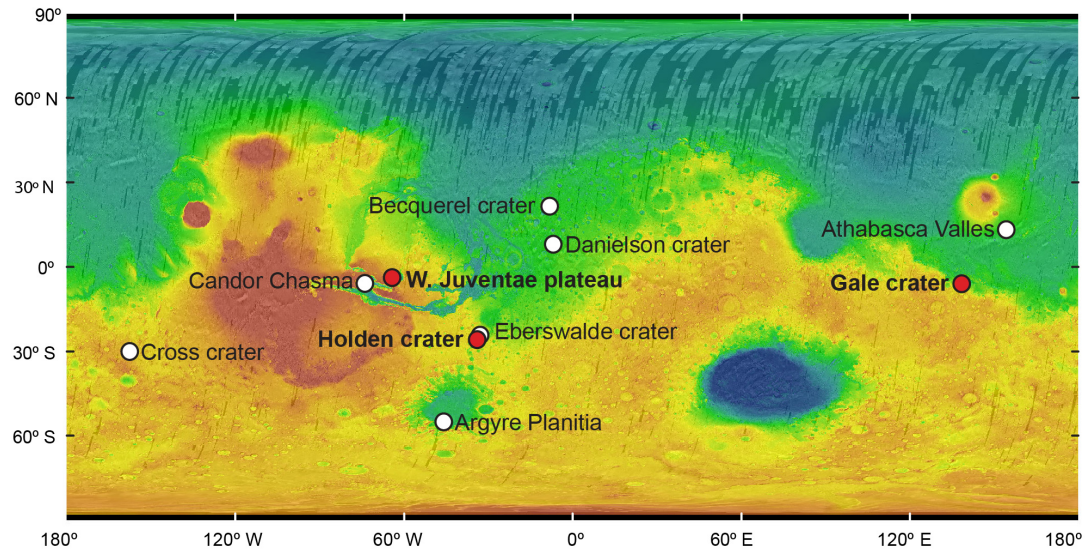


Figure 3.2

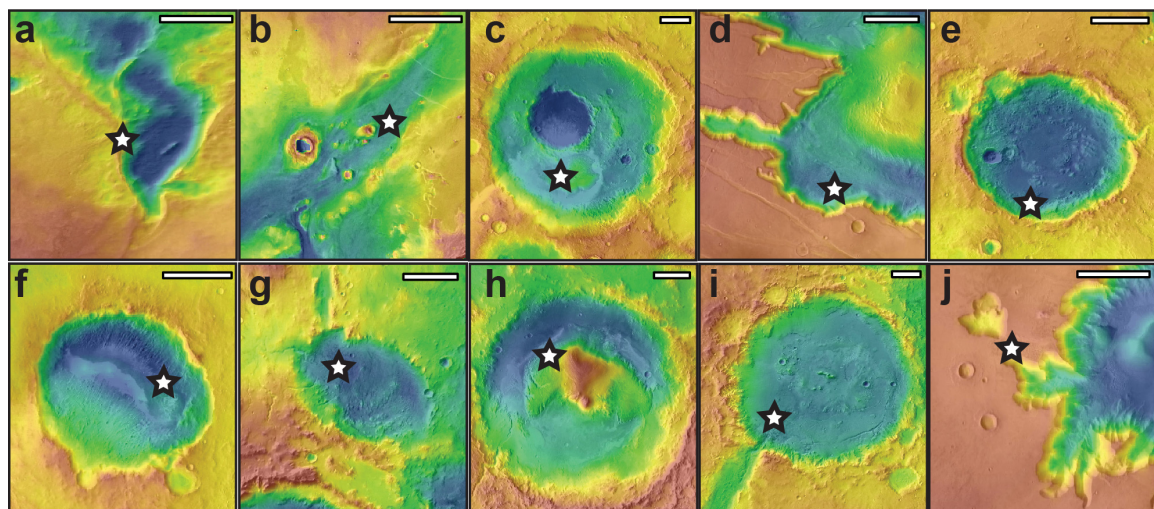


Figure 3.3

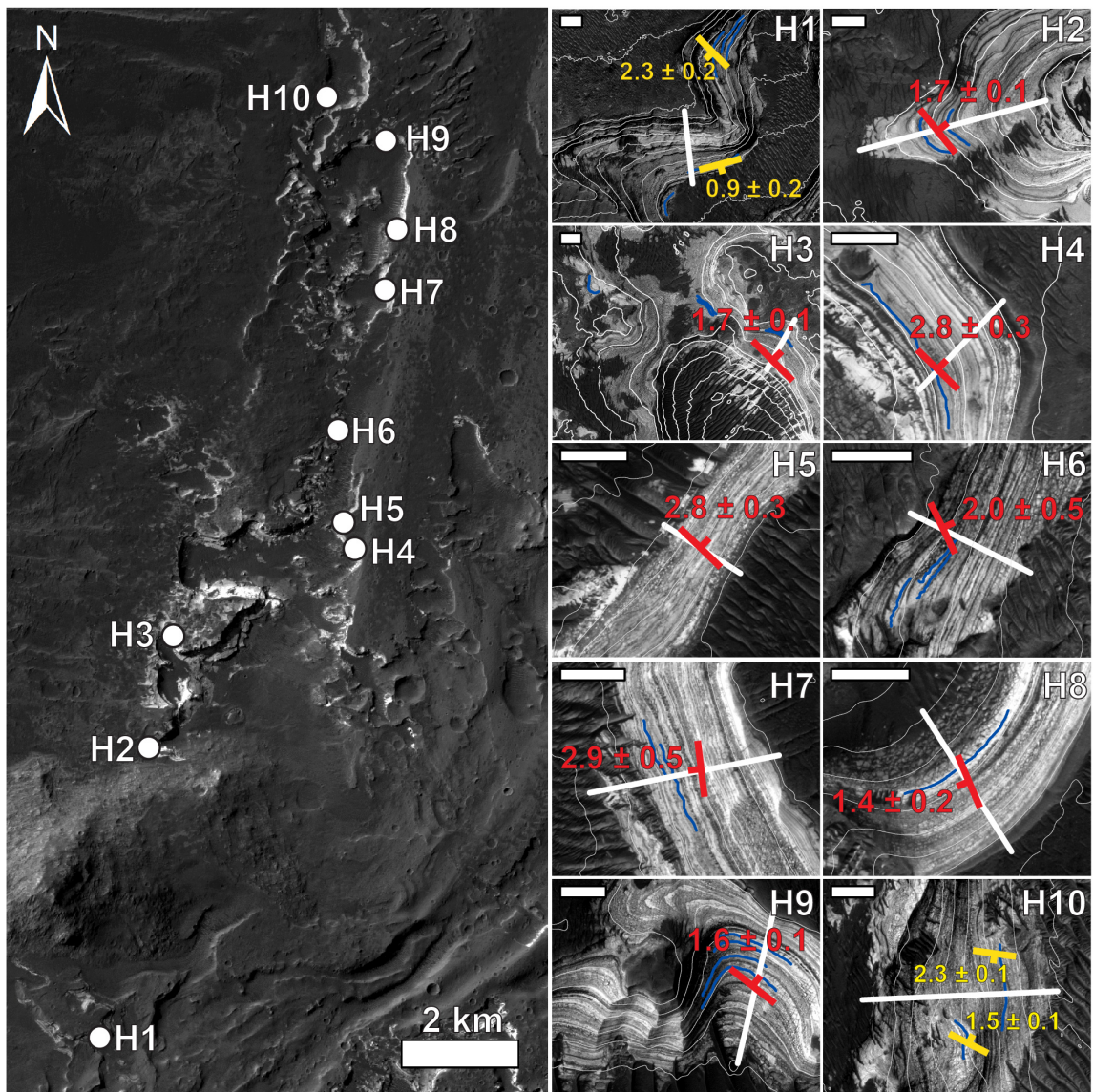


Figure 3.4

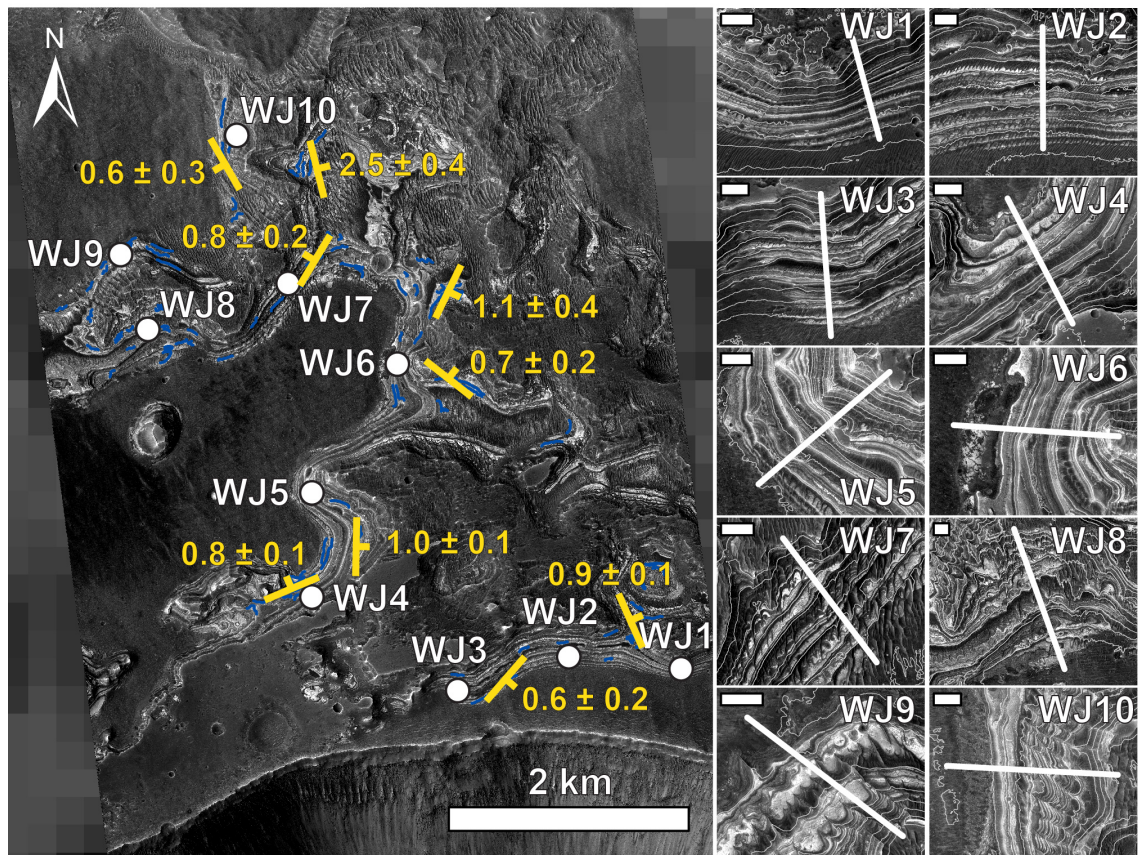


Figure 3.5

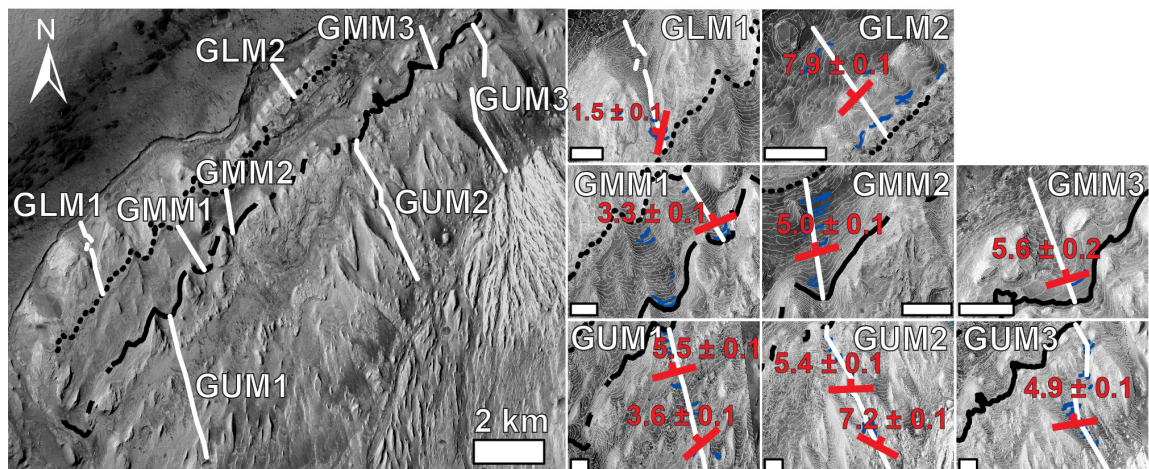


Figure 3.6

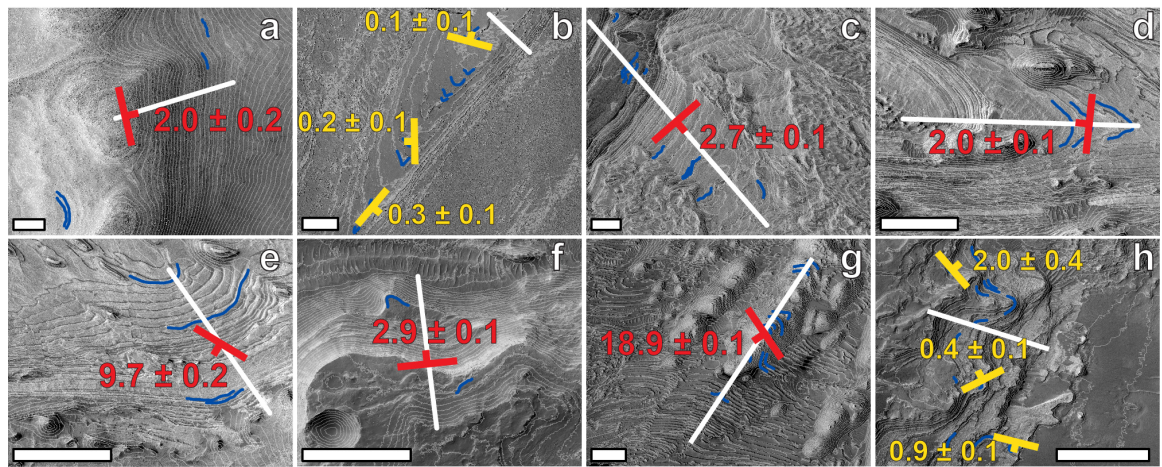


Figure 3.7

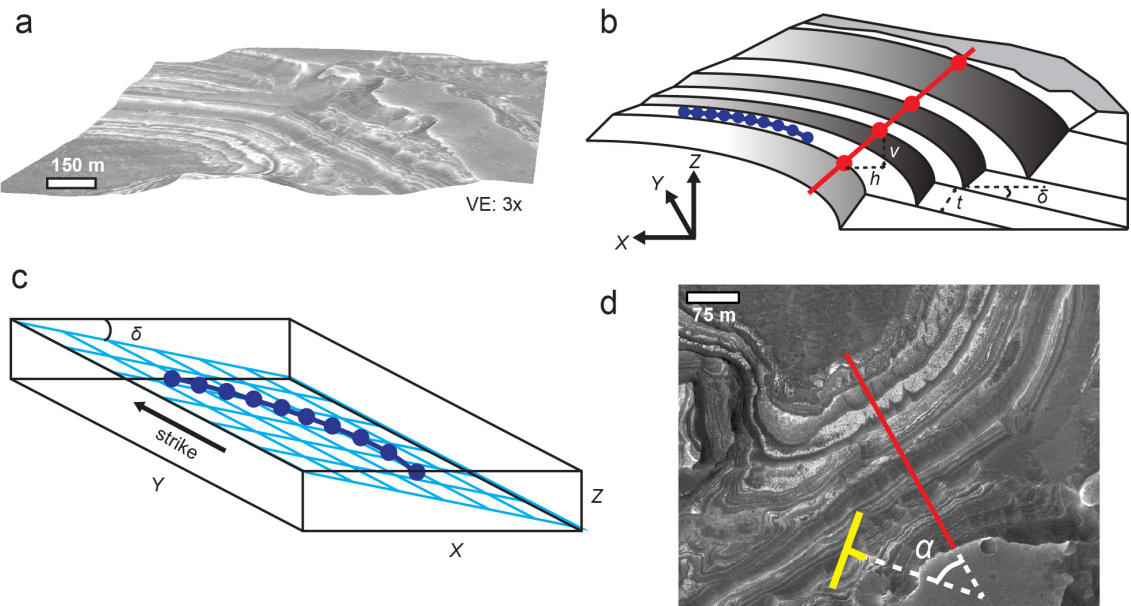


Figure 3.8

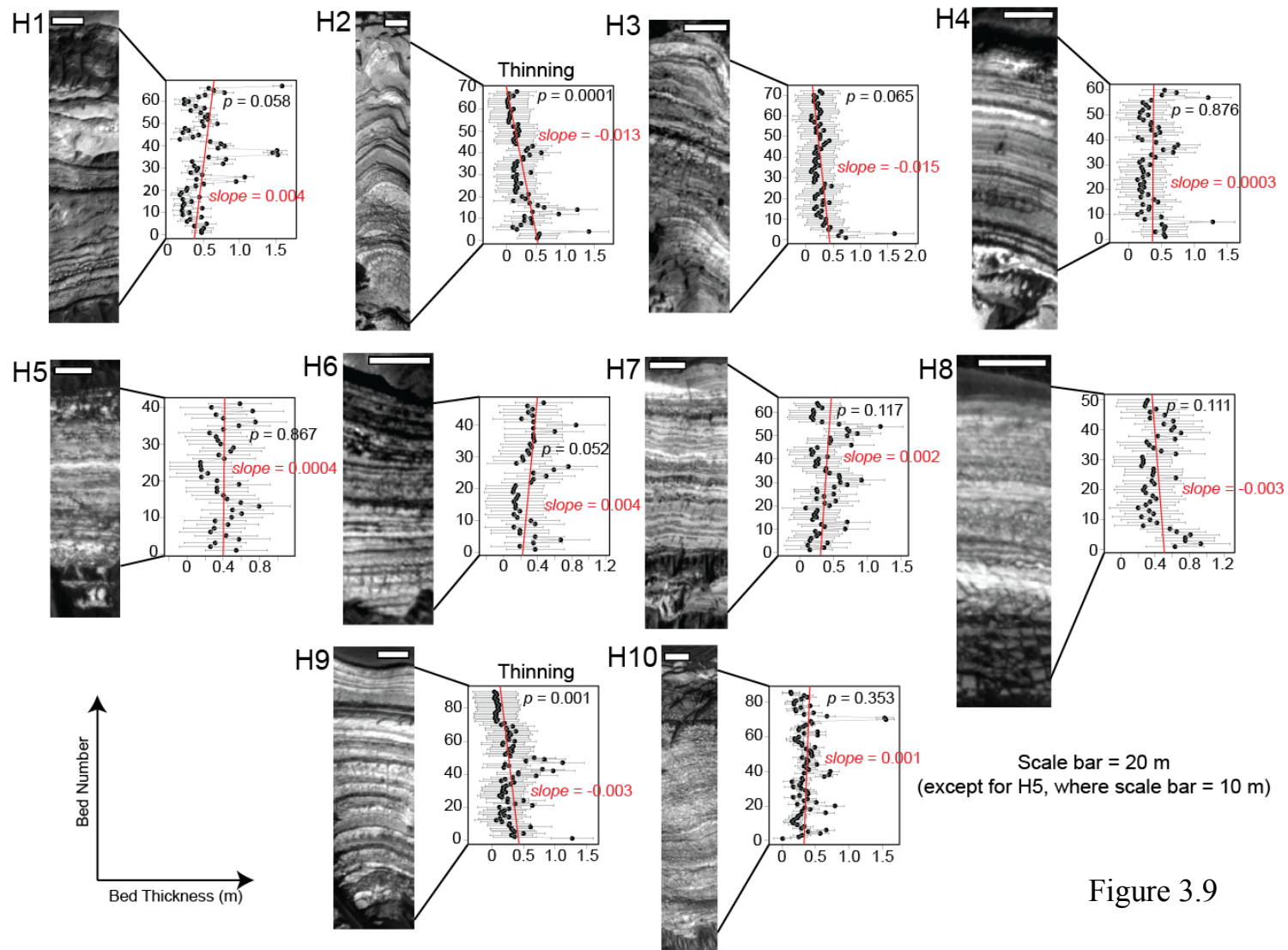


Figure 3.9

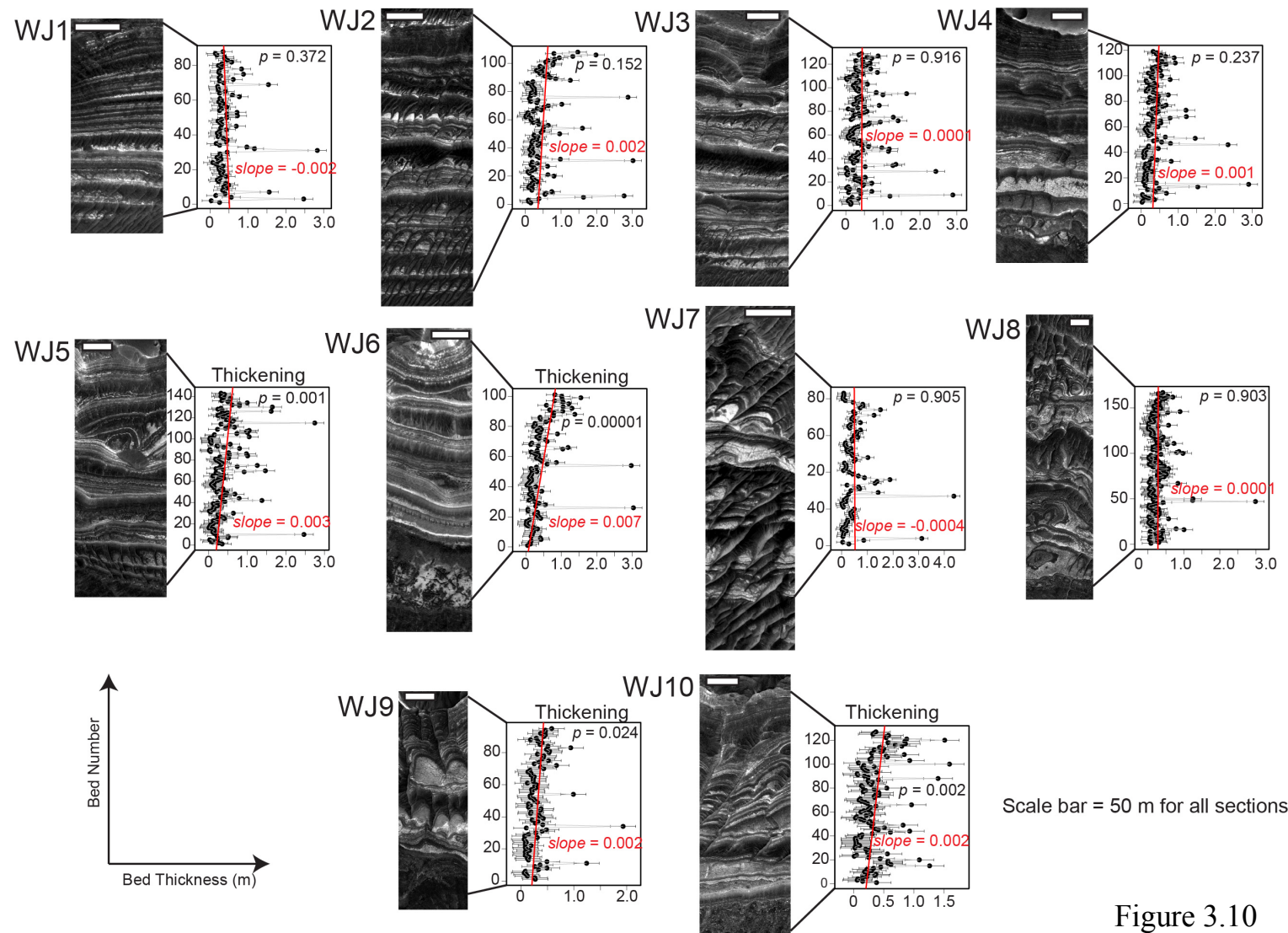


Figure 3.10

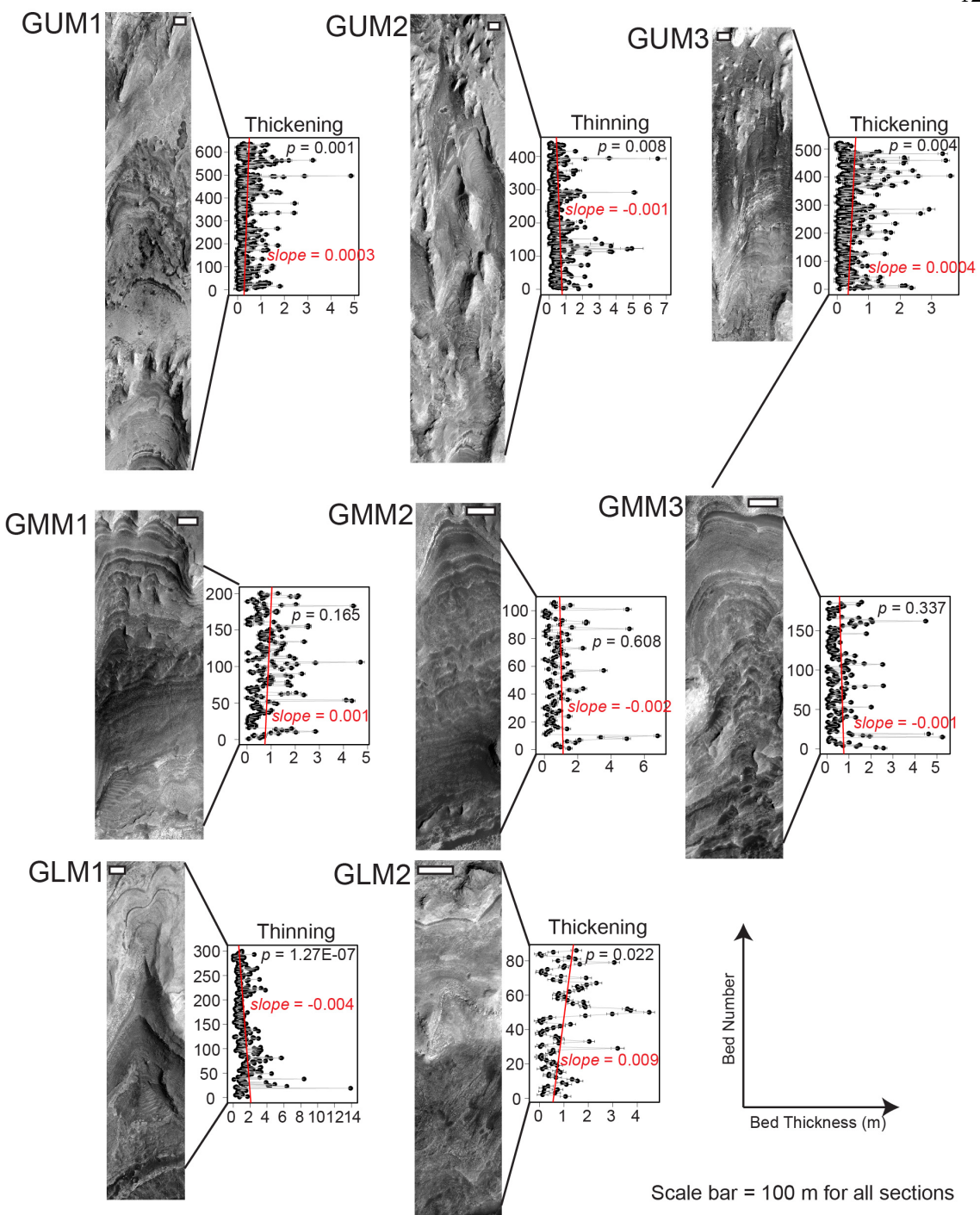


Figure 3.11

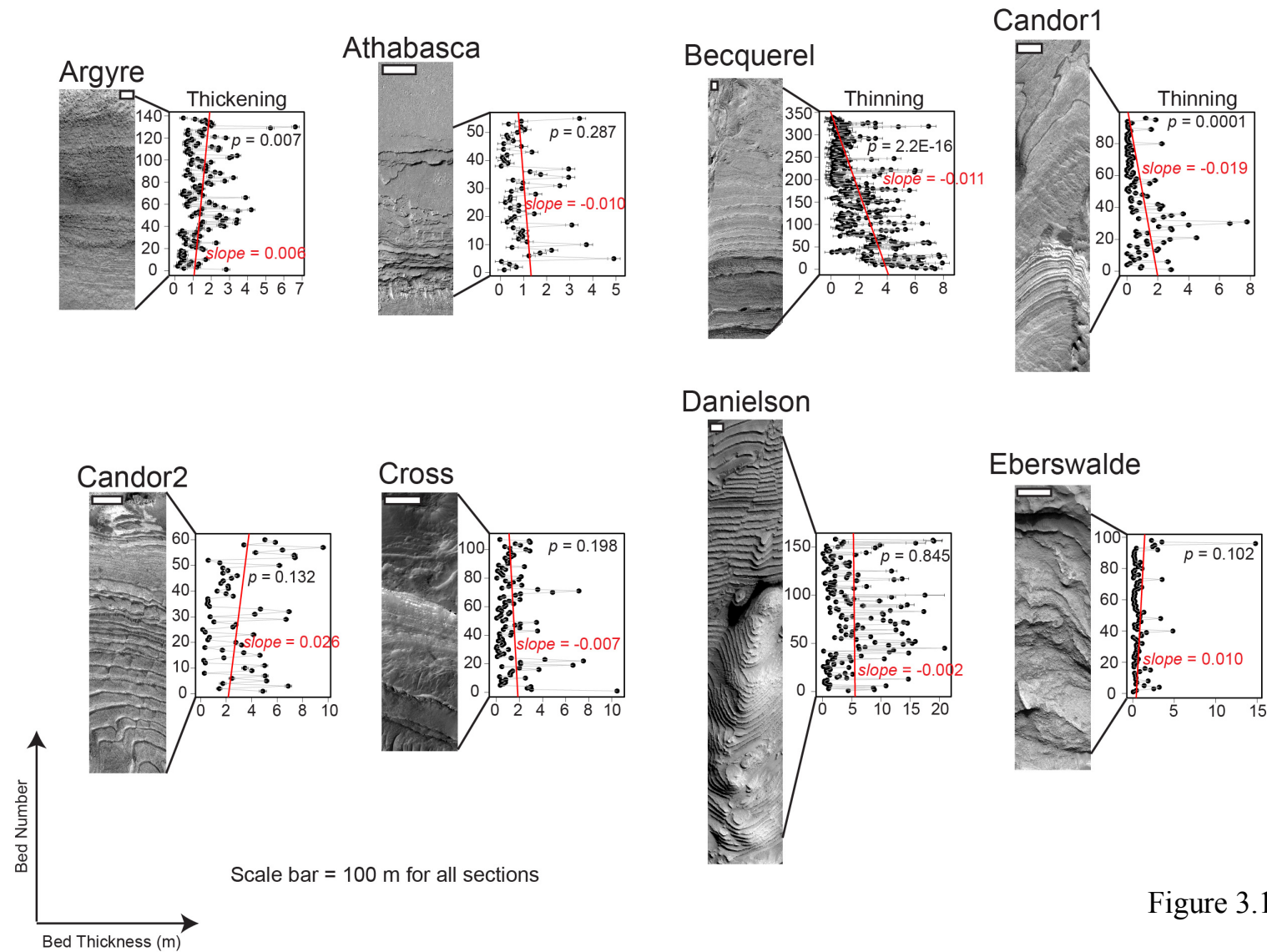


Figure 3.12

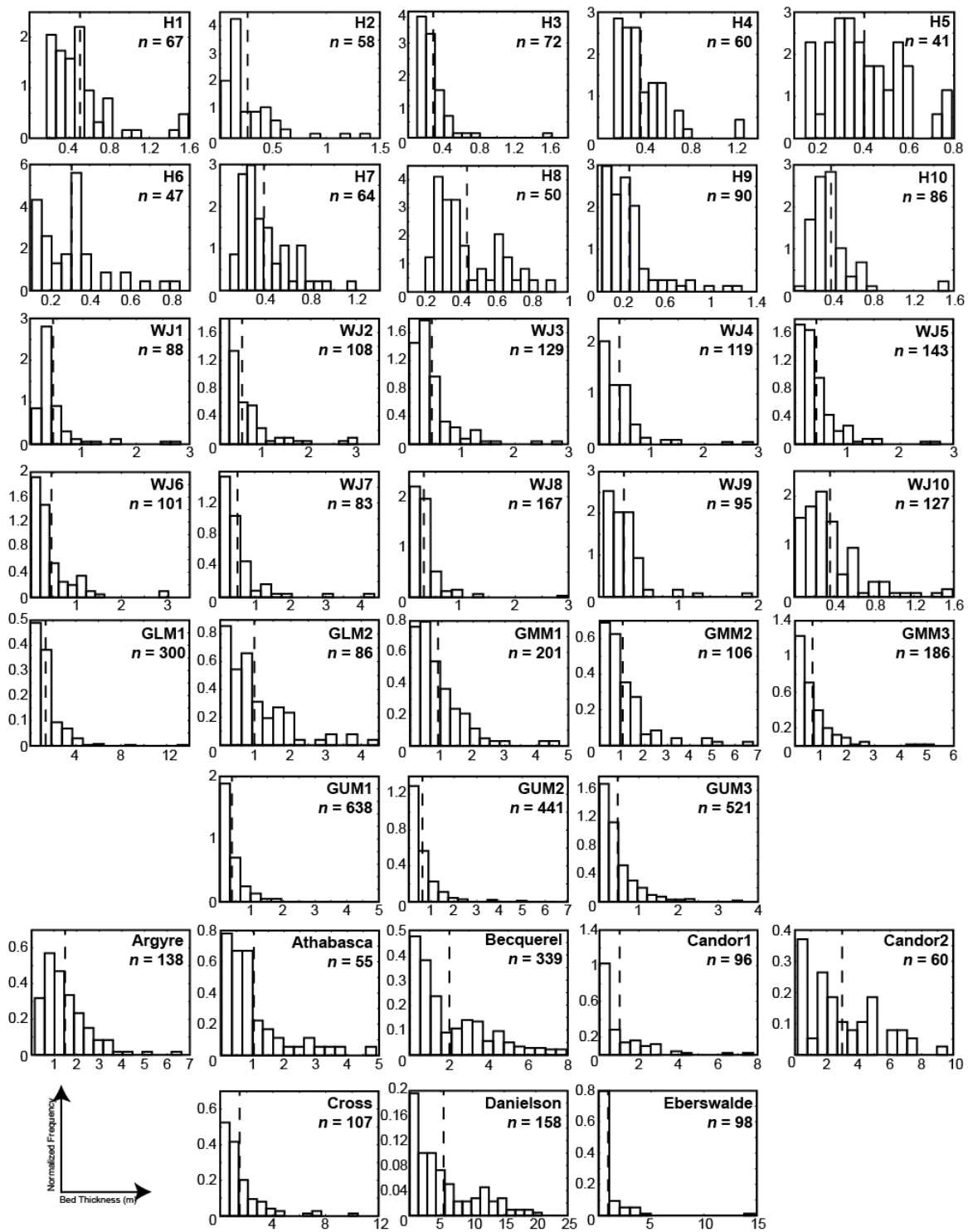


Figure 3.13

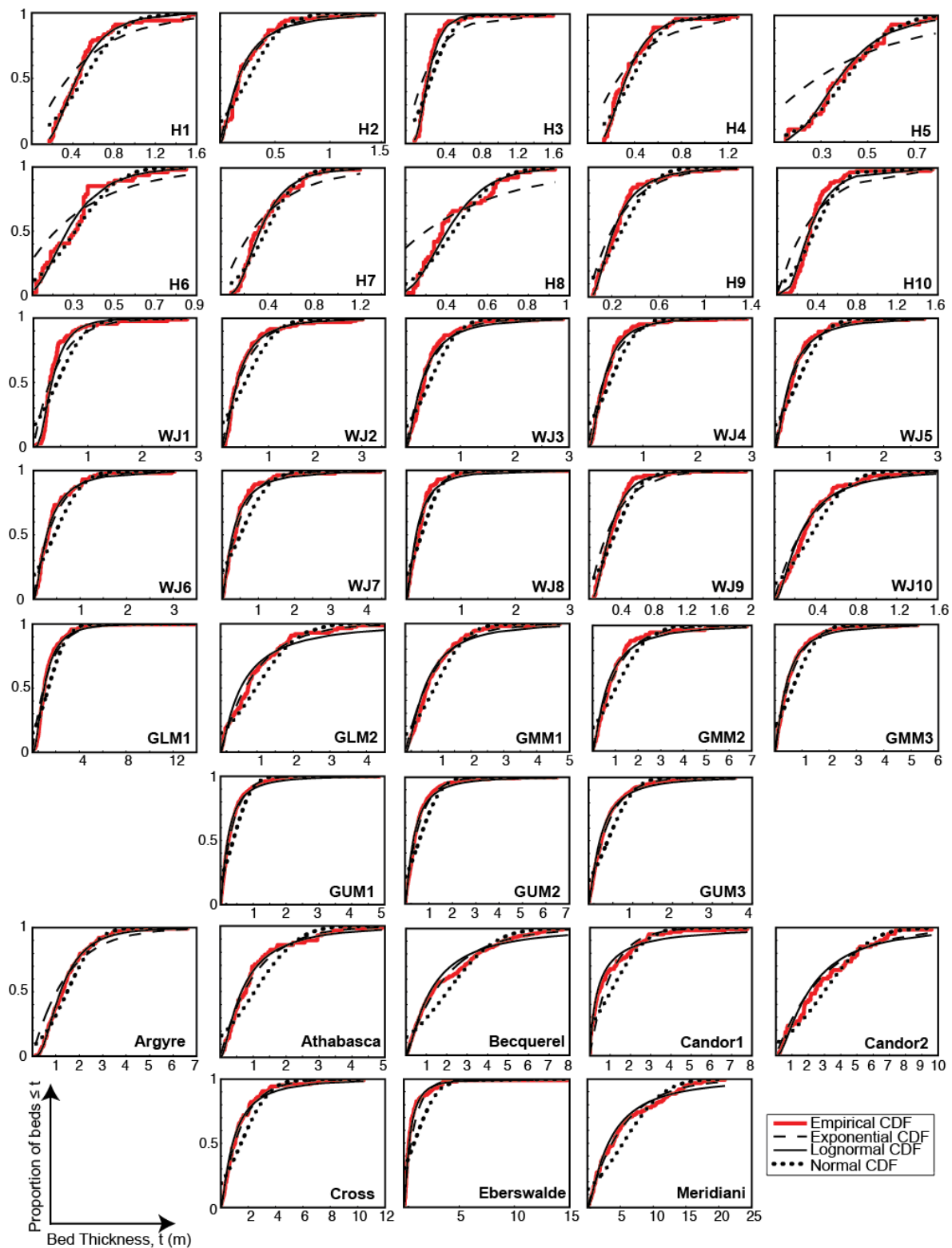


Figure 3.14

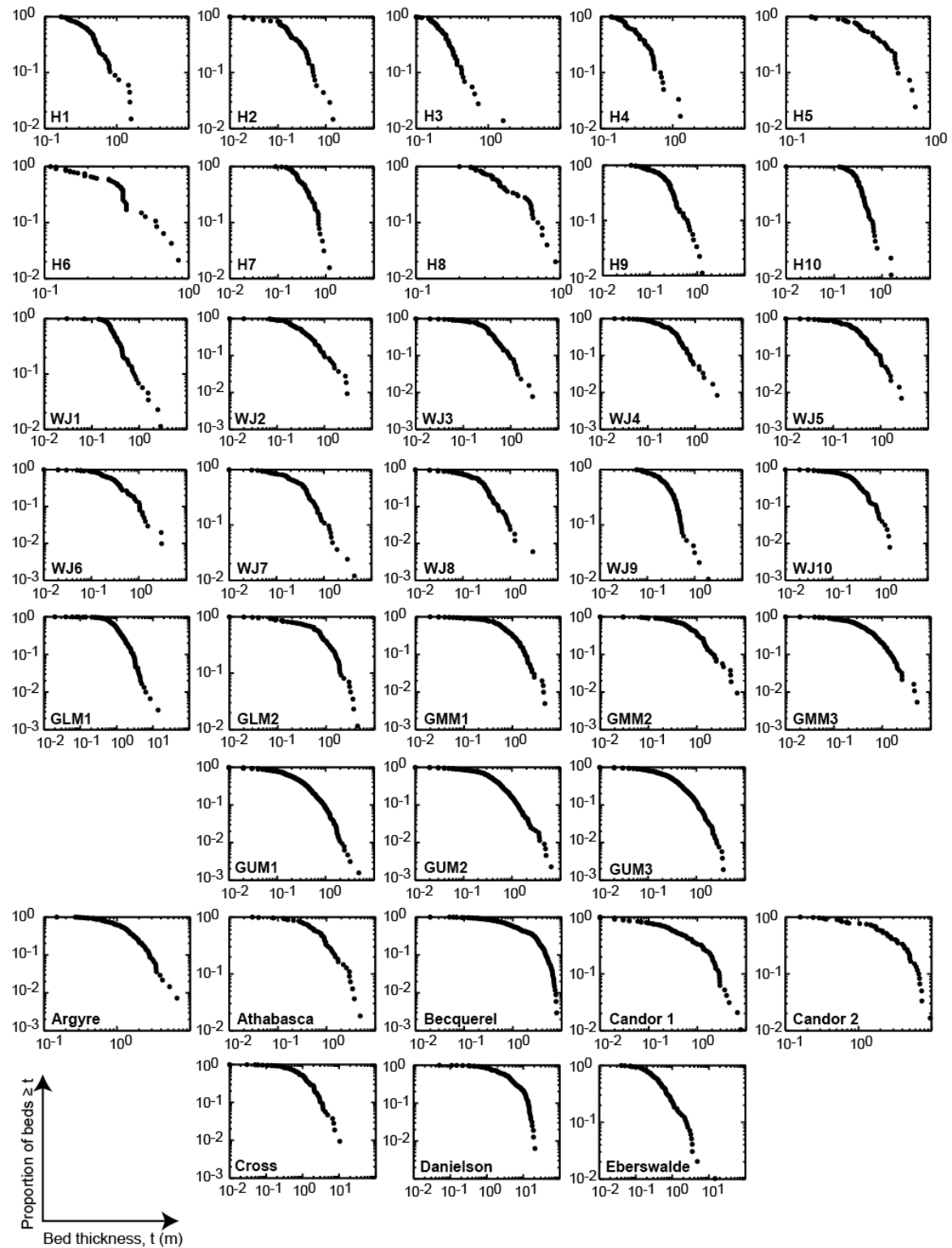


Figure 3.15

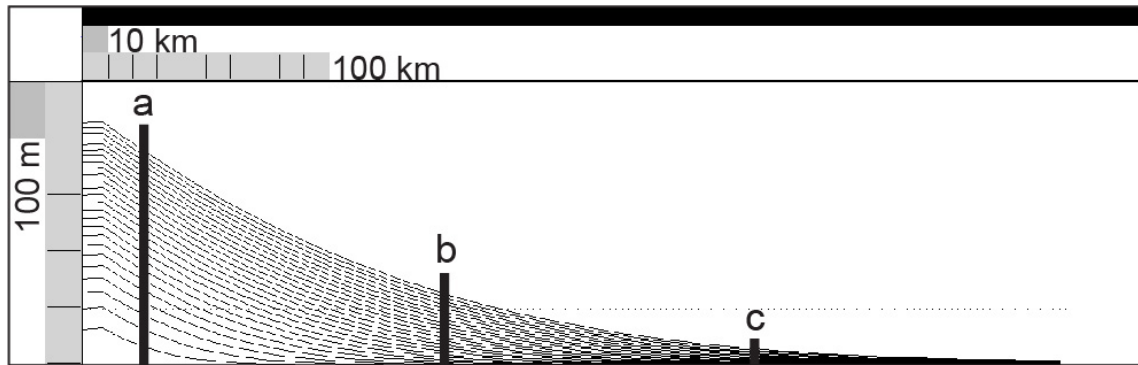


Figure 3.16

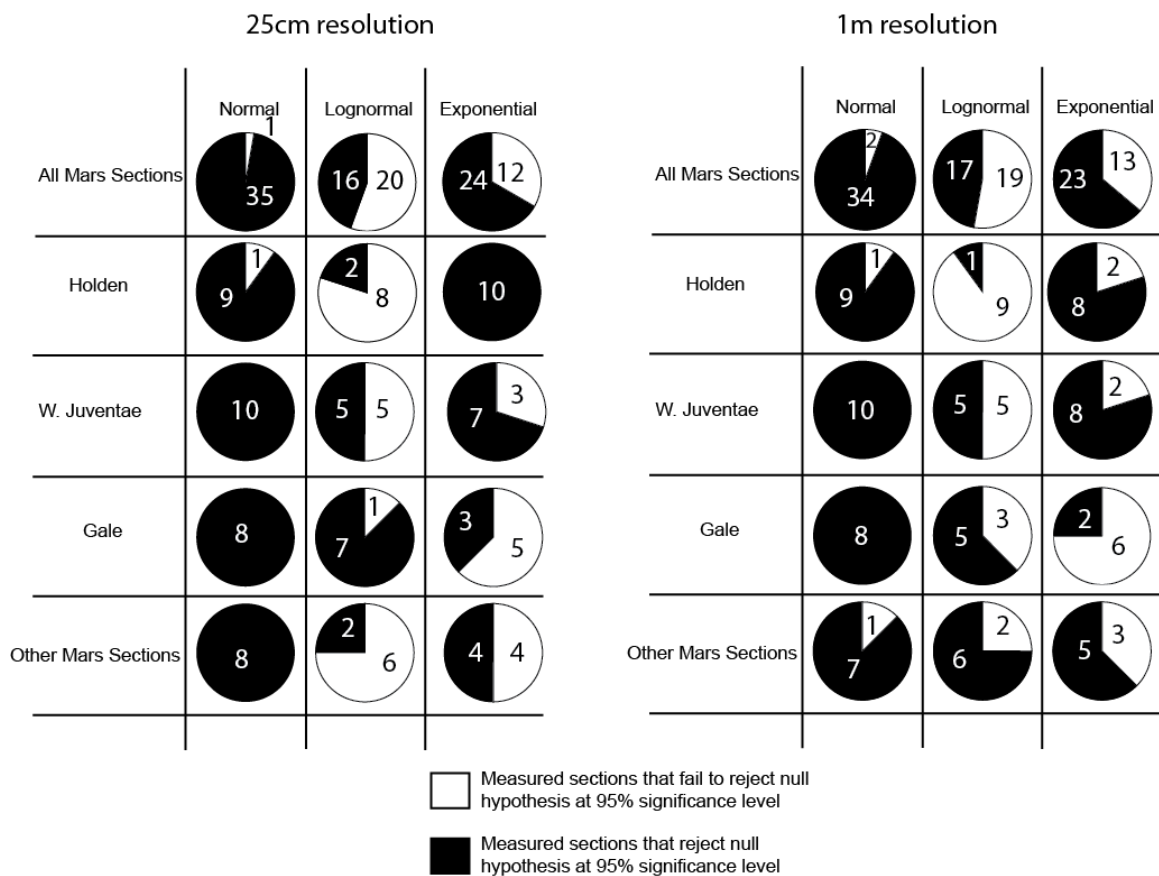


Figure 3.17

MODELING NEAR-INFRARED REFLECTANCE SPECTRA OF CLAY AND SULFATE MIXTURES AND IMPLICATIONS FOR MARS

Submitted:

Stack, K. M. and R. E. Milliken (in revision), Modeling near-infrared reflectance spectra of clay and sulfate mixtures and implications for Mars, *Icarus*.

Abstract

High-resolution mapping by visible and near-infrared orbital spectrometers has revealed a diversity of hydrated mineral deposits on the surface of Mars. Quantitative analysis of mineral abundances within these deposits has the potential to distinguish depositional and diagenetic processes. Such analysis can also provide important constraints on the nature of putative global and local-scale mineralogical transitions on Mars. However, the ability of models to extract quantitative mineral abundances from spectra of mixtures relevant to sedimentary rocks remains largely untested. This is particularly true for clay and sulfate minerals, which often occur as fine-grained components of terrestrial sedimentary rocks and are known to occur in a number of sedimentary deposits on Mars. This study examines the spectral properties of a suite of mixtures containing the Mg-sulfate epsomite mixed with varying proportions of smectitic clay (saponite, nontronite, and montmorillonite). The goal of this work is to test the ability of checkerboard (linear) and intimate (non-linear) mixing models to obtain accurate estimates of mineral abundances under ideal and controlled laboratory conditions. The results of this work suggest that: (1) spectra of clay-sulfate mixtures can be reproduced by checkerboard and intimate mixing models to within

2% absolute reflectance or single scattering albedo, (2) clay and epsomite abundance can be modeled to within 5 wt. % when particle diameter is optimized, and (3) the lower threshold for modeling clay in spectra of clay-epsomite mixtures is approximately 10 wt. %, below which the models often fail to recognize the presence of clay.

4.1 Introduction

Visible-near infrared (VNIR) reflectance spectroscopy can be a powerful tool for identifying ancient records of environmental change on Mars because of its sensitivity to minerals that represent water-rock interaction. Such minerals include, but are not limited to, carbonates, sulfates, and clay minerals. High-resolution mapping by visible and near-infrared orbital spectrometers has revealed a diversity of hydrated minerals on the surface of Mars, suggesting a complex history of aqueous alteration and mineral precipitation [e.g., *Squyres et al.*, 2004; *Poulet et al.*, 2005; *Gendrin et al.*, 2005; *Bibring et al.*, 2005, 2006; *Mustard et al.*, 2008; *Murchie et al.*, 2009; *Carter et al.*, 2013; *Ehlmann and Edwards*, 2014]. The OMEGA (Observatoire pour la Mineralogie, l'Eau, les Glaces et l'Activitie) [*Bibring et al.*, 2004] and CRISM (Compact Reconnaissance Imaging Spectrometer for Mars) [*Murchie et al.*, 2007] orbital spectrometers have detected clay mineral-bearing deposits in the ancient Noachian regions of Mawrth Vallis and Northeast Syrtis Major [*Poulet et al.*, 2005; *Bibring et al.*, 2006; *Mustard et al.*, 2008; *Ehlmann and Mustard*, 2012], whereas detections of mono- and polyhydrated sulfates occur predominantly in light-toned layered deposits in Hesperian-aged regions such as Terra Meridiani, Margaritifer Sinus, and in deposits within and on the plains surrounding Valles Marineris [*Poulet et al.*, 2005; *Gendrin et al.*, 2005; *Bibring et al.*, 2006].

It is generally observed that clay- and sulfate-bearing terrains are spatially and likely temporally distinct on the surface of Mars, a distinction purported to be indicative of global-scale changes in aqueous chemistry and climatic conditions [Bibring *et al.*, 2006]. However, continuing observations from CRISM and OMEGA have revealed a number of locations where clay and sulfate minerals occur together. Clay-bearing layers are overlain and underlain by sulfate-dominated layers in the lower strata of Mt. Sharp [Milliken *et al.*, 2010; Thomson *et al.*, 2011]. Clay-bearing strata underlie sulfate-bearing units in Sinus Meridiani [Bibring *et al.*, 2006; Poulet *et al.*, 2008a; Wiseman *et al.*, 2010] and Ius Chasma in Valles Marineris [Roach *et al.*, 2010], where the relative age relationships between Fe/Mg clays and sulfates is consistent with the transition from a relatively alkaline to a more acidic environment, as proposed by Bibring *et al.* [2006].

Other studies have shown that not all stratigraphic sequences on Mars follow this mineralogical progression. The discovery of the Ca-sulfate bassanite stratigraphically below clay-rich layered deposits in Mawrth Valles [Wray *et al.*, 2010] suggests that conditions favorable for sulfate precipitation may have existed prior to or at the same time as conditions conducive to clay formation, though the role of diagenetic processes in the creation of this apparent mineral stratigraphy are unknown. Similarly, mono- and polyhydrated sulfates interbedded with kaolinite-bearing strata observed in Columbus and Cross craters of the Terra Sirenum region suggest that clay and sulfate formation could have occurred contemporaneously in acidic environments [Wray *et al.*, 2011].

Considering the variety of settings on Earth where clays and sulfates are found together in both modern-day environments and the ancient rock record, the co-occurrence of hydrated clay and sulfate minerals in the Martian rock record is not entirely unexpected.

Evaporitic sulfate formation commonly occurs contemporaneously with detrital clay deposition in modern playa and sabkha environments, i.e., *Smoot and Castens-Seidell* [1994]. There are also examples of modern and ancient saline lakes [Meunier, 2005; Baldridge *et al.*, 2009] and evaporative marine environments [Hover *et al.*, 1999; Martini *et al.*, 2002] where evaporitic sulfate minerals occur together with authigenically-precipitated phyllosilicates.

Clay and sulfate minerals can also occur together in the rock record as a result of diagenetic processes, although hydrated mineral formation need not be contemporaneous in this scenario. At Yellowknife Bay in Gale crater, the Curiosity rover team observed pervasive Ca-sulfate veins cross-cutting the clay-bearing mudstone of the Sheepbed member [Grotzinger *et al.*, 2014; McLennan *et al.*, 2014; Nakhon *et al.*, 2014]. These veins have been interpreted to represent a later stage of diagenesis during which the infiltration of sulfur-rich fluids resulted in sulfate precipitation in void spaces and fractures within the rock [Grotzinger *et al.*, 2014; Nakhon *et al.*, 2014]. In the case of the Sheepbed mudstone in Gale crater, the diagenetic Ca-sulfate component makes up only 1-3 wt. % of the total rock composition [Vaniman *et al.*, 2014]; in contrast, primary evaporate deposits can be composed almost entirely of sulfate minerals. In this particular comparison, the low abundance of sulfate in the Sheepbed mudstone helps point to an origin other than primary depositional evaporite for the sulfate. Although the Sheepbed mudstone provides one specific in-situ example where the abundance of sulfate within the bulk rock offers a clue to its origin, it is possible that the quantitative abundance of hydrated minerals in orbital spectral data can be used to distinguish depositional and diagenetic mineral formation in other Martian deposits as well.

Assessing the geological significance of clay and sulfate minerals detected on Mars requires an understanding of the local, regional, and global variations in the proportions of these minerals, as well as the context in which they occur on the Martian surface. Orbital VNIR reflectance spectroscopy provides an effective way to evaluate the distribution and timing of hydrated mineral formation on Mars, but questions remain about how reliably mineral components can be detected and how well relative or absolute mineral abundances can be derived. Are clay and sulfate minerals truly stratigraphically distinct on Mars, or could clays and sulfates be inter-bedded or occur together as fine-grained mixtures in outcrop? Do sulfate-bearing strata exhibit any spectral evidence for the presence of clays, and vice versa? What are the detection limits for sulfate and clay when they are intimately mixed? Such questions are critical for evaluating the geologic context and relative timing and duration of proposed mineral transitions on Mars.

However, the process of extracting quantitative mineral abundances from VNIR spectra of mixtures is not always straightforward and has been tested in the laboratory or with orbital spectra for only a limited range of mineral compositions. Analyses by *Nash and Conel* [1974] and *Singer* [1981] of particulate mixtures containing minerals commonly found in basalt showed that spectral mixing is nonlinear at visible and near-infrared wavelengths. To address such complexities, *Hapke* [1981; 1993] and *Shkuratov et al.* [1999] developed radiative transfer models in order to account for nonlinear behavior and effects associated with multiple scattering of incident photons. Previous studies have tested the ability of these models to derive absolute mineral abundances from mixtures containing common basaltic minerals such as olivine, pyroxene, Fe-oxides, and plagioclase [*Mustard and Pieters*, 1987a; *Hiroi and Pieters*, 1994; *Poulet and Erard*, 2004]. Other studies have

examined the spectral properties of clay-bearing [e.g., *Orenberg and Handy*, 1992; *Bishop et al.*, 1995a; *Ehlmann et al.*, 2010; *McKeown et al.*, 2010] and sulfate-bearing mixtures [*Cooper and Mustard*, 2002].

Attempts have also been made to quantify clay mineral abundance from orbital spectra of the Martian surface [*Poulet et al.*, 2008b; *Poulet et al.*, 2009]. *Poulet et al.* [2008b] applied Shkuratov modeling to OMEGA data to determine the modal mineralogy of clay-bearing units exposed at Mawrth Vallis and Nili Fossae. Clay minerals modeled in moderate amounts in Nili Fossae (<20%) were linked to hydrothermal alteration, whereas higher clay abundances (>20%) derived for Mawrth Valles were interpreted to represent primary sedimentary deposition or extensive near-surface alteration of volcanic rocks [*Poulet et al.*, 2008b]. *Poulet et al.* [2008b] illustrates the potential importance of VNIR orbital spectral data in distinguishing depositional hypotheses based on quantitative mineral abundances, but the accuracy of the Hapke and Shkuratov models for extracting quantitative mineral abundances from spectra of mixtures relevant to sedimentary rocks remains largely untested. This is particularly true for clays and sulfates, which often occur as fine-grained components of sedimentary rocks in a variety of depositional settings.

The goal of this study is to examine VNIR reflectance spectra of fine-grained clay and sulfate mixtures acquired in a controlled laboratory setting, and to model those spectra using checkerboard and intimate mixing models based on known mineral endmembers and conversion of reflectance spectra to single scattering albedo via the model of *Hapke* [1993]. Though *in situ* rover measurements have shown that clay and sulfate-bearing strata on Mars may contain additional clastic components such as olivine, pyroxene, plagioclase [i.e., *Vaniman et al.*, 2014], we have chosen to first study simple binary mixtures to test mixing

models under well-constrained conditions. Studies that focus on more complex multicomponent systems are certainly warranted, but it is first necessary to understand the limitations and performance of mixing models under the simplest and most ideal conditions before increasing the level of complexity and number of variables. Synthetic mixtures of smectitic clay and hydrous sulfate minerals allow for control of mineral abundance and particle size for each component, enabling an assessment of the thresholds and accuracy of mixing models in deriving known abundances of clay and sulfate in mixtures under idealized conditions. Accordingly, we examined the VNIR reflectance properties of a suite of binary fine-grained mixtures containing hydrated magnesium sulfate (epsomite, $\text{MgSO}_4 \cdot 7\text{H}_2\text{O}$) mixed with varying proportions of iron, magnesium, or aluminum-rich smectite. Using the known spectral endmembers, we assessed the ability of checkerboard and nonlinear (Hapke) intimate mixing models to: 1) reproduce spectra of these mixtures and 2) accurately derive the known mineral abundances. The importance of estimated particle size values implied by the model fits and the implications of these laboratory mixture experiments for the detection and quantification of hydrated minerals in clay and sulfate deposits on Mars are also discussed.

4.2 Spectral Mixing Models

Two models were used in this analysis to model mixture spectra and derive mineral abundances. The first is a linear or “checkerboard” mixing model in which the reflectance spectrum, r , of a mixture is represented as a linear combination of endmember reflectance spectra, r_j , each weighted by their fractional area, F_j :

$$r = \sum_j F_j r_j \quad (4.1)$$

In checkerboard mixing the individual components are weighted by area rather than by volume or mass fraction. Though the latter values are typically sought for addressing geologic questions (e.g., modal mineralogy), it is the former that is of direct importance in how photons interact with individual components in a checkerboard mixture prior to reaching the detector. The derived fractional areas can be converted to mass or volume fraction if values for particle size and density of each component are known or assumed. In the checkerboard mixing model, photons are assumed to interact with only one component of the mixture.

In a nonlinear or “intimate” mixture, the components are in close proximity such that photons leaving the surface of the sample have experienced multiple scattering, likely interacting with more than one component and/or particle before reaching the detector. The model of *Hapke* [1981, 1993] attempts to account for nonlinear, multiple scattering effects by converting reflectance spectra to single-scattering albedo (SSA), a conversion that includes terms to account for various scattering properties. This study employs *Hapke*’s [1993] equation that relates bidirectional reflectance, r , to the SSA, w :

$$r(i, e, g) = w/4\pi(\mu_0/\mu_0 + \mu)\{[1 + B(g)]p(g) + H(\mu_0)H(\mu) - 1\} \quad (4.2)$$

where $\mu_0 = \cos(i)$, $\mu = \cos(e)$, i is the angle of incidence, e is the angle of emergence, g is the phase angle, $p(g)$ is the single particle phase function, $B(g)$ is the backscatter function, and H is the Hapke approximation of Chandrasekhar's function for multiple scattering:

$$H(x) \approx (1 + 2x)/(1 + 2x\sqrt{1 - w}) \quad (4.3)$$

Just as the reflectance spectrum of a checkerboard mixture can be modeled as a linear combination of endmember reflectance spectra, the SSA spectrum, w , of an intimate mixture can be modeled as a linear combination of the SSA spectra of the individual components, w_j , each weighted by a coefficient, f_j , [Hapke, 1993]:

$$w = \sum_j f_j w_j \quad (4.4)$$

The weighting coefficient, f_j , for the j^{th} component in a mixture is related to the number of particles per unit volume, N_j , of that component and the geometric cross-section, σ_j :

$$f_j = N_j \sigma_j / \sum_j N_j \sigma_j \quad (4.5)$$

where σ_j is defined as:

$$\sigma_j = \pi (D_j/2)^2 \quad (4.6)$$

D is the particle diameter of the j^{th} component in the mixture. As shown by *Hapke* [1993], it can be assumed that the volume-average extinction efficiency, Q_E , is equal to unity for a close-packed particulate mixture, so that the volume extinction coefficient, E_j , of the j^{th} component is defined as:

$$E_j = N_j \sigma_j \quad (4.7)$$

where E_j has units of inverse length. By relating Eqs. (5) and (7), it can be seen that the spectral weighting coefficients represent fractional extinction coefficients, not volume or mass fractions. If particles are approximated as spherical, the individual volume extinction coefficients can be directly related to bulk density, M , solid density, ρ , and particle diameter, D , by:

$$E_j = N_j \sigma_j = 3/2(M_j / \rho_j D_j) \quad (4.8)$$

such that

$$f_j = (M_j \rho_j / D_j) / \sum_j (M_j \rho_j / D_j) \quad (4.9)$$

Therefore, weighting coefficients derived from (3) can be converted to estimates of mass fraction if the solid density and particle diameter of each component are known. As

an example, for a binary mixture of clay and sulfate, equation (9) can be rearranged to show that:

$$M_{clay}/M_{sulfate} = (f_{clay}/f_{sulfate})(D_{clay}\rho_{clay}/D_{sulfate}\rho_{sulfate}) \quad (4.10)$$

The mass fraction, m , of a component is equivalent to the fractional bulk density, thus the ratio of bulk density can be converted to a mass fraction:

$$m_{clay} = M_{clay}/(M_{clay} + M_{sulfate}) = 1/(1 + (M_{sulfate}/M_{clay})) \quad (4.11)$$

The spectral weighting coefficients are determined from the model fit and solid density values can be obtained from the literature, thus it is only necessary to measure or assume a value for the ratio of particle diameters to solve Eqs. (10) and (11) for mass fraction. Using the relationships in Eq. (8), Eq. (10) can also be written in terms of f , N , and D so that:

$$f_{clay}/f_{sulfate} = (N_{clay}/N_{sulfate})(D_{clay}/D_{sulfate})^2 \quad (4.12)$$

Therefore, for a given ratio of weighting coefficients, an increase in $D_{clay}:D_{sulfate}$ requires that $N_{clay}:N_{sulfate}$ decrease, implying an inherent tradeoff between particle diameter and number of particles per unit volume.

4.3 Materials and Methods

4.3.1 Laboratory Measurements

For direct relevance to sulfate and clay minerals identified in CRISM and OMEGA spectra of Mars, two saponites (SapCa-2, JCSS-3501), two nontronites (NAu-2, SWa-1), and two montmorillonites (SCa-3, SWy-2) were each mixed with reagent-grade epsomite ($\text{MgSO}_4 \cdot 7\text{H}_2\text{O}$) to create binary powder mixtures containing 5, 10, 20, 50, 80, 90, and 95 % clay by mass. The resulting suite of mixtures included six series (one for each clay endmember), each consisting of seven mixtures, in addition to the seven pure endmember minerals. Prior to mixing, each endmember was individually ground and dry-sieved to a size fraction $<25 \text{ }\mu\text{m}$. The actual particle size distribution of each endmember was estimated by manual measurement of particle diameter using photomicrographs taken with a transmitted light microscope (Figure 4.1). Clay and epsomite endmembers were individually weighed using a balance accurate to 0.0001 g, and mixtures were prepared for measurement by gentle mixing with a spatula and shaking to ensure uniform distribution. The powder mixtures were placed into 1 cm diameter steel sample holders and then gently tapped until the surface of the powder was level.

NIR diffuse reflectance spectra for each mixture were acquired under ambient conditions using a Nicolet Fourier transform infrared (FTIR) spectrometer fitted with an Analect biconical accessory that approximates bidirectional reflectance. Spectra were obtained at 4 cm^{-1} resolution over the wavelength range 1.25 to $2.6 \text{ }\mu\text{m}$ (Figure 4.2) using a CaF_2 beamsplitter in combination with an IR source and a liquid N_2 -cooled MCT detector. The chosen wavelength region includes clay and sulfate absorptions between $1.39\text{--}1.47 \text{ }\mu\text{m}$ caused by overlapping OH and/or H_2O stretch overtones, the $1.9\text{--}1.97 \text{ }\mu\text{m}$ combination

H_2O bend and stretch vibrations, and the narrow cation-OH vibration clay absorption bands between 2.2-2.4 μm [Bishop *et al.*, 1995b]. This wavelength region was chosen because these features are commonly used to identify smectitic clay minerals in CRISM and OMEGA spectra of Mars (e.g., Bibring *et al.* [2004]; Murchie *et al.* [2007]). Spectra were measured relative to a diffuse Infragold reflectance standard at a viewing geometry of $\sim 10^\circ$ for both incident and emergent beam angles. A spectrum was acquired at three different spots on the surface of each mixture to account for possible heterogeneity, with each spectrum representing an average of 200 scans. The three spectra were then averaged to produce a single spectrum representing a total of 600 scans for each mixture and each ‘pure’ endmember, respectively.

4.3.2 Analysis of Band Depths and Band Minima

Wavelength positions of true local band minima (maximum absorption strength) were identified for each reflectance spectrum at the $\sim 1.4 \mu\text{m}$ (OH vibration associated with the clay cation-OH bond), $\sim 1.45 \mu\text{m}$ (clay and epsomite H_2O stretch overtones), ~ 1.9 and $\sim 1.95 \mu\text{m}$ (clay and epsomite H_2O vibrations), and 2.2-2.4 μm (clay cation-OH vibration) wavelength regions [Bishop *et al.*, 1995b]. Band minima positions were then plotted against measured clay mass fraction (Figure 4.3) to assess changes in band position as a function of clay content. To analyze changes in absorption band strength in each mixture series as a function of the mixture composition (Figure 4.4), a spectral continuum was defined for each reflectance spectrum over the entire 1.25-2.6 μm wavelength range using the ENVI continuum removal routine in which a convex hull fit is defined by straight-line

segments connecting local maxima. After continuum removal over the entire wavelength range, the band depths of the true local minima at 1.4, 1.45, 1.9, 1.95, and 2.2-2.4 μm were calculated for each mixture using the method of *Clark and Roush* [1984]:

$$D_b = 1 - (R_b/R_c) \quad (4.13)$$

where D_b is band depth, R_b is the reflectance defined at the band center, and R_c is the reflectance of the defined continuum at the band center.

4.3.3 Linear (Checkerboard) and Nonlinear (Intimate) Spectral Unmixing

To perform nonlinear intimate spectral unmixing, all reflectance mixture spectra were first converted to SSA using Eq. (2). Backscatter was assumed to be negligible ($B(g) = 0$), a reasonable assumption given the phase angles of the spectral measurements, and it was assumed that the fine-grained mixtures were composed of isotropic scatterers ($p(g) = 1$). Though the latter may not be true in the strictest sense, it is likely a small source of uncertainty when comparing results for different mixtures because all spectra were acquired with an identical viewing geometry. In addition, exact phase function values for the clay and sulfate endmembers used here have not been previously reported.

Clay and epsomite endmember spectral weighting coefficients were modeled for each mixture from reflectance (checkerboard mixing model, Eq. (1)) and SSA (intimate mixing model, Eq. (4)) spectra using linear least squares inversion with a constraint of non-negativity implemented in MATLAB using the lsqnonneg function

(www.mathworks.com/help/optim/ug/lsqnonneg.html). Linear least squares was performed for each mixture using the measured mixture spectrum and an input matrix containing the pure clay and epsomite endmember spectra of that series and lines of positive and negative slope. The additional sloped lines were included to allow the model to account for phase behavior and wavelength-dependent scattering effects not accounted for by the mineral endmembers [*Combe et al.*, 2008]. The inversions were performed over the full wavelength range (1.25-2.6 μm) as well as a subset wavelength range (2.1 to 2.6 μm) to exclude H_2O absorptions that are dependent on sample hydration state (water content) and not uniquely linked to clay mineral abundance. Since the modeled spectral fits rely on the spectral endmembers, no a priori assumptions about particle size, optical constants, porosity, etc. were required. In theory the models should be able to accurately fit the mixture spectra simply by varying the proportions of the input spectral endmembers (that is, by varying the fractional contribution of each component), especially given that viewing geometry, sample preparation, and other measurement conditions were identical for all samples.

To converge on the set of spectral weighting coefficients that provided the best model fit to the measured spectrum of each mixture (Table 4.1), the lsqnonneg function performed a series of iterations to minimize the sum of the square of the residuals between the measured and modeled spectral reflectance or SSA. The number of iterations in each optimization was determined by the MATLAB default value for tolerance on the coefficients (www.mathworks.com/help/optim/ug/lsqnonneg.html), so that the iterations terminated when the norm of the difference between coefficients calculated during the n and n+1 iterations was smaller than the allowed tolerance.

Linear and intimate mixing modeled spectra were then calculated by summing the reflectance or SSA endmember spectra, respectively, weighted by the fractional coefficients determined during linear least squares inversion, including the coefficients for positive and negative sloped lines (see Figures 4.5-4.10 for linear mixing model reflectance spectra). Residuals between modeled and measured spectra were plotted to determine which wavelength regions were best or worst fit by the models (Figures 4.5-4.10).

4.3.4 Modeling Mass Fraction

To assess the accuracy of the checkerboard and intimate mixing models for estimating mineral abundances, clay and epsomite mass fractions were calculated using Eqs. (10) and (11) for each mixture within a series, over both the full and partial spectrum wavelength ranges. Solid densities were defined as 2.3 and 1.7 g/cm³ for clay and sulfate endmembers, respectively, in line with the mineral product information provided by the Clay Mineral Society (clays) and Mallinckrodt Baker, Inc. (epsomite). Spectral weighting coefficients for clay and epsomite were determined by the method described in the previous section, although the clay and epsomite coefficients derived for each mixture were first normalized such that the fractional contributions of mineral endmembers summed to one. This normalization step corrected for the positive and negative sloped line contributions, which have no meaning in terms of mineral abundances and typically provided very minor contributions (Table 4.1). Normalization also ensured that model results were geologically and physically plausible given that the prepared mixtures were known to be binary.

Three different values for the particle diameter of each component (mean, mode, and optimized) were used in the model runs, resulting in three sets of modeled mass

fraction values for each endmember series for a given wavelength range (full or partial spectrum). The measured mean and modal particle diameter values of the clay and epsomite endmembers were estimated from optical microscopy point counting (Figure 4.1, Table 4.2). The optimized particle diameter ratio ($D_{\text{clay}}:D_{\text{epsomite}}$) was calculated for each mixture according to Eq. (10), using non-linear least squares (`lsqnonlin` function in MATLAB, www.mathworks.com/help/optim/ug/lsqnonlin.html) to minimize the sum of squared residuals between measured and modeled mass fraction values. In these iterations, the derived clay and epsomite weighting coefficients were those calculated by linear least squares inversion and were considered to be constants since these values provide the best possible fit to the measured spectra. Though there is no strong reason to expect the particle size of clay or epsomite endmembers to vary significantly within a mixture suite, these optimized particle diameter ratios provide insight into the relationship between clay or epsomite abundance, measured particle size distributions, and optical path lengths as clay or epsomite content varies within a mixture suite. In addition, the modeled optimized particle diameter ratios can be directly compared to the mean and mode values estimated from photomicrographs of the samples. We also estimated a single diameter ratio that minimized differences between measured and modeled mass fractions for samples within a mixture suite as a whole (Table 4.2). This single optimized particle diameter ratio was calculated for each mixture suite by simultaneously minimizing the differences between all measured and modeled mass fractions within a series, and this value was used to calculate the optimized modeled mass fractions for each mixture series.

4.4 Results

4.4.1 Spectral Observations

Reflectance spectra of clay-epsomite mixtures measured over the 1.25-2.6 μm wavelength range are presented in Figure 4.2. Spectra containing smectitic clay endmembers exhibit diagnostic absorption bands between 2.2-2.4 μm due to cation-OH vibrations that vary in strength with clay abundance. The saponite endmembers (SapCa-2 and JCSS-3501) exhibit a strong Mg-OH feature with two distinct absorptions and a true local minimum at \sim 2.31 μm . The nontronite endmembers exhibit a distinct absorption band centered at \sim 2.28 μm due to Fe-OH vibrations, with a shoulder on the short wavelength side due to Al-OH. Spectra of the montmorillonite endmembers (SWy-2 and SCa-3) exhibit an absorption band centered near 2.2 μm due to Al-OH vibrations. A slight shoulder is apparent on the long-wavelength side of this feature in the SWy-2 spectrum, possibly due to increased Mg content relative to the SCa-3 sample. In contrast, the spectrum of the epsomite endmember exhibits a negative spectral slope in this region due to the presence of H_2O , and it lacks the narrow absorption features that are characteristic of the clay spectra. The spectra in Figure 4.2 and the plot in Figure 4.3e demonstrate that the positions of the cation-OH absorption band minima found between 2.2-2.4 μm do not change as the clay endmembers are mixed with increasing amounts of epsomite. This indicates that spectral dilution of clay by the presence of sulfate does not affect the identification of clay mineral composition, assuming a high signal-to-noise ratio, even though the sulfate exhibits a strong negative spectral slope at wavelengths >2.3 μm . In contrast, the strength (band depth) of the cation-OH absorptions that occur between 2.2-2.4 μm clearly decreases with decreasing clay content as expected (Figure 4.4e).

Clay endmember spectra (Figure 4.2) also exhibit prominent absorption features with band minima near ~ 1.4 , ~ 1.45 , ~ 1.91 and ~ 1.95 μm due to overlapping absorptions caused by OH and H_2O vibrations [Bishop *et al.*, 1995b]. The epsomite endmember spectrum also exhibits strong absorptions near these wavelengths due to the presence of H_2O , but these features are broader and shifted slightly compared to those observed in the clay spectra. Epsomite exhibits a true local minima near ~ 1.47 μm , but this is just one of at least 4 overlapping absorptions due to H_2O in the mineral structure that form the broad feature between 1.4 - 1.8 μm . The ~ 1.9 μm feature in the epsomite spectrum exhibits local minima at ~ 1.93 and ~ 1.97 μm . Accordingly, the absorptions near ~ 1.4 and ~ 1.9 μm observed in mixture spectra become broader and shift slightly to longer wavelengths as the proportion of epsomite is increased. This change is particularly evident between 1.45 - 1.85 μm , where the convex shape in the clay endmember spectra becomes concave with increasing weight percent epsomite due to the appearance of a sulfate H_2O feature centered near ~ 1.6 μm (Figure 4.2). Increasing epsomite content appears to have little effect on the position of the local band minima located near ~ 1.4 μm (Figure 4.3a), but the local band minima located near ~ 1.45 μm in the clay spectra shift noticeably to longer wavelengths with increasing epsomite content (Figure 4.3b). Similar trends are observed in the ~ 1.9 μm region, where increasing epsomite content results in a shift of the H_2O features centered at ~ 1.91 and ~ 1.95 μm to longer wavelengths (~ 1.93 and ~ 1.97 , respectively) (Figure 4.3c-d). These spectral changes are most dramatic for mixtures containing ≥ 50 wt. % epsomite.

The relative strengths (band depths) of the OH and H_2O features in the 1.4 μm region and the H_2O features in the 1.9 μm region also change with epsomite content (Figure 4.4a-d). Band depth of the absorption at ~ 1.45 μm increases fairly systematically

with increasing epsomite content for all mixture series (Figure 4.4b), but the relationship between band depth and epsomite abundance for the OH overtone absorptions near ~ 1.4 μm varies depending on the clay endmember (i.e., whether the vibration is due to Al-OH, Mg-OH, or Fe-OH; Figure 4.4a). For the suite of mixtures containing nontronite, the band depth of the Fe-OH overtone absorption at ~ 1.43 μm exhibits only minor changes with increasing epsomite content (Figure 4.4). In contrast, the saponite and montmorillonite mixtures exhibit clear decreases in band depth with increasing epsomite content for the corresponding Mg/Al-OH overtones at 1.38-1.39 and 1.41 μm , respectively. The relatively constant, then slightly increasing band depth of the 1.43 μm nontronite OH overtone with increasing epsomite content can be explained by the partial overlap of this feature with the strong absorption edge of the epsomite H_2O band centered at ~ 1.47 μm . Because the cation-OH absorptions in the saponite and montmorillonite spectra are more clearly separated from the sulfate H_2O band near ~ 1.47 μm , the band depths for these clay absorptions are not as strongly influenced by the sulfate band as epsomite content increases in the mixtures.

The band depth at ~ 1.95 μm also increases systematically with epsomite content (Figure 4.4d), but variations in band depth at ~ 1.9 μm are more complex. With increasing epsomite content, the ~ 1.9 μm absorptions first decrease in strength, then increase (Figure 4.4c). This behavior can be explained by the influence of the strong absorption edge of the ~ 1.93 μm epsomite H_2O absorption on the ~ 1.9 μm H_2O bands in the clay spectra. Minor additions of epsomite act to ‘dilute’ the strength of the 1.9 μm clay absorption, but moderate or large additions of sulfate completely swamp the clay H_2O band and this wavelength becomes dominated by H_2O in sulfate.

4.4.2 Full Wavelength Range (1.25 – 2.6 μm) Model Results

4.4.2.1 Measured Versus Modeled Spectra

Plots of measured reflectance spectra and fits determined from a linear ‘checkerboard’ model are presented in Figures 4.5-4.10. Plots of residuals (measured minus modeled) show that the largest discrepancies occur in the 1.4 μm and 1.9 μm wavelength regions (cation-OH and/or H_2O absorptions, as discussed above), followed by discrepancies associated with cation-OH bands near \sim 2.2–2.4 μm (Figure 4.5-4.10). With the exception of the NAu-2 (nontronite) mixture series (Figure 4.7), the modeled spectra consistently underestimate the strength of the bands associated with the clay minerals. Because all samples within a mixture suite were measured under identical conditions on the same day, these residuals are not expected to be related to possible changes in hydration level of samples due to fluctuations in relative humidity in the lab.

Modeled spectra for mixtures containing 50-80 wt. % clay exhibit the largest residuals (greatest deviation from the measured spectra), but in all cases the residual values are \leq 2% absolute reflectance over the full wavelength range and commonly \leq 1% (Figures 4.5-4.10). These results indicate that the checkerboard mixing model based on known spectral endmembers is able to accurately reproduce the spectral characteristics of clay-epsomite mixtures of those endmembers to within \sim 1% absolute reflectance. Though not shown here, model fits using SSA spectra yield nearly identical results. The similarity in spectral fits and residuals between reflectance and SSA inputs suggests the conversion of reflectance to SSA is not necessary to accurately model the clay-sulfate mixture spectra examined here. However, it is important to note that accuracy in spectral fitting need not imply accuracy in derived mineral abundances, which is discussed below.

4.4.2.2 Measured and Optimized Particle Diameter Ratios

As discussed in Section 3.4, three different values for the endmember particle diameter ratio (measured mean, measured mode, and optimized) were used to calculate modeled mass fraction for each mixture series. Visual inspection and point counting of endmember photomicrographs shows that the particle size distributions of clay endmembers are variable (Figure 4.1). JCSS-3501, NAu-2, and SCa-3 have mean diameters close to the mean sieve diameter of 12.5, whereas SapCa-2, SWa-1, and SWy-2 have significantly smaller mean particle diameters compared to the sieve diameter (Figure 4.1). A mean particle diameter of 16.8 μm is measured for the epsomite endmember (Figure 4.1), likely due to the clumping of very small grains to form larger aggregates measurable in the transmitted light photomicrograph. Thus for all mixture suites the measured mean clay:epsomite particle diameter ratios are <1 (Table 4.2). Particle diameter modes estimated for epsomite and clay endmembers range from 2.7 μm (SWa-1) to 10.8 μm (JCSS-3501), but for all endmembers the particle diameter mode is smaller than the measured mean particle diameter (Figure 4.1, Table 4.2). Because clay endmember particle diameter modes are similar to that measured for epsomite (JCSS-3501 is an exception), the modal clay:epsomite particle diameter ratios are larger and closer to unity than the measured mean diameter ratios (Table 4.2).

The optimized particle diameter ratios, defined as the ratio of clay:epsomite particle diameter that minimizes differences between measured and modeled mass fractions for all samples within a mixture suite, are listed in Table 4.2. In contrast to the measured values, the optimized clay:epsomite diameter ratios for the full spectrum mass fraction calculations are nearly all >1 regardless if reflectance or SSA spectra are used (NAu-2 is the exception).

This suggests that in order for the derived weighting coefficients (which produce the best spectral fits) calculated for the full spectral range to be converted to clay and epsomite mass fractions that best match the measured values, it is necessary to model the clay particles as being larger than the epsomite particles. Optimized particle diameter ratios calculated for each individual mixture within a series over the full spectral range are presented in Figure 4.11, which shows that values are generally greater than one and often increase as clay content decreases (e.g., JCSS-3501, SWy-2, SCA-3, SapCa-2, and SWa-1).

4.4.2.3 Modeled Mass Fractions

4.4.2.3.1 Mass Fractions Modeled with Measured Mean and Mode Diameter Ratios

Using the measured mean particle diameters of clay and epsomite (values in Figure 4.1 and Table 4.2) to convert the checkerboard model weighting coefficients to mass fractions results in consistent underestimation of clay abundance (Figure 4.12). There are large discrepancies between measured and modeled abundances, particularly for mixtures containing ~50-80 wt.% clay where the errors can be as high as 30-40 wt. % (Figure 4.12a-c). Intimate mixing model results also show that clay abundance is underestimated for nearly all mixtures when the measured mean diameter is used to calculate mass fractions (Figure 4.12d-f). Mass fraction discrepancies resulting from the intimate mixing SSA model are generally smaller by a few wt. % compared to those resulting from the checkerboard model, indicating that conversion from reflectance to SSA is an improvement for some (but not all) of the samples.

Both checkerboard and intimate mixing model results show a general improvement when the measured particle diameter mode, rather than the mean, of individual clay and

epsomite endmembers is used to convert weighting coefficients to mass fractions (Figure 4.13). Clay abundance calculated with the checkerboard reflectance model is still underestimated for most mixtures within the SapCa-2, SWa-1, SCA-3, and SWy-2 series. For about a quarter of the mixtures, the intimate mixing SSA model improves abundance estimates by 1-6 wt. % over the checkerboard model results. For the remaining mixtures, the intimate mixing model leads to no improvement or an increased discrepancy between measured and modeled clay wt. %. The checkerboard and intimate mixing model results for the 20-50 wt.% mixtures show the largest discrepancies between measured and modeled clay abundance, whereas the 5 and 95 wt.% mixtures are generally the best modeled.

4.4.2.3.2 Mass Fractions Modeled with Optimized Particle Diameter Ratio

When using the optimized particle diameter ratios, the absolute differences between measured and modeled mass fractions obtained from the checkerboard model are less than or equal to 5 wt. % for all mixtures containing more than 20 wt. % clay, a significant improvement compared to results based on measured mean or mode particle diameter ratios (Table 4.3, Figure 4.14a-c). Clay mass fraction is generally under-modeled for the 5-20 wt. % clay mixtures, and in some cases the model fails to recognize the presence of any clay, as is the case for the SWy-2 reflectance 5-20 wt. % mixtures, 5 and 10 wt. % SCA-3 and SWa-1 mixtures, and 5 wt. % NAu-2 mixture (Table 4.3, Figure 4.14c). Mass fractions modeled for SCA-3, SWa-1, and JCSS-3501 mixtures show that clay content is consistently over-modeled and epsomite under-modeled for mixtures containing 50 wt. % or more clay. A comparison between mixture series suggests that clay mass fraction is best modeled with

the checkerboard model for mixtures containing 90-95 wt. % clay, whereas modeled mass fractions calculated for mixtures containing low and intermediate clay abundances deviate the most from the measured values.

Results from the intimate mixing model show that the absolute differences between measured and modeled mass fractions are very similar to checkerboard model results and they are less than or equal to 6 wt. % for all mixtures containing more than 20 wt. % clay (Table 4.3, Figure 4.14d-e). Clay mass fractions are consistently over-modeled (epsomite under-modeled) in the high clay content mixtures (50-95 wt. % clay) and under-modeled in the low clay content mixtures (5-20 wt. %) for all mixture series. Intermediate and high clay content mixtures generally result in modeled clay fractions closest to the measured values, while low clay mixtures (5-20 wt. %) tend to result in modeled mass fractions that deviate the most from the measured values. Figure 4.14 shows that the intimate mixing SSA model fails to model the presence of clay for SWa-1, SCa-3, and SWy-2 mixtures containing ≤ 20 wt. % clay.

4.4.2.4 Relative Uncertainty of Model Fits

The preceding section discussed modeled mass fraction results in terms of absolute discrepancies compared to known values. Though in many cases the absolute deviations are small (<5 wt. %), such values can be extremely large in terms of the relative proportion of clay or epsomite present in the mixtures. Relative uncertainties were calculated as the absolute value of the difference between measured and modeled mass fractions (calculated using optimized particle diameter ratios), divided by measured mass fraction, and multiplied by 100 (Figure 4.15). The relative uncertainties of the modeled mass fractions

calculated with the checkerboard reflectance model are generally between 0 and 10% for mixtures containing 50 wt. % or more clay, but the relative uncertainty increases drastically for the nontronite and montmorillonite mixtures containing \leq 20 wt. % clay (Figure 4.15b-c). For mixtures where no clay is modeled, the relative uncertainty is 100%.

The relative uncertainties of the modeled mass fractions based on SSA spectra are similar to uncertainties calculated from reflectance spectra (Figure 4.15d-f). Relative uncertainty is generally between 0 and 10% for mixtures containing 50% or more clay but increases progressively for all mixtures containing 20% or less clay, regardless of the clay composition. No clay is modeled in the NAu-2, SCA-3, and SWy-2 mixtures containing \leq 20 wt. % clay or the 5 and 10 wt. % SWa-1 mixture, yielding relative uncertainties of 100% for these samples (Figure 4.15e-f). Although relative uncertainty plots for expected epsomite wt. % are not shown here, they would exhibit similar increasing trends in relative uncertainty with decreasing epsomite wt. %, the one difference being that the relative uncertainty never reaches 100% since epsomite is modeled (albeit underestimated) even in mixtures containing only 5-20 wt. % epsomite.

4.4.3 Partial Wavelength Range (2.1 – 2.6 μm) Model Results

Spectral unmixing of reflectance and SSA spectra was also performed using the partial wavelength range subset to 2.1-2.6 μm . This was intended to remove the influence of H_2O bands near \sim 1.4 and \sim 1.9 μm on the model results because these absorption features have a strong control on the spectral fit over the full wavelength region yet they are not uniquely linked to clay abundance.

As was the case for the full spectral range results, optimized particle diameter ratios calculated with the partial reflectance spectra are all greater than 1 (SSA JCSS-3501 is an exception, Table 4.2), but the ratios are commonly lower than those calculated using the full spectral range (NAu-2 and SWa-1 are exceptions). For both the partial reflectance and SSA spectra, the optimized particle diameter ratios are closest to the actual measured modal diameter ratios rather than the measured mean diameter ratios (though JCSS-3501 saponite is an exception). Mixture series show an increase in optimized particle diameter as determined for individual mixtures as clay content decreases (Figure 4.16), as was observed when the full spectral range was used. However, the optimized diameter ratio values from the partial spectra are generally lower than those calculated from the full spectra.

Figure 4.17 shows that large discrepancies between measured and modeled clay mass fraction persist when the measured mean particle diameter ratio is used to calculate mass fractions from partial reflectance or SSA spectra. As was the case for the full spectrum results, clay mass fraction is generally underestimated, particularly for intermediate composition mixtures (50-80 wt. % clay) for which absolute discrepancies are as high as 20-40 wt. %. Using the measured particle diameter modes to calculate mass fraction (Figure 4.18) appears to improve the model results for series containing \geq 50 wt. % clay, reflectance or SSA spectra, except for JCSS-3501, for which clay mass fraction is overestimated. This is likely due to the anomalously large modal diameter measured for this endmember. Table 4.4 and Figure 4.19 show that the modeled clay mass fractions calculated using optimized particle diameter ratios match well with the expected measured clay mass fraction when compared to results using the measured mean or modal particle

diameter ratios. However, for the nontronite and montmorillonite mixture series, the unmixing routines have difficulty modeling the presence of clay in mixtures with low clay abundances (<10-20 wt. %).

Regardless, modeling only the 2.1-2.6 μm range with either reflectance or SSA spectra decreases the discrepancy between measured and modeled mass fractions compared to the results using the full spectral range by several weight percent. As was the case when using the full spectral range, clay mass fractions are generally overestimated for mixtures with high clay abundances (>80 wt. %) and underestimated for mixtures with low clay abundance (Table 4.4). The modeled clay mass fractions calculated from the reflectance and SSA spectra are similar enough to the measured values that it is not readily apparent that one model yields consistently better estimates. In general, the mass fractions calculated with the reflectance data are similar to, or in some cases marginally better than, those calculated with SSA spectra. Relative uncertainties for the results based on the subset wavelength range (Figure 4.20) are comparable or slightly lower than the relative uncertainties of results based on the full wavelength range. Large relative uncertainties persist for mixtures containing ≤ 20 wt. % clay due to the inability of the unmixing routine to recognize the presence of clay in these mixtures.

4.5 Discussion

The results discussed above show that spectra of binary clay-epsomite mixtures can be modeled within <2% absolute reflectance or SSA in an idealized case in which signal to noise is high and the endmembers are of comparable, fine particle size and chosen to reflect what was known to be in the mixtures. As stated above, the goodness of spectral fit does

not necessarily imply that modeled mineral abundances will be accurate. In terms of spectral modeling and reproducing the shape of diagnostic absorption bands, there is little difference between whether reflectance spectra or SSA spectra are used.

Subsetting the spectra to exclude strong OH and H₂O absorptions near 1.4 and 1.9 μm increases the accuracy of both the checkerboard and intimate mixing models to predict clay abundance, commonly by a few weight percent. This improvement is expected given that the models are minimizing the sum of residuals over fewer data points (wavelengths) than for the full spectral range. Residuals for fits over the full spectral range also show that the largest deviations occur near the 1.4 and 1.9 μm absorptions. The 1.4 μm absorption is narrower than the other bands, thus it is comprised of fewer wavelengths and is not weighted as much in terms of its contribution to minimizing the sum of the squared residuals over the full wavelength range during linear least squares inversion. In addition, slight variations in H₂O may have stronger effects on the weak 1.4 μm absorption overtone features, whereas the strong 1.9 band may not be as strongly affected by small changes in H₂O content.

4.5.1 Implications of Measured and Modeled Particle Size

In order to convert the checkerboard and intimate mixing model weighting coefficients to clay and epsomite mass fractions according to Eqs. (10) and (11), values were needed for the particle size diameter ratio of the mixture components. As discussed above, three different options for the particle size diameter ratio were tested in this study: the measured mean and mode particle sizes obtained from point counting of optical photomicrographs and an optimized particle diameter ratio calculated by minimizing the

difference between measured and modeled clay mass fractions. Not only did modeled mass fraction results vary significantly depending on which value was used for the particle diameter ratio, but the choice of particle diameter ratio value has important implications for the way in which the model results are understood and evaluated.

In this study, measuring the mean and mode particle sizes of the clay and epsomite endmembers was the most straightforward and time-efficient way to obtain the representative grain size of each mixture component. Although the mean is a common way to characterize a population, neither the photons interacting with the mixture nor those entering the spectrometer detector have any ‘knowledge’ of the mean grain size of the mixture, rather their behavior is directly affected by the distribution of particles (and associated optical path lengths) they encounter within the mixture. Accordingly, the mode of the particle diameter distribution may be a better representation of the typical grain-photon interaction. The results of this study show that this is the case, as the modeled mass fractions calculated with the modal particle diameter ratio are much closer to the measured values than those calculated with the mean endmember grain size.

For most of the clay endmembers, the mode also represents the finest grains in the particle size distribution. This is not the case for the JCSS-3501 endmember for which the main mode occurs at 10.8 μm , resulting in a modal diameter ratio significantly higher than that measured for the other clay endmembers. Furthermore, the consistent overestimation of modeled mass fractions for the JCSS-3501 mixtures series using the mode grain size suggests that the finest grain-size fraction, rather than the mode, may be more important for achieving the best abundance estimates. Had the minor mode at $\sim 5 \mu\text{m}$ in the grain size distribution of JCSS-3501 (Figure 4.1) been used to calculate the modal particle size

diameter ratio, the error in modeled clay abundance calculated over the full spectral range would have been decreased by nearly 20 wt. % for the 50 wt. % clay mixture, and by 1 to 5 wt. % for the other modeled mixtures in the JCSS-3501 suite. In summary, the mode particle size, rather than the mean, may better represent the typical grain size encountered by photons interacting with the mixture. This is not surprising considering that previous studies have shown the dominant contribution of fine-grained fractions to mixture spectra [Singer *et al.*, 1981; Clark and Lucey, 1984; Hiroi and Pieters, 1994; Milliken and Mustard, 2007].

As expected, modeled mass fractions are closest to the measured mass fractions when the optimized particle diameter ratio for each series is used to calculate mass fractions. A comparison of the optimized particle diameter ratios and the actual diameter ratios calculated using the measured means and modes shows that the optimized values are closest to the measured mode values and not the measured mean values. However, the discrepancies between the measured modal particle diameter ratios and the optimized ratios (Table 4.2), as well as the systematic changes in optimized ratios calculated for individual mixtures within a suite (Figures 4.11 and 4.14), indicate that optimized diameter ratios represent something other than the mode or finest grain size populations in the mixtures. Rather, calculating the optimized particle diameter ratio provides a means to assess whether or not an endmember may have an effect on spectral properties that is disproportionate to its apparent mass or volumetric contribution.

Optimized particle diameter ratios (Table 4.2) show that clay abundance is generally best matched for a mixture series modeled over the full spectrum by increasing the diameter of the clay endmember relative to the epsomite endmember. This increase in

the apparent diameter of the clay endmember particles also implies that the number of clay particles modeled per unit volume (relative to number of epsomite particles) decreases (Eq. 12). Therefore, the optimized particle diameter ratios indicate that the models are best able to replicate the measured clay and epsomite mass fractions obtained from the full spectra when the mixtures are modeled as having slightly larger, but fewer clay particles (and concurrently smaller but more numerous sulfate particles per unit volume). Within a mixture series modeled over the full spectrum, the individual optimized diameter ratios for each mixture increase, sometimes dramatically, for mixtures containing only 5-20 wt. % clay (Figure 4.11). This indicates that in order for the model to achieve the expected clay mass fraction in mixtures containing very little clay (given a fixed ratio of weighting coefficients), it must increase the clay particle size relative to the epsomite particle size, while simultaneously decreasing the number of clay particles relative to epsomite particles.

One explanation for the optimized particle diameter ratios calculated in Table 4.2 and displayed for each mixture series in Figure 4.11 is that the ratios represent the actual physical changes in the grain size of the mixture components. Although there is no a priori reason to suggest that the individual particle sizes of the components would change throughout a mixture series, it is possible that clay particles clump together to form larger but fewer aggregates, particularly in mixtures containing low clay abundances. Indeed, smectitic clays can have surfaces with high charge and can tend to clump together. In the clay-sulfate mixtures this may be manifested as concentrated domains of larger clay aggregates separated by regions composed solely of sulfate. This would be consistent with having to increase the clay particle diameter (and decrease the number of clay particles) to match the known clay abundances in the mixtures. In this sense the mixtures may not be

ideal intimate mixtures but instead represent checkerboard mixing over small length scales, which may explain why the linear mixing models provide reasonable results.

An additional factor may be that the values for optimized particle diameter ratios simply represent parameter manipulation by the model, rather than a phenomenon with physical significance, to get the expected mass fractions given fixed ratios of weighting coefficients and known mass fractions. By changing the particle diameter ratios the model is able to compensate for lower than actual fractional weighting coefficients of clay obtained during least squares linear inversion. This effect is supported by the optimized diameter ratios calculated for full spectrum mixtures containing low clay abundance. Optimized diameter ratios calculated for individual mixtures containing >20 wt. % clay are roughly constant (Figures 4.11 and 4.16), consistent with the successful modeling of the clay present in intermediate and high clay abundance mixtures (Figure 4.15). When clay is underestimated or no clay is modeled in a mixture, i.e., low abundance clay mixtures, the model must compensate for the lower than expected clay weighting coefficient by adjusting the clay particle size and number. The result is that unrealistic particle diameter ratios are retrieved for low clay mixtures, hinting that the models are simply unable to recognize the presence of clay in these mixtures. The models are marginally more successful at recognizing the presence of clay in low abundance mixtures when only the subset spectra are modeled, as opposed to the full spectral range. This is likely because the portions of the spectrum most influenced by the epsomite endmember (e.g., the ~1.44-1.47 μm and ~1.90-1.97 μm bands) have been removed, allowing more emphasis to be placed on the spectral fit to the absorptions in the ~2-2.5 μm region that are diagnostic of clay minerals.

In summary, this analysis suggests that deviations between measured and modeled clay mass fractions observed in this study are primarily controlled by the selection of the input particle diameter ratio or can be explained by the inability of the checkerboard and intimate mixing models to recognize the expected clay contribution to mixture spectra. One possibility is that the mixtures are not completely homogeneously mixed (e.g., due to clumping) such that the small beam of the FTIR, despite averaging over three different locations on the surface of each mixture, is not capturing the bulk mixture composition. However, it is also likely that the clays form larger but fewer aggregates that may act like checkerboard mixtures at a length scale that is relevant to FTIR beam. This would be consistent with the optimized particle diameters that indicate larger but fewer clay particles and the success of the “checkerboard” mixing model to predict clay and sulfate abundance. In addition, it is likely that the diagnostic spectral features of the clay endmembers are simply too weak in mixtures containing <20 wt. % clay to be reliably and consistently modeled by checkerboard or intimate mixing models, in which all wavelengths are inherently weighted as being of equal importance. We also note that the assumption of particle sphericity used to convert weighting coefficients to mass fraction (Eqs. (8) and (9)) may not be true in the strictest sense, particularly for the finest grains within the clay/epsomite mixtures. However, isolating the effect of this assumption on the model results is difficult, since grain shape was not systematically measured for the mixtures.

4.5.2 Checkerboard vs. Intimate Mixing Models

The results presented here show that for mixtures containing varying proportions of clay and epsomite, the overall accuracy of the checkerboard and intimate mixing models is

almost identical when modeling either the full spectral range (1.25-2.6 μm) or the partial spectral range (2.1-2.6 μm). For some mixtures, the intimate mixing model results in minor improvements of several weight percent to the predictions of mineral abundance, but for most mixture series the checkerboard model results are either equivalent to or a slight improvement on the intimate mixing modeled mass fractions. Particle sizes similar to or smaller than the wavelength of incident light are known to complicate mixture modeling [Mustard and Hays, 1997; Piatek *et al.*, 2004], but both the checkerboard and intimate mixing model results of this study are consistent with those of Hiroi and Pieters (1994) for basaltic mixtures. Hiroi and Pieters (1994) showed that Hapke modeling of fine-grained mixtures containing olivine, plagioclase, and pyroxene could accurately quantify mineral abundances to within 4 wt. % when the grain size is optimized, even if the grain size is very fine and individual particle diameters are on the order of the wavelength of light.

Previous studies of band minima position and band depths have shown that reflectance spectra of fine-grained ($< 25 \mu\text{m}$) intimate mixtures are a nonlinear combination of the endmember spectra [Nash and Conel, 1974; Hapke, 1981; Singer, 1981; Clark, 1983]. As a result, it is generally assumed that radiative transfer models like those developed by Hapke [1993] and Shkuratov [1999] that treat spectral mixing as a nonlinear process are better able to describe the spectral properties of fine-grained intimate mixtures than simple linear additions of mixture spectra. However, the success of the checkerboard model at modeling mineral abundances relative to the SSA model in this study calls into question the basic assumption of nonlinearity for all fine-grained intimate mixtures.

Band depth of the cation-OH absorptions between 2.2-2.4 μm scale linearly with epsomite content because the epsomite spectrum is nearly featureless over this range

(Figure 4.4e). The 1.4, 1.45, 1.9, and 1.95 μm absorption band depths exhibit some minor deviations from linear behavior for mixtures containing very low or high clay mass fractions, but band depths for these features generally behave linearly as well for the mixture suites as a whole (Figure 4.4). An examination of previously published studies reveals that the nonlinearity of mixture spectra has been described almost exclusively for mixtures of minerals where one of the mixture components is more opaque or transparent than the other mixture component (i.e., addition of olivine or a darkening agent such as magnetite or ilmenite) [Singer, 1981; Nash and Conel, 1974; Clark, 1983], or when the mean grain size of the mixture components is quite different (i.e., very fine-grained limonite mixed with olivine and pyroxene; [Singer, 1981]). In contrast, the clay and sulfate endmembers used in this study have roughly similar grain sizes and albedos. These similarities in size and optical properties between the clay and sulfate components offer the best explanation for the relative success of the checkerboard mixing model and the linearity of the mixture suites examined here. Alternatively, if the mixture components clumped during mixing and shaking, it is possible that the distribution of clumps created an areal rather than an intimate mixture over the scale of the FTIR beam, as mentioned above.

4.5.3 Relevance for Quantifying Hydrated Minerals on Mars

The spectral properties observed for clay-epsomite mixtures indicate that absorption band position and width in the ~ 1.4 and $\sim 1.9 \mu\text{m}$ wavelength regions may be a useful parameter for modeling the presence of sulfate, or possibly other hydrated salts, on the surface of Mars when mixed with clay minerals. Absolute band depths in these wavelength regions, however, may be less diagnostic as they are subject to the amount of water in the

mineral endmembers, which can be affected by relative humidity. In addition, this study has focused only on Mg-sulfates because they are likely the most common variety on Mars, but reflectance spectra of other sulfates (e.g., Ca-sulfates such as gypsum and Fe-sulfates such as jarosite) exhibit numerous diagnostic absorptions that are not present in Mg-varieties. It is unclear how detection limits in clay-epsomite mixtures might compare to those for clay-Ca/Fe-sulfate mixtures, and additional study is warranted. Regardless, analyses based solely on band depth are largely qualitative and here results are discussed in the context of spectral modeling as a tool for determining *quantitative* mineralogy in clay-Mg sulfate mixtures.

The OH vibrational absorptions between 2.2-2.4 μm are commonly used to identify clay minerals in Mars orbital data, and the results presented here suggest that modeling only this wavelength region provides the most accurate estimates of actual clay abundance given endmember components of comparable, fine particle sizes. Furthermore, there do not appear to be systematic differences in the model results between the endmember mixture series examined here, suggesting that clay minerals, if they exist together with epsomite as mixtures on Mars, should be equally detectable whether the mixtures contain saponite, nontronite, or montmorillonite. Both clay and epsomite are difficult to model with the spectral models discussed here when present in mixtures at low abundances, particularly for the smectites examined in this work. Large uncertainties in clay and epsomite abundance can also occur if the chosen particle diameter ratio does not accurately reflect the distribution of particle sizes present in the mixture.

Although a number of studies have shown that linear unmixing models are sufficient for modeling mineral abundance in orbital spectra data [Combe *et al.*, 2008;

Themelis et al., 2012], more complex nonlinear radiative transfer models, like Shkuratov or Hapke, have been employed to quantify modal mineralogy in orbital spectra given the widely accepted recognition that fine-grained, intimate mixture spectra are nonlinear combinations of endmember spectra [*Poulet et al.*, 2008; 2009]. The results of this study show that for binary mixtures of clay and epsomite with comparable, fine grain sizes, a checkerboard model is also capable of accurately modeling clay abundance to within ≤ 5 wt % of actual abundance for mixtures containing >20 wt. % clay if the endmembers are known.

The results presented here describe powder mixtures in a highly controlled laboratory setting where the endmember spectra and grain size are known, but the results of this study suggest that checkerboard models may be valid in some cases for extracting quantitative modal abundances from orbital spectral data, especially for particulate mixtures dominated by hydrated sulfate and clay. However, it must be acknowledged that decreased signal to noise, more complex mixtures, uncertainties in spectral/mineral endmembers, assumptions about grain size and shape, and other factors would all likely act to decrease the accuracy, and possibly validity, of the models compared to the idealized scenario presented here. Future studies that build on this groundwork and that focus on more complex mixtures or the effects of increased noise are warranted and necessary to understand the full implications for modeling VNIR spectra of Mars.

Both the checkerboard and intimate mixing models tested in this study are capable of modeling clay with relatively low uncertainties for mixtures containing >20 wt.% clay. For clay-epsomite mixtures with <20 wt.% clay, clay abundance is underestimated or in some cases not modeled at all. This suggests that a minimum modeling threshold of ~ 10

wt. % clay may be reasonable when applying mixing models to orbital observations of fine-grained clay and sulfate mixtures on the surface of Mars. However, we note that the residuals between the measured and modeled spectra are often greater in the wavelength regions of known clay absorptions for mixtures with low clay abundance (e.g., Al/Mg/Fe-OH bands at ~1.4 and 2.2-2.4 μm ; see Figure 4.5f-h as an example). This indicates that the spectral features of the clay component are present in the mixture spectra but they are very weak in the context of minimizing the residuals over the full wavelength region of interest. Nevertheless, examining the residuals between modeled and measured spectra of Mars may also be useful for detecting minor mineral components. In this sense it could be possible to detect the presence of a mineral (e.g., clay) at low abundances on Mars even if it is not possible to accurately estimate that abundance. Additional studies are required to understand the limitations of clay and sulfate detections in more complex mixtures that may be of direct relevance to Mars.

4.7. Conclusions

The goal of this study was to use laboratory spectra to assess the ability of checkerboard and intimate mixing models to extract quantitative mineral abundance for fine-grained clay and epsomite mixtures under idealized and controlled conditions. Though highly simplified when compared to the complexities of the actual Martian surface, these results provide a framework for understanding how such models perform in a best-case scenario. We examined the spectral properties of fine-grained Mg-sulfate (epsomite) mixed with varying proportions of saponite, nontronite, and montmorillonite clay endmembers. These endmember compositions were chosen for direct relevance to potential mixed clay-

sulfate sedimentary deposits that have been observed on the Martian surface. Results of this study show that:

- (1) Despite the fine grain size of the powder endmembers used in this study ($<25 \mu\text{m}$), suggesting that the mixtures should behave as intimate mixtures, plots of band minima shifts and band depths suggest that the endmember spectra combine linearly as in an areal or ‘checkerboard’ mixture.
- (2) Both checkerboard and intimate mixing models of binary particulate mixtures containing epsomite mixed with saponite, nontronite, and montmorillonite endmembers are capable of predicting clay abundance to 5 wt. % or better for nearly all mixture compositions above 20 wt. % clay when the particle diameter ratio is optimized. Results of the intimate (nonlinear) mixing model are not always an improvement over those calculated with the checkerboard (linear) model. However, when actual mean or mode grain size is used to estimate the particle diameter ratio, both models are significantly less successful at accurately modeling clay abundance.
- (3) Optimized particle diameter ratios are most similar to the ratio of endmember diameter modes rather than the ratio of endmember diameter mean; optimized particle diameter ratios indicate that photon interaction with larger but fewer clay particles yields the best estimates of mineral abundances. This is consistent with the fine-grained clays forming larger aggregates in the mineral mixtures.

(4) Restricting spectral fits to a wavelength range that excludes H₂O absorptions results in improved predictions of clay abundance.

(5) Clay content is often overestimated by a few weight percent for mixtures containing high abundances of clay (>80 wt. % clay) and underestimated for mixtures containing less than 20 wt% clay.

(6) Although the differences between modeled and measured clay mass fractions are less than 10 wt. % (absolute) for all mixtures that used an optimized particle diameter, the relative uncertainty of the model fits is quite large for mixtures containing <20 wt. % clay. This suggests that the lower limit for confidently identifying clay by *modeling* the spectra of clay and sulfate mixtures is ~10 wt. %. Residuals between observed and modeled spectra may be examined to detect the presence of smaller amounts of clay.

(7) Nonlinear mixing models like those of Hapke may not always be necessary to obtain reasonable quantitative estimates of clay and/or sulfate abundances from NIR reflectance data of fine-grained mixtures. Additional study is needed to understand the extent to which these laboratory results may be applied to larger-scale orbital observations of Martian soil or sedimentary rock outcrops, where other clastic or authigenic components are likely to be present.

Notation

B	backscatter
D	particle size
D_b	band depth
E	volume extinction coefficient
e	angle of emergence
F	fractional area
f	Hapke weighting coefficient
g	phase angle
H	Hapke approximation of Chandrasekhar's function
i	angle of incidence
M	bulk density
m	mass
N	number of particles per unit volume
ρ	density
R_b	reflectance at band center
R_c	reflectance of continuum at band center
r	reflectance
σ	geometric cross-section

TABLES

Table 4.1. Constrained Model Coefficients

Clay	Clay Mass Fraction	Checkerboard Model (Reflectance Spectra)						Intimate Mixing Model (SSA Spectra)									
		Full			Subset			Full			Subset						
Clay	Epsomite	Pos Line	Neg Line	Clay	Epsomite	Pos Line	Neg Line	Clay	Epsomite	Pos Line	Neg Line	Clay	Epsomite	Pos Line	Neg Line		
JCSS-3501	1	1.00	0.00	0.00	1.00	0.00	0.00	0.00	1.00	0.00	0.00	0.00	1.00	0.00	0.00	0.00	
	0.95	0.85	0.09	0.02	0.95	0.05	0.01	0.00	0.85	0.05	0.09	0.09	0.91	0.02	0.06	0.06	
	0.9	0.78	0.16	0.03	0.03	0.92	0.09	0.01	0.00	0.78	0.10	0.11	0.12	0.88	0.04	0.06	0.06
	0.8	0.57	0.42	0.01	0.01	0.66	0.35	0.01	0.00	0.62	0.29	0.07	0.08	0.71	0.25	0.04	0.04
	0.5	0.34	0.67	0.01	0.00	0.41	0.60	0.01	0.00	0.38	0.54	0.08	0.08	0.47	0.48	0.05	0.04
	0.2	0.07	0.90	0.00	0.00	0.10	0.87	0.00	0.00	0.09	0.91	0.00	0.00	0.12	0.87	0.00	0.00
	0.1	0.03	0.97	0.00	0.00	0.05	0.96	0.00	0.00	0.04	0.95	0.01	0.00	0.07	0.94	0.00	0.00
	0.05	0.02	1.00	0.00	0.00	0.02	0.99	0.00	0.00	0.02	0.97	0.01	0.01	0.04	0.96	0.00	0.00
	0	0.00	1.00	0.00	0.00	0.00	1.00	0.00	0.00	0.00	1.00	0.00	0.00	0.00	1.00	0.00	0.00
	1	1.00	0.00	0.00	0.00	1.00	0.00	0.00	0.00	1.00	0.00	0.00	0.00	1.00	0.00	0.00	0.00
SapCa-2	0.95	0.94	0.09	0.00	0.00	0.95	0.09	0.00	0.00	0.90	0.07	0.03	0.03	0.92	0.06	0.02	0.02
	0.9	0.83	0.16	0.01	0.02	0.86	0.15	0.01	0.01	0.77	0.13	0.10	0.10	0.81	0.11	0.08	0.08
	0.8	0.73	0.30	0.00	0.00	0.74	0.31	0.00	0.00	0.70	0.25	0.05	0.05	0.72	0.23	0.05	0.05
	0.5	0.36	0.63	0.00	0.00	0.36	0.63	0.00	0.00	0.39	0.61	0.00	0.00	0.42	0.57	0.00	0.00
	0.2	0.11	0.85	0.00	0.00	0.12	0.85	0.00	0.00	0.11	0.88	0.00	0.00	0.14	0.85	0.00	0.00
	0.1	0.05	0.91	0.00	0.00	0.05	0.91	0.00	0.00	0.02	0.96	0.01	0.01	0.05	0.94	0.00	0.00
	0.05	0.02	0.93	0.00	0.00	0.02	0.94	0.00	0.00	0.00	0.98	0.01	0.01	0.02	0.97	0.00	0.00
	0	0.00	1.00	0.00	0.00	0.00	1.00	0.00	0.00	0.00	1.00	0.00	0.00	0.00	1.00	0.00	0.00
	1	1.00	0.00	0.00	0.00	1.00	0.00	0.00	0.00	1.00	0.00	0.00	0.00	1.00	0.00	0.00	0.00
	0.95	0.92	0.06	0.00	0.00	0.90	0.07	0.00	0.00	0.92	0.07	0.00	0.00	0.93	0.06	0.00	0.01
NAu-2	0.9	0.82	0.11	0.00	0.00	0.79	0.14	0.00	0.00	0.83	0.15	0.00	0.00	0.85	0.12	0.00	0.01
	0.8	0.73	0.23	0.00	0.00	0.66	0.31	0.00	0.00	0.70	0.29	0.00	0.00	0.72	0.27	0.00	0.00
	0.5	0.45	0.50	0.00	0.00	0.36	0.59	0.00	0.01	0.37	0.62	0.00	0.00	0.41	0.57	0.00	0.01
	0.2	0.19	0.77	0.00	0.00	0.12	0.83	0.00	0.01	0.11	0.88	0.00	0.00	0.13	0.85	0.00	0.01
	0.1	0.07	0.89	0.00	0.00	0.04	0.90	0.00	0.01	0.00	0.99	0.00	0.00	0.02	0.96	0.00	0.01
	0.05	0.00	0.96	0.00	0.01	0.01	0.94	0.00	0.01	0.00	0.98	0.00	0.01	0.00	0.98	0.00	0.02
	0	0.00	1.00	0.00	0.00	0.00	1.00	0.00	0.00	0.00	1.00	0.00	0.00	0.00	1.00	0.00	0.00
	1	1.00	0.00	0.00	0.00	1.00	0.00	0.00	0.00	1.00	0.00	0.00	0.00	1.00	0.00	0.00	0.00
	0.95	0.81	0.12	0.00	0.00	0.80	0.12	0.00	0.01	0.85	0.13	0.00	0.01	0.86	0.11	0.00	0.02
	0.9	0.78	0.12	0.00	0.01	0.74	0.14	0.00	0.01	0.83	0.14	0.00	0.02	0.83	0.13	0.00	0.03
SWa-1	0.8	0.60	0.33	0.00	0.01	0.55	0.34	0.00	0.02	0.66	0.32	0.00	0.02	0.64	0.32	0.00	0.03
	0.5	0.22	0.71	0.00	0.00	0.21	0.69	0.00	0.01	0.21	0.77	0.00	0.01	0.24	0.72	0.00	0.02
	0.2	0.01	1.00	0.00	0.00	0.03	0.93	0.00	0.02	0.00	1.00	0.00	0.00	0.03	0.96	0.00	0.02
	0.1	0.00	0.95	0.00	0.01	0.00	0.88	0.00	0.02	0.00	0.96	0.00	0.04	0.00	0.93	0.00	0.05
	0.05	0.00	0.87	0.00	0.02	0.00	0.82	0.00	0.02	0.00	0.92	0.00	0.07	0.00	0.89	0.00	0.08
	0	0.00	1.00	0.00	0.00	0.00	1.00	0.00	0.00	0.00	1.00	0.00	0.00	0.00	1.00	0.00	0.00
	1	1.00	0.00	0.00	0.00	1.00	0.00	0.00	0.00	1.00	0.00	0.00	0.00	1.00	0.00	0.00	0.00
	0.95	0.97	0.07	0.01	0.00	1.00	0.06	0.00	0.00	0.87	0.07	0.07	0.07	0.88	0.06	0.07	0.07
	0.9	0.81	0.17	0.00	0.00	0.83	0.15	0.00	0.00	0.82	0.18	0.00	0.00	0.84	0.15	0.00	0.00
	0.8	0.66	0.32	0.00	0.00	0.68	0.30	0.00	0.00	0.66	0.33	0.00	0.00	0.69	0.30	0.00	0.00
SCa-3	0.5	0.27	0.65	0.00	0.00	0.32	0.59	0.00	0.00	0.23	0.74	0.00	0.02	0.27	0.68	0.00	0.02
	0.2	0.02	0.90	0.00	0.00	0.06	0.83	0.00	0.01	0.00	0.96	0.00	0.03	0.00	0.95	0.00	0.03
	0.1	0.00	0.97	0.00	0.00	0.00	0.93	0.00	0.01	0.00	0.98	0.00	0.02	0.00	0.96	0.00	0.03
	0.05	0.00	0.93	0.00	0.01	0.00	0.88	0.00	0.02	0.00	0.95	0.00	0.04	0.00	0.93	0.00	0.05
	0	0.00	1.00	0.00	0.00	0.00	1.00	0.00	0.00	0.00	1.00	0.00	0.00	0.00	1.00	0.00	0.00
	1	1.00	0.00	0.00	0.00	1.00	0.00	0.00	0.00	1.00	0.00	0.00	0.00	1.00	0.00	0.00	0.00
	0.95	0.82	0.06	0.01	0.02	0.88	0.03	0.00	0.00	0.91	0.07	0.00	0.01	0.93	0.04	0.00	0.01
	0.9	0.81	0.18	0.00	0.00	0.83	0.16	0.00	0.00	0.85	0.15	0.00	0.00	0.86	0.13	0.00	0.00
	0.8	0.64	0.32	0.02	0.02	0.71	0.29	0.01	0.00	0.64	0.27	0.08	0.08	0.69	0.24	0.06	0.06
	0.5	0.29	0.71	0.00	0.00	0.32	0.67	0.00	0.00	0.34	0.66	0.00	0.00	0.37	0.63	0.00	0.00
SWy-2	0.2	0.00	0.98	0.00	0.00	0.04	0.91	0.00	0.00	0.00	0.99	0.00	0.01	0.01	0.98	0.00	0.01
	0.1	0.00	0.99	0.00	0.01	0.01	0.95	0.00	0.01	0.00	0.99	0.00	0.01	0.00	0.98	0.00	0.01
	0.05	0.00	0.92	0.00	0.02	0.00	0.88	0.00	0.01	0.00	0.95	0.00	0.04	0.00	0.93	0.00	0.05
	0	0.00	1.00	0.00	0.00	0.00	1.00	0.00	0.00	0.00	1.00	0.00	0.00	0.00	1.00	0.00	0.00
	1	1.00	0.00	0.00	0.00	1.00	0.00	0.00	0.00	1.00	0.00	0.00	0.00	1.00	0.00	0.00	0.00
	0.95	0.82	0.06	0.01	0.02	0.88	0.03	0.00	0.00	0.91	0.07	0.00	0.01	0.93	0.04	0.00	0.01

Table 4.2. Optimized Particle Diameter Ratios

Endmember	Measured Mean Diameter Ratio	Measured Modal Diameter Ratio	Checkerboard Model (Reflectance Spectra)		Intimate Mixing Model (SSA Spectra)	
			1.25-2.6 μm	2.1-2.6 μm	1.25-2.6 μm	2.1-2.6 μm
JCSS-3501	0.8273	3.484	1.743	1.267	1.191	0.871
SapCa-2	0.357	1.000	1.316	1.282	1.190	1.006
NAu-2	0.655	0.968	0.823	1.258	1.258	1.079
SWa-1	0.274	0.871	2.183	2.372	2.273	2.175
SCa-3	0.631	0.968	1.741	1.397	2.028	1.608
SWy-2	0.375	1.065	1.648	1.617	1.321	1.184

Table 4.3. Modeled Mass Fractions Using Full Spectrum and Optimized Diameter

Clay	Measured	Ratio			
		Checkerboard Model		Intimate Mixing Model	
		Unconstrained	Normalized	Unconstrained	Normalized
JCSS-3501	1.00	1.00	0.00	1.00	0.00
	0.94	0.96	-0.01	0.97	-0.02
	0.90	0.92	-0.02	0.94	-0.03
	0.80	0.76	0.04	0.78	0.02
	0.50	0.54	-0.04	0.54	-0.04
	0.20	0.16	0.03	0.13	0.06
	0.10	0.08	0.02	0.07	0.03
	0.06	0.04	0.02	0.03	0.03
	0.00	0.00	0.00	0.00	0.00
SapCa-2	1.00	1.00	0.00	1.00	0.00
	0.95	0.95	0.00	0.96	-0.01
	0.91	0.90	0.00	0.92	-0.02
	0.80	0.81	-0.01	0.82	-0.03
	0.50	0.50	0.00	0.51	-0.01
	0.19	0.19	0.01	0.16	0.04
	0.10	0.08	0.02	0.04	0.06
	0.06	0.04	0.01	0.00	0.06
	0.00	0.00	0.00	0.00	0.00
NAu-2	1.00	1.00	0.00	1.00	0.00
	0.95	0.95	0.00	0.96	-0.01
	0.90	0.90	0.00	0.91	-0.01
	0.80	0.78	0.02	0.80	0.00
	0.50	0.51	-0.01	0.51	-0.01
	0.20	0.21	-0.01	0.18	0.02
	0.10	0.08	0.03	0.00	0.10
	0.05	0.00	0.05	0.00	0.05
	0.00	0.00	0.00	0.00	0.00
SWa-1	1.00	1.00	0.00	1.00	0.00
	0.95	0.95	0.00	0.95	0.00
	0.90	0.95	-0.05	0.95	-0.05
	0.80	0.85	-0.05	0.87	-0.06
	0.50	0.48	0.02	0.46	0.04
	0.20	0.02	0.18	0.00	0.20
	0.10	0.00	0.10	0.00	0.10
	0.05	0.00	0.05	0.00	0.05
	0.00	0.00	0.00	0.00	0.00
SCa-3	1.00	1.00	0.00	1.00	0.00
	0.95	0.97	-0.02	0.97	-0.02
	0.90	0.92	-0.02	0.93	-0.03
	0.80	0.83	-0.04	0.85	-0.05
	0.50	0.50	0.00	0.46	0.04
	0.20	0.06	0.14	0.00	0.20
	0.10	0.00	0.10	0.00	0.10
	0.05	0.00	0.05	0.00	0.05
	0.00	0.00	0.00	0.00	0.00
SWy-2	1.00	1.00	0.00	1.00	0.00
	0.95	0.97	-0.02	0.96	-0.01
	0.90	0.91	-0.02	0.91	-0.02
	0.80	0.82	-0.03	0.82	-0.02
	0.50	0.48	0.02	0.48	0.02
	0.20	0.00	0.20	0.00	0.20
	0.11	0.00	0.11	0.00	0.11
	0.05	0.00	0.05	0.00	0.05
	0.00	0.00	0.00	0.00	0.00

Table 4.4. Modeled Mass Fractions Using Partial Spectrum and Optimized Diameter

Clay	Measured	Ratio			
		Checkerboard Model		Intimate Mixing Model	
		Unconstrained	Normalized	Unconstrained	Normalized
JCSS-3501	1.00	1.00	0.00	1.00	0.00
	0.94	0.96	-0.01	0.97	-0.02
	0.90	0.92	-0.02	0.94	-0.03
	0.80	0.76	0.04	0.78	0.02
	0.50	0.54	-0.04	0.54	-0.04
	0.20	0.16	0.03	0.13	0.06
	0.10	0.08	0.02	0.07	0.03
	0.06	0.04	0.02	0.03	0.03
	0.00	0.00	0.00	0.00	0.00
SapCa-2	1.00	1.00	0.00	1.00	0.00
	0.95	0.95	0.00	0.95	-0.01
	0.91	0.91	-0.01	0.92	-0.02
	0.80	0.80	0.00	0.81	-0.01
	0.50	0.50	0.00	0.50	0.00
	0.19	0.19	0.01	0.18	0.02
	0.10	0.08	0.02	0.07	0.03
	0.06	0.04	0.01	0.03	0.03
	0.00	0.00	0.00	0.00	0.00
NAu-2	1.00	1.00	0.00	1.00	0.00
	0.95	0.96	-0.01	0.96	-0.02
	0.90	0.91	-0.01	0.91	-0.02
	0.80	0.79	0.01	0.80	0.00
	0.50	0.51	-0.01	0.51	-0.02
	0.20	0.20	0.00	0.18	0.02
	0.10	0.07	0.04	0.03	0.08
	0.05	0.02	0.04	0.00	0.05
	0.00	0.00	0.00	0.00	0.00
SWa-1	1.00	1.00	0.00	1.00	0.00
	0.95	0.96	-0.01	0.96	-0.01
	0.90	0.95	-0.05	0.95	-0.05
	0.80	0.85	-0.04	0.86	-0.05
	0.50	0.50	0.00	0.50	0.00
	0.20	0.08	0.12	0.08	0.12
	0.10	0.00	0.10	0.00	0.10
	0.05	0.00	0.05	0.00	0.05
	0.00	0.00	0.00	0.00	0.00
SCa-3	1.00	1.00	0.00	1.00	0.00
	0.95	0.97	-0.02	0.97	-0.02
	0.90	0.92	-0.02	0.93	-0.03
	0.80	0.81	-0.01	0.83	-0.04
	0.50	0.52	-0.02	0.47	0.03
	0.20	0.12	0.08	0.00	0.20
	0.10	0.00	0.10	0.00	0.10
	0.05	0.00	0.05	0.00	0.05
	0.00	0.00	0.00	0.00	0.00
SWy-2	1.00	1.00	0.00	1.00	0.00
	0.95	0.98	-0.04	0.97	-0.02
	0.90	0.92	-0.02	0.91	-0.02
	0.80	0.84	-0.05	0.83	-0.03
	0.50	0.51	-0.01	0.48	0.02
	0.20	0.10	0.11	0.01	0.19
	0.11	0.03	0.08	0.00	0.11
	0.05	0.00	0.05	0.00	0.05
	0.00	0.00	0.00	0.00	0.00

FIGURE CAPTIONS

Figure 4.1. Endmember particle diameter measurements. (a) Histogram of epsomite endmember particle diameter (left) manually measured from an optical photomicrograph (right). (b-g) Histograms of clay endmember particle diameter manually measured from accompanying photomicrographs. Each histogram contains 100 bins, and n is the number of particles measured in each photomicrograph. The scale bar for each photomicrograph is 100 micrometers.

Figure 4.2. NIR diffuse reflectance spectra of all mixtures and endmember components acquired with an FTIR spectrometer. Each spectrum represents the average of three spectra (each representing 200 scans) acquired at different locations on the surface of each powder mixture or endmember.

Figure 4.3. Wavelength position of local band minima measured in reflectance spectra versus measured clay mass fraction. (a) $\sim 1.4 \mu\text{m}$ absorption, (b) $\sim 1.45 \mu\text{m}$ absorption, (c) $1.9 \mu\text{m}$ absorption, (d) $1.95 \mu\text{m}$ absorption and (e) $2.2\text{-}2.4 \mu\text{m}$ absorption.

Figure 4.4. Reflectance band depth versus measured clay mass fraction. (a) $1.4 \mu\text{m}$ absorption, (b) $1.45 \mu\text{m}$ absorption, (c) $1.9 \mu\text{m}$ absorption, (d) $1.95 \mu\text{m}$ absorption, and (e) $2.2\text{-}2.4 \mu\text{m}$ absorption.

Figure 4.5. JCSS-3501 saponite and epsomite measured and modeled mixture spectra. (a) Reflectance spectra of the saponite JCSS-3501 mixture series offset along the y-axis for clarity. (b-h) Measured reflectance spectra plotted with the checkerboard model spectra for each JCSS-3501 mixture. Residuals (measured – modeled) are plotted below each spectral plot.

Figure 4.6. SapCa-2 saponite and epsomite measured and modeled mixture spectra. (a) Reflectance spectra of the saponite SapCa-2 mixture series offset along the y-axis for clarity. (b-h) Measured reflectance spectra plotted with the checkerboard model spectra for each SapCa-2 mixture. Residuals (measured – modeled) are plotted below each spectral plot.

Figure 4.7. NAu-2 nontronite and epsomite measured and modeled mixture spectra. (a) Reflectance spectra of the nontronite NAu-2 mixture series offset along the y-axis for clarity. (b-h) Measured reflectance spectra plotted with the checkerboard model spectra for each NAu-2 mixture. Residuals (measured – modeled) are plotted below each spectral plot.

Figure 4.8. SWa-1 nontronite and epsomite measured and modeled mixture spectra. (a) Reflectance spectra of the nontronite SWa-1 mixture series offset along the y-axis for clarity. (b-h) Measured reflectance spectra plotted with the checkerboard model spectra for each SWa-1 mixture. Residuals (measured – modeled) are plotted below each spectral plot.

Figure 4.9. SCa-3 montmorillonite and epsomite measured and modeled mixture spectra.

(a) Reflectance spectra of the montmorillonite SCa-3 mixture series offset along the y-axis for clarity. (b-h) Measured reflectance spectra plotted with the checkerboard model spectra for each SCa-3 mixture. Residuals (measured – modeled) are plotted below each spectral plot.

Figure 4.10. SWy-2 montmorillonite and epsomite measured and modeled mixture spectra.

(a) Reflectance spectra of the montmorillonite SWy-2 mixture series offset along the y-axis for clarity. (b-h) Measured reflectance spectra plotted with the checkerboard model spectra for each SWy-2 mixture. Residuals (measured – modeled) are plotted below each spectral plot.

Figure 4.11. Optimized particle diameter ratios calculated for each individual mixture within a series. (a-f) full reflectance spectral range (1.25-2.6 μm), and (g-l) full SSA spectral range (1.25-2.6 μm). Each plot should contain one point for each of the seven mixtures within the series, but individual particle diameter ratios could not be calculated for mixtures modeled to contain no clay (i.e. nontronite and montmorillonite plots).

Figure 4.12. Modeled versus measured clay mass fractions calculated using the measured mean particle sizes and the full spectral range (1.25-2.6 μm). (a-c) Mass fractions calculated from checkerboard modeling of reflectance spectra. (d-f) Mass fractions calculated from intimate mixing modeling of SSA spectra.

Figure 4.13. Modeled versus measured clay mass fractions calculated using the measured mode particle sizes and the full spectral range (1.25-2.6 μm). (a-c) Mass fractions calculated from checkerboard modeling of reflectance spectra. (d-f) Mass fractions calculated from intimate mixing modeling of SSA spectra.

Figure 4.14. Modeled versus measured clay mass fractions calculated using the optimized particle sizes and the full spectral range (1.25-2.6 μm). (a-c) Mass fractions calculated from checkerboard modeling of reflectance spectra. (d-f) Mass fractions calculated from intimate mixing modeling of SSA spectra.

Figure 4.15. Relative uncertainties based on optimized particle diameter mass fraction results calculated from full spectra (1.25-2.6 μm). Relative uncertainty was calculated as the absolute difference between measured and modeled mass fractions divided by measured mass fraction and multiplied by 100.

Figure 4.16. Optimized particle diameter ratios calculated for each individual mixture within a series. (a-f) Subset (2.1-2.6 μm) reflectance spectra, and (g-l) subset (2.1-2.6 μm) SSA spectra. Each plot should contain one point for each of the seven mixtures within the series, but individual particle diameter ratios could not be calculated for mixtures modeled by the checkerboard or intimate mixing models to contain no clay (i.e. SSA SWa-1, SCA-3, and SWy-2 plots).

Figure 4.17. Modeled versus measured clay mass fractions calculated using the measured mean particle sizes and the partial spectral range (2.1-2.6 μm). (a-c) Mass fractions calculated from checkerboard modeling of reflectance spectra. (d-f) Mass fractions calculated from intimate mixing modeling of SSA spectra.

Figure 4.18. Modeled versus measured clay mass fractions calculated using the measured mode particle sizes and the partial spectral range (2.1-2.6 μm). (a-c) Mass fractions calculated from checkerboard modeling of reflectance spectra. (d-f) Mass fractions calculated from intimate mixing modeling of SSA spectra.

Figure 4.19. Modeled versus measured clay mass fractions calculated using the optimized particle diameter ratios and the partial spectral range (2.1-2.6 μm). (a-c) Mass fractions calculated from checkerboard modeling of reflectance spectra. (d-f) Mass fractions calculated from intimate mixing modeling of SSA spectra.

Figure 4.20. Relative uncertainties based on optimized particle diameter mass fraction results calculated from subset spectra (2.1-2.6 μm). Relative uncertainty was calculated as the absolute difference between measured and modeled mass fractions divided by measured mass fraction and multiplied by 100.

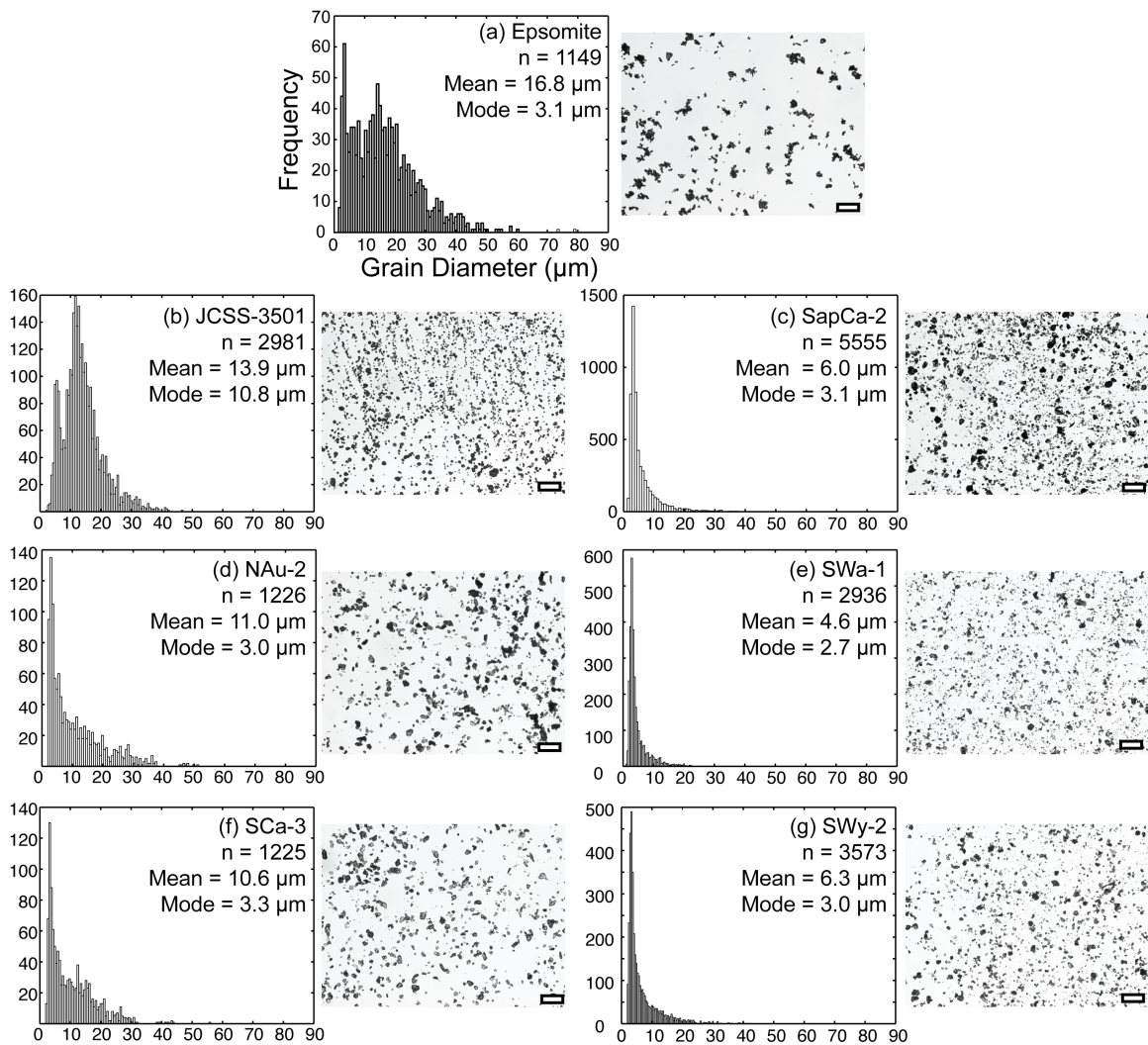


Figure 4.1

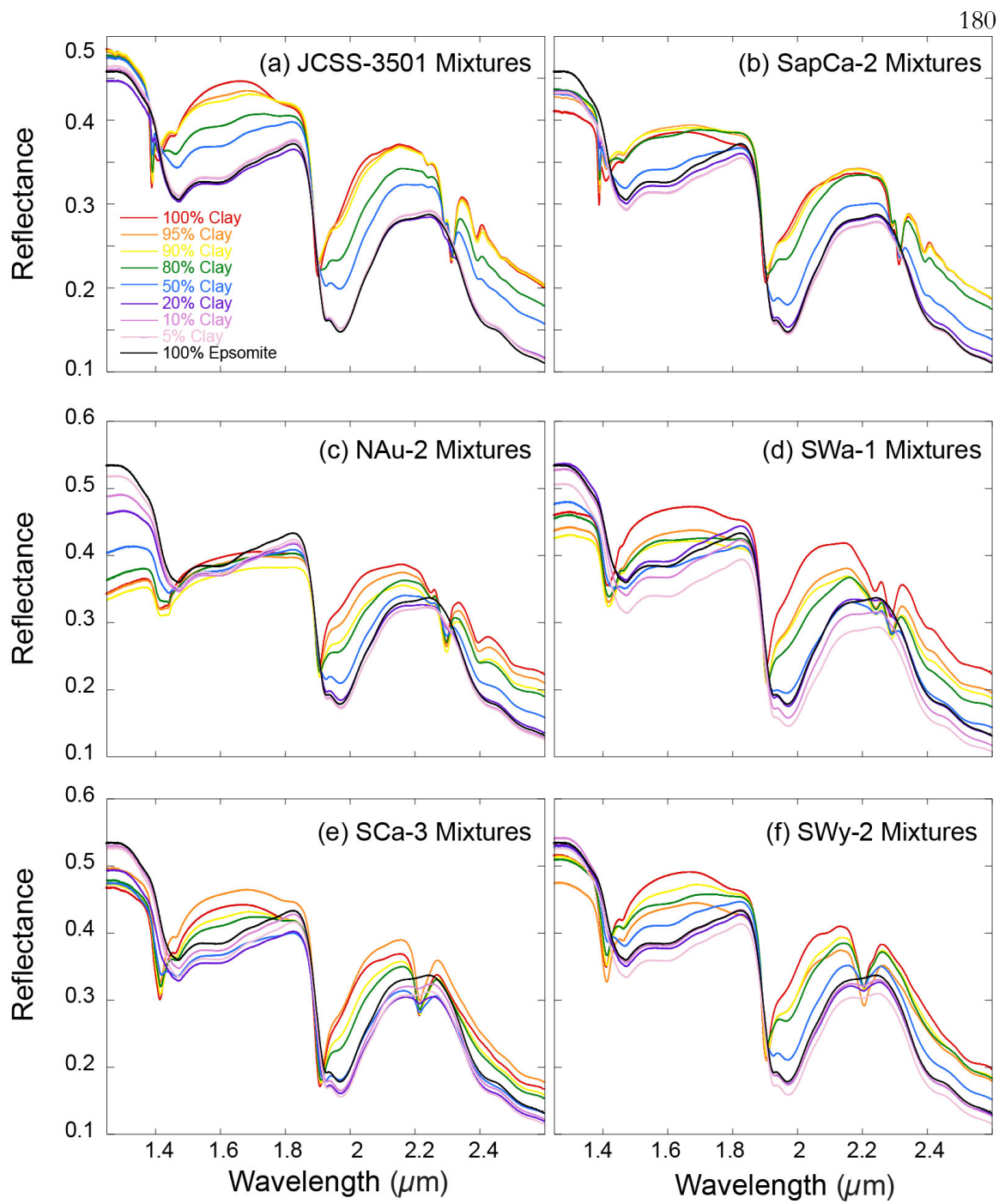


Figure 4.2

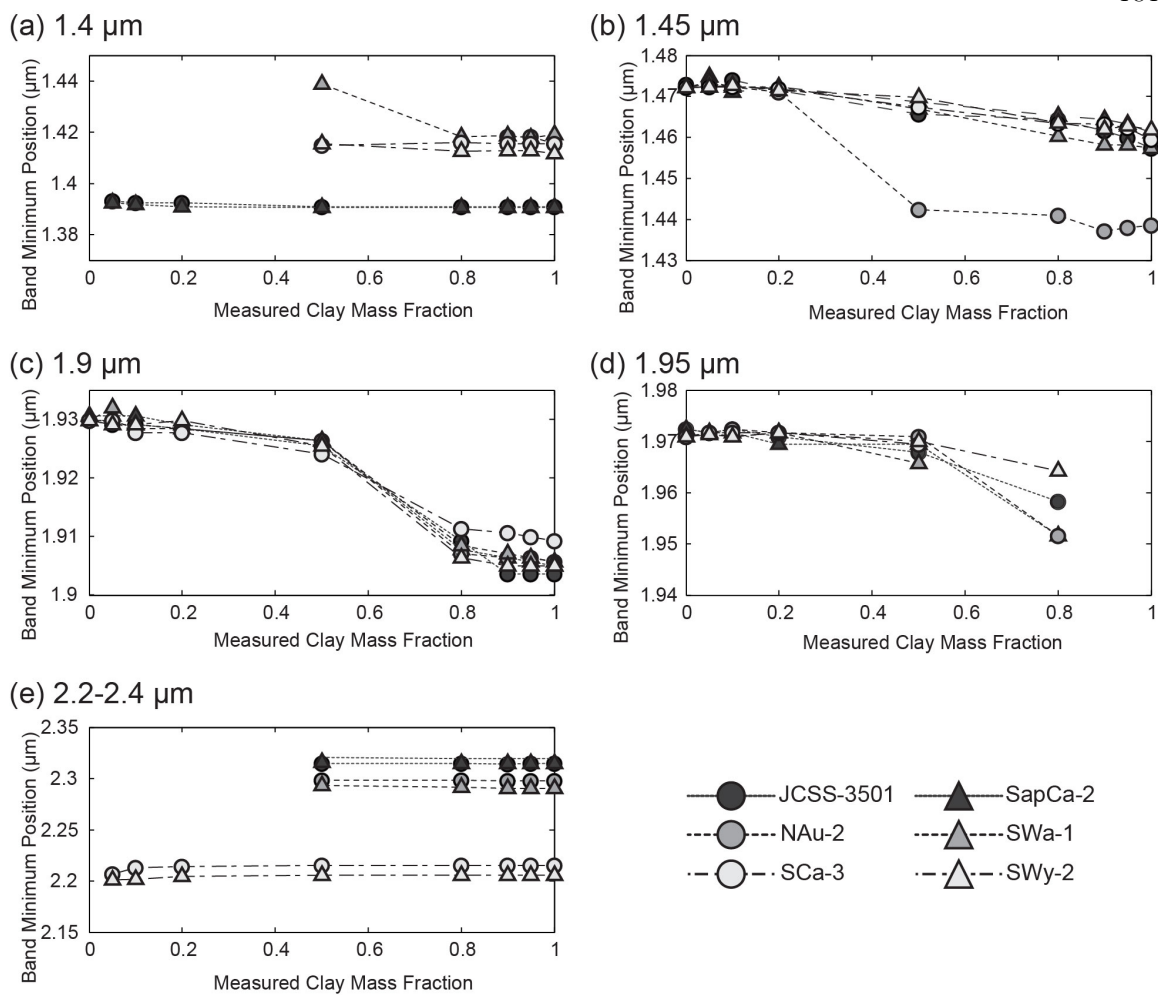


Figure 4.3

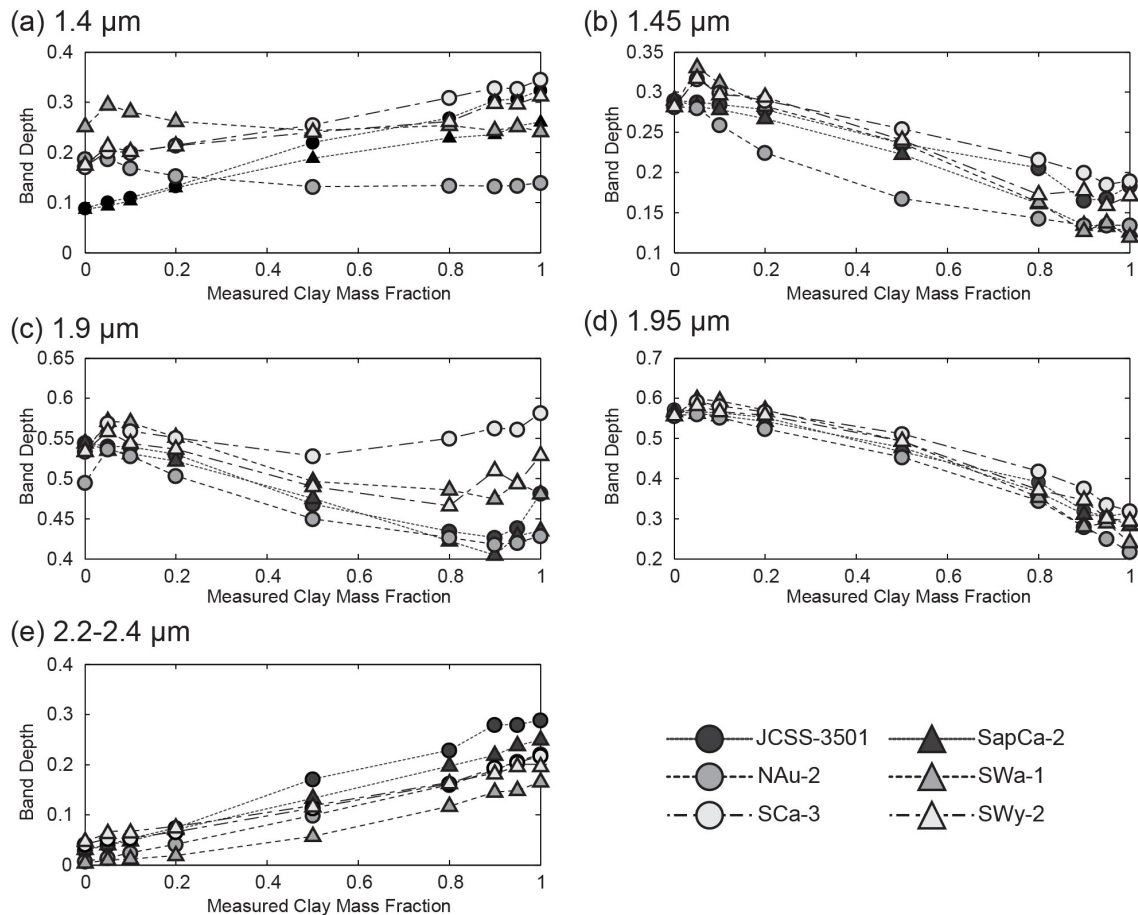


Figure 4.4

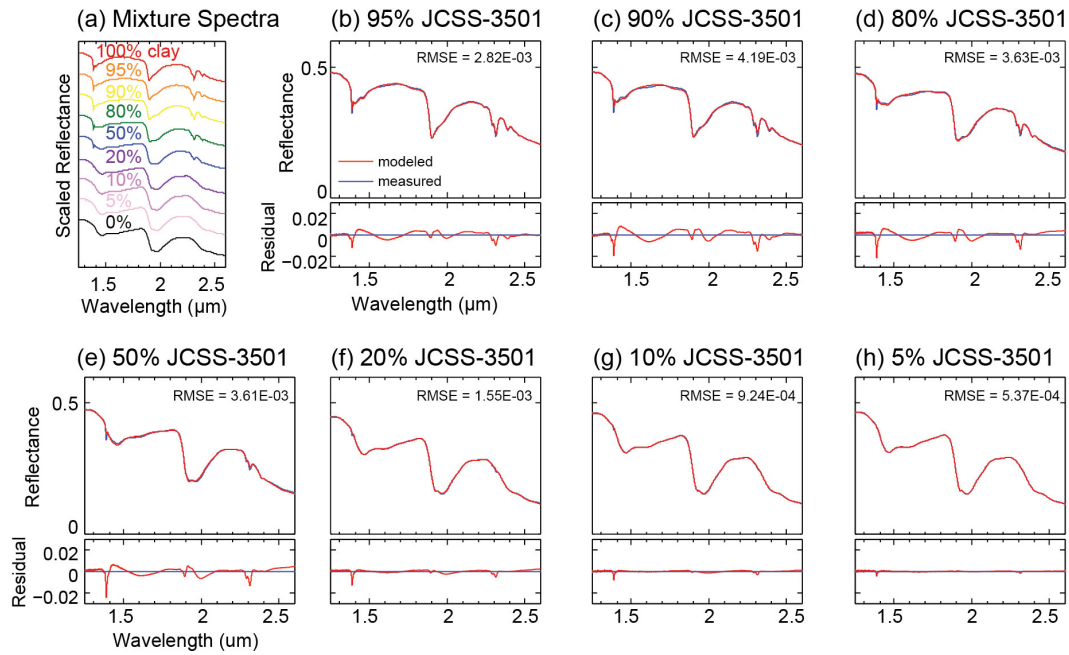


Figure 4.5

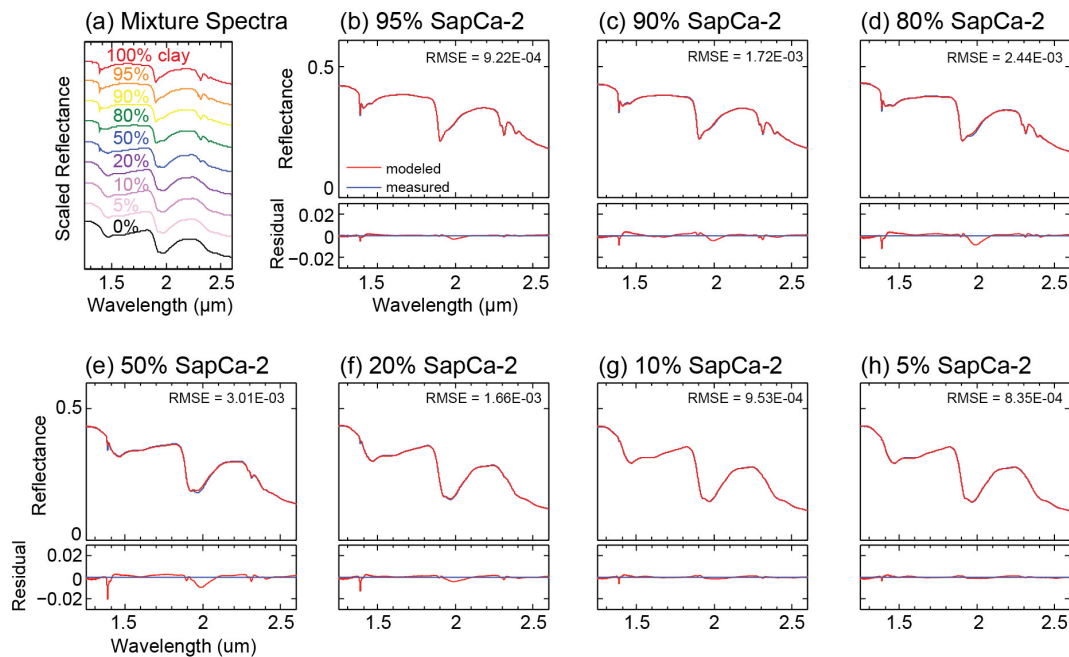


Figure 4.6

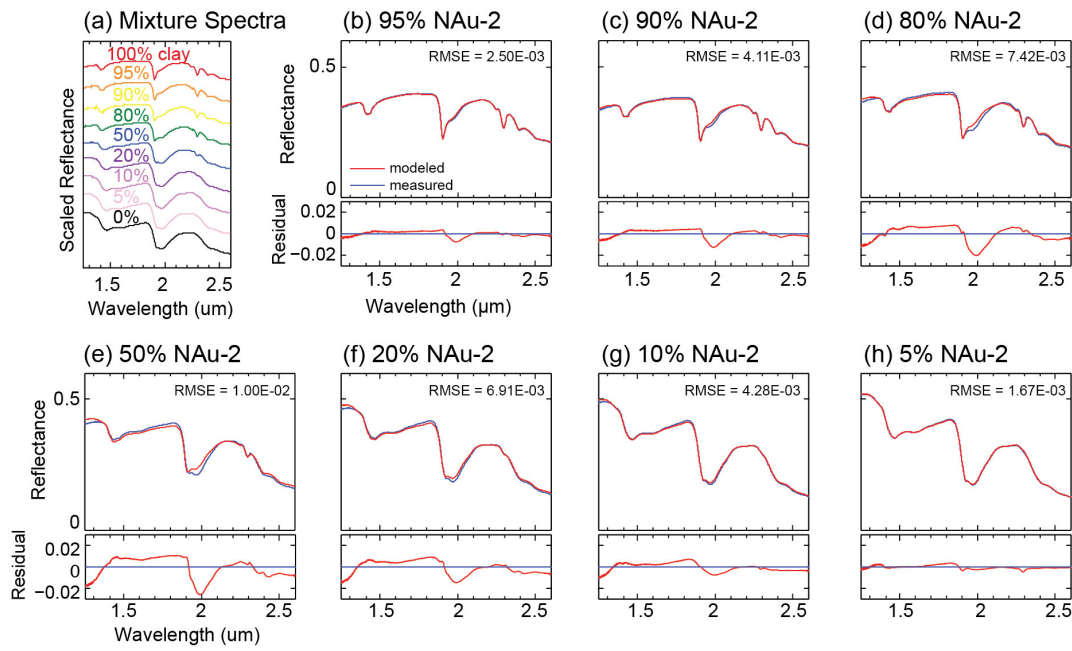


Figure 4.7

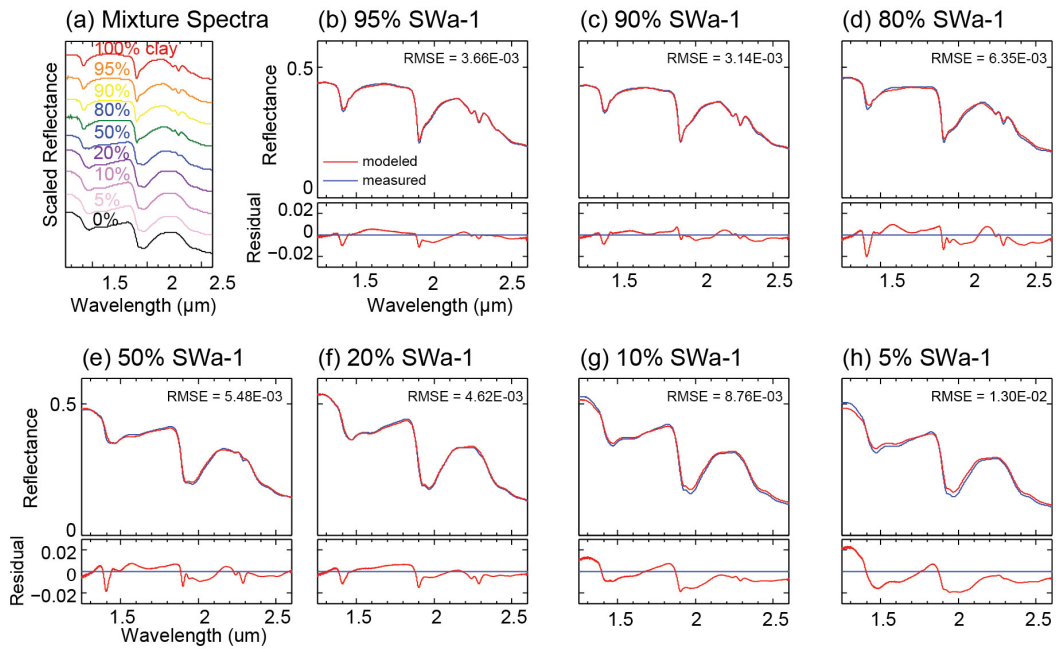


Figure 4.8

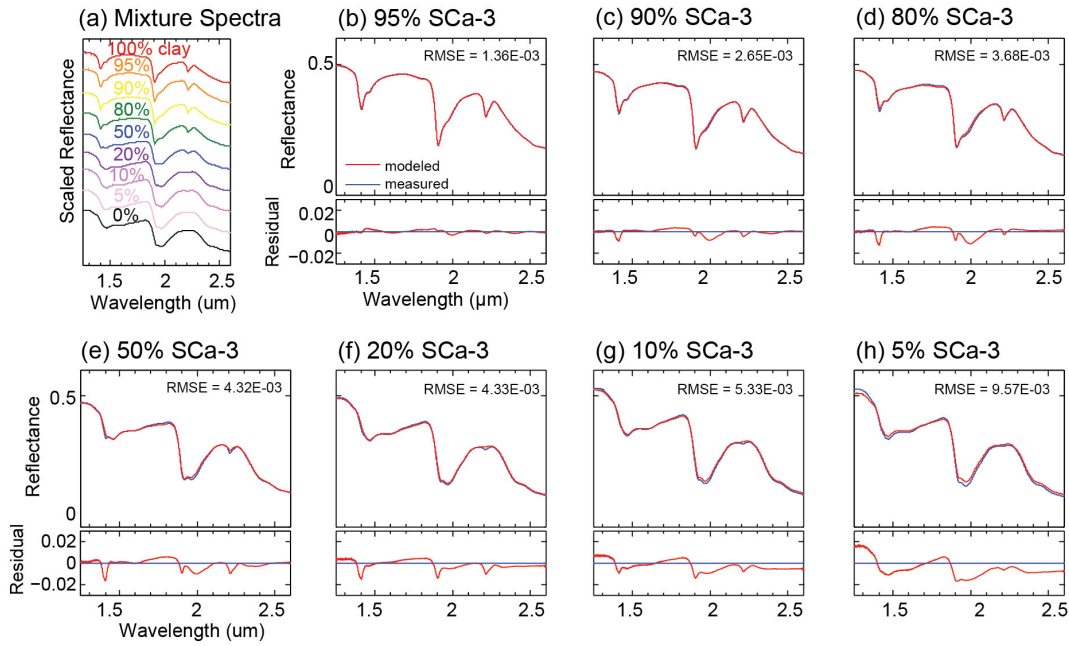


Figure 4.9

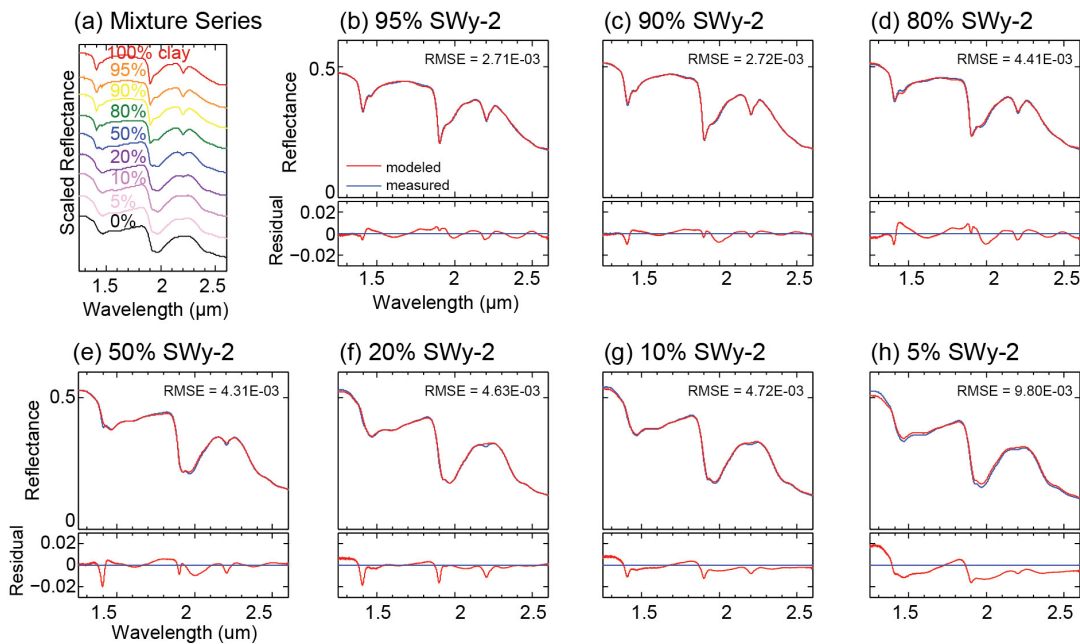


Figure 4.10

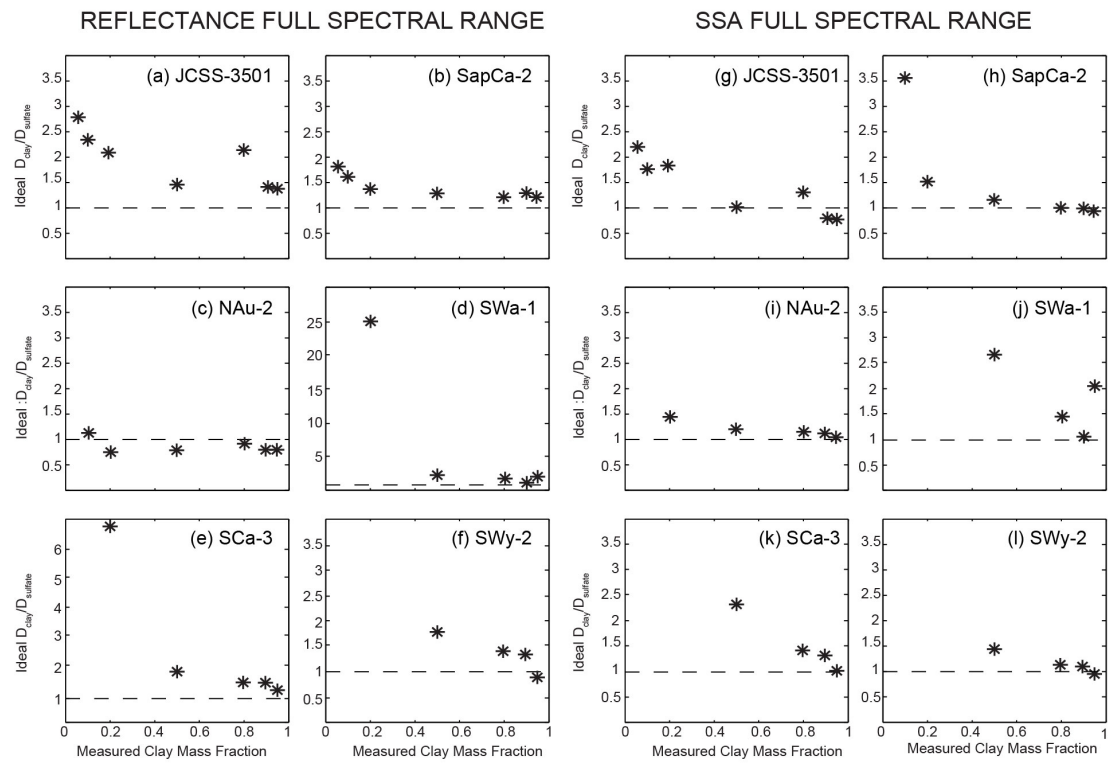


Figure 4.11

FULL SPECTRAL RANGE, MEAN PARTICLE DIAMETER RATIO

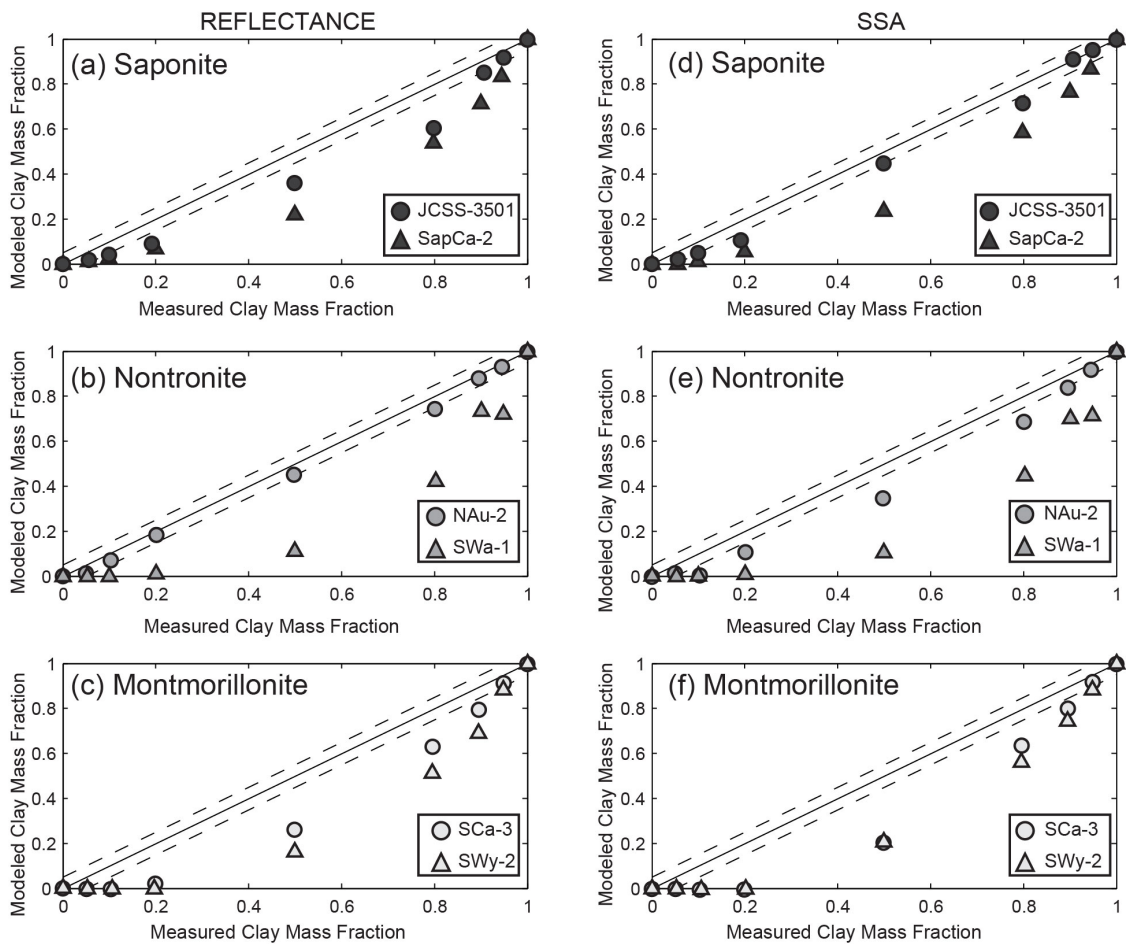


Figure 4.12

FULL SPECTRAL RANGE, MODAL PARTICLE DIAMETER RATIO

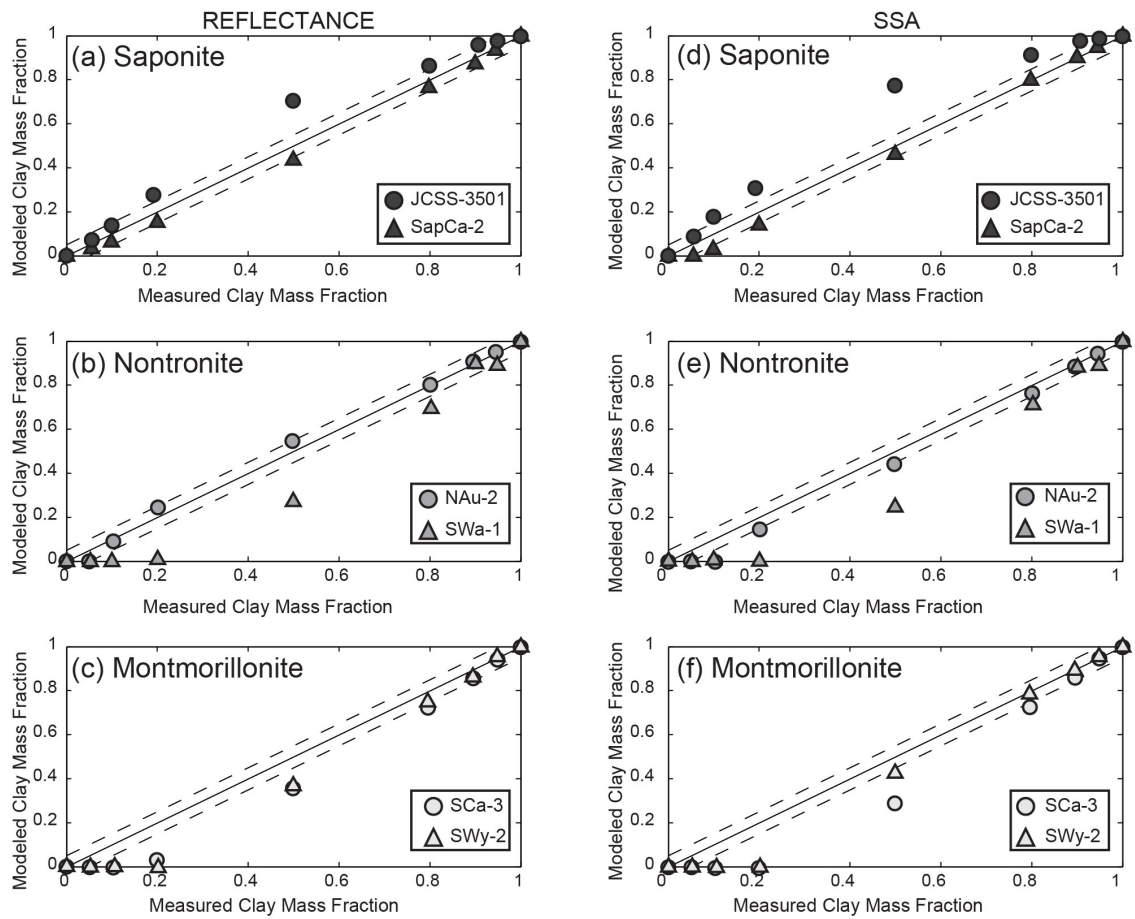


Figure 4.13

FULL SPECTRAL RANGE, OPTIMIZED PARTICLE DIAMETER RATIO

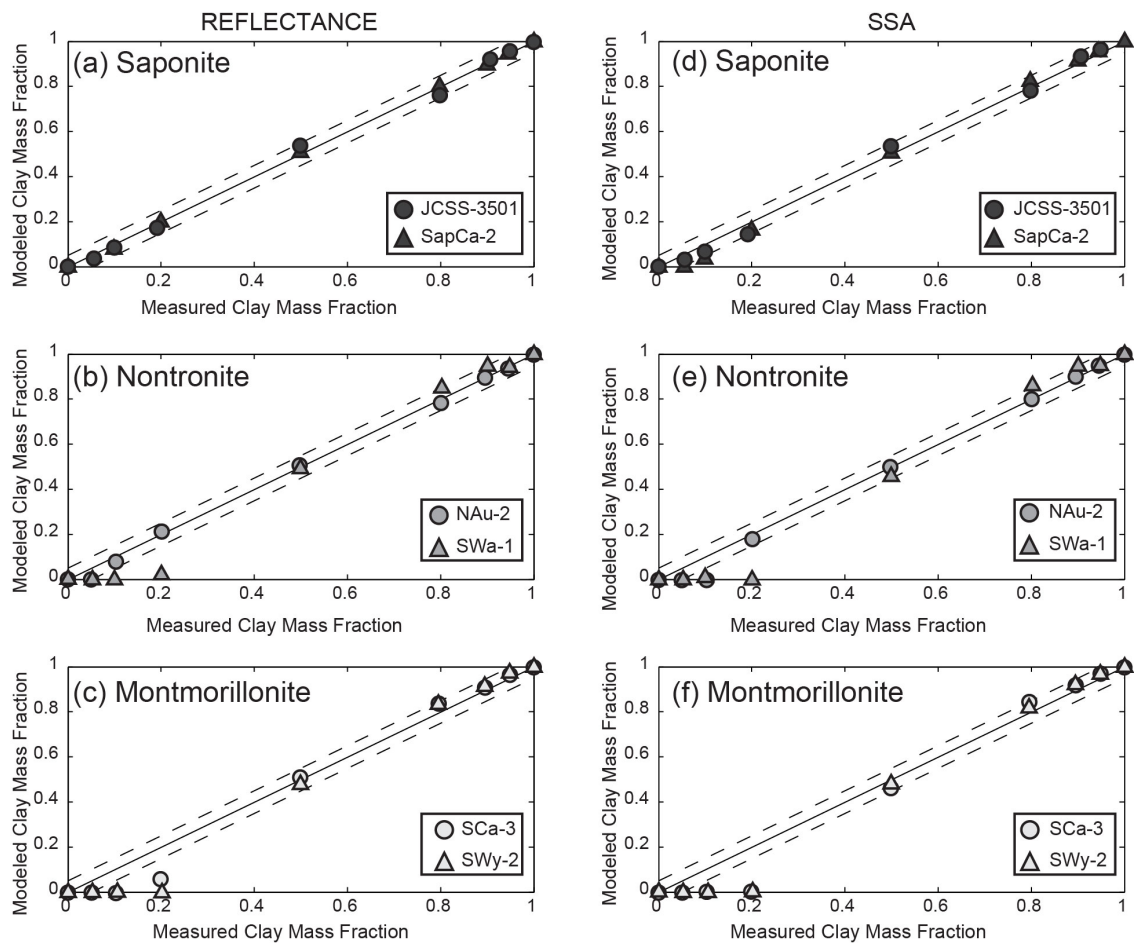


Figure 4.14

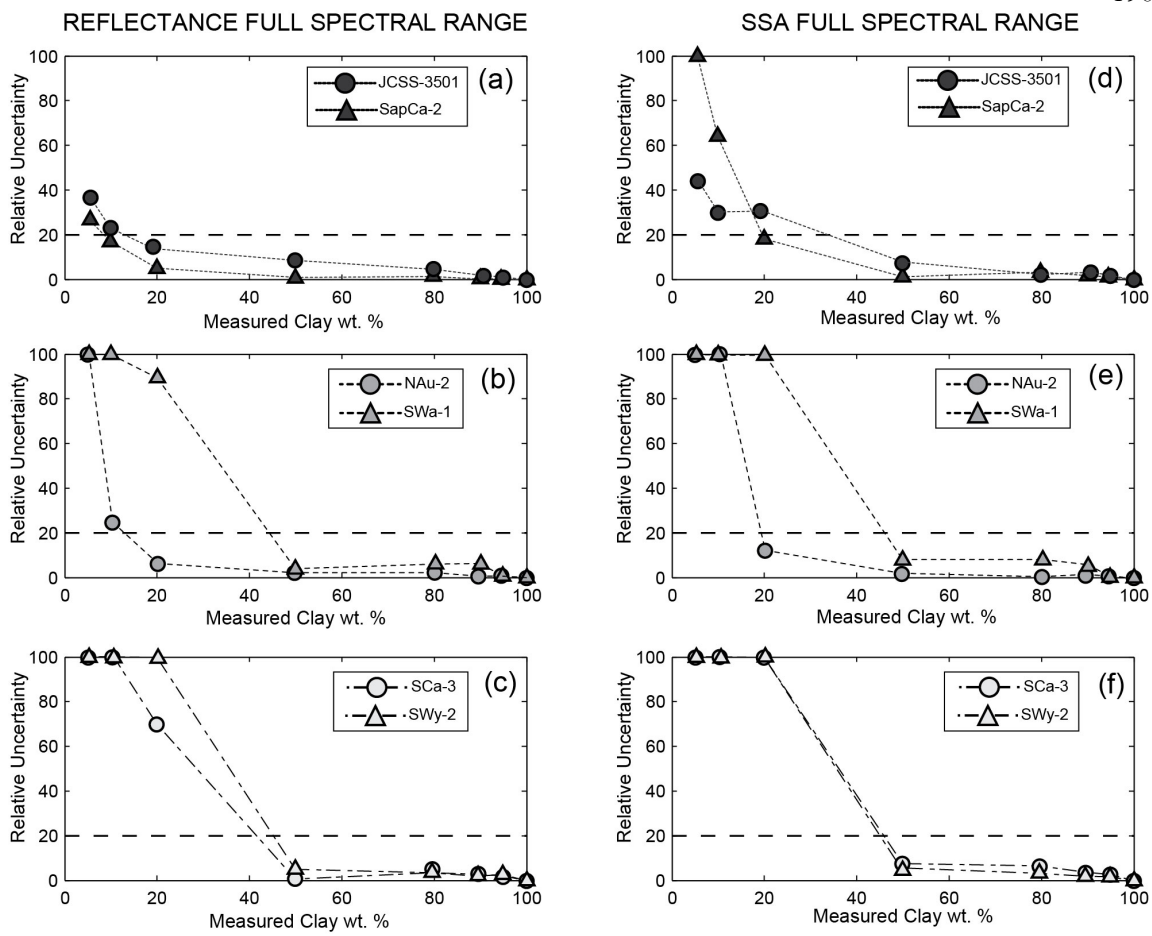


Figure 4.15

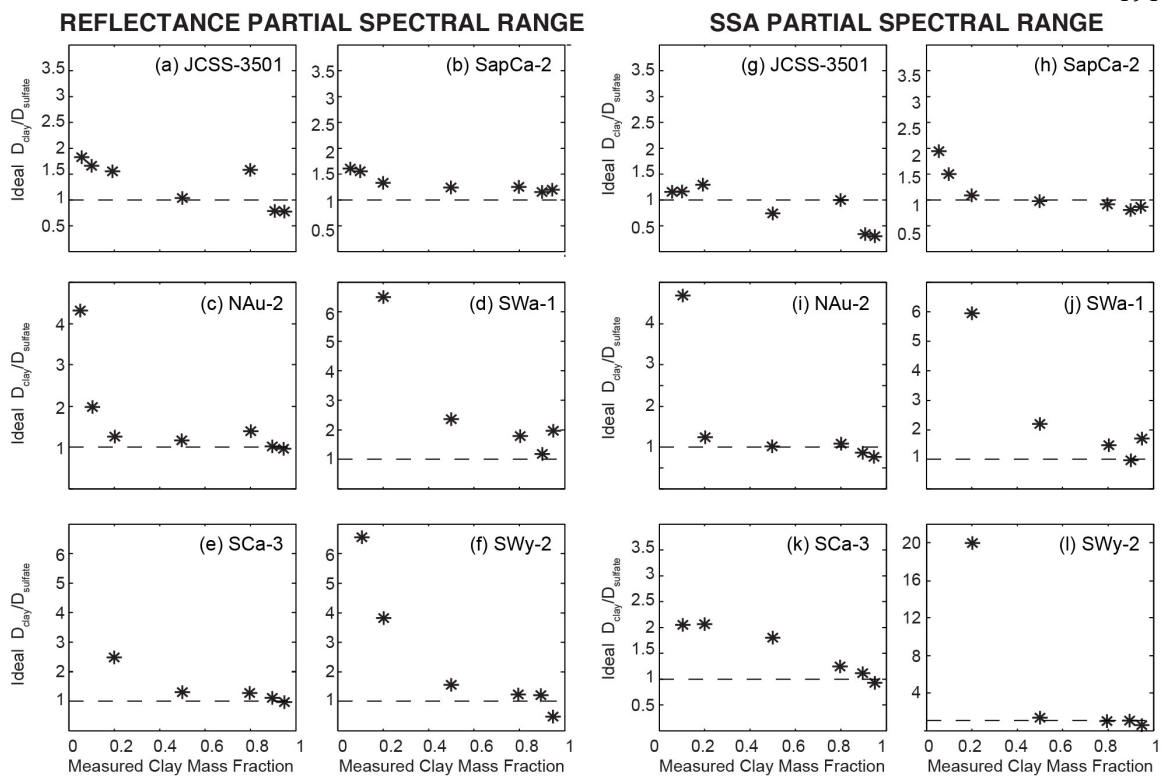


Figure 4.16

PARTIAL SPECTRAL RANGE, MEAN PARTICLE DIAMETER RATIO

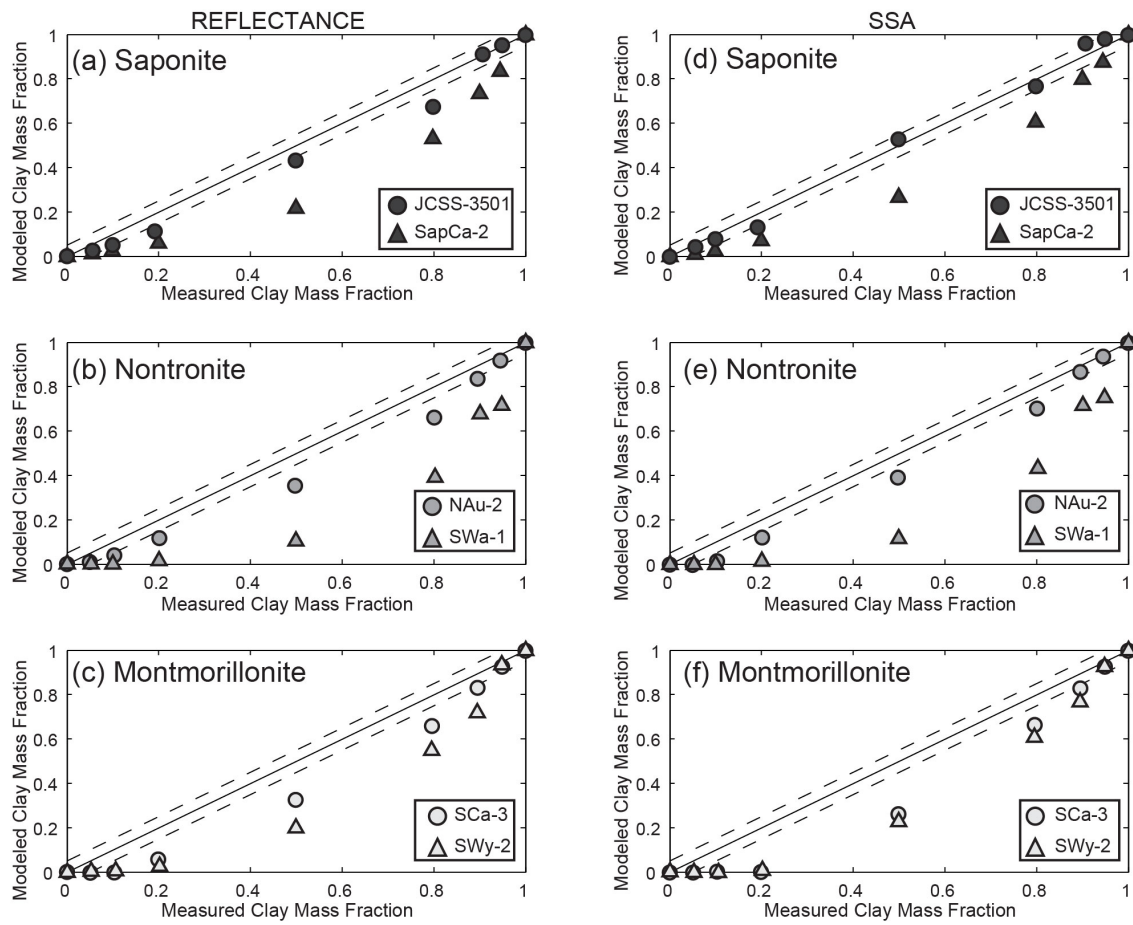


Figure 4.17

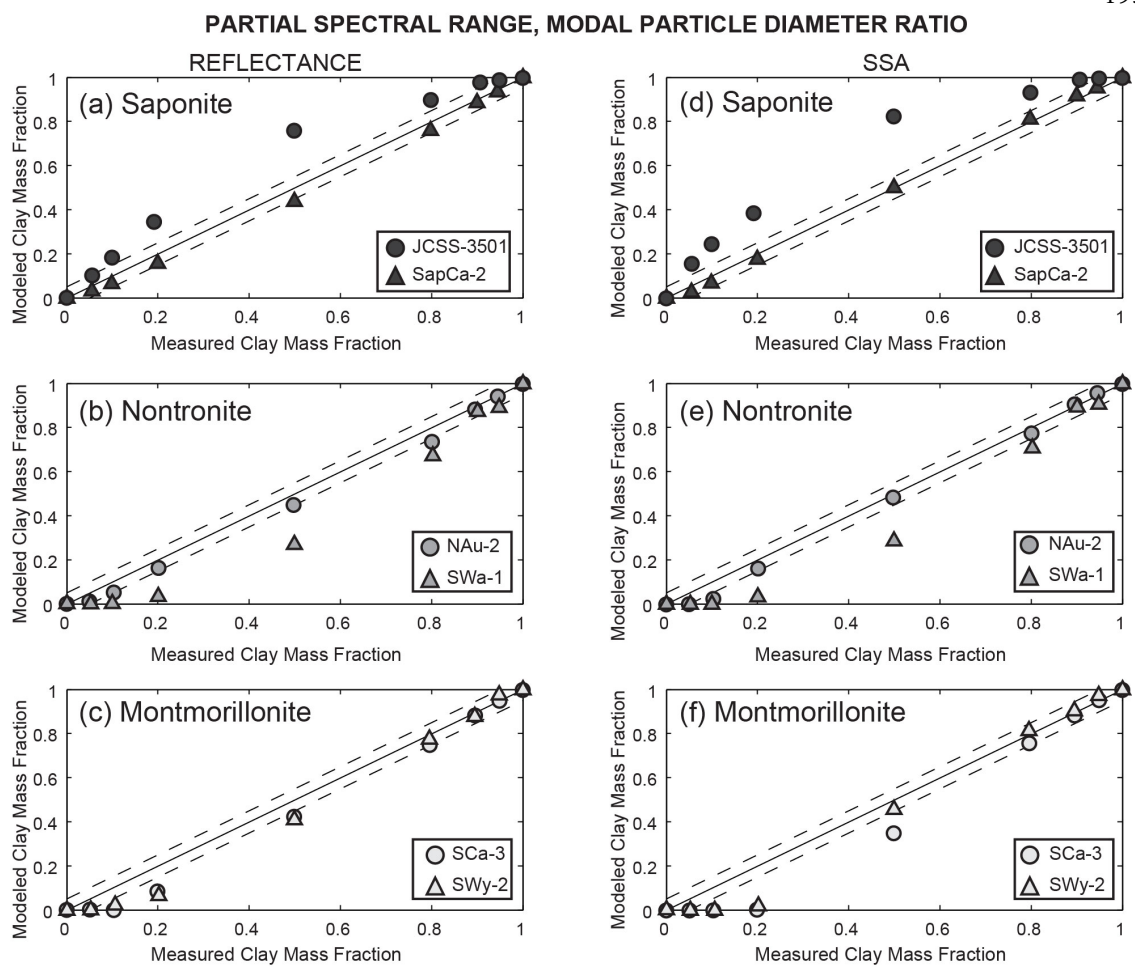


Figure 4.18

PARTIAL SPECTRAL RANGE, OPTIMIZED PARTICLE DIAMETER RATIO

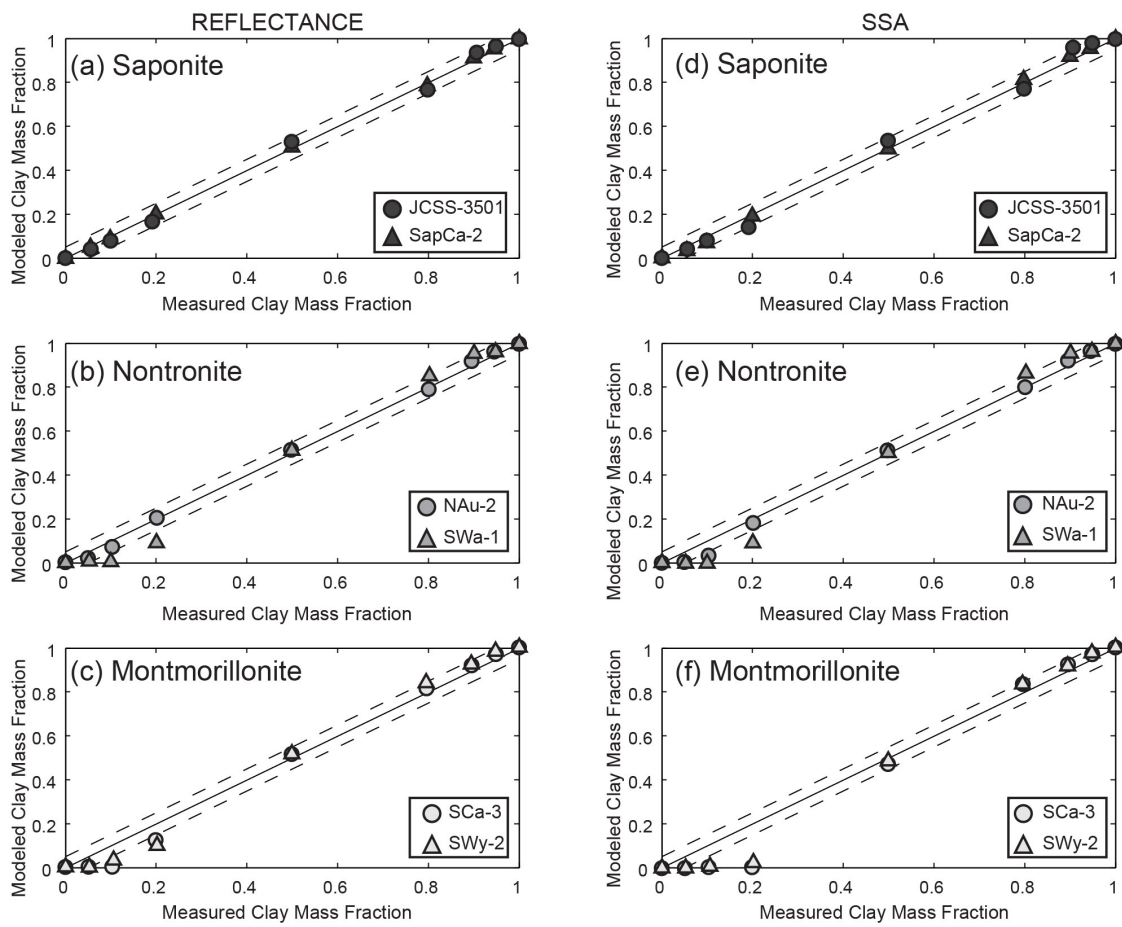


Figure 4.19

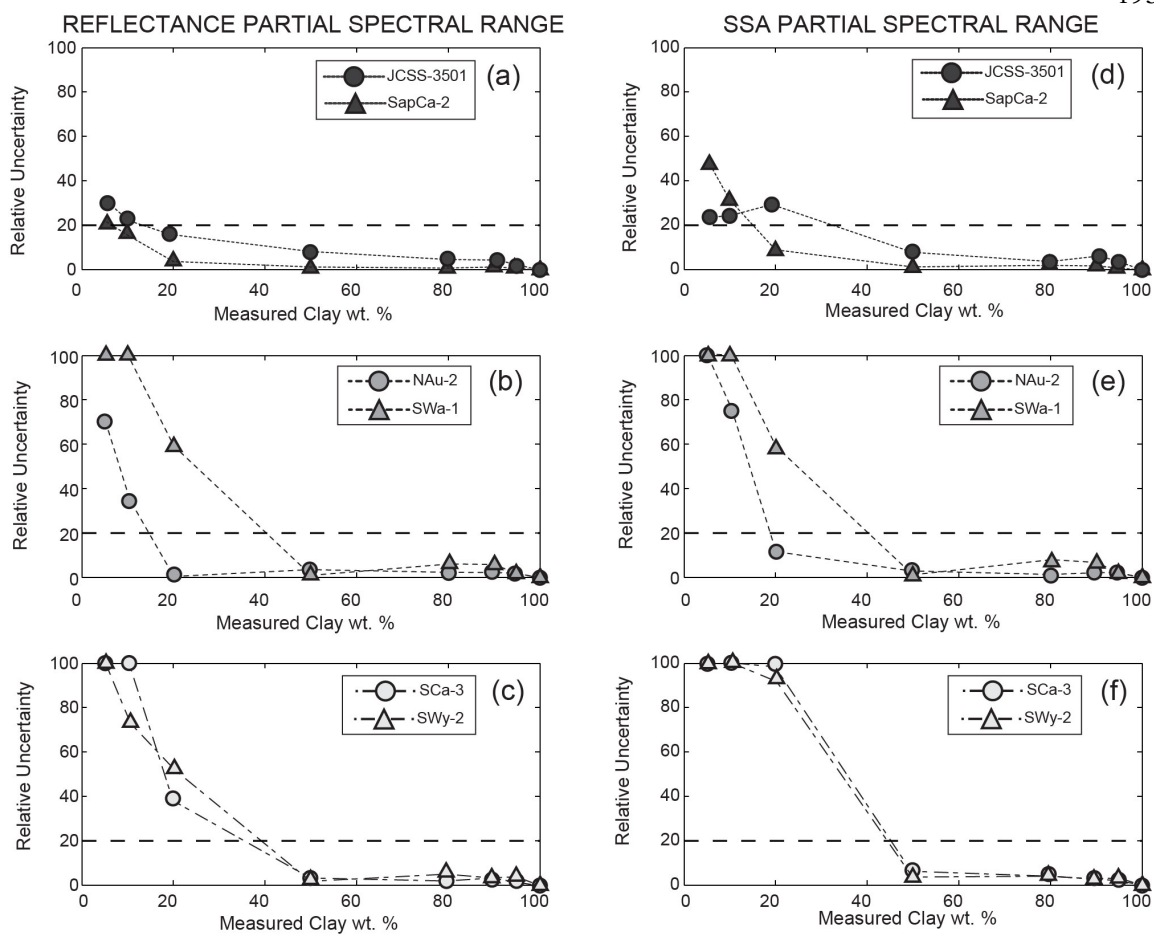


Figure 4.20

**DIAGENETIC ORIGIN OF NODULES IN THE SHEEPBED MEMBER,
YELLOWKNIFE BAY FORMATION, GALE CRATER, MARS**

Published:

Stack, K. M., J. P. Grotzinger, L. C. Kah, M. E. Schmidt, N. Mangold, K. S. Edgett, D. Y. Sumner, K. L. Siebach, M. Nachon, R. Lee, D. L. Blaney, L. P. Deflores, L. A. Edgar, A. G. Fairen, L. A. Leshin, S. Maurice, D. Z. Oehler, M. S. Rice, R. C. Weins (2014), Diagenetic origin of nodules in the Sheepbed member, Yellowknife Bay formation, Gale Crater, Mars, *Journal of Geophysical Research- Planets*.

Abstract

The Sheepbed member of the Yellowknife Bay formation in Gale crater contains mm-scale nodules that represent an array of morphologies unlike those previously observed in sedimentary deposits on Mars. Three types of nodules have been identified in the Sheepbed member in order of decreasing abundance: solid nodules, hollow nodules, and filled nodules, a variant of hollow nodules whose voids have been filled with sulfate minerals. This study uses Mast Camera (Mastcam) and Mars Hand Lens Imager (MAHLI) images from the Mars Science Laboratory Curiosity rover to determine the size, shape, and spatial distribution of the Sheepbed nodules. The Alpha Particle X-Ray Spectrometer (APXS) and ChemCam instruments provide geochemical data to help interpret nodule origins. Based on their physical characteristics, spatial distribution, and composition, the nodules are interpreted as concretions formed during early diagenesis. Several hypotheses are considered for hollow nodule formation, including origins as primary or secondary voids. The occurrence of concretions interpreted in the Sheepbed mudstone and in several

other sedimentary sequences on Mars suggests that active groundwater systems play an important role in the diagenesis of Martian sedimentary rocks. When concretions are formed during early diagenetic cementation, as interpreted for the Sheepbed nodules, they have the potential to create a taphonomic window favorable for the preservation of Martian organics.

5.1 Introduction

The Mars Science Laboratory (MSL) Curiosity rover spent the first year of its mission in Gale crater exploring the record of a Hesperian-aged [Grant *et al.*, 2014] fluvio-lacustrine environment at Yellowknife Bay (Figure 5.1a, [Grotzinger *et al.*, 2014]). In this embayment of bedded, fractured rock, the rover team examined the Yellowknife Bay formation, a 5 m thick assemblage of siliciclastic sedimentary rocks of bulk basaltic composition (Figure 5.1b, Grotzinger *et al.* [2014]). The basal member of the Yellowknife Bay formation, the Sheepbed member, is a mudstone containing nearly 30% saponitic smectite clay [Vaniman *et al.*, 2014], suggesting a sustained interaction between Sheepbed sediments and surface or pore fluids with a circum-neutral pH [McLennan *et al.*, 2014]. The uniformly fine-grained nature of the Sheepbed member and the lateral preservation of thin beds (1-2 cm) indicate an origin via suspension settling in a low-energy, lacustrine setting [Grotzinger *et al.*, 2014]. Evidence for neutral water chemistry, variable redox states, and high water activity sustained at the surface of Mars for potentially thousands of years indicates that the Sheepbed mudstone records a habitable environment [Grotzinger *et al.*, 2014].

The Sheepbed member contains a variety of diagenetic textures that suggests a complex post-depositional aqueous history for this sedimentary rock [Grotzinger *et al.*, 2014; McLennan *et al.*, 2014; Vaniman *et al.*, 2014]. Within this set of textures, Grotzinger *et al.* [2014] documented the presence of nodules, cf. “solid nodules” of this paper, hollow nodules, and a variety of hollow nodules that are filled with sulfate minerals, cf. “filled nodules” of this paper, in the Sheepbed member (Figure 5.2). Mastcam images taken between sols 126 and 303 revealed that solid nodules are present throughout the entire 1.5 m interval of the Sheepbed member examined by the rover team, and likely occur along at least 50 m of exposed outcrop as defined by the Wilson_Island target to the south and the Rowatt target to the north (Figure 5.1a). Hollow nodules and filled nodules were first observed in the Sheepbed member at the Selwyn section, and later in the vicinity of the John_Klein and Cumberland drill sites (Figure 5.1a). Solid, hollow, and filled nodules appear to be restricted to the Sheepbed member, and have not been observed in the overlying Gillespie Lake or Glenelg members [Grotzinger *et al.*, 2014]. Grotzinger *et al.* [2014] interpreted all nodule types as diagenetic concretions, and hypothesized that the hollow nodules formed when very early diagenetic fluids precipitated concretionary rims around gas bubbles trapped in the unlithified, uncompacted Sheepbed sediments. Filled nodules were interpreted as evidence for a later stage of diagenesis in which Ca-sulfate precipitated within the primary voids of some hollow nodules [Grotzinger *et al.*, 2014]. The presence of iron-bearing minerals, i.e., magnetite and akaganeite, in the Cumberland drill sample of a nodule-rich area of the Sheepbed outcrop led Vaniman *et al.* [2014] and McLennan *et al.* [2014] to propose a possible link between nodule formation and iron-bearing compounds.

This study builds on the work of *Grotzinger et al.* [2014] and *McLennan et al.* [2014] by presenting a quantitative analysis of the size, shape, and spatial distribution of Sheepbed member nodules. These observations are used to test potential nodule origins, and will be used to show that a diagenetic concretionary origin is the most parsimonious explanation for the Sheepbed nodules. Nodule size and shape measured with Mars Hand Lens Imager (MAHLI) images are used to understand petrophysical and compositional properties of the Sheepbed sediments and the relative timing of nodule formation. Lateral and vertical distributions of nodules measured in Mastcam mosaics provide insight into fluid availability and cm-scale heterogeneities in the Sheepbed sediments at the time of nodule formation, as well as the relationship between nodules and other diagenetic features observed in the Sheepbed mudstone. Geochemical data from the Alpha Particle X-Ray Spectrometer (APXS) and ChemCam Laser Induced Breakdown Spectrometer (LIBS) provide additional constraints on models for nodule growth. Understanding the origin and distribution of the nodules in the Sheepbed member is essential for assessing the aqueous history of the Yellowknife Bay formation, the potential habitability of Gale crater, and the significance of aqueous diagenesis in the Martian sedimentary rock record.

5.2 Data and Methods

5.2.1 Nodule Classification and Nomenclature

Nodules were defined by *Grotzinger et al.* [2014] as “millimeter-scale protrusions of the outcrop with 3D differential relief suggesting crudely spherical geometries,” while hollow nodules were defined as “millimeter-scale circular rims with hollow centers.” Filled hollow nodules were described by *Grotzinger et al.* [2014] as circular rims surrounding an

interior of sulfate, and were interpreted as hollow nodules that had been filled by Ca-sulfate during a later phase of diagenesis.

This study also recognizes three types of nodules, but employs a slightly modified version of *Grotzinger et al.* [2014] nomenclature to describe the nodule types observed in the Sheepbed member. In this study, the term “nodule” is used in a generic way to refer to all features in the Sheepbed that are millimeter-scale, generally spheroidal protrusions from the outcrop. Nodules that exhibit no discernable interior structure and are defined exclusively by external shape, size, and relief are referred to as solid nodules (Figure 5.2a). Solid nodules described herein are equivalent to *Grotzinger et al.* [2014] “nodules.” Nodules that exhibit internal structure are classified here as either hollow nodules or filled nodules. As in *Grotzinger et al.* [2014], hollow nodules are nodules whose interiors are exposed, showing a central void surrounded by a circular raised rim (Figure 5.2b and 5.2c). Filled nodules are defined here as nodules containing two distinct phases within their interior, a circular raised rim similar in appearance to the host rock and a sulfate mineral-filled interior (Figure 5.2d and 5.2f), and are equivalent to *Grotzinger et al.* [2014] sulfate-filled hollow nodules.

5.2.2 MAHLI

MAHLI is a 2-megapixel camera mounted on the Curiosity rover arm capable of imaging subjects at working distances between 2.1 cm and infinity at a maximum resolution of $\sim 14 \mu\text{m}$ [*Edgett et al.*, 2012]. The sizes of individual solid, hollow, and filled nodules were measured in 20 MAHLI images obtained between sols 150 and 291 (Figure 5.3 and Table 5.1). The MAHLI images used in this study were acquired at working

distances between 2.8 and 11.2 cm, resulting in image resolutions ranging from 16.7 to 46.3 $\mu\text{m}/\text{pixel}$ (Table 5.1). Of the 20 MAHLI images used in this study, half were planned by the MSL science team with the express purpose of targeting nodule-bearing portions of the Sheepbed outcrop. The other 10 images were acquired for other purposes, but happen to contain nodules. For each MAHLI image, nodules in the imaged scene were first identified and classified as solid, hollow, or filled. Then the two-dimensional outline of each nodule was traced manually using ArcGIS software (Figure B1). Individual traces were converted to circles using the minimum bounding geometry algorithm in ArcGIS to obtain a diameter for each feature. These data were used to calculate size statistics, make histograms, and to compare rim thickness and interior void diameter of hollow nodules (Figures 5.4 and 5.5 and Table 5.2). Diameters were also used to estimate areal concentration, C , of each nodule type within the outcrop covered by each MAHLI image using the formula of *McLennan et al.* [2005]:

$$C = \pi n d^2 / 6A \quad (5.1)$$

where n is the number of features on an assumed planar rock surface with area A , and d is the mean diameter of these features (Table 5.1).

Calculating nodule diameter using the minimum bounding geometry assumes that each nodule is spherical, and thus yields circular cross sections. To test this assumption, diameter traces were also fit to a rectangle by width using the minimum bounding geometry in ArcGIS. This algorithm provided two perpendicular axes for each rectangular

fit, and permitted calculation of an aspect ratio (*AR*) for each nodule (Table 5.2). Nodule shapes were classified according to *Blatt et al.* [1972] and *McBride et al.* [1999], who describe features with aspect ratios less than 1.5:1 as equant or circular, while those with aspects greater than 2.5:1 are elongate. Those of intermediate aspect between 1.5:1 and 2.5:1 are considered subequant or subcircular.

Wilcoxon rank sum testing in MATLAB was used to determine whether the size and shape of one type of nodule is statistically similar or distinct from the other nodule types. The Wilcoxon rank sum test tests the null hypotheses that the diameters and aspect ratios of two nodule types are sampled from continuous distributions with equal medians (Table 5.3). This test assumes that the two samples are independent, but does not require the samples to follow a normal distribution because it tests for equal medians, not means. The null hypothesis is rejected at a 5% significance level (significance probability, p , < 0.05).

5.2.3 Mastcam

Images of the Sheepbed outcrop taken with the focusable M-100 (100 mm fixed focal length) camera mounted on the rover mast were mosaicked to facilitate mapping of the lateral and vertical distributions of nodule types (Figure 5.6). The four mosaics (John Klein, Cumberland 1, Cumberland 2, and Raised Ridges and Nodules) used in this study to map the lateral distribution of nodules, i.e., within the same stratigraphic level, were acquired in the nearfield workspace area of the rover, and cover relatively flat, wind-exposed outcrop surfaces of the Sheepbed mudstone (Figures 5.6 and Figures 5.7-5.10). Because the M-100 camera was pointed nearly downward during image acquisition,

mosaics were projected to a viewing geometry normal to the outcrop surface so that the mosaic resolution, 0.1 mm/pixel, was constant across the mosaic. These projections resulted in minimal feature distortion and permitted quantification of nodule distribution.

For each of the four mosaics, nodules were manually tabulated by point counting in ArcGIS software after the mosaics were enhanced in contrast and brightness to enable feature identification. Since much of the Sheepbed member is thinly, but variably, coated with dust, distinguishing hollow nodules from filled nodules was sometimes difficult at the mosaic resolution (0.1 mm/pixel). Distinguishing hollow/filled nodules from solid nodules was also challenging when hollow and filled nodule interior diameters approached the mosaic resolution. As a result, hollow and filled nodules were point counted together, and are likely underrepresented relative to solid nodules. The point counts of solid and hollow/filled nodules were then used to create concentration maps in ArcGIS (Figures 5.7-5.10), and to calculate average nearest neighbor statistics using the ArcGIS Spatial Statistics Toolbox (Table 5.4). The Average Nearest Neighbor tool measures the average distance between a feature and its nearest neighbor, and compares this value with the expected average distance for features that are randomly distributed. If the ratio of measured distance to expected distance is less than one, the features exhibit clustering. If the ratio is greater than one, the features are dispersed. The null hypothesis that the features are distributed randomly is rejected at a 5% significance level.

The vertical distribution of solid and hollow/filled nodules, i.e., across stratigraphic intervals, within the Sheepbed member was also examined in two spherically projected mosaics (Selwyn and Yellowknife Bay Egress) produced by Malin Space Science Systems, both targeted near an area of the Sheepbed informally named the Selwyn section (Figures

5.6 and 5.12 and 5.13). These mosaics could not be vertically projected or georectified without significant distortion or loss of image resolution, so the pixel scale of these mosaics differs throughout the image scene. As a result, nodule distributions illustrated in these mosaics are qualitative, rather than quantitative, and nearest neighbor statistics were not calculated.

5.2.4 APXS

APXS elemental data were acquired for 17 individual rock targets spanning 1.5 m of the Sheepbed member stratigraphic section over Sols 129 to 271. All analyses were conducted on non-brushed rock surfaces, which were variably coated by fine dust. Two of these targets (including Wernecke) were also analyzed after brushing with the Dust Removal Tool (DRT; *Anderson et al. [2012]*). Six APXS targets have nodules visible within the APXS field of view (FOV) in corresponding MAHLI images (Figure 5.14a-b). For these six targets, elemental ratios were plotted against nodule abundance within the APXS FOV to help identify trends indicative of nodule composition (Figure 5.14a-b). To quantify the nodule abundance in the APXS field of view, MAHLI image contrast was enhanced with Adobe Photoshop, and ImageJ was used to find the fraction of the area containing visible nodules.

5.2.5 ChemCam

ChemCam [*Wiens et al., 2012; Wiens et al., 2013*] was also used to assess compositional differences between the nodules and host Sheepbed mudstone. Two types of observations were made with ChemCam. The first strategy involved a comparison between

the average composition of the Sheepbed member and the composition of areas enriched in nodules (Table 5.5). In this case, the 30 shots fired at each LIBS location have the potential to record a difference in composition related to the presence of nodules. A total of 128 ChemCam LIBS shot sites in areas with a high concentration of nodules were selected: DT-RP5 (sol 166), Kazan (sol 187, 274), Cumberland (sol 187, 274, 275), Rae (sol 189, sol 192), Ruth (sol 232), and Duluth (sol 292). These observations were compared to 354 other shot sites that visually appear to have analyzed pure mudstone. Quantification of ChemCam data utilized a partial least square (PLS) method corresponding to a comparison of multiple emission lines of each major element with a laboratory database performed on Earth (see *Wiens et al.* [2013]). A second ChemCam strategy utilized depth profiles that correspond to an intense burst of 150 to 600 shots laser shots at a single location. Whereas 30 shots can penetrate several tens of μm in the softest rocks, 150 shots likely penetrates $>100 \mu\text{m}$ [*Wiens et al.*, 2012]. The ChemCam observation DT-RP5 (sol 166) consisted of four locations with 150 shots each in a nodule-rich area near the John Klein drill hole (Figure 5.15).

5.3 Shape and Size Distributions

5.3.1 Solid Nodules

A total of 1729 solid nodules embedded in the outcrop were identified and measured in 20 MAHLI images of the Sheepbed member. Mean solid nodule diameter is 0.80 mm, with a minimum measured diameter of 0.20 mm and a maximum diameter of 4.11 mm (Table 5.2). The size-frequency distribution of solid nodule diameters is positively skewed around a mode of 0.5 mm (Figure 5.4a). For diameters larger than this

mode, frequency decreases as solid nodule diameter increases, following a lognormal distribution. The areal concentration of solid nodules varies from target to target, ranging from 0.2% at Ekwir_1 to 4.3% at Persillon (Table 5.1). The overall areal concentration of solid nodules is 1.8%, obtained by averaging all 20 MAHLI target concentrations.

Solid nodules are generally circular in cross-section, with an average measured aspect ratio of 1.2 (Table 5.2). Of the 1729 solid nodules measured, 1574 (91%) are circular ($AR < 1.5:1$), 153 (9%) are subcircular circular ($1.5:1 > AR < 2.5:1$), and only 2 (0.1%) are elongate ($AR > 2.5:1$). Solid nodules are generally circular or subcircular whether exposed on horizontal, i.e., Wernecke_3 (Figure 5.2f) or vertical, i.e., Persillon (Figure 5.2a) exposures, and appear to exhibit spherical rather than prolate or oblate spheroidal shapes. Solid nodules do not exhibit any internal lamination, and are not observed to contain through-going laminae. In the few intervals where intercalated beds do occur within the Sheepbed, solid nodules do not appear to influence or be influenced by bedding. Individual solid nodules are generally isolated within the matrix, but in some areas of particularly high nodule concentration, e.g., Persillon, agglutinated solid nodules (twins, triplets, and even sextuplets) are not uncommon (Figure 5.2a).

5.3.2 Hollow Nodules

513 hollow nodules were identified in the MAHLI image set (Table 5.1). Although hollow nodules are generically defined as protrusions whose interiors are exposed, showing a central void surrounded by a circular raised rim, a range of hollow nodule morphologies was observed in the MAHLI images. Some hollow nodules were characterized by prominent, positive relief rims and subtle interior voids that appeared as dimples or slight

impression in the center of the nodule (Figure 5.2b-c), while other hollow nodules are characterized by empty bowl-like voids and more subtle positive relief rims (Figure 5.2e and 5.2f). Still other hollow nodules exhibit morphologies intermediate between bowl and dimple-like voids. A variety of hollow nodule morphologies co-exist within the individual MAHLI image scenes and do not appear to be spatial segregated in a systematic way. As such, combined size and shape measurements for all hollow nodules morphologies are reported below.

The mean hollow nodule diameter is 1.35 mm (Table 5.2), and diameters range from 0.29 mm to 5.40 mm. A histogram of diameter frequency (Figure 5.4b) shows a nearly Gaussian distribution between 0-2.5 mm centered on a mode just greater than 1 mm, but the infrequent occurrence of hollow nodules greater than 2.5 mm gives the distribution a positive skew. The areal concentration of hollow nodules varies from target to target (Table 5.1): Autridge has the lowest concentration of hollow nodules at 0.2%, while Cumberland_DRT has the highest concentration at 3.1%. Average areal concentration for all MAHLI target images containing hollow nodules (excludes Yukon) is 1.4%. The average aspect ratio measured for hollow nodules is 1.17 (Table 5.2), suggesting that these features are generally circular in cross-section. Of the 513 hollow nodules measured, 501 (98%) are circular ($AR < 1.5:1$) while 12 (2%) are subcircular ($1.5:1 < AR > 2.5:1$). None are considered elongate.

The average diameter of preserved void space within the hollow nodules is 0.86 mm ($n = 513$) (Table 5.2), ranging from 0.16 mm to 4.13 mm. As with external diameters, preserved voids show a nearly Gaussian distribution (Figure 5.4d) between 0-1.5 mm, centered around a mode just less than 1 mm. The low frequency occurrence of hollow

nodule interiors greater than 2 mm gives the distribution a positive skew. The average aspect ratio measured for hollow nodule interiors is 1.24 (Table 5.2), suggesting that interior voids are generally circular in cross-section. Of the 513 hollow nodule interiors measured, 471 (92%) are circular ($AR < 1.5:1$), 39 (8%) are subcircular ($1.5:1 < AR > 2.5:1$), and 3 interiors (.6%) are considered elongate ($AR > 2.5:1$).

Rim thickness was calculated for each hollow nodule by determining the difference between external and interior diameters, then dividing by two. This method assumes a circular cross-section and that the interior hollow is perfectly centered within the nodule. This is clearly not the case for every hollow nodule, but this calculation provides a reasonable estimate for hollow nodule rim thickness. In the Ekwir_1 target image (Figure B1), not all nodules identified as hollow nodules have rims as a result of erosion and abrasion of the rock surface by the DRT brush bristles. As a result, the 22 hollow nodules whose rims are no longer identifiable are not included in the histogram of rim thickness. The average rim thickness estimated from 491 hollow nodules is 0.25 mm (Table 5.2), ranging from 0.01 mm to just larger than 1 mm. Rim thickness values also follow a Gaussian distribution between ~ 0.02 mm and 0.6 mm, with a mode just greater than 0.2 mm (Figure 5.4e). The distribution as a whole exhibits a slight positive skew due to the presence of several rims thicker than 0.6 mm. A plot of interior hollow diameter versus rim thickness (Figure 5.5a) shows a linear relationship where increasing interior hollow diameter results in increasing rim thickness with a slope of 0.14. The linear regression model finds this slope to be significant and non-zero despite the large amount of scatter in the data. It was suspected that the two largest interior hollow diameters around 4 mm might be exerting disproportionate influence on the linear fit, but removal of these two points still

resulted in a statistically significant, non-zero slope for the linear model, suggesting that rim thickness scales with hollow interior diameter (Figure 5.5b).

5.3.3 Filled Nodules

Only 30 filled nodules were identified in the 20 MAHLI images listed in Table 5.1. There are a variety of irregularly-shaped white blebs observed in the Sheepbed outcrop, but only those with identifiable raised rims were tabulated as filled nodules. This distinction permits the possibility that secondary porosity could have resulted from fluid migration associated with reprecipitation of calcium sulfate. As noted by *Grotzinger et al.* [2014], filled nodules are usually associated with thin, hairline, mineralized veins that extend radially outward from the raised rim and connect with larger calcium sulfate filled fractures (Figure 5.2e and 5.2f). The mean diameter of filled nodules is 2.75 mm, ranging from 1.18 mm to up to 5.15 mm. The small number of filled nodules makes it difficult to interpret size trends, although there appears to be a general decrease in filled nodules with increasing diameter (Figure 5.4c). The average areal concentration calculated from 11 MAHLI images containing filled nodules is 0.7%, although minimum areal concentration is as low as 0.1% for Brock_Inlier, Autridge, and Cumberland_DRT and as high as 2.2% for Persillon and Drill_RP (Table 5.1). The average aspect ratio measured for hollow nodule interiors is 1.16, suggesting that these features are generally circular in cross-section. Of the 30 hollow nodule interiors measured, 29 (97%) are circular ($AR < 1.5:1$), and only 1 (3%) is subcircular ($1.5:1 < AR > 2.5:1$).

5.3.5 Statistical Testing

The results of Wilcoxon rank sum testing are presented in Table 5.3. The null hypothesis that two data sets represent samples from a continuous distribution with equal medians is rejected at a 5% significance level or smaller for all permutations of diameter and aspect ratio comparisons except for one, which compares hollow nodule versus filled nodule aspect ratios. These results suggest that solid nodules and hollow nodules are distinct from each other in size and shape, but that hollow nodules and filled nodules likely originate from distributions with equal aspect ratio medians.

5.3.6 Summary

Three types of nodules are present in the Sheepbed member in order of decreasing abundance: solid nodules, hollow nodules, and filled nodules. Solid nodules outnumber hollow nodules in the MAHLI image set by a factor of three, and only 30 filled nodules were observed. Although all nodule types are generally circular in cross-section and mm-scale, statistical testing of solid nodule and hollow nodule diameter and aspect ratio confirm that these two nodule types are statistically different in size and shape. Mean hollow nodule diameter is larger than mean solid nodule diameter and the diameter histograms of these two features are distinct; solid nodule diameters appear to follow a lognormal distribution, while the hollow nodule diameters are normally distributed. Hollow and filled nodules show statistically significant differences in size, but the shape of these two nodule types are statistically indistinguishable. Lastly, there is a statistically significant relationship, despite a large amount of scatter, between hollow nodule rim thickness and the diameter of hollow nodule interior voids.

5.4. Spatial distribution

5.4.1 *Lateral Distribution*

Solid, hollow, and filled nodules are well exposed on relatively flat, bedding plain surfaces of the upper Sheepbed member in the vicinity of the John_Klein and Cumberland drill sites (Figure 5.3b). Four Mastcam mosaics of these surfaces illustrate the lateral distribution of solid nodules and hollow/filled nodules in the Sheepbed member (Figure 5.6).

5.4.1.1 John Klein Drill Site

The John Klein drill site was imaged by the M-100 camera on sol 166 (Figure 5.7). Solid nodule and hollow/filled nodule point counts of this mosaic reveal that solid nodules and hollow/filled nodules occur across the image scene, albeit in variable concentrations, except in the immediate vicinity of a small network of raised ridges, 5-10 cm long mineralized and spindle-ended fractures, in the top part of the mosaic (Figure 5.7a). The solid nodule concentration map (Figure 5.7c) shows several areas of very high concentration in the right part of the mosaic (>12 nodules/cm 2), while the majority of the image scene exhibit relatively medium to low concentrations (<7 nodules/cm 2). The highest concentration of solid nodules, the two red zones in the upper right corner of the image where concentrations are between 15-19 solid nodules/cm 2 , occur along an elongate, sublinear raised feature \sim 30 cm in length that trends from the upper right to lower left. Solid nodules in this area are generally smaller (<1 mm in diameter) than those present in regions of lower concentration. Similarly, the highest concentration of hollow/filled nodules (1.7-2.7 nodules/cm 2) occurs in a small patch located in the lower left corner of the

image (Figure 5.7d). Hollow/filled nodule concentrations across the scene range between 0.3-1.7 nodules/cm². Hollow and filled nodules are conspicuously absent from regions containing raised ridges (Figure 5.7d). An intermediate concentration of hollow/filled nodules (0.6-1.7 nodules/cm²) occurs on the right side of the mosaic, coincident with the highest concentration of solid nodules. In the vicinity of the actual John_Klein drill hole, solid nodule concentration is 3.8-5.3 nodules/cm² and hollow/filled nodule concentration is 0.6-1.7 nodules/cm².

Average nearest neighbor statistics (Table 5.4) reveal that both nodules and hollow/filled nodules are clustered in the outcrop surface, rather than occurring in a random or dispersed pattern. This means that the ratio of measured distance between nodules to expected distance for nodules that are randomly distributed is less than one. The observed mean distance between solid nodules is 2.3 mm, which is smaller than the expected mean distance of 3.2 mm for a hypothetical random distribution, and the observed mean distance between hollow/filled nodules is 4.9 mm, which is smaller than the expected distance of 7.8 mm for a random distribution.

5.4.1.2 Cumberland Drill Site

Mastcam mosaics taken by the M-100 camera on sols 185 (Cumberland 1) and 275 (Cumberland 2) (Figures 5.8 and 5.9) cover the Cumberland drill location and surrounding region. The concentration map of the Cumberland 1 mosaic reveals an area of particularly high solid nodule (10-12 nodules/cm²) and hollow/filled nodule (2-3 nodules/cm²) concentration in the lower left corner of the mosaic (Figure 5.8c). This region corresponds with an area that appears slightly raised compared to the broader surface, and may

represent a region of enhanced resistance from erosion resulting from the high concentration of nodules. The area just below and to the right of this high concentration area contains few nodules (Figure 5.8c and 5.8d). Solid nodules do not occur in concentrations higher than 5-6 nodules/cm² across the rest of the image, but there are several areas of relatively high hollow/filled nodule concentration (1-2 nodules/cm²) along the flagstone edge on the right side of the mosaic (Figure 5.8d).

The Cumberland 2 mosaic (Figure 5.9) includes the Cumberland drill site, chosen for its apparent high concentration of hollow nodules. However, the hollow/filled nodule concentration in the vicinity of the actual drill hole is 0.3-0.7 nodules/cm² (Figure 5.9d), an intermediate to low concentration according to the concentration map; the highest concentration of hollow/filled nodules occurs in the upper left portion of the mosaic (0.7-1.4 nodules/cm²). The rest of the mosaic contains a fairly low concentration of hollow/filled nodules (0-0.7 nodules/cm²), especially in the area just below the Cumberland drill area on the Mastcam image. The solid nodule point count (Figure 5.9c) shows the highest concentration (4-7 nodules/cm²) in a linear pattern trending from the upper left to the lower right in the upper-right portion of the mosaic. Besides this area of relatively high solid nodule concentration, most of the mosaic contains a low concentration of solid nodules (< 2 nodules/cm²).

Average nearest neighbor statistics reveal that the distribution of solid nodules and hollow/filled nodules in the Cumberland mosaics, as with the John Klein site, is clustered (Table 5.4). For both Cumberland mosaics, the observed mean distance between solid nodules and hollow/filled nodules, respectively, is smaller than the expected mean distance for a hypothetical random distribution.

5.4.1.3 Raised Ridges and Nodules

The Raised Ridges and Nodules mosaic taken by the M-100 camera on sol 164 (Figure 5.6) was chosen to explore the spatial distribution of nodules with respect to a network of raised ridges. Point counting reveals that solid nodules and hollow/filled nodules are present around and between some of the more sparsely distributed raised ridges, but there are few, if any, nodules where the network of raised ridges is relatively dense (Figure 5.6c and 5.6d). Hollow/filled nodules are particularly sparse in these regions (Figure 5.6d). As with several of the mosaics, the areas of highest solid nodule concentration (containing between 10-12 nodules/cm²) generally contain smaller nodules (<1 mm) than those areas with lower concentrations.

Average nearest neighbor statistics reveal that the distributions of solid nodules and hollow/filled nodules in this mosaic are clustered, as opposed to random or dispersed (Table 5.4). The observed mean distance between solid nodules is 2.5 mm, which is smaller than the expected mean distance of 3.3 mm. The observed mean distance between hollow/filled nodules is 7.2 mm, which is smaller than the expected distance of 1.1 cm.

5.4.2 Vertical Distribution

The vertical distribution of nodules is best observed at a 0.5 m thick exposure of the Sheepbed member, informally named the Selwyn section, located ~5 m southwest of the John_Klein drill site (Figures 5.1 and 5.6). Here the rover traversed the most vertically complete section of the Sheepbed mudstone from sols 150-167 and again on sols 296-300 during the exit from Yellowknife Bay.

5.4.2.1 Selwyn

The Selwyn mosaic, obtained by the M-100 camera on sol 159, shows a ~15 cm thick interval of the 50 cm thick Selwyn section (Figures 5.11 and 5.12). This mosaic captures an irregular boundary defined, in part, by a poorly developed raised ridge and a high concentration of large hollow nodules and filled nodules (Figure 5.11a). *McLennan et al.* [2014] also identified this boundary as a compositional distinction between the “lower” and “upper” parts of the Sheepbed member. Stratigraphically lower strata exhibit lower and more variable $\text{TiO}_2/\text{Al}_2\text{O}_3$ and less Ni than the stratigraphically higher interval, suggested to represent a subtle change in provenance [*McLennan et al.*, 2014]. Below this boundary the Sheepbed member is distinctly red in color (although this likely results from the distribution of windblown dust) and contains abundant large nodules greater than 1 mm in diameter (Figure 5.11b). The upper Sheepbed appears gray in color and contains nodules generally less than 1 mm in diameter (Figure 5.11d versus Figure 5.11b). Although the nodules in the stratigraphically lower part are larger and more conspicuous, the highest concentration of nodules actually occurs in the upper Sheepbed, where several irregular patches of very small (< 1 mm) solid nodules and hollow/filled nodules occur (Figure 5.12c). Hollow/filled nodules are concentrated at the boundary between the upper and lower Sheepbed and in a patch of large, dense nodules on the left side of the mosaic (Figures 5.11c and 5.12d). This mosaic also contains a large number of loose pebbles accumulated in cracks and on the outcrop surface. Upon close inspection, many, but not all, pebbles contain small dimples or depressions, suggesting that they are eroded remnants of hollow nodules.

5.4.2.2 Yellowknife Bay Egress

An M-100 mosaic obtained on sol 298 shows the Sheepbed-Gillespie Lake contact as imaged during Curiosity's egress from Yellowknife Bay (Figure 5.13). This section occurs approximately 2 m to the southwest of the Selwyn section and mcam00864 (Figures 5.6 and 5.13). The mosaic covers a 35 cm-thick interval of the Sheepbed member, although the lower portion of the outcrop is discontinuous and the blocks near the bottom of the image may be out of place. Solid nodules are present throughout the section, but hollow/filled nodules are sparse in this part of the Sheepbed member. Solid nodules are largest (~1 mm) and most clearly observed in a ~10 cm thick interval near the center of the mosaic that is pervasively cut by mineralized white veins. However, the highest concentration of solid nodules occurs in two small, irregularly shaped patches just below the Sheepbed-Gillespie boundary. Solid nodules in these patches are smaller (< 1 mm) than solid nodules present elsewhere in the mosaic.

5.4.3 *Summary*

The six Mastcam maps presented here show that solid and hollow/filled nodule distributions are patchy and statistically clustered both laterally and vertically throughout the examined portions of the Sheepbed member. Solid nodules outnumber filled/hollow nodules by factors of 4 to 20 in the Mastcam mosaics examined in this study, although there is likely some bias towards solid nodule identification resulting from the lower resolution of the Mastcam mosaics (Figures 5.7-5.13). Different nodule types co-exist throughout these outcrops, but areas of highest solid nodule concentration do not always coincide with areas of highest hollow/filled nodule concentration. Solid nodules and

hollow/filled nodules, in particular, are not present in high concentrations in the immediate vicinity of dense raised ridge networks.

5.5 Chemical Composition of the Sheepbed Nodules

5.5.1 APXS

Nodules (solid, hollow, and filled tabulated together) account for ~2 to 17% of the area analyzed by APXS within the instrument FOV at the six nodule-bearing targets (Figure 5.14). There is no apparent correlation between the abundance of nodules and most elemental abundances, such as Si, Al, or S. However, there is an apparent correlation between nodule abundance and FeO* (in which FeO* assumes all Fe is present as FeO) and MnO concentration in nodule-bearing targets, particularly when these oxides are ratioed (Figure 5.14c). This correlation suggests that precipitation of Fe-oxide may have been involved in nodule formation. Possible iron-bearing cementing minerals are magnetite (Fe_3O_4), present as 3.8 and 4.4 wt. % of the John Klein and Cumberland drill powders, respectively [Vaniman *et al.*, 2014], or akageneite ($\text{Fe}^{3+}\text{O}(\text{OH},\text{Cl})$), observed at 1.1 and 1.7 wt. % in the John Klein and Cumberland drill powders, respectively. However, the APXS data show no obvious correlation between Cl and nodule-bearing areas, as might be expected for akageneite. Hematite is present in the drill samples at or near the detection limit of the CheMin instrument (0.6 wt. % in John Klein, 0.7 wt. % in Cumberland), so hematite is not considered to be the likely cementing mineral given the abundance of nodules within the Sheepbed member. An important caveat of the iron enrichment observed in APXS analyses of nodule-bearing targets is the high degree of variability that exists in the FeO*/MnO of nodule-free rock targets, which

may be related to stratigraphic variations in rock composition [McLennan *et al.*, 2014], such as from disseminated Fe-oxides within the mudstone matrix. The rock targets Bonnet Plume and nodule-free Nastapoka both have a darker appearance and FeO^*/MnO ratios between 80 and 100 (Figure 5.14) consistent with this interpretation.

5.5.2 *ChemCam*

During the ChemCam depth profile experiment at targeted observation DT-RP5, the laser hit filled nodules in the three first locations of the 2x2 depth profile array, although contact was only on the filled nodule edge for points 1 and 3. In contrast, the second location shows a clear ablation hole coincident with a nodule center (Figure 5.15). ChemCam data on locations 1 and 3 do not show significant compositional variation beyond dust contamination in the first shots. Location 2, however, records distinct variations in Ca and Al (Figure 5.15c). Over a large number of shots, the plasma becomes progressively confined to the pit it creates, leading to a general decrease of the total emission, and an associated decrease of all element emission lines. This is observed in the case of location 2 for most emission lines (and illustrated for Fe and Ti in Figure 5.15), and no increase in H is detected that would suggest a specific hydrous phase. By contrast, Ca and Al emission does not drop along with the other elements, suggesting that these elements are enriched at depth, perhaps in the interior of the filled nodule. These small changes could be part of the natural variability of the overall rock, and it is a possibility that the ablation cavity was not deep enough to reach the interior of the nodule. Therefore, the depth profile experiment with ChemCam does not uniquely support a contrast between the composition of the mudstone and the composition of the nodules analyzed.

ChemCam data recorded in Table 5.5, which represents a comparison between nodule-free Sheepbed mudstone and the average of 128 nodule-bearing shot locations, suggests that the composition of the Sheepbed mudstone in nodule-rich areas is not distinct from the overall composition of the Sheepbed mudstone observed over the broader expanse of Yellowknife Bay. For instance, no enrichment in Fe is observed in the nodule-rich areas. Only minor differences exist between datasets, such as a slight depletion in the nodule-rich areas in Mg, and a slight enrichment in Ca. The latter could result from the presence of filled nodules containing Ca-sulfates [Grotzinger *et al.*, 2014; Nachon *et al.*, in revision].

In summary, these observations indicate that the filled nodules are indeed associated with calcium sulfate minerals, but do not help to identify a specific composition for the primary nodule-forming cement. ChemCam data show no enrichment in iron that could confirm the presence of magnetite, akaganeite, or other distinct Fe minerals.

5.5.3 Summary of Geochemical Results

APXS analyses presented here show that nodule-rich areas correlate with FeO* concentration, particularly when FeO* is ratioed with MnO. This correlation suggests that solid, hollow, and filled nodules may contain a higher concentration of an iron-bearing mineral than the host mudstone. These APXS results are consistent with the CheMin detection of the Fe-oxide minerals magnetite and akaganeite at the John_Klein and Cumberland drill sites [Vaniman *et al.*, 2014], although APXS cannot conclusively identify the specific iron-bearing mineral due to the potential contribution of dust to the analysis.

Unlike APXS, ChemCam does not detect any correlation between Fe and nodule abundance (Table 5.5), although this disparity is not unexpected given the difference in

analytical capabilities of the two instruments. The typical 30 shots that comprise a ChemCam analysis may not provide enough penetration ($<100\text{ }\mu\text{m}$) into the nodules to observe a conclusive elemental enrichment. In addition, the ChemCam depth profiles (150 shots, or $>100\text{ }\mu\text{m}$ penetration) have only locally penetrated the interiors of filled nodules whose compositions may not be representative of solid or hollow nodules. Although ChemCam data do not show an Fe-enrichment of the nodules indicated by both APXS and CheMin, they do suggest that compositional difference between the host mudstone and the nodules is quite subtle.

5.6. Discussion

5.6.1 Petrogenesis of Sheepbed Nodules

Several processes could result in mm-scale, spherical textural elements in Martian sedimentary rocks. Potential explanations for the Sheepbed nodules include accretionary sedimentary grains, impact or volcanic accretionary lapilli, impact or volcanic glass spherules, or diagenetic concretions [Grotzinger *et al.*, 2014]. Sheepbed nodules distinctly lack internal concentric growth bands, which eliminates an accretionary sedimentary origin as ooids or pisoids. Lack of concentric growth bands also suggests that an origin as volcanic or impact accretionary lapilli is unlikely. Fralick *et al.* [2012] distinguish impact accretionary lapilli deposits by the presence of ubiquitously-associated breccias deposited during ground movement and entrainment of debris in the leading edge of impact-induced base surges. No such deposits have been identified in the Sheepbed mudstone or any other member of the Yellowknife Bay formation. Furthermore, accretionary grains deposited in fluvial-lacustrine settings inferred for the Sheepbed member and overlying Gillespie Lake

member would be expected to exhibit hydraulic sorting or segregation of spherules by size; Sheepbed nodules and hollow nodules are neither graded nor concentrated.

An origin for the Sheepbed nodules as volcanic melt spherules is also unlikely. Volcanic melt spherules on Earth generally occur with other non-spheroidal particles [Simonson, 2003; Simonson and Glass, 2004], which is not supported by the strongly spherical aspect ratios of nodules in the Sheepbed member. An origin as impact spherules, spheroidal molten particles that form from the melting and vaporization of material during an impact [Simonson and Glass, 2004] may be more consistent with the characteristics of Sheepbed nodules. The Sheepbed nodules, like impact melt spherules, are dominantly spheroidal, less than 5 mm in diameter, and smaller nodules (1-2 mm) tend to be more spherical [Simonson and Glass, 2004]. The subtle chemical signature of the nodules makes it impossible to eliminate an impact spherule origin based solely on composition, as McLennan *et al.* [2005] did for the Meridiani hematite spherules. Furthermore, a generally diverse suite of internal structures commonly used to distinguish impact melt spherules cannot be used to evaluate the origin of Sheepbed nodules. However, it is unlikely that glassy spherules—of either volcanic or impact origin—would be preserved in outcrop given that aqueous conditions during or soon after Sheepbed deposition resulted in the near complete alteration of olivine to smectite clay minerals [Vaniman *et al.*, 2014].

Additionally, possible impact spherules have been identified in the modern Rocknest eolian sediments of Gale crater [Minitti *et al.*, 2013], and these spherules differ from nodules within the Sheepbed member in several important ways. Impact spherules documented within the Rocknest deposit are typically substantially smaller (ranging from 100-800 μm in diameter) than the nodules described here, and are distinctly spherical (with

aspect ratios indistinguishable from 1.0). Additionally, observed spherules preserve a glassy luster, which results in a uniform distribution of light reflection off of the grain surface. This is very different from the grainy texture of nodules within the Sheepbed mudstone. Finally, the impact spherules observed in Gale occur dominantly within unlithified surficial sediment [Minitti *et al.*, 2013], although there are several potential examples within coarser, well-lithified sandstone units [Newsom *et al.*, in revision]. Regardless, observed impact spherules appear sparsely distributed within Gale crater materials. In terrestrial examples, spherules commonly occur as discrete event beds that are laterally extensive and can remain undiluted by other detrital grains for hundreds to thousands of kilometers [Simonson, 2003; Fralick *et al.*, 2012]. This would be true especially for depositional facies originating from settling of grains from suspension, as inferred for the Sheepbed mudstone. Nodules in the Sheepbed member do not occur in distinct beds and are patchily distributed both vertically and horizontally throughout the outcrop, inconsistent with the characteristics of an impact spherule layer. Finally, impact spherules deposited in a potentially lacustrine environment should also show normal grading and uniform thickness [Fralick *et al.*, 2012]. The Sheepbed nodules and hollow nodules are neither graded nor present in beds of uniform thickness, so an origin as impact melt spherules is unlikely.

Precipitation of authigenic minerals from diagenetic pore fluids to form concretions is the most parsimonious interpretation for the origin of Sheepbed nodules. Their size, shape, distribution, and depositional setting are all consistent with concretion formation in fluid-saturated, fine-grained sediments, e.g., Chan *et al.* [2004], McLennan *et al.* [2005], and Calvin *et al.* [2008]. Also, the nearly ubiquitous coexistence of solid, hollow, and filled

nodules throughout the Sheepbed member suggests that these nodules share a common concretionary origin. Mechanisms of concretionary growth that can account for the full range of observed nodule morphology are explored further below.

5.6.2 Controls on Nodule Shape and Size

Solid, hollow, and filled nodules in the Sheepbed member reveal near-circular geometries in geometrically diverse outcrop exposure, indicating that all nodule types are predominantly spherical in three dimensions. Concretionary bodies generally form spherical shapes when cementing ions are supplied by diffusion to single-point nucleation sites [Bjørkum and Walderhaug, 1990; McBride *et al.*, 1994; McBride *et al.*, 1999; Chan *et al.*, 2004], as opposed to either diffusion to non-point nucleations or ion supply by advection, both of which tend to form elongate concretions. In the case of advection, elongate concretions provide a measure of the direction of fluid flow [Schultz, 1941; McBride *et al.*, 1994; Chan *et al.*, 2012]. Alternatively, spherical concretion growth has also been interpreted to result primarily from surface reactions, in which each unit surface area has the same growth rate during surface reaction-controlled growth [Bjørkum and Walderhaug, 1990; Raiswell, 1988]. Accordingly, the spherical shape of the Sheepbed nodules suggests that a combination of diffusion and/or mineral surface reactions influenced nodule cementation, but in the absence of either strongly oriented nucleation surfaces or groundwater flow.

The shape of concretions on Earth has also been linked to sediment permeability and variations in the local availability of cementing agents. Anisotropic permeability is thought to result in elongate and preferentially oriented concretions [Sorby, 1908; Deegan,

1971; *Gluyas*, 1984; *Dix and Mullins*, 1987; *Hudson and Andrews*, 1987; *Seilacher*, 2001;

Chan et al., 2012]. Oriented concretions can also form due to differential concentrations of cementing agents in the vertical or horizontal directions [Bjørkum and Walderhaug, 1990].

Since the Sheepbed nodules are generally spherical and do not appear to be preferentially oriented, the Sheepbed sediments were likely homogeneous at the scale of individual nodule sites, exhibiting local isotropic permeability and a uniform distribution of cementing ions.

Sediment and fluid properties can also influence concretion size [Chan et al., 2004]. The abundance of nodules in the Sheepbed member indicates a scenario in which a high density of nucleation sites formed within the sediments. However, the small mm-scale size of the nodules suggests that transport of fluids and/or diffusion of cementing ions to these nucleation sites may have been limited, perhaps by the low permeability of clay-rich Sheepbed sediments. Slight variations in the porosity and permeability of the upper and lower Sheepbed may explain the abundant growth of numerous small nodules (<1 mm) in the upper Sheepbed versus fewer but larger nodules (>1 mm) in the lower Sheepbed (Figures 11b, 11c, and 11d).

Measurements of solid and hollow nodule diameter and aspect ratio indicate that models for nodule growth should take into account size and shape statistics as well as morphological characteristics. Hollow nodule growth mechanisms should be consistent with the uniform size distributions of both whole hollow nodules and hollow nodule void interiors (Figure 5.4), as well as the subtle relationship between interior void diameter and hollow nodule rim thickness (Figure 5.5) which suggests that interior void generation is linked to the growth of hollow nodule rims.

Comparison between hollow and filled nodule size statistics is hindered by the small sample size of filled nodules, but Wilcoxon rank sum testing and the morphological similarities between hollow and filled nodules are consistent with *Grotzinger et al.*'s [2014] interpretation of filled nodules as hollow nodules that have been filled during later diagenesis. The size difference between hollow nodules and filled nodules suggests that larger hollow nodules may have been more susceptible to later diagenetic fracturing and fluid flow that led to the precipitation of sulfate minerals within hollow nodule interiors.

5.6.3 Controls on Nodule Spacing

Nearest neighbor statistics show that solid nodules and hollow/filled nodules are non-uniformly and nonrandomly clustered both laterally and vertically throughout the Sheepbed member. The occurrence of nodules in irregular patches rather than beds is one of the strongest lines of evidence supporting a diagenetic concretionary origin for the nodules. Clustered distributions of concretions are thought to be the result of several factors, including the presence of favorable nucleation sites controlled by heterogeneities in sediment permeability or chemical composition, or the influence of concretions on each other [Raiswell and White, 1978]. Examples of such heterogeneities at the cm-scale can be observed at the Selwyn section. The presence of a raised ridge and a high concentration of nodules (Figure 11) coincides with a compositional transition between the upper and lower Sheepbed. APXS analyses from the lower Sheepbed at the Selwyn section shows that this interval exhibits lower $\text{Al}_2\text{O}_3/\text{TiO}_2$ and lower Ni than the upper Sheepbed at Selwyn [McLennan *et al.*, 2014]. These geochemical differences, which *McLennan et al.* [2014] attribute to subtle changes in sediment provenance, coupled with

permeability variations discussed in the previous section could have influenced the development of a diagenetic front at the upper-lower Sheepbed boundary.

Sedimentary structures including bedding or bedforms can also influence the development of concretions, although the generally uniform and massive nature of the Sheepbed member makes such control on the distribution of nodules and hollow/filled nodules unlikely. In the few locations where thin intercalated beds are present [Grotzinger *et al.*, 2014] bedding does not appear to influence the size, shape, or distribution of nodules. However, raised ridges appear to have an antithetical relationship with nodules. This is mostly clearly evident in the point counts and concentration maps of the John Klein and the Raised Ridges and Nodules mosaics (Figures 5.7 and 5.10), where solid nodules and particularly hollow/filled nodules are absent where dense networks of raised ridges occur. Two possible scenarios can explain this relationship: (1) nodules and raised ridges formed contemporaneously, but their respective distributions were controlled by rheological or compositional variations within the Sheepbed sediments, or (2) nodules and raised ridges formed at different times, but the prior existence of one type of feature prevented the uniform distribution of the other type of feature, perhaps through the restriction or concentration of diagenetic fluids non-uniformly throughout the outcrop. Distinguishing between these scenarios requires an evaluation of potential growth mechanisms for solid and hollow/filled nodules, which is discussed in detail below.

5.6.4 Growth of Solid Nodules

The conventional model for concretionary growth involves the passive precipitation of a cementing phase in sediment pore spaces in a concentric, accretionary pattern that

radiates outward from a central nucleation point [Dana, 1863; Newberry, 1873; Tomkiew, 1927; Galimov and Girin, 1968; Knoke, 1966; Raiswell, 1971; Criss *et al.*, 1988]. However, the recognition of replacive, displacive, and incomplete cementation textures in concretions indicates that passive precipitation within pore space alone is likely an oversimplification [Raiswell and Fisher, 2000]. An alternative model for concretionary growth in mudrocks involves pervasive, rather than concentric growth [Mozley, 1996; Raiswell and Fisher, 2000]. In this model, individual nuclei – that will eventually form a single concretion – grow concentrically so that a cluster of crystals forms a solid, framework over time [Raiswell and Fisher, 2000]. Pervasive growth is capable of leaving significant porosity throughout the volume of the concretion that could be filled with later cements.

The Sheepbed solid nodules show no evidence for internal concentric layering, the most diagnostic evidence for the conventional concentric growth model. However, conclusively distinguishing between the concentric versus pervasive modes of growth--particularly in the absence of clear concentric zonation--requires microscale textural evidence not attainable with the payload of the Curiosity rover. With this caveat considered, the pervasive growth model may be most consistent with the subtle compositional difference observed in APXS and ChemCam data between the solid nodules and host Sheepbed mudstone. Raiswell and Fisher [2000] suggest that concretions forming by pervasive growth contain relatively small amounts of cement in the early stages of growth and thus often retain physical and compositional properties very similar to the host sediment.

5.6.5 Growth of Hollow Nodules

The patchy distribution of hollow nodules within the Sheepbed member, the variable rim and void morphologies, occurrence of conjoined forms, and co-occurrence of solid nodules and hollow nodules is consistent with a diagenetic concretionary origin for the hollow nodules. However, no straightforward analog for concretion formation on Earth explains the presence of the central void that characterizes Sheepbed hollow nodules. Therefore, three competing hypotheses for the origin of hollow nodule interior voids are considered: (1) hollow nodule voids represent scour pits resulting from preferential erosion at the outcrop surface of a less well-cemented concretion interior, (2) hollow nodule voids represent secondary porosity caused by the dissolution and selective leaching of a more soluble mineral phase that once existed in the center of the nodule, or (3) voids within the hollow nodules represent primary porosity created by the exsolution of gas bubbles from saturated pore fluids in unlithified Sheepbed sediments. Exsolved gas bubbles would then have served as nucleation sites for the precipitation of concretionary rims. The latter two hypotheses were originally proposed by *Grotzinger et al.* [2014], but are evaluated in further detail here using the data presented in this study.

There is no geochemical or visual evidence that a precursor mineral phase once occupied the hollow nodule voids, but the absence of a present-day interior phase does not preclude the possibility that one may have existed. Therefore, the first two models evaluated here consider the possibility that material, whether similar to the host sediment or a distinct mineral phase, once existed within the hollow nodule voids but was later removed at the surface by erosion (hypothesis 1), or at depth by dissolution (hypothesis 2). According to the first hypothesis, Sheepbed hollow nodules would have formed originally

as differentially cemented concretions whose less well-cemented interiors eroded at the present-day outcrop surface to form the interior voids. Differentially cemented concretions have been documented on Earth, and *Mozley and Davis* [2005], for example, described “composite concretions” from the Sante Fe Group, New Mexico. At this locality, some concretions are completely cemented, while others contain uncemented sand in their interiors. Differentially cemented composite concretions are thought to form by pervasive growth wherein a reaction front forms at the margins of a zone of pore-water whose chemistry is favorable for cement precipitation [*Mozley and Davis*, 2005]. If this reaction front remains stationary for an extended period of time, a strongly cemented rim could form around a weakly cemented interior. Differentially cemented “rind concretions” are also observed in the Jurassic Navajo Sandstone of the southern Utah and northern Arizona [*Potter et al.*, 2011; *Chan et al.*, 2012]. Rind concretions exhibit a well-cemented zone containing hydrous ferric oxides surrounding a cement-poor interior, and are variably interpreted to have formed by pervasive, but incomplete, growth in zones of diffusive mass transfer [*Potter et al.*, 2011].

If the Sheepbed hollow nodules were once differentially cemented concretions, it is possible that exposure at the present-day surface could result in the preferential erosion of less well-cemented interiors. However, the presence of filled nodules in the Sheepbed member, interpreted here and in *Grotzinger et al.* [2014] as hollow nodules filled during later diagenesis, suggests that the hollow nodule voids existed prior to their exposure at the present-day outcrop surface. The sulfate-filled fractures observed leading into and out from the filled nodules are consistent with an origin as hydraulic fractures formed in the burial regime under high hydrostatic pressures [*Grotzinger et al.*, 2014]. In this case, extraction of

hollow nodule core material would be required to have occurred in the subsurface, before later fracturing and infilling with sulfate minerals, making it unlikely that hollow nodule voids were formed by the preferential weathering of differentially cemented concretions at the present-day outcrop surface.

The second possibility is that hollow nodule voids represent secondary porosity caused by the dissolution or selective leaching of a more soluble mineral phase that once existed in the cores of the hollow nodules (Figure 5.16a). Iron oxide-cemented rinds in concretions of the Cretaceous Dakota Formation [Loope *et al.*, 2012], the Navajo sandstone [Kettler *et al.*, 2011; Loope *et al.*, 2012], and Quaternary sediments in the Netherlands [Van der Burg, 1969; Van der Burg, 1970] are interpreted as forming during the dissolution of early diagenetic siderite spherules caused by changing redox conditions [Loope *et al.*, 2012]. In cohesive muddy sediments, siderite nodules grow displacively, and subsequent oxidation of these nodules during diagenesis leaves behind an iron oxide rind surrounding a central cavity [Loope *et al.*, 2012]. In theory, dissolution-precipitation reactions like that involving siderite during changing redox conditions could produce morphologies similar to those observed in the Sheepbed hollow nodules. In such a scenario, spherules precipitated during early diagenesis of the Sheepbed mudstone would have been dissolved by a later phase of aqueous alteration involving oxidizing pore fluids, thereby creating secondary porosity within the hollow nodules and a source of ions to support the inward growth of hollow nodule rims. Such a process could be consistent with the generally uniform size distribution of the hollow nodule voids and the subtle scaling relationship observed between hollow nodule interior void diameter and rim thickness—larger spherules (more reactant) would have been capable of supporting the formation of thicker rims.

The secondary dissolution hypothesis invokes examples from the Earth sedimentary record that offer a reasonable morphological analog to the Sheepbed hollow nodules, but neither the imaged-based observations and geochemical data presented here nor the available mineralogical data from the SAM and CheMin instruments [Ming *et al.*, 2014; Vaniman *et al.*, 2014] indicate the presence or composition of a particular precursor mineral phase within the hollow nodules. Given the lack of constraints on hollow nodule composition and possible precursor spherule mineralogy, any number of precipitation-dissolution reactions that could be invoked to produce hollow nodule voids according to this hypothesis.

In a third model, hollow nodule void space represents primary porosity formed by the exsolution of gas bubbles from early diagenetic pore fluids (Figure 5.16b). Gas is a common constituent in sedimentary pore fluids on Earth [Maxson, 1940; Cloud, 1960; Martens and Berner, 1974; Hovland *et al.*, 1993; Fleischer *et al.*, 2001], and gas bubbles, often spheroidal in shape [Reed *et al.*, 2005], are known to form in muddy sediments in a wide variety of terrestrial depositional environments [Emery, 1945; Shinn, 1968; Martens and Berner, 1974; Sills and Gonzalez, 2001; Reed *et al.*, 2005; Boudreau *et al.*, 2005]. While most interstitial gas in pore fluids on Earth is formed during the decomposition of organic matter, there are several abiotic processes that could produce gas in sedimentary pore fluids on Mars [Grotzinger *et al.*, 2014]. Extreme changes in either temperature or pressure could cause the exsolution of dissolved atmospheric gases, such as CO₂, from pore fluids. Alternatively, the alteration of forsteritic olivine to saponitic smectite clay that occurred in the Sheepbed mudstone during early diagenesis [Vaniman *et al.*, 2014] could have provided a source of gas (H₂) to form the bubbles and clay minerals to increase the

strength of the sediment and aid in the potential retention of gas-induced pore space.

Although available rover data does not permit a conclusive determination of the most likely gas composition, its source, or the precipitation reactions that might have led to hollow nodule rim formation, the gas bubble hypothesis is consistent with several of the observations presented here. First, the observed scaling relationship between rim thickness and hollow interior diameter (Figure 5.5), although not particularly strong, supports a model in which larger bubbles are capable of changing the pore fluid chemistry in a larger volume surrounding the bubble, thereby resulting in the precipitation of thicker rims. This scenario is consistent with the model of *van Kessel and van Kesteren* [2002] in which bubbles grow by diffusion of dissolved gas toward the bubble, such that larger bubbles have a greater region of influence than do smaller bubbles. The gas bubble hypothesis may also offer an explanation for the antithetical spatial relationship observed between nodules (particularly hollow/filled nodules) and raised ridge networks observed in the John Klein and Raised Ridges and Nodules mosaics (Figures 5.7 and 5.10). In high-strength substrates, such as those containing a significant proportion of clay minerals, bubbles tend to remain confined by the surrounding substrate until relatively high gas pressures are reached that exceed substrate strength. Failure of the substrate results in migration of the gas bubble and crack formation [*Pollack et al.*, 2006]. Therefore, variations in substrate strength or institial gas pressure within Sheepbed sediments could explain the formation of hollow nodules (stationary gas bubbles) in portions of the Sheepbed exclusive of raised ridges (cracks, i.e., *Siebach et al.* [2014]).

The effects of compaction and bioturbation often destroy gas-related structures prior to sediment lithification on Earth, but early diagenetic cementation can preserve these

features. Birdseye structures, or sedimentary fenestrae, are common features in shallow marine sedimentary rocks on Earth and reflect early cementation of primary void space produced by gas bubbles. Fenestrae typically range from 1-3 mm [Shinn, 1968], consistent with the size range of Sheepbed hollow nodules, yet often show a substantially wider range of shapes likely associated with differential cohesive strength of organic-rich substrates. Spheroidal bubble-like features are also part of a continuum of early diagenetic, presumably gas-related [Furniss *et al.*, 1998; Marshall and Anglin, 2004; Pollock *et al.*, 2006] void morphologies collectively known as “molar-tooth structures” found in Precambrian shales [Bishop and Sumner, 2006; Gilleaudeau and Kah, 2010] and carbonate mudstones [Bauerman, 1885; Smith, 1968; O’Connor, 1972]. Neither birds-eye structures nor molar-tooth structures are direct morphological or compositional analogs for the hollow nodules observed in the Sheepbed member, but these features from the Earth sedimentary record offer known examples of interstitial gas bubbles preservation in sediments during early diagenesis.

5.6.6 Timing of Concretion Formation

The co-occurrence of solid nodules and hollow nodules throughout the Sheepbed outcrop suggests that both nodule types formed contemporaneously, and the spherical shape of the nodules points towards an early diagenetic origin prior to compaction. If hollow nodules represent concretionary growths around primary gas bubble void space, the nodules must have formed during a phase of very early diagenesis prior to lithification of the Sheepbed mudstone. In order for gas bubbles to form and grow in the Sheepbed by displacement of sedimentary grains, these sediments would have been largely uncompacted

and unlithified at the time of hollow nodule formation. The gas bubble hypothesis for hollow nodule formation, coupled with *Siebach et al.*'s [in review] interpretation of the raised ridges as early diagenetic subaqueous shrinkage cracks, implies contemporaneous formation of both nodules (solid and hollow) and raised ridges prior to Sheepbed lithification.

If hollow nodules represent the dissolution of a more soluble interior phase, the age constraints on solid and hollow nodules are slightly relaxed. In this scenario, the nodules need not have formed contemporaneously with the raised ridges prior to Sheepbed lithification, although the nodules must still have formed before: 1) the percolation of diagenetic fluids that removed the interior cores of the hollow nodules, 2) the phase of fracturing that affected the entire Yellowknife Bay formation sequence [*Grotzinger et al.*, 2014], and 3) the diagenetic event that precipitated Ca-sulfate in veins formed during fracturing and in hollow nodule interiors to form filled nodules [*Grotzinger et al.*, 2014; *McLennan et al.*, 2014]. Accordingly, a relatively early diagenetic interpretation is favored for the nodules in the dissolution scenario as well.

5.6.7 Nodules on Mars: Gale Crater vs. Meridiani Planum

Solid nodules, reminiscent of the Sheepbed nodules, have also been observed on Mars at Meridiani Planum, the field site of the MER Opportunity rover. Since landing in 2004, the Opportunity team has observed two types of nodules: hematite-rich nodules lacking internal structure, or “blueberries”, recognized first in the sulfate-rich sandstones of the Burns formation at Eagle crater, Endurance crater, and Victoria crater [*Chan et al.* 2004; *Squyres et al.*, 2004; *Chan et al.*, 2005; *McLennan et al.*, 2005; *Calvin et al.*, 2008],

and “newberries,” small nodules observed in the Whitewater Lake rock type, a fine sandstone in the Endeavor crater rim interpreted as Noachian crust older than the sulfate-rich Burns formation [Arvidson *et al.*, 2014]. Hematite spherules were interpreted as concretions that formed during diagenesis by recharge of an active groundwater system [Chan *et al.*, 2004; Chan *et al.*, 2005; McLennan *et al.*, 2005], while “newberries” have been interpreted as either impact accretionary lapilli or diagenetic concretions [Arvidson *et al.*, 2014]. In addition, features described as “hollowed spherules” have been identified at several locations in Meridiani in association with both hematite spherules and “newberries” [Fairén *et al.*, 2014], although their origin is unknown.

According to the size measurements made here, Sheepbed solid nodules (mean diameter = 0.80 mm) are generally smaller than the hematite spherules observed at Meridiani Planum (mean diameter = 3.6 mm, Calvin *et al.* [2008]) and the “newberries” observed in Endeavor crater (typical diameters between 2-3 mm, Arvidson *et al.* [2014]). Sheepbed solid nodules are most similar in size to “mini”-spherules at Eagle crater [Calvin *et al.*, 2008], which average only 0.795 mm in diameter. One similarity between the Sheepbed solid nodules and the Meridiani “newberries” is that both features show only subtle compositional differences compared to surrounding host rock. Both Sheepbed solid nodules and “newberries” show a slight enrichment in iron, raising the possibility that the “newberries”, if they are concretions, may be cemented by a similar mineral or contain similar proportions of cement. This is in contrast to the hematite spherules, which exhibit a highly distinctive Fe-enrichment compared to the host rock. Compositional and morphological differences between the Sheepbed solid nodules, hematite spherules, and “newberries” are not unexpected given the wide variation of diagenetic concretions known

to exist on Earth [Seilacher *et al.*, 2001]. What is perhaps more intriguing is that diagenetic concretions have been interpreted at 3 of the 4 major terrains (Meridiani Burns formation, Endeavor crater, Yellowknife Bay formation of Gale crater) on the surface of Mars that have been explored by rover teams. Diagenetic concretions were not observed with the Spirit rover at Columbia Hills. Although this data set is small, the occurrence of diagenetic concretions at Meridiani Planum and Gale crater suggests that diagenetic aqueous alteration is not unusual in Martian sedimentary environments. However, diagenetic concretions are not ubiquitous in sedimentary deposits on Mars, as illustrated by their absence in other members of the Yellowknife Bay formation [Grotzinger *et al.*, 2014], and at Home Plate at Gusev crater [Squyres *et al.*, 2007]. The formation of concretions therefore requires a special set of conditions (permeable sediments, active groundwater system, saturated to super-saturated pore-fluids) not met in all sedimentary deposits on Mars, but also not rare, and possibly more common than on Earth.

In addition to the general conditions conducive to concretion formation listed above, the formation of hollow nodules like those in the Sheepbed member likely requires an even more specific set of conditions. If hollow nodules represent cemented gas bubbles, their formation requires gas-charged sediments cohesive enough to retain gas bubbles and early fluid flow through the sediments prior to compaction and lithification. The absence of hollow nodules in any of the sandstones in Yellowknife Bay may suggest that the increased cohesion of a clay-rich mudstone, like that of the Sheepbed member, may be necessary to retain gas bubbles prior to early lithification. If hollow nodules represent dissolution of a more soluble phase, specific geochemical and redox conditions must be met during diagenesis. It is possible that the conditions necessary to form hollow nodules occurred in

other Martian deposits, but the specific sediment properties, composition, and timing required to form hollow nodules may not be particularly common.

5.6.8 *Concretions and the Preservation of Martian Organics*

Permeability is one of the most important factors controlling the preservation of organic matter in sediments, as permeability determines how easily oxidizing diagenetic fluids can interact with and destroy reducing compounds. Just as the low permeability of shales and cherts on Earth creates conditions conducive to organic matter preservation [Sumner, 2004], the decrease of permeability due to the precipitation of early diagenetic concretionary cements has the potential to protect and preserve organic material. Evidence for this in sedimentary rocks on Earth can be observed in the long-term preferential preservation of organic compounds and paleoecological indicators in early diagenetic concretions compared to the surrounding host rocks, e.g., Maples [1986], Martill [1990], Orr *et al.* [2000], Raiswell and Fisher [2000], Weber *et al.*, [2012]. Although organics preserved in early diagenetic concretions on Earth are typically biological in origin, this need not be the case on Mars where an abiotic origin for organic matter must be ruled out before a biological one is considered. Regardless of the origin of organic matter that may be present on Mars, early diagenetic concretions in Martian sediments have the potential to create a “taphonomic window” in which reduced compounds, e.g., organic molecules, can be preserved in otherwise oxidizing diagenetic environments. The potential for early diagenetic concretions to preserve organic material suggests that these features are among the most desirable targets in the search for organics on Mars, particularly in sediments containing reduced mineral species. Although organics have not been definitively identified

in the Sheepbed mudstone [Ming *et al.*, 2014], the favorable mineralogy (clays) and the abundance of early diagenetic concretions in the Sheepbed mudstone indicates that this stratigraphic interval represents the best candidate for the preservation of organic matter explored to-date by rover missions on Mars.

5.7 Conclusions

- (1) Three types of nodules are identified in the Sheepbed member in decreasing abundance: solid nodules, hollow nodules, and filled nodules.
- (2) Measurements of nodule aspect ratio show that all nodule types are generally spheroidal in shape.
- (3) Solid nodules range in size between 0.2 and 4.11 mm, average 0.80 mm in diameter, and exhibit a lognormal size distribution. Hollow nodules range in size between 0.29 and 5.40 mm, average 1.35 mm in diameter, and exhibit a normal size distribution. Average hollow nodule interior void diameter is 0.86 mm and average hollow nodule rim thickness is 0.25 mm. Filled nodules range in size between 1.18 and 5.15 mm, average 2.75 mm in diameter, and exhibit a normal size distribution.
- (4) Size and shape measurements suggest that hollow and filled nodules represent one population that is statistically distinct from solid nodules. This is consistent with the interpretation of *Grotzinger et al.* [2014] that filled nodules are a variant of hollow nodules that have been filled by a later phase of sulfate mineralization.
- (5) Solid, hollow, and filled nodules co-exist in outcrop throughout the Sheepbed, although the nodule types sometimes exhibit distinct distributions. Hollow nodules, in particular,

exhibit an antithetical spatial relationship with raised ridges, spindle-shaped mineralized cracks.

(6) Both solid nodules and hollow/filled nodules occur in a clustered, rather than random or dispersed, pattern laterally and vertically within the Sheepbed outcrop.

(7) APXS analyses indicate the presence of an Fe-bearing cement within the nodules, but ChemCam measurements suggest that the difference between nodule and host rock compositions is extremely subtle.

(8) Based on the size, shape, distribution, and composition of the Sheepbed nodules, all nodule types are interpreted to be concretions formed during the early aqueous alteration of the Sheepbed mudstone by diagenetic pore fluids.

(9) Hollow nodules may represent either the dissolution of a more soluble interior phase within some concretions, or concretionary growth around primary void space caused by gas bubbles trapped in the cohesive, but unlithified clay-rich Sheepbed sediments.

(10) Active groundwater systems may often be involved in the diagenesis of sedimentary sequences on Mars, explaining the occurrence of concretions in multiple Martian sedimentary sequences on Mars, but the specific conditions and timing of events necessary for hollow nodule formation may be less common.

(11) Sediments containing nodules and hollow nodules are good candidates for the possible preservation of organic material because diagenetic concretions can create a favorable taphonomic window.

Notation

A	area, mm^2
AR	aspect ratio
C	areal concentration, %
d	mean feature diameter, mm
n	number of features on a surface
σ	standard deviation
p	significance probability
μ	mean

TABLES

Table 5.1. MAHLI Images Used to Measure Size, Shape, and Concentration of Nodules.

Target	Sol	Image ID	Product Type	Working Distance (cm)	Pixel Scale ($\mu\text{m}/\text{pixel}$)	$n_{\text{solid nodules}}$	$C_{\text{solid nodules}} (\%)$	$n_{\text{hollow nodules}}$	$C_{\text{hollow nodules}} (\%)$	$n_{\text{filled nodules}}$	$C_{\text{filled nodules}} (\%)$
Ekwir_1	150	0150MH00016300001014 32R00	onboard focus merge	6.7	30.4	11	0.2	47	2.0	2	0.3
Persillon	154	0154MH00017100001015 24R00	onboard focus merge	7.0	31.5	277	4.3	24	2.0	5	2.2
Mavor	158	0158MH00018500001016 99R00	onboard focus merge	7.1	32.5	100	1.3	13	0.5	-	-
Twitya	159	0159MH00009000001017 30R00	onboard focus merge	6.7	30.4	42	0.9	8	2.2	-	-
Yukon	161	0161MH00016300001019 18R00	onboard focus merge	6.9	31.2	49	2.8	-	-	-	-
Bonnet_Plume_1	161	0161MH00019200001019 08R00	onboard focus merge	6.8	30.8	235	1.8	20	0.4	-	-
Bonnet_Plume_2	161	0161MH00019200001019 10R00	onboard focus merge	2.8	16.7	49	1.4	2	0.4	-	-
Hudson_Bay	161	0161MH00016300001019 22R00	onboard focus merge	4.1	21.4	84	1.6	6	0.5	-	-
Hay_Creek	162	0162MH00019300001019 64R00	onboard focus merge	6.9	31.1	49	2.7	16	1.3	1	0.4
Drill_RP	168	0168MH00016300001021 66R00	onboard focus merge	6.7	30.2	36	1.2	27	2.3	6	2.2
Brock_Inlier	169	0169MH00016300001022 40R00	onboard focus merge	6.9	31.0	73	2.0	34	2.0	1	0.1
Autridge	173	0173MH00022700001023 18R00	onboard focus merge	4.7	23.4	35	1.3	3	0.2	2	0.1
Wernecke_3	173	0173MH00022700001023 14R00	onboard focus merge	6.2	28.6	135	1.0	50	1.6	2	0.3
Divot	174	0174MH00014600101023 25E01	full-frame based on autofocus sub-frame	10.8	45.0	209	2.8	34	1.0	-	-
Mini Drill Hole	178	0178MH00021100001024 75R00	onboard focus merge	6.5	29.5	33	1.3	21	1.3	4	1.1
Fort_Confidence	179	0179MH00020200001025 10R00	onboard focus merge	4.1	21.2	24	2.0	3	0.5	1	0.4
McNaughton	181	0181MH00016300001026 14R00	onboard focus merge	6.6	30.0	102	2.4	29	1.6	5	0.4
McLeary	181	0181MH00016300001026 20R00	onboard focus merge	6.4	29.2	35	1.4	21	1.3	-	-
Cumberland_New	275	0275MH00025800001029 91R00	onboard focus merge	11.2	46.3	100	2.5	81	2.5	-	-
Cumberland_DRT	291	0291MH00027700101033 92C00	full-frame based on autofocus sub-frame	7.0	31.7	51	1.3	74	3.1	1	0.1

Table 5.2. Nodule Size and Shape Statistics.

	<i>n</i>	Diameter, <i>d</i>				Aspect Ratio, <i>AR</i>			
		μ_d (mm)	σ_d (mm)	Medi an <i>d</i> (mm)	Min <i>d</i> (mm)	Max <i>d</i> (mm)	μ_{AR}	σ_{AR}	Medi an <i>AR</i> (mm)
Solid Nodules	1729	0.80	0.44	0.66	0.20	4.11	1.23	0.21	1.17
Hollow Nodules (Whole)	513	1.35	0.59	1.27	0.29	5.40	1.17	0.13	1.13
Hollow Nodule Interior Voids	513	0.86	0.44	0.81	0.16	4.13	1.24	0.22	1.19
Hollow Nodule Rim Thickness	491	0.25	0.14	0.23	0.01	1.07	-	-	-
Filled Nodules	30	2.75	1.14	2.72	1.18	5.15	1.16	0.17	1.12
									1.01
									1.97

Table 5.3. Wilcoxon Rank Sum Test Results

Data Sets Tested	Parameter	<i>p</i>	Null hypothesis rejected?
Solid nodule vs. hollow nodule	<i>d</i>	8.00E-96	Yes
Solid nodule vs. filled nodule	<i>d</i>	1.28E-18	Yes
Hollow nodule vs. filled nodule	<i>d</i>	5.49E-12	Yes
Solid nodule vs. hollow nodule	<i>AR</i>	8.55E-09	Yes
Solid nodule vs. filled nodule	<i>AR</i>	0.0469	Yes
Hollow nodule vs. filled nodule	<i>AR</i>	0.3795	No

Table 5.4. Nearest Neighbor Statistics for Lateral Solid Nodule and Hollow/Filled Nodule Distributions

Mosaic	Nodule Type	Observed Mean Distance (mm)	Expected	Nearest Neighbor Ratio	Pattern
			Mean Distance (mm)		
John Klein	solid	2.3	3.2	0.73	Clustered
	hollow/filled	4.9	7.8	0.63	Clustered
Cumberland 1	solid	3.0	3.6	0.82	Clustered
	hollow/filled	4.9	7.0	0.70	Clustered
Cumberland 2	solid	4.3	5.0	0.86	Clustered
	hollow/filled	8.1	10.7	0.75	Clustered
Raised Ridges and Nodules	solid	2.5	3.3	0.76	Clustered
	hollow/filled	7.2	10.8	0.67	Clustered

Table 5.5. ChemCam Comparison (wt. %) Between the Nodule-Rich and Nodule-Free Sheepbed Mudstone.

	SiO ₂	TiO ₂	Al ₂ O ₃	FeO	MgO	CaO	Na ₂ O	K ₂ O
Sheepbed (354 pts)	46.6	1.1	8.1	16.9	6.3	6.2	2.4	0.6
Nodule-rich area (128 pts)	45.7	1	8.2	16.6	5.6	6.5	2.4	0.6

¹See Mangold et al., [submitted] for a discussion of the error analysis associated with these values.

FIGURE CAPTIONS

Figure 5.1. Adapted from *Grotzinger et al.* [2014] and *McLennan et al.* [2014]. (a) HiRISE image (PSP_010573_1755) of Yellowknife Bay showing the contacts between major geologic and geomorphic units, and the location of rover targets mentioned in the text. Red line represents the rover traverse up to sol 166. Inset shows the location of Yellowknife Bay in Gale crater on MOLA topography draped over a THEMIS Day IR mosaic. (b) Stratigraphic column of the Yellowknife Bay formation.

Figure 5.2. MAHLI images of solid, hollow, and filled nodules. (a) MAHLI image 0154MH0001710000101524R00 of target Persillon taken on sol 154. This area contains abundant solid nodules. The white arrow points towards a sextuplet of six concatenated solid nodules. (b) MAHLI image 0169MH0001630000102238R00 of target Brock_Inlier taken on sol 169 showing “dimpled” hollow nodule morphology. (c) MAHLI image 0275MH0002580000102991R00 of dimpled hollow nodules of the Cumberland target taken on sol 275. White arrow points to a sulfate-filled fracture that cross-cuts dimpled hollow nodules. (d) MAHLI image 0154MH0001710000101524R00 of target Persillon showing filled nodules. Filled nodules are interpreted as hollow nodules filled with sulfate minerals during a later phase of diagenesis. (e) MAHLI image 0291MH0002770010103392C00 of brushed target Cumberland_DRT taken on sol 291 showing dimpled and bowl-like hollow nodule voids (white arrows) and a sulfate-filled bleb (black arrow) connected by hairline fractures. (f) MAHLI image 0173MH0002270000102314R00 of brushed target Wernecke_3 showing dimpled and

bowl-like hollow nodules (white arrows) and a filled nodule doublet (black arrow) associated with sulfate-filled hairline cracks.

Figure 5.3. MAHLI targets from the (a) Selwyn section plotted on an M-100 Mastcam mosaic acquired on sol 137. (b) John Klein and Cumberland drill locations plotted on an M-100 Mastcam mosaic acquired on sol 138. Dashed white lines indicate the contact between the Sheepbed and Gillespie Lake members.

Figure 5.4. Size frequency histograms of (a) solid nodule diameter. (b) hollow nodule diameter. (c) filled nodule diameter. (d) hollow nodule interior void diameter. (e) hollow nodule rim thickness.

Figure 5.5. Plots of hollow nodule rim thickness vs. hollow nodule interior void diameter. (a) Linear regression model of 491 rims and corresponding hollow void interiors measured in MAHLI images, Two potential outliers circled in gray. (b) Linear model and scatter plot for data set excluding the two potential outliers identified in (a). For both data sets, slope p -values << 0.05 indicating that the null hypothesis that the slope is zero is rejected.

Figure 5.6. Navigation camera (Navcam) overhead projection showing image footprints of the four Mastcam mosaics used to map lateral distributions of solid and hollow/filled nodules (red), and the two Mastcam mosaics used to map vertical distributions of solid and hollow/filled nodules (yellow). Dashed white line indicates the Sheepbed-Gillespie Lake contact.

Figure 5.7. Solid and hollow/filled nodules mapped in the vicinity of the John_Klein drill site (red star) in an M-100 mosaic taken on sol 166. See Appendix B for a list of image IDs.

(a) John Klein mosaic. The red star represents the location of the John_Klein drill hole; the white arrow points to a dense network of raised ridges. (b) Point count of solid nodules and hollow/filled nodules. (c) Map showing the distribution and concentration of solid nodules. Black arrow points to the area of highest solid nodule concentration. (d) Map showing the distribution and concentration of hollow/filled nodules. White arrow highlights the area around the raised ridge network where hollow/filled nodules are largely absent. Black arrows point to regions of relatively high hollow/filled nodule concentration.

Figure 5.8. Cumberland 1 M-100 mosaic taken on sol 185 showing solid and hollow/filled nodules in the vicinity of the Cumberland drill hole. See Appendix B for a list of image IDs. (a) Cumberland 1 mosaic. (b) Point count of solid nodules and hollow/filled nodules. (c) Map showing the distribution and concentration of solid nodules. Black arrow points to the area of highest solid nodule concentration. (d) Map showing the distribution and concentration of hollow/filled nodules. White arrow points to an area largely devoid of hollow/filled nodules. Black arrows point to relatively intermediate to high concentrations of hollow/filled nodules along the edge of the outcrop block.

Figure 5.9. Cumberland 2 mosaic showing solid nodules and hollow/filled nodules in the vicinity of the Cumberland drill hole (red star) in an M-100 mosaic taken on sol 275. See

Appendix B for a list of image IDs. (a) Cumberland 2 mosaic. (b) Point count of solid and hollow/filled nodules. (c) Map showing the distribution and concentration of solid nodules. Black arrows point to areas of highest solid nodule concentration. (d) Map showing the distribution and concentration of hollow/filled nodules. White arrow points to a portion of the outcrop devoid of hollow/filled nodules. Black arrow points to region of highest hollow/filled nodule concentration.

Figure 5.10. Solid and hollow/filled nodules in the vicinity of a dense network of raised ridges in an M-100 mosaic taken on sol 164. See Appendix B for list of image IDs. (a) Raised Ridges and Nodules mosaic. (b) Point count of solid and hollow/filled nodules. (c) Map showing the distribution and concentration of solid nodules. (d) Map showing the distribution and concentration of hollow/filled nodules. White arrows point to an area of the outcrop containing raised ridges, but sparse solid and hollow/filled nodules.

Figure 5.11. Selwyn M-100 mosaic taken on sol 159. See Appendix B for list of image IDs. (a) The irregular boundary between the upper and lower Sheepbed member. Arrow points to the poorly developed raised ridge that defines this boundary. (b) Large (>1 mm) solid nodules and hollow nodules characteristic of the lower Sheepbed member. (c) Large (>1 mm) filled and hollow nodules at the boundary between the upper and lower Sheepbed. Left and right arrows point to a filled and hollow nodule, respectively. (d) High concentration area of very small solid nodules (<1 mm) indicated by the white arrow that is characteristic of the upper Sheepbed.

Figure 5.12. Solid nodules and hollow/filled nodules distributed vertically through the Selwyn section in the vicinity of the lower to upper Sheepbed transition in an M-100 mosaic taken on sol 159. See Appendix B for list of image IDs. (a) Selwyn mosaic. (b) Point count of solid and hollow/filled nodules. (c) Map showing the distribution and concentration of solid nodules across the lower to upper Sheepbed boundary. Black arrow points to an area of high solid nodule concentration in the upper Sheepbed. (d) Map showing the distribution and concentration of hollow/filled nodules through the Sheepbed.

Figure 5.13. Solid and hollow/filled nodules distributed vertically through the Sheepbed in the Yellowknife Bay (YB) Egress mosaic taken with the M-100 camera on sol 298. See Appendix B for list of image IDs. (a) Yellowknife Bay Egress mosaic. Overhanging blocks at the top of the image mark the Sheepbed-Gillespie contact. (b) Point count of solid and hollow/filled nodules. (c) Map showing the distribution and concentration of solid nodules through the Sheepbed. Due to the low concentration of hollow/filled nodules in the scene, a map was not created for the hollow/filled nodules.

Figure 5.14. (a) MAHLI focus merge product (0161MH0001920000101910R00) showing target Bonnet Plume. Yellow circle shows the area analyzed by APXS. White shapes represent nodules (both solid and hollow/filled nodules). (b) MAHLI focus merge product 0276MH0002650000103019R00 showing the Cumberland drill site before it was drilled. Yellow circle shows the area analyzed by APXS. (c) Plot of nodule areal coverage in the APXS field of view vs. FeO^*/MnO as determined by APXS.

Figure 5.15. Mastcam image 0166MR0008880120201641E01 in the vicinity of the John Klein drill showing the gray, dust-free area blasted by the ChemCam laser shots. (b) ChemCam/RMI image of target DT-RP5 (CR0_412227292EDR_F0052270CCAM01166M) after the 4 depth profiles were performed. (c) Portion of the ChemCam spectra on location 2 showing the spectra of every tenth shot. The higher emission lines of Ca and Al for reddish spectra show an enrichment at depth.

Figure 5.16. Two models for hollow nodule and filled nodule formation. (a) Model in which hollow nodule voids are produced by the dissolution of a soluble interior during changing redox conditions. In this model, spherules form during early diagenesis of the Sheepbed mudstone. Changing redox conditions result in the dissolution of the spherule at the expense of an inwardly growing rim. (b) Gas bubble model for hollow nodule interior void formation. Dissolved gases exsolve from saturated pore fluids to form bubbles in the Sheepbed mudstone. As bubbles grow by diffusion and incorporation of exsolved gas, the pore fluid chemistry changes in an area immediately surrounding the growing gas bubble. These pore fluid changes create a zone around the bubble favorable for precipitation of an early diagenetic cement, likely an Fe-bearing mineral. Preferential cementation around the bubble creates a resistant rim, which preserves and protects the interior void space from subsequent compaction. (c) Filled nodules form when some hollow nodules experience a later stage of fracturing and interaction with calcium and sulfate-bearing diagenetic fluids that results in the precipitation of calcium sulfate fills in the interior void of some hollow nodules.

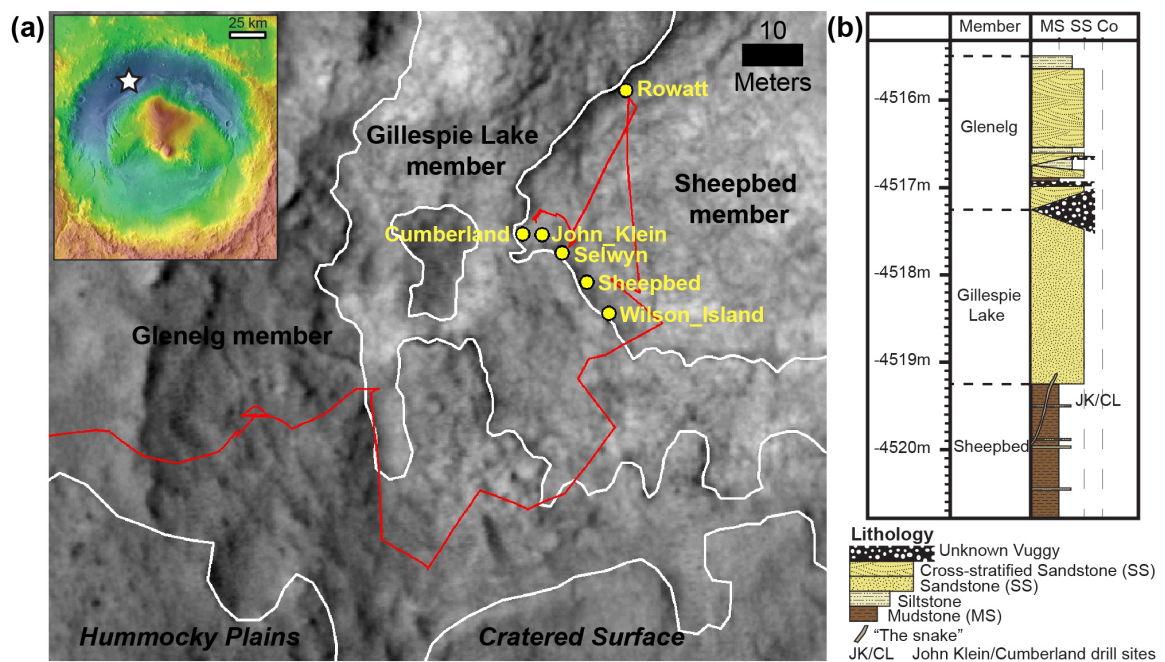


Figure 5.1

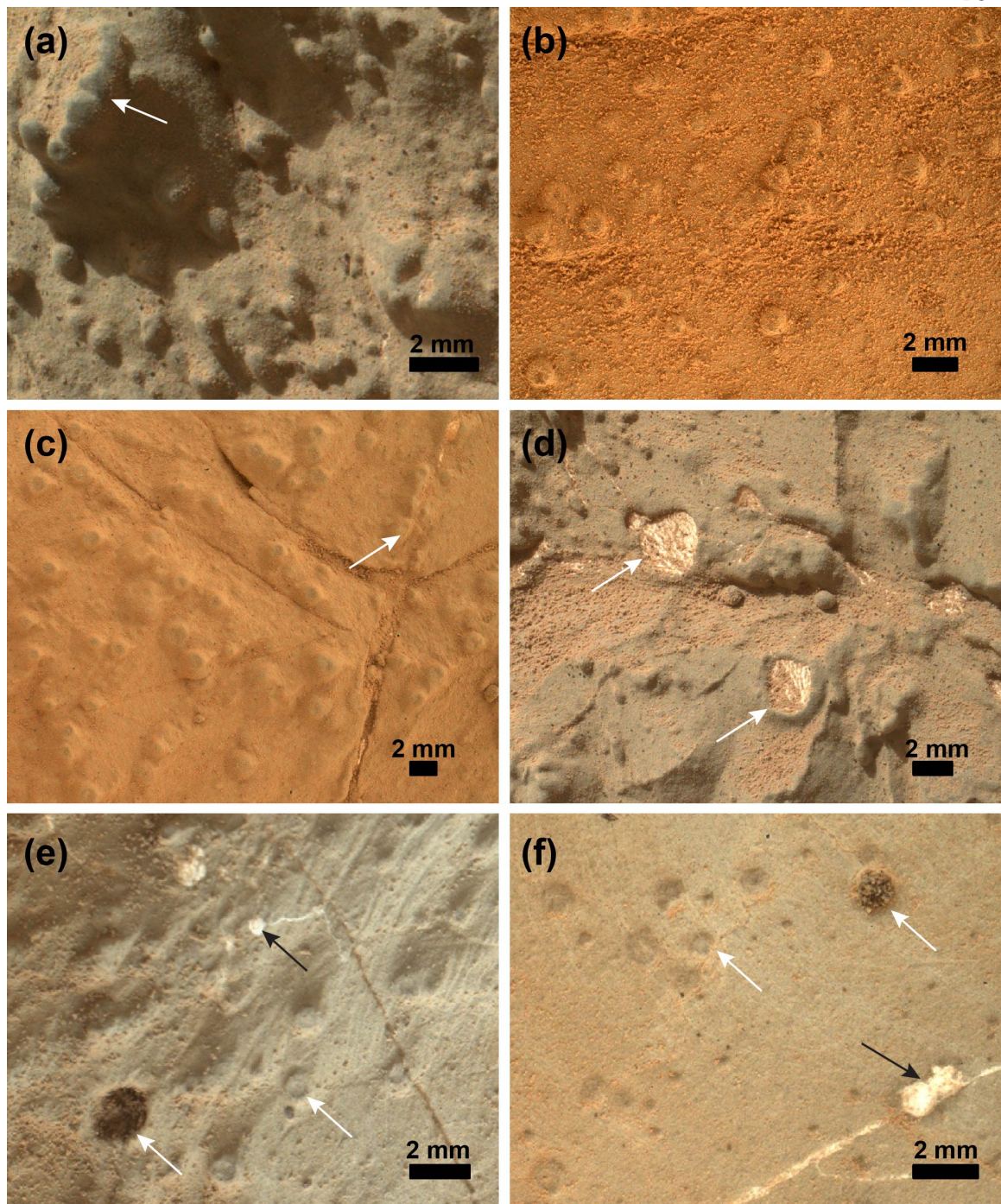


Figure 5.2

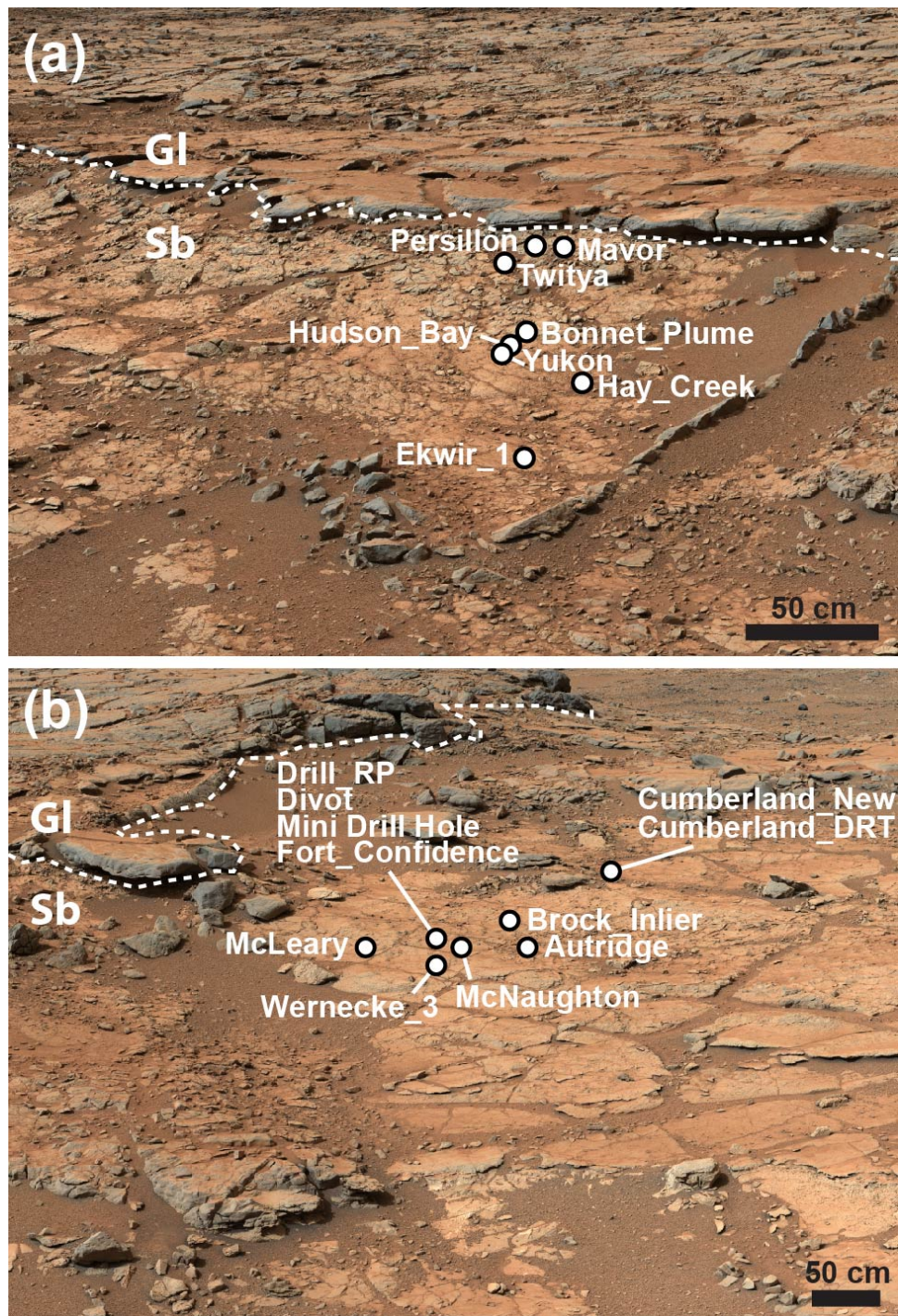


Figure 5.3

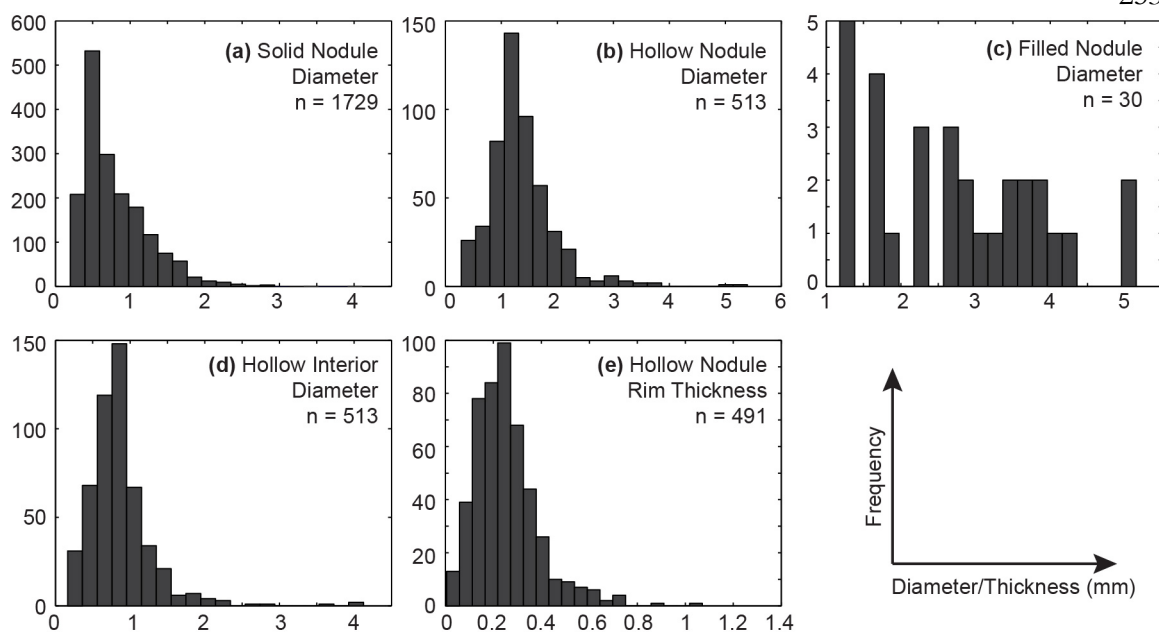


Figure 5.4

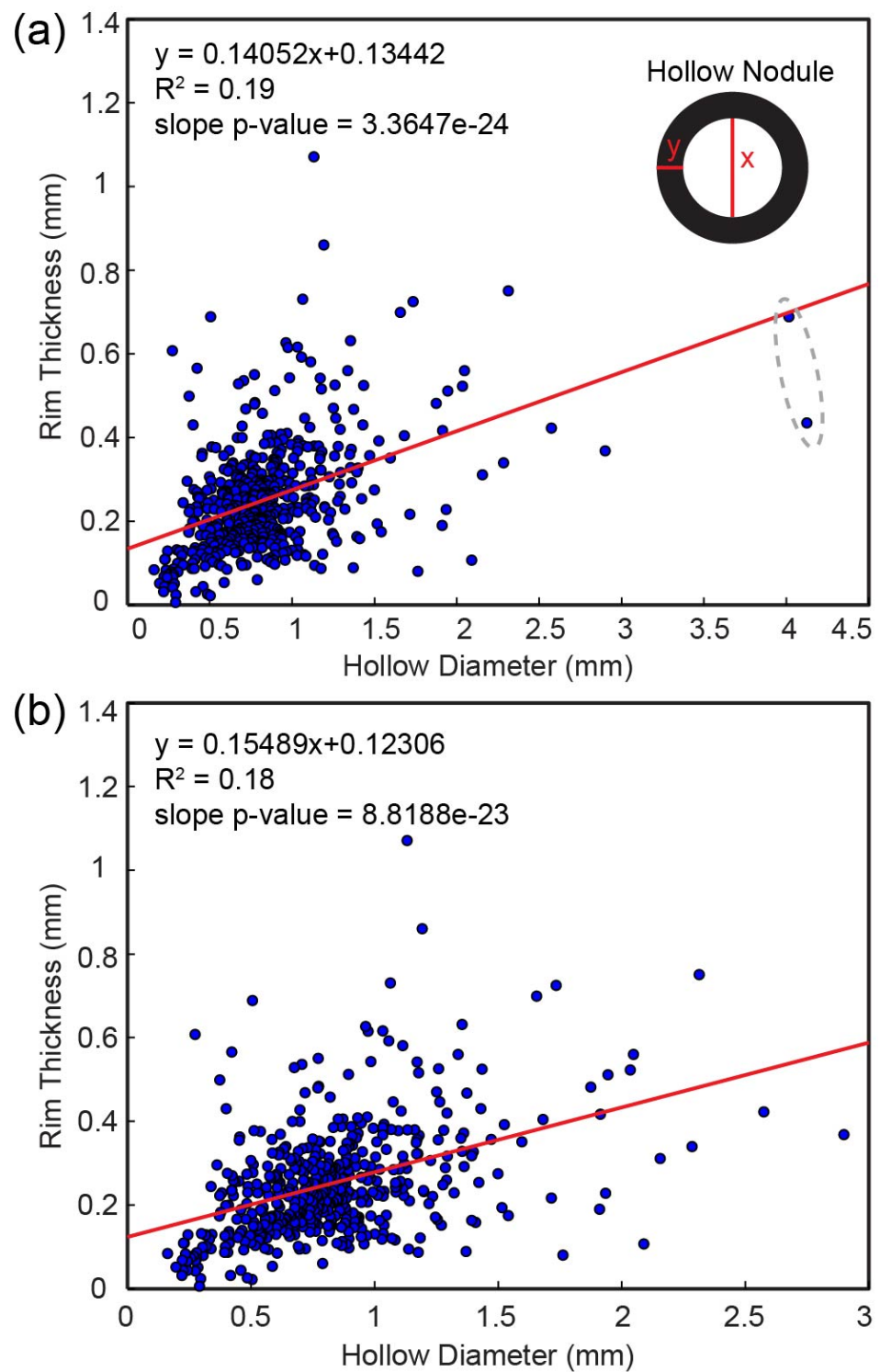


Figure 5.5

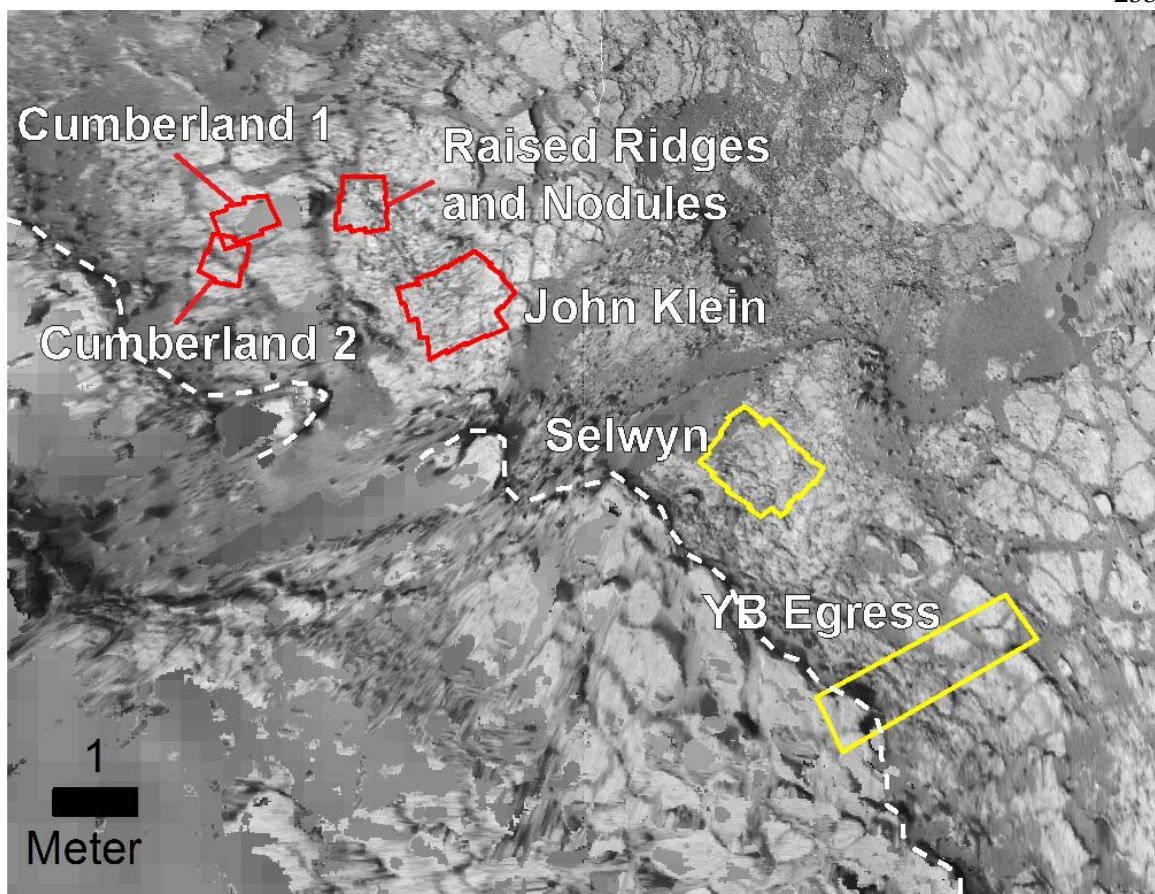


Figure 5.6

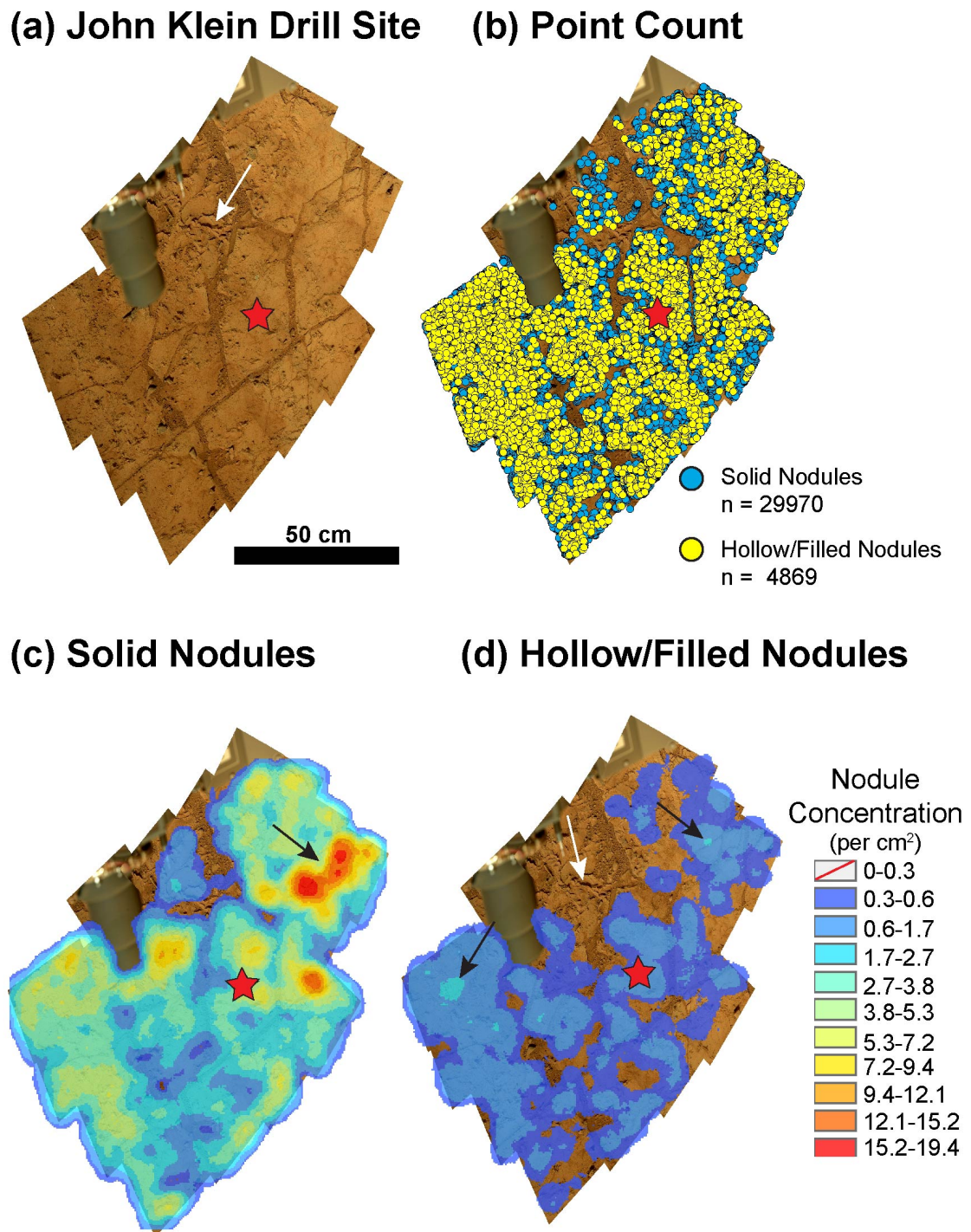


Figure 5.7

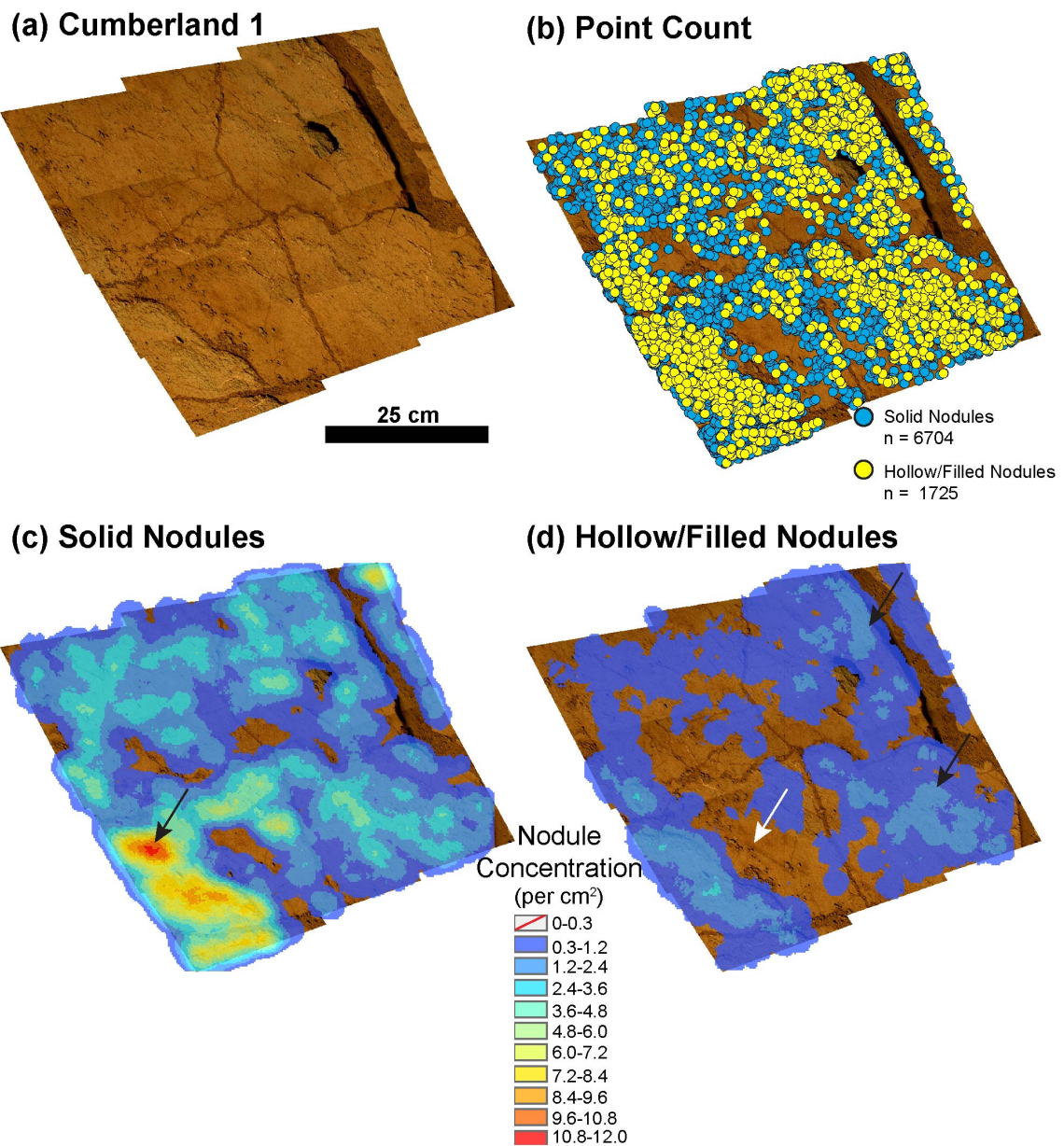


Figure 5.8

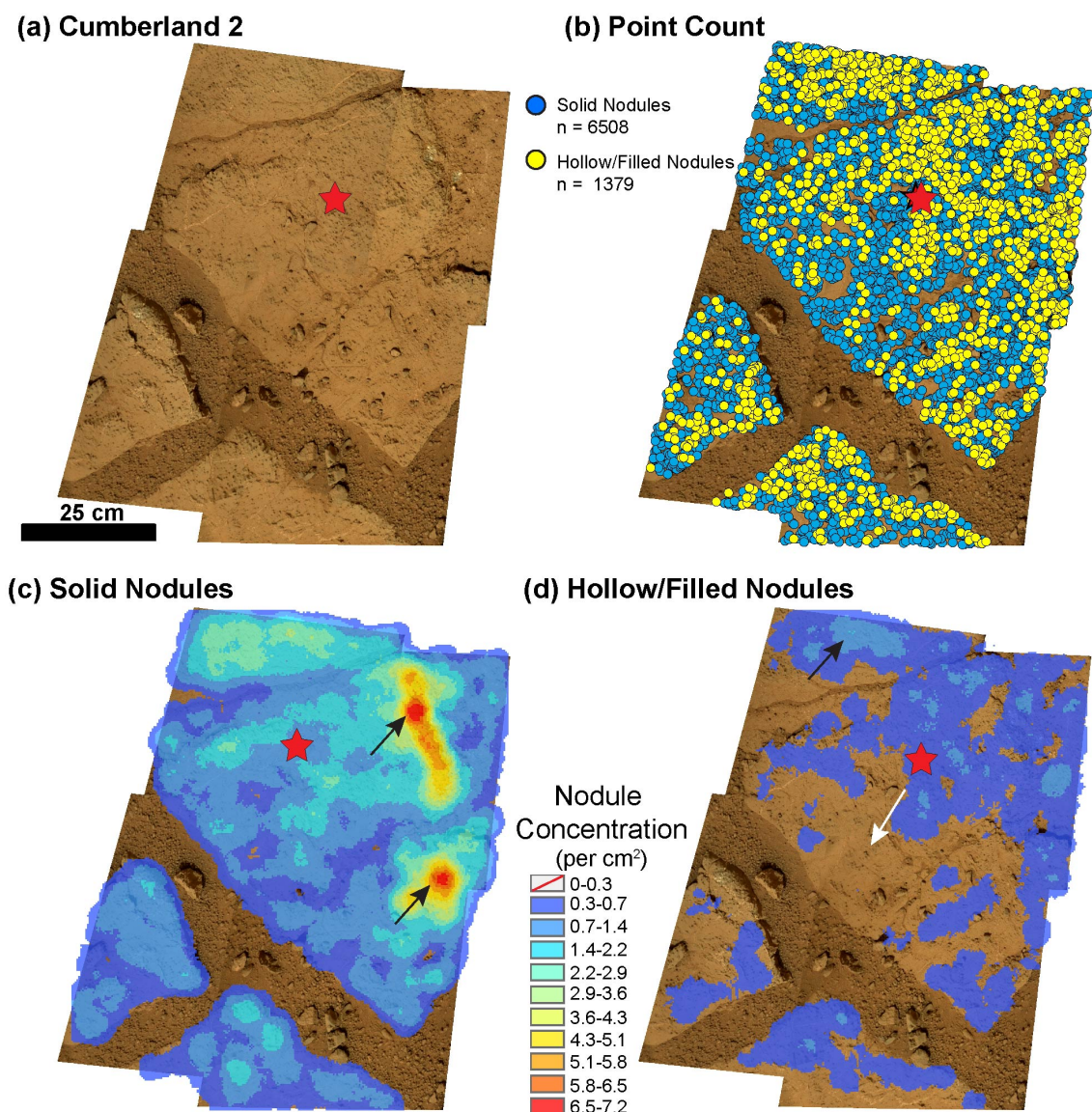


Figure 5.9

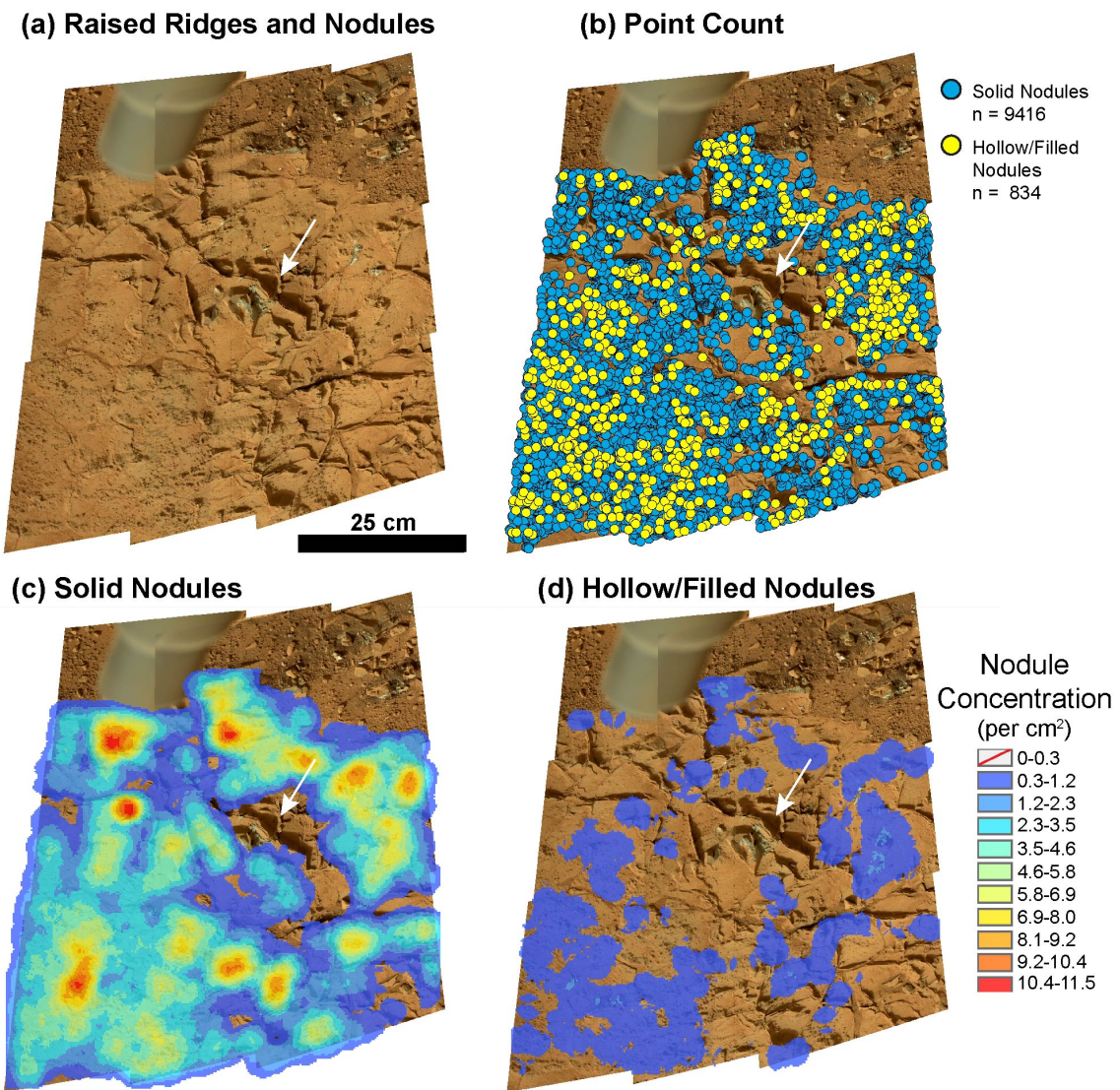


Figure 5.10

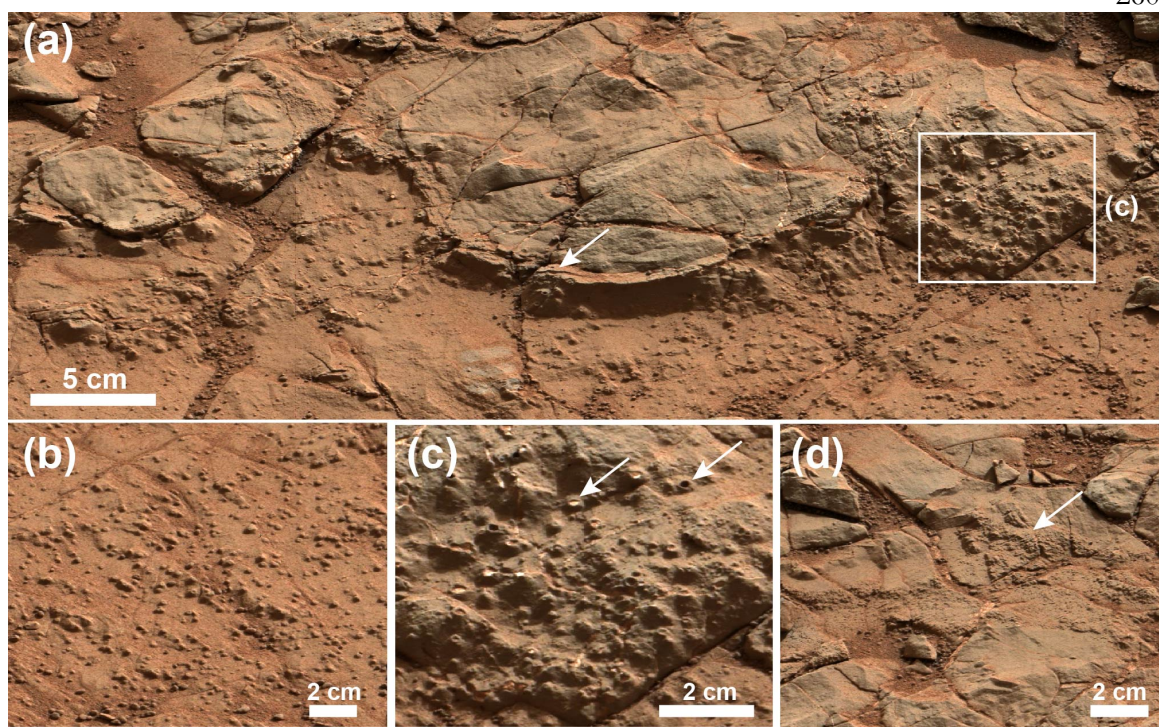
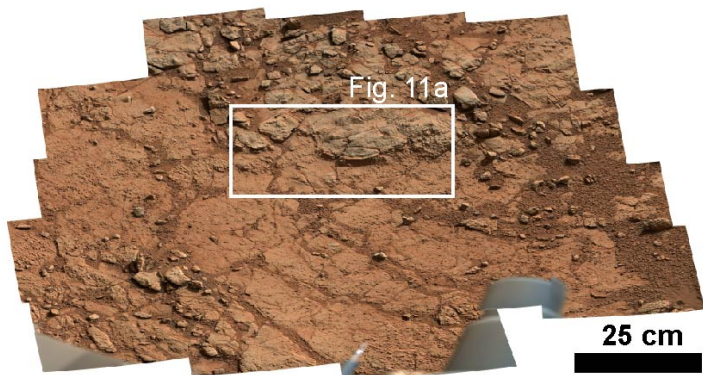
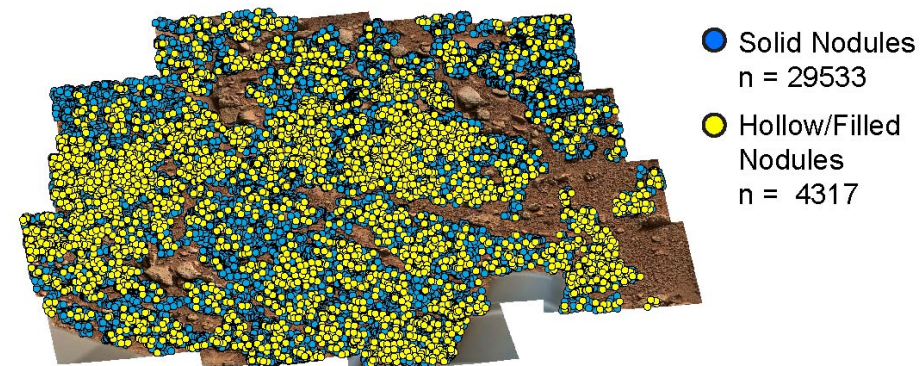


Figure 5.11

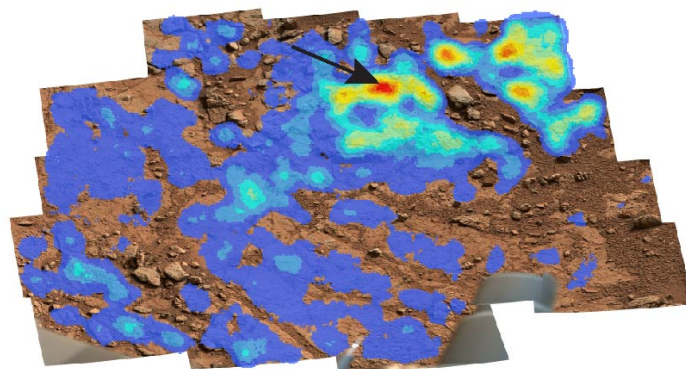
(a) Selwyn



(b) Point Count



(c) Solid Nodules



(d) Hollow/Filled Nodules

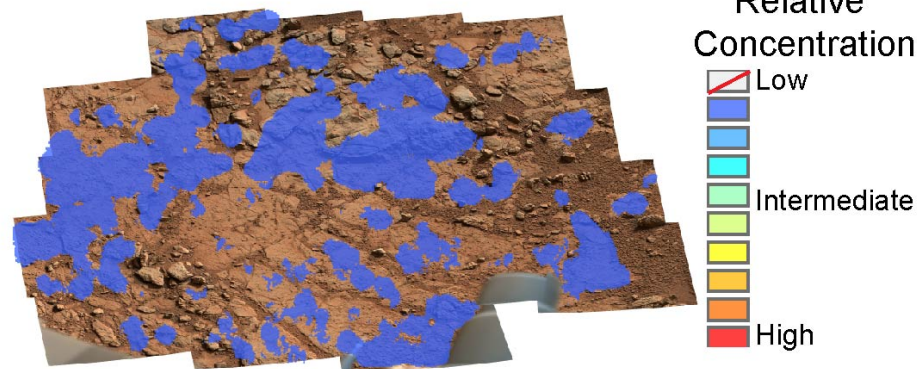


Figure 5.12

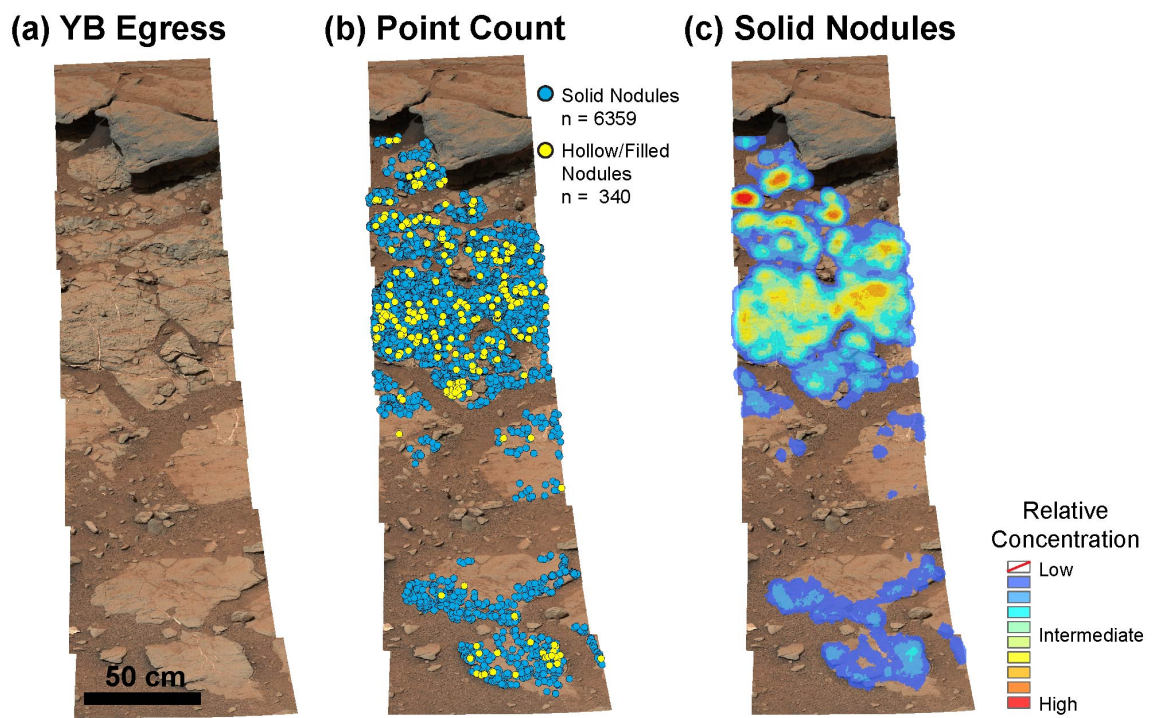


Figure 5.13

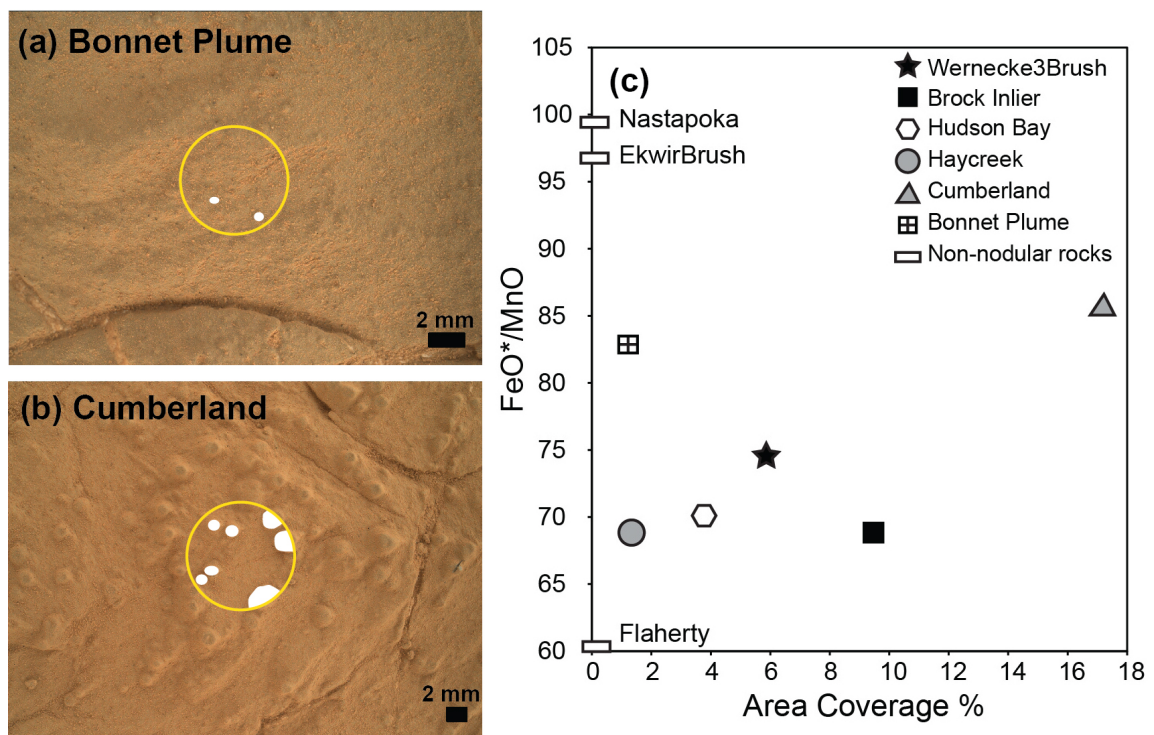


Figure 5.14

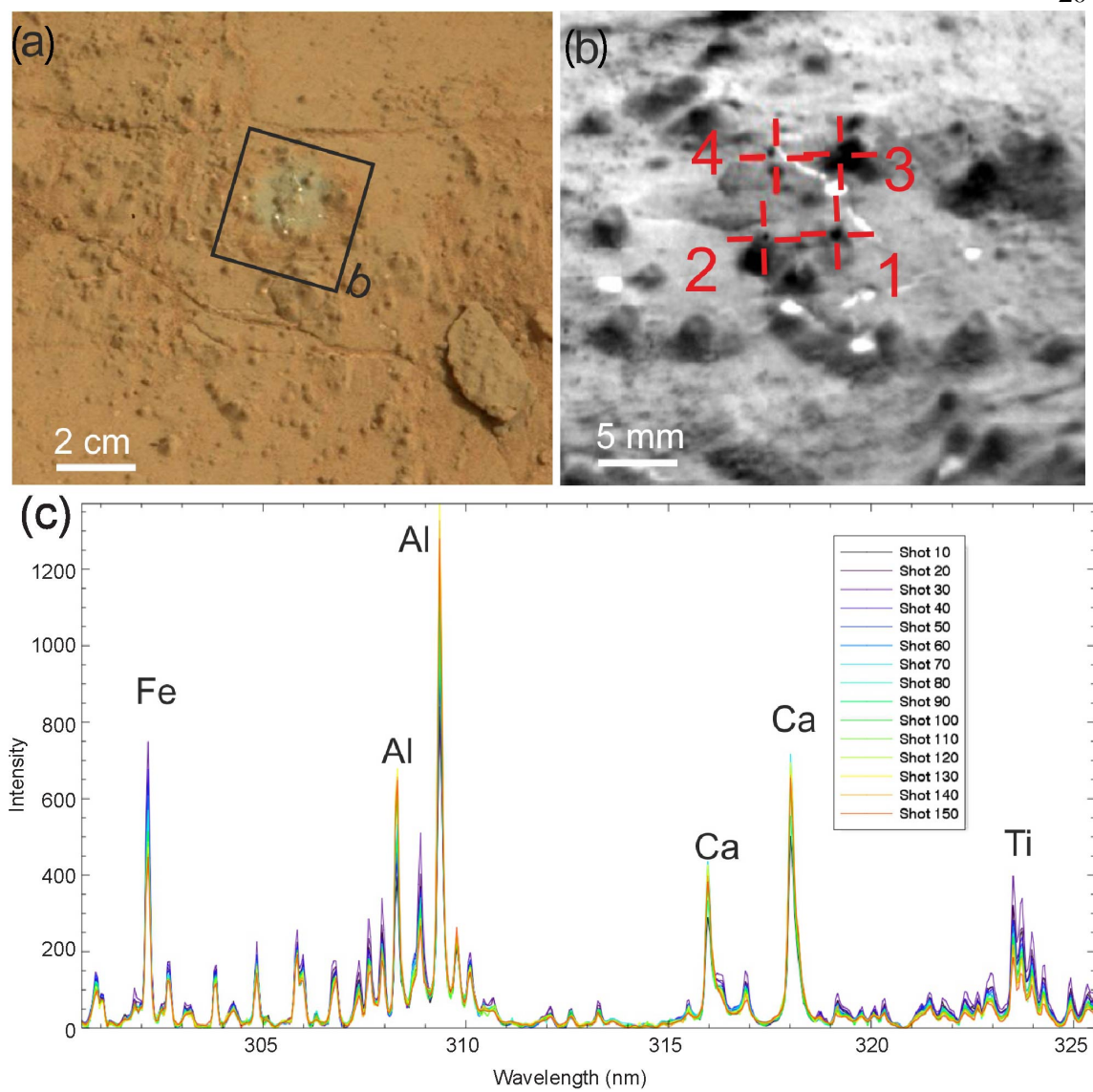


Figure 5.15

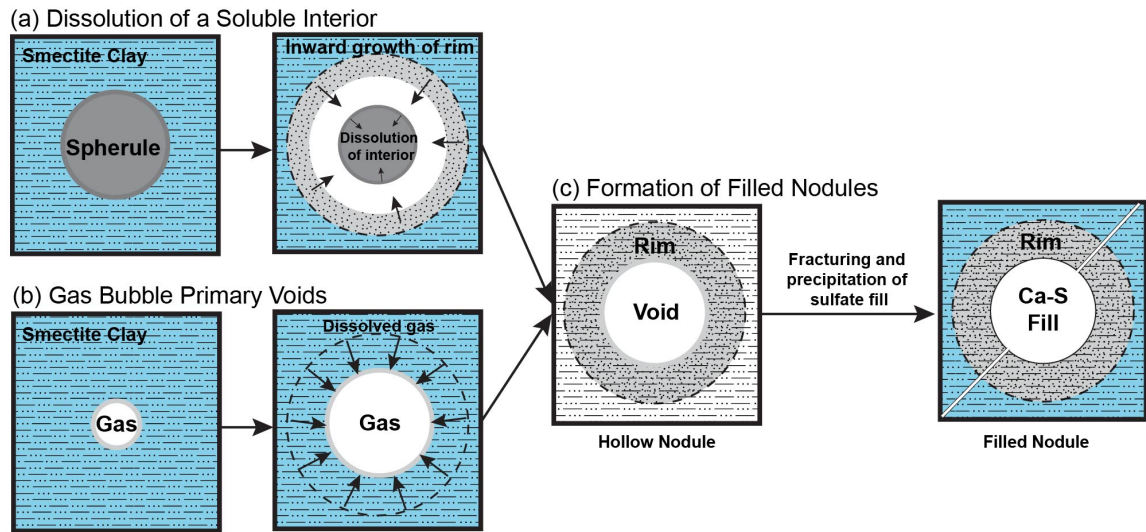


Figure 5.16

REFERENCES

Albee, A. L., et al. (2001), Overview of the Mars Global Surveyor Mission, *J. Geophys. Res.*, 106(E10), 23291-23316, doi:10.1029/2000JE001306.

Anderson, R. C., et al. (2012), Collecting samples in Gale crater, Mars; an overview of the Mars Science Laboratory Sample Acquisition, Sample Processing and Handling System, *Space Sci. Rev.*, 170(1-4), 57-75, doi:10.1007/s11214-012-9898-9.

Andrews-Hanna J. C., and K. W. Lewis (2011), Early Mars Hydrology: 2. Hydrological evolution in the Noachian and Hesperian Epochs, *J. Geophys. Res.*, 116(E02007), doi:10.1029/2010JE003709.

Andrews-Hanna, J. C., et al. (2010), Early Mars hydrology: Meridiani playa deposits and the sedimentary record of Arabia Terra, *J. Geophys. Res.*, 115(E6), doi:10.1029/2009je003485.

Arvidson, R. E., et al. (1989), The Martian Surface as Imaged, Sampled, and Analyzed by the Viking Landers, *Reviews of Geophysics*, 27(1), 39-60, doi:10.1029/RG027i001p00039.

Arvidson, R. E., et al. (2005), Spectral Reflectance and Morphologic Correlations in Eastern Terra Meridiani, Mars, *Science*, 307(5715), 1591-1594, doi:10.1126/science.1109509.

Arvidson, R. E., et al. (2014), Ancient Aqueous Environments at Endeavour Crater, Mars, *Science*, 343, doi: 10.1126/science.1248097.

Atkinson, D. J. (1962), Tectonic Control of Sedimentation and the Interpretation of Sediment Alternation in the Tertiary of Prince Charles Foreland, Spitsbergen, *Geol.*

Soc. of Am. Bull., 73(3), 343-364, doi:10.1130/0016-7606(1962)73[343:TCOSAT]

2.0.CO;2.

Awadallah, S. A. M., et al. (2001), Turbidite facies and bed-thickness characteristics inferred from microresistivity (FMS) images of Lower to Upper Pliocene rift-basin deposits, Woodlark Basin, offshore Papua New Guinea, in *Proc. ODP, Science Results*, vol. 180, edited by P. Huchon et al., pp. 1-29, ODP, College Station, TX, doi:10.2973/odp.proc.sr.180.166.2001.

Bandfield, J. L., et al. (2013), The dual nature of the martian crust: Young lavas and old clastic materials, *Icarus*, 222, 188-199, doi:10.1016/j.icarus.2012.10.023.

Baldridge, A. M., et al. (2009), Contemporaneous deposition of phyllosilicates and sulfates: Using Australian acidic saline lake deposits to describe geochemical variability on Mars, *Geophys. Res. Letts.*, 36(L19201), doi:10.1029/2009GL040069.

Banks, M. E., et al. (2009), An analysis of sinuous ridges in the southern Argyre Planitia, Mars using HiRISE and CTX images and MOLA data, *J. Geophys. Res.*, 114(E9), E09003, doi:10.1029/2008JE003244.

Bauerman, H. (1885), Report on the geology of the country near the forty-ninth parallel of north latitude west of the Rocky Mountains, from observations made 1859-61, *Canada Geol. Survey Rept. Prog. 1882-4*, 1-41.

Beattie, P. D., and W. B. Dade (1996), Is scaling in turbidite deposition consistent with forcing by earthquakes?, *J. of Sediment. Res.*, 66(5), 909-915, doi:10.1306/D4268437-2B26-11D7-8648000102C1865D.

Bhattacharya, J. P., et al. (2005), Dynamic river channels suggest a long-lived Noachian crater lake on Mars, *Geophys. Res. Lett.*, 32(10), L10201,

doi:10.1029/2005GL022747.

Bibring, J.-P., et al. (2004), OMEGA: Observatoire pour la Minéralogie, l'Eau, les Glaces et l'Activité, in *Mars Express: the scientific payload*, edited by A. Wilson, scientific coordination by A. Chicarro. pp. 37-49, ESA SP-1240, Noordwijk, Netherlands, ESA Publications Division, ISBN 92-9092-556-6.

Bibring, J.-P., et al. (2005), Mars Surface Diversity as Revealed by the OMEGA/Mars Express Observations, *Science*, 307(5715), 1576-1581, doi:10.1126/science.1108806.

Bibring, J.-P., et al. (2006), Global Mineralogical and Aqueous Mars History Derived from OMEGA/Mars Express Data, *Science*, 312(5772), 400-404. doi:10.1126/science.1122659.

Bibring, J.-P., et al. (2007), Coupled ferric oxides and sulfates on the Martian surface, *Science*, 317, 1206-1210, doi: 10.1126/science.1144174.

Bishop, J. L., et al. (1995a), Reflectance Spectroscopy of Ferric Sulfate-Bearing Montmorillonites as Mars Soil Analog Materials, *Icarus*, 117(1), 101-119. doi:10.1006/icar.1995.1145.

Bishop, J. L., C. M. Pieters, and J. O. Edwards (1995b), Infrared spectroscopic analyses on the nature of water in montmorillonite, *Clay and Clay Minerals*, 42, 702-716.

Bishop, J. L., et al. (2009), Mineralogy of Juventae Chasma: Sulfates in the light-toned mounds, mafic minerals in the bedrock, and hydrated silica and hydroxylated ferric sulfate on the plain, *J. Geophys. Res.*, 114(E00D09), doi:10.1029/2009JE003352.

Bishop, J. W., and D. Y. Sumner (2006), Molar tooth structures of the Neoarchean Monteville Formation, Transvaal Supergroup, South Africa. I: Constraints on

microcrystalline CaCO₃ precipitation, *Sedimentology*, 53(5), 1049-1068, doi:10.1111/j.1365-3091.2006.00801.x.

Bjørkum, P. A., and O. Walderhaug (1990), Geometrical arrangement of calcite cementation within shallow marine sandstones, *Earth-Sci. Rev.*, 29(1-4), 145-161, doi:[http://dx.doi.org/10.1016/0012-8252\(0\)90033-R](http://dx.doi.org/10.1016/0012-8252(0)90033-R).

Blackwelder, E., and H. H. Barrows (1911), *Elements of Geology*, 475 pp., American Book Company, New York, NY.

Blatt, H., et al. (1972), *Origin of Sedimentary Rocks*, 634 pp., Prentice-Hall, Englewood Cliffs, N. J.

Boudreau, B. P. et al. (2005), Bubble growth and rise in soft sediments, *Geology*, 33(6), 517-520, doi:10.1130/G21259.1.

Burgess, P. M. (2008), The nature of shallow-water carbonate lithofacies thickness distributions, *Geology*, 36(3), 235-238, doi:10.1130/G243326A.1.

Burr, D. M. (2003), Hydraulic modelling of Athabasca Vallis, Mars, *Hydrolog. Sci. J.*, 48(4), 655-664, doi:10.1623/hysj.48.4.655.51407.

Burr, D. (2005), Clustered streamlined forms in Athabasca Valles, Mars: Evidence for sediment deposition during floodwater ponding, *Geomorphology*, 69(1-4), 242-252, doi:10.1016/j.geomorph.2005.01.009.

Cadieux, S. B. (2011), *Constraining martian sedimentation via analysis of stratal packaging, intracrater layered deposits, Arabia Terra, Mars*, M. Sci. dissertation, University of Tennessee, Knoxville, TN.

Calvin, W. M., et al. (2008), Hematite spherules at Meridiani: Results from MI, Mini-TES, and Pancam, *J. Geophys. Res.*, 113(E12), E12S37, doi:10.1029/2007JE003048.

Campbell, J. L., et al. (2012), Calibration of the Mars Science Laboratory Alpha Particle X-ray Spectrometer, *Space Sci Rev*, 170(1-4), 319-340, doi:10.1007/s11214-012-9873-5.

Carlson, J., and J. P. Grotzinger (2001), Submarine fan environment inferred from turbidite thickness distributions, *Sedimentology*, 48(6), 1331-1351, doi:10.1046/j.1365-3091.2001.00426.x.

Carr, M. H. (1996), *Water on Mars*, 248 pp., Oxford University Press, New York, NY.

Carr, M. H. (2001), Mars Global Surveyor observations of Martian fretted terrain, *J. Geophys. Res.*, 106, 23571-23593, doi:10.1029/2000JE001316.

Carter, J., et al. (2013), Hydrous minerals on Mars as seen by the CRISM and OMEGA imaging spectrometers: Updated global view, *J. Geophys. Res.: Planets*, 118(4), 831-858, doi:10.1029/2012JE004145.

Caudill, C. M., et al. (2012), Layered MegaBlocks in the central uplifts of impact craters, *Icarus*, 221, 710-720, doi:10.1016/j.icarus.2012.08.033.

Chan, M. A., et al. (2004), A possible terrestrial analogue for hematite concretions on Mars, *Nature*, 429, 731-734, doi:10.1038/nature02600.

Chan, M. A., et al. (2005), Red Rock and Red Planet Diagenesis: Comparisons of Earth and Mars Concretions, *GSA Today*, 15(8), 4-10, doi:10.1130/1052-5173(2005)15[4:RRARPD]2.0.CO;2.

Chen, C., and R. N. Hiscott (1999), Statistical analysis of turbidite cycles in submarine fan successions; tests for short-term persistence, *J. of Sediment. Res.*, 69(2), 486-504.

Chan, M. A., et al. (2012), Characteristics of terrestrial ferric oxide concretions and implications for Mars, in *Sedimentary Geology of Mars*, SEPM Special Publication

No. 102, edited by J. P. Grotzinger and R. E. Milliken, pp. 253-270, SEPM, Tulsa, O. K., doi:10.2110/pec.12.102.0253.

Chicarro, A., et al. (2009), Mars Express: Summary of Scientific Results, in *ESA SP-129: Mars Express- The Scientific Investigations*, edited by A. Chicarro, pp. 3-11.

Christie-Blick, N., and N. W. Driscoll (1995), Sequence Stratigraphy, *Annu. Rev. Earth Planet. Sci.*, 23, 451-478, doi: 10.1146/annurev.earth.23.1.451.

Clark, R. N. (1983), Spectral properties of mixtures of montmorillonite and dark carbon grains: Implications for remote sensing minerals containing chemically and physically adsorbed water, *J. Geophys. Res.: Solid Earth*, 88(B12), 10635-10644, doi:10.1029/JB088iB12p10635.

Clark, R. N., and T. L. Roush (1984), Reflectance spectroscopy: Quantitative analysis techniques for remote sensing applications, *J. Geophys. Res.: Solid Earth*, 89(B7), 6329-6340, doi:10.1029/JB089iB07p06329.

Cloud, P. A. (1960), Gas as a sedimentary and diagenetic agent: *Am. Jour. Science*, 258-A (Bradley vol.), 35-45.

Combe, J. P., et al. (2008), Analysis of OMEGA/Mars Express data hyperspectral data using a Multiple-Endmember Linear Spectral Unmixing Model (MELSUM): Methodology and first results, *Planet. Space Sci.*, 56(7), 951-975, doi: 10.1016/j.pss.2007.12.007.

Cooper, C. D., and J. F. Mustard (1999), Effects of Very Fine Particle Size on Reflectance Spectra of Smectite and Palagonitic Soil, *Icarus*, 142(2), 557-570, doi:10.1006/icar.1999.6221.

Cooper, C. D., and J. F. Mustard (2002), Spectroscopy of Loose and Cemented Sulfate-Bearing Soils: Implications for Duricrust on Mars, *Icarus*, 158(1), 42-55, doi:10.1006/icar.2002.6874.

Criss, R.E., et al. (1988), *An Organic Origin for the Carbonate Concretions of the Ohio Shale*, pp. 21, U.S. Geological Survey Bull. 1836, U.S. Government Printing Office, Denver, CO.

Cutts, J. A. (1973), Nature and Origin of Layered Deposits of the Martian Polar Regions, *J. Geophys. Res.*, 78(20), 4231-4249, doi:10.1029/JB078i020p04231.

Dana, J. D. (1863), *Manual of geology*, Bliss & Co., Philadelphia, P.A.

Davis, J. C. (2002), *Statistics and Data Analysis in Geology*, 3rd ed., pp. 638, John Wiley & Sons, New York, NY.

Deegan, C. E. (1971), The mode of origin of some late diagenetic sandstone concretions from the Scottish Carboniferous, *Scottish J. of Geol.*, 7(4), 357-365, doi:10.1144/sjg07040357.

Dix, G. R. and H. T. Mullins (1987), Shallow, subsurface growth and burial alteration of Middle Devonian calcite concretions, *J. Sed. Petrol.*, 57(1), 140-152, doi:10.1306/212F8ACB-2B24-11D7-8648000102C1865D.

Drummond, C. N., and B. H. Wilkinson (1996), Statal thickness frequencies and the prevalence of orderedness in stratigraphic sequences, *J. Geol.*, 104(1), 1-18, doi:10.1086/629798.

Edgett, K. S. (2005), The sedimentary rocks of Sinus Meridiani: Five key observations from data acquired by the Mars Global Surveyor and Mars Odyssey orbiters, *Mars*, 1, 5-58, doi:10.1555/mars.2005.0002.

Edgett, K. S., and M. C. Malin (2002), Martian sedimentary rock stratigraphy: Outcrops and interbedded craters of northwest Sinus Meridiani and southwest Arabia Terra, *Geophys. Res. Lett.*, 29(24), 2179, doi:10.1029/2002GL016515.

Edgett, K. S., et al. (2012), Curiosity's Mars Hand Lens Imager (MAHLI) Investigation, *Space Sci. Rev.*, 170(1-4), 259-317, doi:10.1007/s11214-012-9910-4.

Edwards, C. S., et al. (2009), Global distribution of bedrock exposures on Mars using THEMIS high-resolution thermal inertia, *J. Geophys. Res.*, 114(E1101), doi:10.1029/2009JE003363.

Ehlmann, B. L. and J. F. Mustard (2012), An in-situ record of major environmental transitions on early Mars at Northeast Syrtis Major, *Geophys. Res. Lett.*, 39(L11202), doi:10.1029/2012GL051594.

Ehlmann, B. L., and C. S. Edwards (2014), Mineralogy of the Martian Surface, *Ann. Rev. of Earth and Planet. Sci.*, 42, 291-315, doi:10.1146/annurev-earth-060313-055024.

Ehlmann, B. L., et al. (2008), Orbital Identification of Carbonate-Bearing Rocks on Mars, *Science*, 322(5909), 1828-1832, doi:10.1126/science.1164759.

Ehlmann, B. L., et al. (2011), Subsurface water and clay mineral formation during the early history of Mars, *Nature*, 479, 53-60, doi:10.1038/nature10582.

Ehlmann, B. L., et al. (2011), Estimating modal mineralogy of mixtures with phyllosilicates using radiative transfer modeling of visible/near infrared spectra, 42nd Lunar Planet. Sci., Abstract 1704.

Emery, K. O. (1945), Entrapment of Air in Beach Sand, *J. Sed. Petrol.*, 15(2), 39-49.

Fairén, A., et al. (2014), Hollowed spherules identified with the MER Opportunity near and at Cape York, western rim of Endeavor Crater, Mars, 45th Lunar Planet. Sci.,

Abstract 1566.

Farley, K. A., et al. (2014), In Situ Radiometric and Exposure Age Dating of the Martian Surface, *Science*, 343(6169), doi:10.1126/science.1247166.

Fischer, A.G. (1964) The Lofer cyclothsems of the Alpine Triassic, in *Symposium on Cyclic Sedimentation*, vol. 169, edited by D. R. Merriam, pp. 107-149, KGS, Univ. of Kansas, Lawrence, KS.

Fishbaugh, K. E., et al. (2010a), Evaluating the meaning of “layer” in the Martian north polar layered deposits and the impact on the climate connection, *Icarus*, 205(1), 269-282, doi:10.1016/j.icarus.2009.04.011.

Fishbaugh, K. E., et al. (2010b), First high-resolution stratigraphic column of the Martian north polar layered deposits, *Geophys. Res. Lett.*, 37(7), L07201, doi:10.1029/2009GL041642.

Fleischer, P., et al. (2001), Distribution of free gas in marine sediments: a global overview, *Geo-Mar Lett*, 21(2), 103-122, doi:10.1007/s003670100072.

Flemings, P. B., and J. P. Grotzinger (1996), STRATA: Freeware for analyzing classic stratigraphic problems, *GSA Today*, 6(12).

Fralick, P., et al. (2012), Potential recognition of accretionary lapilli in distal impact deposits on Mars, in *Sedimentary Geology of Mars, SEPM Special Publication No. 102*, edited by J. P. Grotzinger and R. E. Milliken, pp. 211-227, SEPM, Tulsa, O. K, doi:10.2110/pec.12.102.0211.

Fueten, F., et al. (2008), Stratigraphy and structure of interior layered deposits in west Candor Chasma, Mars, from High Resolution Stereo Camera (HRSC) stereo imagery and derived elevations, *J. Geophys. Res.: Planets*, 113(E10), E10008, doi:

10.1029/2007JE003053.

Fueten, F., et al. (2011), Layer thickness determination of interior layered deposits, with particular emphasis on Candor Mensa, Mars, *Lunar Planet. Sci.*, XLII, Abstract 1255.

Furniss, G., et al. (1998), Gas bubble and expansion crack origin of "molar-tooth" calcite structures in the middle Proterozoic Belt Supergroup, western Montana, *J. Sediment. Res.*, 68(1), 104-114, doi:10.2110/jsr.68.104.

Galimov, E.M., and Y.P. Girin (1968), Variation in isotopic composition of carbon in the process of formation of carbonate concretions, *Geochem. Internat.*, 5(1), 178-182.

Gendrin, A., et al. (2005), Sulfates in Martian Layered Terrains: The OMEGA/Mars Express View, *Science*, 307(5715), 1587-1591, doi:10.1126/science.1109087.

Gilleaudeau, G. J., and L. C. Kah (2010), Molar-tooth crack formation and the Proterozoic marine substrate: Insights from the Belt Supergroup, Montana and the Atar Group, Mauritania, GSA Annual Meeting, Paper No. 51-7.

Gluyas, J. G. (1984), Early carbonate diagenesis within Phanerozoic shales and sandstones of the NW European shelf, *Clay Minerals*, 19(3), 309-321.

Grant, J. A., et al. (2008), HiRISE imaging of impact megabreccia and sub-meter aqueous strata in Holden Crater, Mars, *Geology*, 36(3), 195-198, doi:10.1130/G24340A.1.

Grant, J. A., et al. (2011), A lake in Uzboi Vallis and implications for Late Noachian-Early Hesperian climate on Mars, *Icarus*, 212 (1), 110-122, doi:10.1016/j.icarus.2010.11.024.

Grant, J. A., et al. (2014), The timing of alluvial activity in Gale crater, Mars, *Geophys. Res. Lett.*, 41(4), 1142-1149, doi:10.1002/2013GL058909.

Greeley, R., and J. E. Guest (1987), Geologic map of the eastern equatorial region of Mars, *U.S. Geol. Surv. Misc. Invest. Ser., I-1802B*.

Groshong, R. H. Jr. (1999), *3-D Structural Geology*, pp. 324, Springer, New York, NY.

Golombek, M. P., and N. T. Bridges (2000), Erosion rates on Mars and implications for climate change: Constraints from the Pathfinder landing site, *J. Geophys. Res.*, *105*(E1), 1841-1853, doi:10.1029/1999JE001043.

Golombek, M. P., et al. (2006), Erosion rates at the Mars Exploration Rover landing sites and long-term climate change on Mars, *J. Geophys. Res.*, *111*(E12S10), doi:10.1029/2006JE002754.

Golombek, M. P., et al. (1999), Overview of the Mars Pathfinder Mission: Launch through landing, surface operations, data sets, and science results, *J. Geophys. Res.*, *104*(E4), 8523-8553, doi:10.1029/98JE02554.

Grotzinger, J. P., et al. (2005), Stratigraphy and sedimentology of a dry to wet eolian depositional system, Burns formation, Meridiani Planum, Mars, *Earth and Planet. Sci. Lett.*, *240*(1), 11-72, doi:10.1016/j.epsl.2005.09.039.

Grotzinger, J., et al. (2011), The sedimentary record of Mars, *The Sediment. Rec.*, *9*(2), 4-8, doi:10.2110/sedred/2011.2.4.

Grotzinger, J. P., and R. E. Milliken (2012), The sedimentary rock record of Mars: Distribution, origins, and global stratigraphy, in *Sedimentary Geology of Mars, SEPM Special Publication No. 102*, edited by J. P. Grotzinger and R. E. Milliken, pp. 1-48, SEPM, Tulsa, OK.

Grotzinger, J. P., et al. (2012), Mars Science Laboratory Mission and Science Investigation, *Space Sci Rev*, *170*(1-4), 5-56, doi:10.1007/s11214-012-9892-2.

Grotzinger, J. P., et al. (2014), A Habitable Fluvio-Lacustrine Environment at Yellowknife Bay, Gale Crater, Mars, *Science*, 343(6169), doi:10.1126/science.1242777.

Hapke, B. (1993), *Theory of Reflectance and Emittance Spectroscopy*, 1st ed., Cambridge University Press, Cambridge, United Kingdom.

Harrison, T. N., et al. (2014), Global documentation of gullies with the Mars Reconnaissance Orbiter Context Camera (CTX) and implications for their formation, 45th Lunar Planet. Sci., Abstract 2124.

Hartmann, W. K., and G. Neukem (2001), Cratering chronology and the evolution of Mars, *Space Sci. Rev.*, 96(104), doi:10.1023/A:1011945222010.

Head, J. W., et al. (2003), Recent ice ages on Mars, *Nature*, 426, 797-802, doi:10.1038/nature02114.

Hiesinger, H., and J. W. Head III (2002), Topography and morphology of the Argyre Basin, Mars: implications for its geologic and hydrologic history, *Planet. and Space Sci.*, 50(10–11), 939-981, doi:10.1016/S0032-0633(02)00054-5.

Hinnov, L. A., and R. K. Goldhammer (1991), Spectral analysis of the Middle Triassic Latemar Limestone, *J. of Sediment. Res.*, 61(7), 1173-1193, doi:10.1306/D4267861-2B26-11D7-8648000102C1865D.

Hiroi, T., and C. M. Pieters (1994), Estimation of grain sizes and mixing ratios of fine powder mixtures of common geologic minerals, *J. Geophys. Res.: Planets*, 99(E5), 10867-10879. doi:10.1029/94JE00841.

Hover, V. C. et al. (1999), Mg-Smectite Authigenesis in a Marine Evaporative Environment, Salina Ometepec, Baja California, *Clays and Clay Minerals*, 47(3), 252-268.

Hovland, M. et al. (1993), The global flux of methane from shallow submarine sediments, *Chemosphere*, 26, 559-578, doi:10.1016/0045-6535(93)90442-8.

Howard, A. D. (1981), Etched plateau and braided ridges of the south polar region of Mars: Features produced by melting of ground ice?, in *Reports of Planetary Geology Program-1981*, NASA Tech. Memo, 84211, pp. 286 – 289, NASA Office of Space Science, Washington, D.C.

Hudson, J. D., and J. E. Andrews (1987), The diagenesis of the Great Estuarine Group, Middle Jurassic, Inner Hebrides, Scotland, *Geol. Soc., London, Spec. Pub.*, 36(1), 259-276, doi:10.1144/gsl.sp.1987.036.01.19.

Jaeger, W. L., et al. (2007), HiRISE observations of Athabasca Valles, Mars: A lava-draped channel system, *Science*, 317(5845), 1709–1711, doi:10.1126/science.1143315.

Jaeger, W. L., et al. (2010), Emplacement of the youngest flood lava on Mars: A short, turbulent story, *Icarus*, 205(1), 230-243, doi:10.1016/j.icarus.2009.09.011.

Jaumann, R., et al. (2007), The high-resolution stereo camera (HRSC) experiment on Mars Express: Instrument aspects and experiment conduct from interplanetary cruise through the nominal mission, *Planet. and Space Sci.*, 55(7–8), 928-952, doi:10.1016/j.pss.2006.12.003.

Jerolmack, D. J., and C. Paola (2010), Shredding of environmental signals by sediment transport, *Geophys. Res. Lett.*, 37(19), L19401, doi:10.1029/2010GL044638.

Kettler, R. M., et al. (2011), Follow the water: Connecting a CO₂ reservoir and bleacher sandstone to iron-rich concretions in the Navajo Sandstone of south-central Utah, REPLY to COMMENT, *Geology*, 39(11), E251-E252, doi:10.1130/G32550Y.1.

Lang, H. R., et al. (1987), Multispectral Remote Sensing as Stratigraphic and Structural Tool, Wind River Basin and Big Horn Basin Areas, Wyoming, *AAPG Bulletin*, 71(4), 389-402.

Laskar, J., et al. (2002), Orbital forcing of the Martian polar layered deposits, *Nature*, 419(6905), 375-377, doi:10.1038/nature01066.

Le Deit, L., et al. (2010), Morphology, stratigraphy, and mineralogical composition of a layered formation covering the plateaus around Valles Marineris, Mars: Implications for its geological history, *Icarus*, 208(2), 684-703, doi: 10.1016/j.icarus.2010.03.012.

Lewis, K. W. (2009), *The rock record of Mars: structure, sedimentology and stratigraphy*, Ph.D. dissertation, Dept. of Geol. and Planet. Sci., Caltech, Pasadena, CA.

Lewis, K. W., and O. Aharonson (2006), Stratigraphic analysis of the distributary fan in Eberswalde crater using stereo imagery, *J. Geophys. Res.*, 111(E6), E06001, doi:10.1029/2005JE002558.

Lewis, K. W., et al. (2008), Quasi-Periodic Bedding in the Sedimentary Rock Record of Mars, *Science*, 322(5907), 1532-1535, doi:10.1126/science.1161870.

Lewis, K. W., et al. (2010), Global significance of cyclic sedimentary deposits on Mars, *Lunar Planet. Sci.*, XLI, Abstract 2648.

Leverington, D. W. (2004), Volcanic rilles, streamlined islands, and the origin of outflow channels on Mars, *J. Geophys. Res.*, 109(E10), E10011, doi:10.1029/2004JE002311.

Lilliefors, H. W. (1967), On the Kolmogorov-Smirnov Test for Normality with Mean and Variance Unknown, *J. Am. Stat. Assoc.*, 62(318), 399-402.

Lilliefors, H. W. (1969), On the Kolmogorov-Smirnov Test for the Exponential Distribution with Mean Unknown, *J. Am. Stat. Assoc.*, 64(325), 387-389.

Limaye, A. B. S., et al. (2012), Detailed stratigraphy and bed thickness of the Mars north and south polar layered deposits, *J. Geophys. Res.*, 117(E6), E06009, doi:10.1029/2011JE003961.

Lowey, G. W. (1992), Variation in bed thickness in a turbidite succession, Dezadeash Formation (Jurassic-Cretaceous), Yukon, Canada: evidence of thinning-upward and thickening-upward cycles, *Sediment. Geol.*, 78(3-4), 217-232, doi:10.1016/0037-0738(92)90021-i.

Lucchitta B. K., et al. (1992), The canyon system of Mars, in *Mars*, edited by H. H. Kieffer et al., pp. 453-492, University of Arizona Press, Tucson.

Kargel, J. S., and R. G. Strom (1992), Ancient glaciation on Mars, *Geology*, 20(1), 3-7, doi:10.1130/0091-7613(1992)020<0003:AGOM>2.3.CO;2.

Kerber, L., et al. (2012), The dispersal of pyroclasts from ancient explosive volcanoes on Mars: Implications for the friable layered deposits, *Icarus*, 219, 358-381, doi:10.1016/j.icarus.2012.03.016.

Kirk, R. L., et al. (2008), Ultrahigh resolution topographic mapping of Mars with MRO HiRISE stereo images: Meter-scale slopes of candidate Phoenix landing sites, *J. Geophys. Res.*, 113(E3), E00A24, doi:10.1029/2007JE003000.

Knoke, R. (1966), Untersuchungen zur Diagenese und Kalkkonkretionen un umgebenden Tonschiefern. *Contributions to Mineral. and Petrol.*, 12, 139- 167.

Koch, G. S., and R. F. Link (1980), *Statistical Analysis of Geological Data*, pp. 832, Dover Publications, Inc., Mineola, NY.

Loope, D., et al. (2012), Rinded iron-oxide concretions: Hallmarks of altered siderite masses of both early and late diagenetic origin, *Sedimentology*, 59, 1769-1781, doi:10.1111/j.1365-3091.2012.01325.x.

Maki, J., et al. (2012), The Mars Science Laboratory Engineering Cameras, *Space Sci Rev*, 170(1-4), 77-93, doi:10.1007/s11214-012-9882-4.

Malin, M. C., and K. S. Edgett (2000), Sedimentary Rocks of Early Mars, *Science*, 290(5498), 1927-1937, doi:10.1126/science.290.5498.1927.

Malin, M. C., and K. S. Edgett (2001), Mars Global Surveyor Mars Orbiter Camera: Interplanetary cruise through primary mission, *J. Geophys. Res.*, 106(E10), 23429-23570, doi:10.1029/2000JE001455.

Malinverno, A. (1997), On the power law size distribution of turbidite beds, *Basin Res.*, 9(4), 263-274, doi:10.1046/j.1365-2117.1997.00044.x.

Mangold, N., et al. (2008), Spectral and geological study of the sulfate-rich region of West Candor Chasma, Mars, *Icarus*, 194(2), 519-543, doi:10.1029/2008JE003245.

Mangold, N., et al. (in review), Chemical variations of Yellowknife Bay Formation sediments analyzed by the Curiosity Rover on Mars, *J. Geophys. Res.: Planets*.

Maples, C. G. (1986), Enhanced paleoecological and paleoenvironmental interpretations result from analysis of early diagenetic concretions in Pennsylvanian shales, *PALAIOS*, 1(5), 512-516, doi:10.2307/3514633.

Marshall, D., and C. D. Anglin (2004), CO₂-clathrate destabilization: a new model of formation for molar tooth structures, *Precambrian Res.*, 129(3-4), 325-341, doi:<http://dx.doi.org/10.1016/j.precamres.2003.10.007>.

Martens, C. S., and R. A. Berner (1974), Methane Production in the Interstitial Waters of

Sulfate-Depleted Marine Sediments, *Science*, 185(4157), 1167-1169, doi:10.1126/science.185.4157.1167.

Martini, A. M. et al. (2002), Significance of early-diagenetic water-rock interactions in a modern marine siliciclastic/evaporate environment: Salina Ometepec, Baja California, *GSA Bulletin*, 114(9), 1055-1069.

Martill, D. M. (1990), Macromolecular resolution of fossilized muscle tissue from an elopomorph fish, *Nature*, 346(6280), 171-172.

Masursky, H. (1973), An overview of geological results from Mariner 9, *J. Geophys. Res.*, 78(20), 4009-4030, doi:10.1029/JB078i020p04009.

Maurice, S., et al. (2012), The ChemCam Instrument Suite on the Mars Science Laboratory (MSL) Rover: Science Objectives and Mast Unit Description, *Space Sci Rev*, 170(1-4), 95-166, doi:10.1007/s11214-012-9912-2.

Maxson, J. H. (1940), Gas pits in non-marine sediments, *J. Sediment. Res.*, 10(3), 142-145, doi:10.1306/d42690bc-2b26-11d7-8648000102c1865d.

McBride, E. F., et al. (1994), Oriented concretions, Ionian Coast, Italy; evidence of groundwater flow direction, *J. Sed. Res.*, 64(3a), 535-540, doi:10.1306/d4267dfc-2b26-11d7-8648000102c1865d.

McBride, E. F., et al. (1999), Origin of spheroidal chert nodules, Drunka Formation (Lower Eocene), Egypt, *Sedimentology*, 46(4), 733-755, doi:10.1046/j.1365-3091.1999.00253.x.

McEwen, A. S., et al. (2007), Mars Reconnaissance Orbiter's High Resolution Imaging Experiment (HiRISE), *J. Geophys. Res.*, 112(E05S02), doi:10.1029/2005JE002605.

McEwen, A. S., et al. (2010), The High Resolution Imaging Science Experiment (HiRISE)

during MRO's Primary Science Phase (PSP), *Icarus*, 205(1), 2-37, doi:10.1016/j.icarus.2009.04.023.

McKeown, N. K., et al. (2010), Spectral mixtures of clays and their impact on CRISM mineral identifications, 41st Lunar Planet. Sci., Abstract 2510.

McLennan, S. M., et al. (2005), Provenance and diagenesis of the evaporite-bearing Burns formation, Meridiani Planum, Mars, *Earth and Planet. Sci. Lett.*, 240(1), 95-121, doi:<http://dx.doi.org/10.1016/j.epsl.2005.09.041>.

McLennan, S. M., and J. P. Grotzinger (2008), The sedimentary rock cycle of Mars, in *The Martian Surface: Composition, Mineralogy, and Physical Properties*, edited by J. F. Bell III, pp. 541-577, Cambridge Univ. Press, Cambridge.

McLennan, S. M., et al. (2014), Elemental Geochemistry of Sedimentary Rocks at Yellowknife Bay, Gale Crater, Mars, *Science*, 343(6169), doi:10.1126/science.1244734.

Meunier, A. (2005), *Clays*, Springer Science and Business Media, 472 pp.

Metz, J. M. (2010), *A study of the record of ancient sedimentary rocks on Mars using MER, HiRISE, and CRISM images*, Ph.D. dissertation, Dept. of Geol. and Planet. Sci., Caltech, Pasadena, CA.

Milkovich, S. M., and J. W. Head, III (2005), North polar cap of Mars: Polar layered deposit characterization and identification of a fundamental climate signal, *J. Geophys. Res.*, 110(E1), E01005, doi:10.1029/2004JE002349.

Milliken, R. E., and J. F. Mustard (2007), Estimating the water content of hydrated minerals using reflectance spectroscopy: I. Effects of darkening agents and low-albedo materials, *Icarus*, 189(2), 550-573, doi:10.1016/j.icarus.2007.02.017.

Milliken, R. E., and D. L. Bish (2010), Sources and sinks of clay minerals on Mars, *Phil. Mag.*, 90(17-18), 2293-2308, doi:10.1080/14786430903575132.

Milliken, R. E., et al. (2003), Viscous flow features on the surface of Mars: Observations from high-resolution Mars Orbiter Camera (MOC) images, *J. Geophys. Res.*, 108(E6), 5057, doi:10.1029/2002JE002005.

Milliken, R. E., et al. (2008), Opaline silica in young deposits on Mars, *Geology*, 36(11), 847-850, doi:1130/G24967A.

Milliken, R. E., et al. (2010), Paleoclimate of Mars as captured by the stratigraphic record in Gale Crater, *Geophys. Res. Lett.*, 37(4), L04201, doi:10.1029/2009GL041870.

Ming, D.W., et al. (2014), Volatile and Organic Compositions of Sedimentary Rocks in Yellowknife Bay, Gale Crater, Mars, *Science*, 343(6169), doi:10.1126/science.1245267.

Minitti, M. E., et al. (2013), MAHLI at the Rocknest sand shadow: Science and science-enabling activities, *J. Geophys. Res.: Planets*, 118(11), 2013JE004426, doi:10.1002/2013JE004426.

Mitchum, R. M., Jr., and P. R. Vail (1977), Seismic stratigraphy and global changes of sea-level, Part 7: Stratigraphic interpretation of seismic reflection patterns in depositional sequences in *Seismic Stratigraphy- Applications to Hydrocarbon Exploration, AAPG Special Volumes*, vol. M 26, edited by C. E. Payton, pp.135-144, AAPG, Tulsa, OK.

Moore, J. M., and A. D. Howard (2005), Large alluvial fans on Mars, *J. Geophys. Res.*, 110(E4), E04005, doi:10.1029/2004je002352.

Moore, J. M., et al. (2003), Martian Layered Fluvial Deposits: Implications for Noachian

Climate Scenarios, *Geophys. Res. Lett.*, 30(24), 2292, doi:10.1029/2003GL019002.

Mozley, P. S., and J. M. Davis (2005), Internal structure and mode of growth of elongate calcite concretions: Evidence for small-scale, microbially induced, chemical heterogeneity in groundwater, *Geol. Soc. of Am. Bull.*, 117(11-12), 1400-1412, doi:10.1130/b25618.1.

Mozley, P. S. (1996), The internal structure of carbonate concretions in mudrocks: a critical evaluation of the conventional concentric model of concretion growth, *Sediment. Geol.*, 103(1-2), 85-91, doi:[http://dx.doi.org/10.1016/0037-0738\(95\)00087-9](http://dx.doi.org/10.1016/0037-0738(95)00087-9).

Murchie, S., et al. (2007), Compact Reconnaissance Imaging Spectrometer for Mars (CRISM) on Mars Reconnaissance Orbiter (MRO), *J. Geophys. Res.: Planets*, 112(E5), E05S03, doi:10.1029/2006JE002682.

Murchie, S., et al. (2009), Evidence for the origin of layered deposits in Candor Chasma, Mars, from mineral composition and hydrologic modeling, *J. Geophys. Res.*, 114, E00D05, doi:10.1029/2009JE003343.

Murray, B. C., et al. (1972), Geological framework of the south polar region of Mars, *Icarus*, 17(2), 328-345, doi:10.1016/0019-1035(72)90004-8.

Mustard, J. F., and C. M. Pieters (1987), Quantitative abundance estimates from bidirectional reflectance measurements, *J. Geophys. Res.: Solid Earth*, 92(B4), E617-E626, doi:10.1029/JB092iB04p0E617.

Mustard, J. F., and J. E. Hays (1997), Effects of Hyperfine Particles on Reflectance Spectra from 0.3 to 25 μm , *Icarus*, 125(1), 145-163, <http://dx.doi.org/10.1006/icar.1996.5583>.

Mustard, J. F., et al. (2001), Evidence for recent climate change on Mars from the identification of youthful near-surface ground ice, *Nature*, 412, 411-414, doi:10.1038/35086515.

Mustard, J. F., et al. (2008), Hydrated silicate minerals on Mars observed by the Mars Reconnaissance Orbiter CRISM instrument, *Nature*, 454(7202), 305-309, doi:10.1038/nature07097.

Nachon, M., et al. (2014) Calcium sulfate veins characterized by ChemCam/Curiosity at Gale Crater, Mars, *J. Geophys. Res- Planets*, doi:10.1002/2013JE004588.

Nash, D. B., and J. E. Conel (1974), Spectral reflectance systematics for mixtures of powdered hypersthene, labradorite, and ilmenite, *J. Geophys. Res.*, 79(11), 1615-1621, doi:10.1029/JB079i011p01615.

Neukum, G., et al. (2004), Recent and episodic volcanic and glacial activity on Mars revealed by the High Resolution Stereo Camera, *Nature*, 432(7020), 971-979, doi:10.1038/nature03231.

Newberry, J. S. (1873), Geology and Palaeontology, Part II. Palaeontology, *Rep. of the Geol. Survey of Ohio*, Volume 1, Nevins & Myers, Columbus, OH.

O'Connor, M.P. (1972), Classification and environmental interpretation of the cryptalgal organosedimentary “molar-tooth” structure from the late Precambrian Belt-Purcell Supergroup, *J. Geol.*, 80(5): 592-610, doi:10.1086/627783.

Okubo, C. H. (2010), Structural geology of Amazonian-aged layered sedimentary deposits in southwest Candor Chasma, Mars, *Icarus*, 207(1), 210-225, doi:10.1016/j.icarus.2009.11.012.

Okubo, C. H., and A. S. McEwen (2007), Fracture-Controlled Paleo-Fluid Flow in Candor

Chasma, Mars, *Science*, 315(5814), 983-985, doi:10.1126/science.1136855.

Orenberg, J., and J. Handy (1992), Reflectance spectroscopy of palagonite and iron-rich montmorillonite clay mixtures: Implications for the surface composition of Mars, *Icarus*, 96(2), 219-225. doi:10.1016/0019-1035(92)90076-J.

Orr, P. J., et al. (2000), Three-dimensional preservation of a non-biomineralized arthropod in concretions in Silurian volcaniclastic rocks from Herefordshire, England, *J. Geol. Soc.*, 157(1), 173-186, doi:10.1144/jgs.157.1.173.

Osterloo, M. M., et al. (2008), Chloride-Bearing Materials in the Southern Highlands of Mars, *Science*, 319(5870), 1651-1654, doi:10.1126/science.1150690.

Parker, T. J., et al. (1986), Morphology and distribution of sinuous ridges in central and southern Argyre, in *Reports of the Planetary Geology and Geophysics Program, NASA Tech. Memo 88383*, pp. 468-470, NASA Office of Space Sci., Washington, D.C.

Piatek, J. L., et al. (2004), Scattering properties of planetary regolith analogs, *Icarus*, 171(2), 531-545, doi:10.1016/j.icarus.2004.05.019.

Pollock, M. D., et al. (2006), Morphology of Molar-Tooth Structures in Precambrian Carbonates: Influence of Substrate Rheology and Implications for Genesis, *J. Sediment. Res.*, 76(2), 310-323, doi:10.2110/jsr.2006.021.

Pondrelli, M., et al. (2005), Complex evolution of paleolacustrine systems on Mars: An example from the Holden crater, *J. Geophys. Res.*, 110(E4), E04016, doi:10.1029/2004JE002335.

Pondrelli, M., et al. (2008), Evolution and depositional environments of the Eberswalde fan

delta, Mars, *Icarus*, 197(2), 429-451, doi:10.1016/j.icarus.2008.05.018.

Potter, S. L., et al. (2011), Characterization of Navajo Sandstone concretions: Mars comparison and criteria for distinguishing diagenetic origins, *Earth and Plan. Sci. Lett.*, 301, 444-456, doi:10.1016/j.epsl.2010.11.027.

Poulet, F., and S. Erard (2004), Nonlinear spectral mixing: Quantitative analysis of laboratory mineral mixtures, *J. Geophys. Res.: Planets*, 109(E2), E02009, doi:10.1029/2003JE002179.

Poulet, F., et al. (2005), Phyllosilicates on Mars and implications for early martian climate, *Nature*, 438(7068), 623-627. doi:10.1038/nature04274.

Poulet, F., R. E. Arvidson, C. Gomez, R. V. Morris, J.-P. Bibring, Y. Langevin, B. Gondet, J. Griffes (2008a), Mineralogy of Terra Meridiani and western Arabia Terra from OMEGA/MEx and implications for their formation, *Icarus*, 195(1), 106-130, doi:10.1016/j.icarus.2007.11.031.

Poulet, F., N. Mangold, D. Loizeau, J.-P. Bibring, Y. Langevin, J. Michalski, and B. Gondet (2008b), Abundance of minerals in the phyllosilicate-rich units on Mars, *A&A*, 487(2), L41-L44.

Poulet, F., et al. (2009), Quantitative compositional analysis of martian mafic regions using the MEX/OMEGA reflectance data 1. Methodology, uncertainties and examples of application, *Icarus*, 201(1), 69-83, doi:10.1016/j.icarus.2008.12.025.

Quantin, C., et al. (2012), Composition and structures of the subsurface in the vicinity of Valles Marineris as revealed by central uplifts of impact craters, *Icarus*, 221, 436-452, doi:10.1016/j.icarus.2012.07.031.

Raiswell, R. (1971), The Growth of Cambrian and Liassic Concretions, *Sedimentology*, 17(3-4), 147-171, doi:10.1111/j.1365-3091.1971.tb01773.x.

Raiswell, R. (1988), Evidence for surface reaction-controlled growth of carbonate concretions in shales, *Sedimentology*, 35(4), 571-575, doi:10.1111/j.1365-3091.1988.tb01236.x.

Raiswell, R. and N. J. M. White (1978), Spatial Aspects of Concretionary Growth in the Upper Lias of Northeast England, *Sed. Geol.*, 20, 291-300, doi:10.1016/0037-0738(78)90059-3.

Raiswell, R., and Q. J. Fisher (2000), Mudrock-hosted carbonate concretions: a review of growth mechanisms and their influence on chemical and isotopic composition, *J. Geol. Soc.*, 157(1), 239-251, doi:10.1144/jgs.157.1.239.

Read, J. F., and R. K. Goldhammer (1988), Use of Fischer plots to define third-order sea-level curves in Ordovician peritidal cyclic carbonates, Appalachians, *Geology*, 16(10), 895-899, doi:10.1130/0091-7613(1988)016<0895:UOFP>2.3.CO;2.

Reed, A. H., et al. (2005), Morphology of Gas Bubbles in Mud: A Microcomputed Tomographic Evaluation, *Proceedings of the International Conference "Underwater Acoustic Measurements: Technologies & Results"*, Herklion, Crete, Greece, 28th June- 1st July.

Ricci Lucchi, F. (1969), Channelized deposits in the Middle Miocene flysch of Romagna (Italy), *Giorn. Geol.*, 36(2), 203-282.

Rice, J. W., et al. (2003), Martian fluvial landforms: a THEMIS perspective after one year at Mars, *Lunar Planet. Sci.*, XXXIV, Abstract 2091.

Roach, L. H., et al. (2010), Hydrated mineral stratigraphy of Ius Chasma, Valles Marineris, *Icarus*, 206(1), 253-268, doi:10.1016/j.icarus.2009.09.003.

Rothman, D. H., and J. P. Grotzinger (1995), Scaling properties of gravity-driven sediments, *Nonlin. Process. Geophys.*, 2(3-4), 178-185, doi:10.5194/npg-2-178-1995.

Rothman, D. H., et al. (1994), Scaling in turbidite deposition, *J. Sediment. Res.*, 64(1a), 59-67, doi:10.1306/D4267D07-2B26-11D7-8648000102C1865D.

Sadler, P. M. (1981), Sediment accumulation rates and the completeness of stratigraphic sections, *J. Geol.*, 89(5), 569-584, doi:10.1086/628623.

Salvatore, M. R. and P. R. Christiansen (2014), Evidence for widespread aqueous sedimentation in the northern plains of Mars, *Geology*, doi:11.1130/G35319.1.

Schon, S. C., et al. (2009), A recent ice age on Mars: Evidence for climate oscillations from regional layering in mid-latitude mantling deposits, *Geophys. Res. Lett.*, 36(L15202), doi:10.1029/2009GL038554.

Schultz, C.B. (1941), The pipy concretions of the Arikaree, *Bulletin of the University of Nebraska State Museum*, 2(8), 69-81.

Scott, D. H. and K. L. Tanaka (1986), Geologic map of the western equatorial region of Mars, *U.S. Geol. Surv. Misc. Invest. Ser.*, I-1802A.

Seilacher, A. (2001), Concretion morphologies reflecting diagenetic and epigenetic pathways, *Sed. Geol.*, 143(1-2), 41-57, doi:[http://dx.doi.org/10.1016/S0037-0738\(01\)00092-6](http://dx.doi.org/10.1016/S0037-0738(01)00092-6).

Sgavetti, M., et al. (1995), Stratigraphic Correlation by Integrating Photostratigraphy and Remote Sensing Multispectral Data: An Example from Jurassic-Eocene Strata,

Northern Somalia, *AAPG Bulletin*, 79(11), 1571-1589.

Sharp, R. P. (1973), Mars: Troughed Terrain, *J. Geophys. Res.*, 78(20), 4063-4072, doi:10.1029/JB078i020p04063.

Shinn, E. A. (1968), Practical significance of birdseye structures in carbonate rocks, *J. Sediment. Res.*, 38(1), 215-223, doi:10.1306/74d7191f-2b21-11d7-8648000102c1865d.

Shkuratov, Y. G., et al. (1999), Opposition Effect from Clementine Data and Mechanisms of Backscatter, *Icarus*, 141(1), 132-155, doi: 10.1006/icar.1999.6154.

Siebach, K.L. et al. (2014) Subaqueous Shrinkage Cracks in the Sheepbed Mudstone: Implications for Early Fluid Diagenesis, Gale Crater, Mars, *J. Geophys. Res.*, doi:10.1002/2014JE004623.

Sills, G. C. and R. Gonzalez (2001), Consolidation of naturally gassy soft soil, *Geotechnique*, 51(7), 629-639, doi:10.1680/geot.2001.51.7.629.

Simonson, B. M. (2003), Petrographic criteria for recognizing certain types of impact spherules in well-preserved precambrian successions, *Astrobiology*, 3(1), 49-65, doi:10.1089/153110703321632417.

Simonson, B. M., and B. P. Glass (2004), Spherule Layers—Records of Ancient Impacts, *Ann. Rev. Earth and Planet. Sci.*, 32(1), 329-361, doi: 10.1146/annurev.earth.32.101802.120458.

Singer, R. B. (1981), Near-infrared spectral reflectance of mineral mixtures: Systematic combinations of pyroxenes, olivine, and iron oxides, *J. Geophys. Res.: Solid Earth*, 86(B9), 7967-7982. doi:10.1029/JB086iB09p07967.

Sloss, L. L. (1963), Sequences in the Cratonic Interior of North America, *Geol. Soc. Am.*

Bull., 74(2), 93-114, doi:10.1130/0016-7606(1963)74[93:SITCIO]2.0.CO;2.

Smith, A. G. (1968), The Origin and Deformation of Some "Molar-Tooth" Structures in the Precambrian Belt-Purcell Supergroup, *J. Geol.*, 76(4), 426-443, doi:10.1086/627341.

Smith, D. E., et al. (2001), Mars Orbiter Laser Altimeter: Experiment summary after the first year of global mapping of Mars, *J. Geophys. Res.*, 106(E10), 23689-23722, doi:10.1029/2000JE001364.

Smith, P. H., et al. (2009), H₂O at the Phoenix Landing Site, *Science*, 325(5936), 58-61, doi:10.1126/science.1172339.

Snyder, C. W. (1979), The extended mission of Viking, *J. Geophys. Res.: Solid Earth*, 84(B14), 7917-7933, doi:10.1029/JB084iB14p07917.

Soderblom, L. A., et al. (1973), Mariner 9 Observations of the Surface of Mars in the North Polar Region, *J. Geophys. Res.*, 78(20), 4197-4210, doi:10.1029/JB078i020p04197.

Soffen, G. A. (1976), Scientific Results of the Viking Missions, *Science*, 194(4271), 1274-1276, doi:10.1126/science.194.4271.1274.

Sorby, H. C. (1908), On the Application of Quantitative Methods to the Study of the Structure and History of Rocks, *Quarterly J. Geol. Soc.*, 64(1-4), 171-232, NP-NP, 233, doi:10.1144/gsl.jgs.1908.064.01-04.12.

Souness, C., et al. (2012), An inventory and population-scale analysis of martian glacier-like forms, *Icarus*, 217, 243-255, doi:10.1016/j.icarus.2011.10.020.

Squyres, S. W., and M. H. Carr (1986), Geomorphic evidence for the distribution of ground ice on Mars, *Science*, 231(4735), 249-252, doi:10.1126/science.231.4735.249.

Squyres, S. W., et al. (2003), The Athena Mars rover science investigation, *J. Geophys. Res.*, 108, 8062, doi:10.1029/2003JE002121.

Squyres, S. W., et al. (2004a), The Spirit rover's Athena science investigation at Gusev Crater, Mars, *Science*, 305(5685), 794-799, doi:10.1126/science.3050794.

Squyres, S. W., et al. (2004b), The Opportunity Rover's Athena Science Investigation at Meridiani Planum, Mars, *Science*, 306(5702), 1698-1703, doi:10.1126/science.1106171.

Squyres, S. W., et al. (2004c), In Situ Evidence for an Ancient Aqueous Environment at Meridiani Planum, Mars, *Science*, 306(5702), 1709-1714, doi:10.1126/science.1104559.

Squyres, S. W., et al. (2007), Pyroclastic Activity at Home Plate in Gusev Crater, Mars, *Science*, 316(5825), 738-742, doi:10.1126/science.1139045.

Sumner, D. Y. (2004), Poor preservation potential of organics in Meridiani Planum hematite-bearing sedimentary rocks, *J. Geophys. Res.: Planets*, 109(E12), E12007, doi:10.1029/2004JE002321.

Sylvester, Z. (2007), Turbidite bed thickness distributions: methods and pitfalls of analysis and modelling, *Sedimentology*, 54(4), 847-870, doi:10.1111/j.1365-3091.2007.00863.x.

Talling, P. J. (2001), On the frequency distribution of turbidite thickness, *Sedimentology*, 48(6), 1297-1329, doi:10.1046/j.1365-3091.2001.00423.x.

Tanaka, K. L. (1986), The Stratigraphy of Mars, *J. Geophys. Res.*, 91(B13), E139-E158, doi:10.1029/JB091iB13p0E139.

Tanaka, K. L., and D. H. Scott (1987), Geologic map of the polar regions of Mars, *U.S.*

Geol. Surv. Misc. Invest. Ser., I-1802C.

Tarbuck, E. J., et al. (2004), *Earth: An Introduction to Physical Geology*, 8th ed., pp. 736, Prentice Hall.

Themelis, K. E., et al. (2012), On the unmixing of MEx/OMEGA hyperspectral data,

Planet. Space Sci., 68(1), 34-41, doi:10.1016/j.pss.2011.11.015.

Thomson, B. J., et al. (2011), Constraints on the origin and evolution of the layered mound in Gale Crater, Mars using Mars Reconnaissance Orbiter data, *Icarus*, 214(2), 413-432, doi:10.1016/j.icarus.2011.05.002.

Tomkiew, S. (1927), On the occurrence and mode of origin of certain kaolinite-bearing nodules in the coal measures, *Proc. Geolog. Assoc.*, 38(4), 518-IN518, doi:[http://dx.doi.org/10.1016/S0016-7878\(27\)80017-9](http://dx.doi.org/10.1016/S0016-7878(27)80017-9).

Tornabene, L. L., et al. (2010), A crater-exposed bedrock database for mars with applications for determining the composition and structure of the upper crust, 41st Lun. Planet. Sci., Abstract 1737.

van der Burg, W. J. (1969), The formation of rattle stones and the climatological factors which limited their distribution in the Dutch Pleistocene, 1. The formation of rattle stones, *Palaeogeog., Palaeoclim., Palaeoecol.*, 6, 105-124, doi:10.1016.0031-0182(69)90007-8.

van der Burg, W. J. (1970), The formation of rattle stones and the climatological factors which limited their distribution in the Dutch Pleistocene, 2. The climatological factors, *Palaeogeog., Palaeoclim., Palaeoecol.*, 7, 297-308, doi:10.1016.0031-0182(70)90098-2.

van Kessel, T., and W. G. van Kesteren (2002), Gas production and transport in artificial sludge depots, *Waste Management*, 22(1), 19-28.

Vaniman, D. T., et al. (2014), Mineralogy of a Mudstone at Yellowknife Bay, Gale Crater, Mars, *Science*, 343(6169), doi:10.1126/science.1243480.

Watters, W. A., et al. (2011), Origin of the structure and planform of small impact craters in fractured targets: Endurance Crater at Meridiani Planum, Mars, *Icarus*, 211(1), 472-497, doi:10.1016/j.icarus.2010.08.030.

Weber, K. et al. (2012), Biosignatures link microorganisms to iron mineralization in a paleoaquifer, *Geology*, 40, 747-750, doi:10.1130/G33062.1.

Weitz, C. M., et al. (2008), Light-toned strata and inverted channels adjacent to Juventae and Ganges chasmata, Mars, *Geophys. Res. Lett.*, 35(19), L19202, doi:10.1029/2008GL035317.

Weitz, C. M., et al. (2010), Mars Reconnaissance Orbiter observations of light-toned layered deposits and associated fluvial landforms on the plateau adjacent to Valles Marineris, *Icarus*, 205(1), 73-102, doi:10.1016/j.icarus.2009.04.017.

Wheeler, H. E. (1958), Time-stratigraphy, *AAPG Bull.*, 42(5), 1047-1063.

Wheeler, H. E. (1959), Unconformity-bounded units in stratigraphy, Note 24 of American Commission on Stratigraphic Nomenclature, *AAPG Bull.*, 43(8), 1975-1977, doi:10.1306/0BDA5E85-16BD-11D7-8645000102C1865D.

Wiens, R., et al. (2012), The ChemCam Instrument Suite on the Mars Science Laboratory (MSL) Rover: Body Unit and Combined System Tests, *Space Sci Rev*, 170(1-4), 167-227, doi:10.1007/s11214-012-9902-4.

Wiens R. C., et al., (2013), Pre-flight calibration and initial data processing for the ChemCam laser-induced breakdown spectroscopy (LIBS) instrument on the Mars Science Laboratory rover, *Spectrochim. Acta, Part B*, 82, 1-27, doi:10.1016/j.sab.2013.02.003.

Wilkinson, B. H., and C. N. Drummond (2004), Facies Mosaics Across the Persian Gulf and Around Antigua—Stochastic and Deterministic Products of Shallow-Water Sediment Accumulation, *J. Sediment. Res.*, 74(4), 513-526, doi:10.1306/123103740513.

Wilkinson, B. H., et al. (1997), Stratigraphic order in peritidal carbonate sequences, *J. Sediment. Res.*, 67(6), 1068-1082, doi:10.1306/D42686CB-2B26-11D7-8648000102C1865D.

Wilkinson, B. H., et al. (1999), Poisson processes of carbonate accumulation on Paleozoic and Holocene platforms, *J. Sediment. Res.*, 69(2), 338-350.

Williams, R. M. E. (2007), Global Spatial Distribution of Raised Curvilinear Features on Mars, *Lunar Planet. Sci.*, XXXVIII, Abstract 1821.

Williams, R. M. E., et al. (2013), Martian Fluvial Conglomerates at Gale Crater, *Science*, 340(6136), 1068-1072, doi:10.1126/science.1237317.

Wiseman, S. M., et al. (2010), Spectral and stratigraphic mapping of hydrated sulfate and phyllosilicate-bearing deposits in northern Sinus Meridiani, Mars, *J. Geophys. Res.: Planets*, 115(E7), E00D18, doi:10.1029/2009JE003354.

Wray, J. J., et al. (2010), Identification of the Ca-sulfate bassanite in Mawrth Vallis, Mars, *Icarus*, 209(2), 416-421, doi:10.1016/j.icarus.2010.06.001.

Wray, J. J., et al. (2011), Columbus crater and other possible groundwater-fed paleolakes of Terra Sirenum, Mars, *J. Geophys. Res.*, 116, E01001, doi:10.1029/2010JE003694.

Zurek, R. W. and S. E. Smrekar (2007), An overview of the Mars Reconnaissance Orbiter (MRO) Science Mission, *J. Geophys. Res.*, 112(E5), doi:10.1029/2006JE002701.

APPENDIX A

Auxiliary material for Chapter 3 Bed Thickness Distributions on Mars: An Orbital Perspective

Introduction

The auxiliary materials contain a detailed description of the error analysis performed on bed thickness measurements and subsequent averages and totals presented in Table 3.3. Also included in this appendix is Table A1 which the individual measurements of bed orientation made at each study site used to calculate thickness values presented in the main body of the text. Table A2 contains linear regression results testing for thinning and thickening trends in sections measured with the 1 m orthoimages. This dataset supports statements made in the main text of Chapter 3. Topographic profiles along which bed thickness were measured are presented in are presented in Figure A1. These profiles were extracted from HiRISE DTMs.

Error Analysis, a detailed explanation of error analysis performed on bed thickness measurements.

Table A1. Individual measurements and averages of bed orientation at each study location that were used in the calculation of true bed thickness.

Table A2. Linear regression results for the 1 m stratigraphic sections, used to determine whether or not statistically significant thinning or thickening upwards trends existed in the data.

Figure A1 DTM-extracted topographic profiles along which stratigraphic sections and bed thickness were measured.

Error Analysis

The purpose of this section is to explain the calculation of error and error bars for orientation and bed thickness measurements presented in the manuscript.

Error of α

Error was calculated for each α according to the following equation, using the error of strike measurements (listed in ts01):

$$\Delta\alpha = 1/n \times \sqrt{\sum_{i=1}^n \Delta\text{strike}_i^2} \quad (\text{A1})$$

Error of δ

Error was calculated for the average dip measurements according to the following equation, using the error of individual dip measurements (listed in ts01):

$$\Delta\delta = 1/n \times \sqrt{\sum_{i=1}^n \Delta\delta_i^2} \quad (\text{A2})$$

Error of bed thickness, t , measurements

To calculate error bars for each bed thickness measurement, we propagate the errors of orientation measurements (α, δ) as well as the errors in the DTM (DTM resolution and vertical precision), according to the mathematical operations in the Eqs. 5 and 6 presented in the main text.

Bed thickness is calculated according to the following equations:

$$t = |h \cos \alpha \sin \delta - v \cos \delta| \quad (3.5)$$

$$t = h \cos \alpha \sin \delta + v \cos \delta \quad (3.6)$$

Depending on whether the dip of the beds is in the same or opposite direction as the topographic slope. Thickness error is:

$$\Delta t = \sqrt{(\Delta h \cos \alpha \sin \delta)^2 + (\Delta v \cos \delta)^2} \quad (\text{A3})$$

The horizontal distance, h , along the measured section line between the upper and lower bed boundaries is calculated using (x, y) coordinates extracted from the DTM and the distance formula.

$$h = \sqrt{(x_2 - x_1)^2 + (y_2 - y_1)^2} \quad (\text{A4})$$

The absolute error of h is therefore:

$$\Delta h = 1/2 \times h \times \{\Delta[(x_2 - x_1)^2 + (y_2 - y_1)^2]/[(x_2 - x_1)^2 + (y_2 - y_1)^2]\} \quad (\text{A5})$$

Where:

$$\Delta[(x_2 - x_1)^2 + (y_2 - y_1)^2] = \sqrt{[\Delta(x_2 - x_1)]^2 + [\Delta(y_2 - y_1)]^2} \quad (\text{A6})$$

$$\Delta[(x_2 - x_1)^2] = 2 \times (x_2 - x_1)^2 \times \sqrt{\Delta(x_2 - x_1)}/(x_2 - x_1) \quad (\text{A7})$$

$$\Delta[(y_2 - y_1)^2] = 2 \times (y_2 - y_1)^2 \times \sqrt{\Delta(y_2 - y_1)}/(y_2 - y_1) \quad (\text{A8})$$

Since DEM horizontal resolution is 1 m:

$$\Delta(x_2 - x_1) = \sqrt{(\Delta DEM)^2 + (\Delta DEM)^2} = \sqrt{1^2 + 1^2} = \sqrt{2} \quad (\text{A9})$$

$$\Delta(y_2 - y_1) = \sqrt{(\Delta DEM)^2 + (\Delta DEM)^2} = \sqrt{1^2 + 1^2} = \sqrt{2} \quad (\text{A10})$$

The elevation difference between the upper and lower boundaries for each bed is calculated according to the formula:

$$v = |z_2 - z_1| \quad (\text{A11})$$

The absolute error of v is calculated by propagating the error of the two elevation values, assumed here to be the expected vertical precision of the DEM, EP :

$$\Delta v = \sqrt{(EP)^2 + (EP)^2} \quad (\text{A12})$$

$$\Delta(v \cos \delta) = v \cos \delta \times \sqrt{(\Delta v/v)^2 + (\Delta(\cos \delta)/\cos \delta)^2} \quad (\text{A13})$$

Where error is approximated in trigonometric functions by the following equations:

$$\Delta(\cos \alpha) = |\cos \alpha - \cos(\alpha + \Delta \alpha)| \quad (\text{A14})$$

$$\Delta(\sin \delta) = |\sin \delta - \sin(\delta + \Delta \delta)| \quad (\text{A15})$$

$$\Delta(\cos \delta) = |\cos \delta - \cos(\delta + \Delta \delta)| \quad (\text{A16})$$

By substituting Eqs. A1, A2, and A4-A16 into Eq. A3, the following equation is derived for the propagated absolute error of each thickness measurement:

$$\Delta t = \sqrt{(h \cos\alpha \sin\delta \sqrt{(1/2 \times \sqrt{(2\sqrt{2}(x_i - x_j))^2 + (2\sqrt{2}(y_i - y_j))^2})^2 + (\frac{|\cos\alpha - \cos(\alpha + \Delta\alpha)|}{\cos\alpha})^2 + (\frac{|\sin\delta - \sin(\delta + \Delta\delta)|}{\sin\delta})^2)}^2 + (v \cos\delta \sqrt{(\frac{\sqrt{(EP)^2 + (EP)^2}}{v})^2 + (\frac{|\cos\delta - \cos(\delta + \Delta\delta)|}{\cos\delta})^2})^2} \quad (A17)$$

For sections where no correction is made for the dip of the beds, bed thickness error is:

$$\Delta t = \Delta v = \sqrt{(EP)^2 + (EP)^2} \quad (A18)$$

where EP is the DTM expected precision.

Error of Total Section Thickness

Since the total section thickness (Table 3) was calculated by adding all individual bed thickness measurements for a section, the error of total section thickness was calculated by the formula:

$$\Delta TotalThickness = \sqrt{\sum_{i=1}^n \Delta t_i^2} \quad (A19)$$

Error of Mean Bed Thickness

Mean bed thickness for each section was calculated by adding all individual bed thickness measurements for a section, then dividing by the number of beds. Error of mean bed thickness is calculated by the formula:

$$\Delta MeanThickness = 1/n \times \sqrt{\sum_{i=1}^n \Delta t_i^2} \quad (A20)$$

Table A1. Bed Orientation Measurements

Measurement	Strike	Error strike	Dip	Error dip	Std resid	Collinearity	Dip_dir	Alpha	Dir_slope
H1_0	307	10	0.6	0.1	3.31	3.96E-05			
H1_2	75	20	0.9	0.2	0.52	6.33E-04			
H1_5	174	4	3.6	0.5	2.21	3.90E-03			
H1_6	70	16	3.0	0.2	2.11	1.37E-03			
H1_7	135	6	2.3	0.2	2.11	7.27E-04			
H2_0	320	8	1.2	0.1	1.17	5.45E-04			
H2_2	321	3	2.1	0.1	0.50	2.16E-04			
average	321 ± 4		1.7 ± 0.1				51 ± 4	23 ± 4	same
H3_9	26	12	1.4	0.1	5.38	6.63E-04			
H3_15	295	21	1.7	0.2	2.27	1.27E-03			
H3_16	296	14	2.1	0.2	1.37	1.21E-03			
H3_18	297	12	1.0	0.1	1.85	1.06E-04			
H3_19	300	9	2.3	0.2	0.53	1.45E-03			
H3_20	318	22	1.3	0.3	4.78	2.18E-03			
average	315 ± 6		1.7 ± 0.1				45 ± 6	0 ± 6	opposite
H4_23	314 ± 9	9	2.8 ± 0.3	0.3	1.20	4.52E-03	44 ± 9	0 ± 9	opposite
H6_74	334 ± 10	10	2.0 ± 0.5	0.5	6.07	6.69E-03	64 ± 10	50 ± 10	same
H7_47	179	6	1.8	0.5	4.60	4.16E-03			
H7_48	167	5	4.0	0.8	0.74	3.91E-03			
average	173 ± 4		2.9 ± 0.5				263 ± 4	0 ± 4	same
H8_50	157 ± 8	8	1.4 ± 0.2	0.2	4.17	1.23E-03	247 ± 8	80 ± 8	same
H9_59	311	6	1.2	0.1	1.08	2.32E-04			
H9_60	297	10	2.1	0.3	1.08	9.27E-04			
H9_61	297	5	1.6	0.1	1.28	1.73E-04			
H9_62	328	2	1.5	0.0	0.97	7.69E-05			
average	308 ± 3		1.6 ± 0.1				38 ± 3	22 ± 3	opposite
H10_70	98	2	2.3	0.4	0.90	2.47E-03			
H10_71	276	3	1.5	0.2	1.29	4.15E-04			
wj_0	278	34	1.6	0.1	1.91	4.85E-04			
wj_1	242	9	1.2	0.1	2.65	1.41E-04			
wj_3	277	25	1.2	0.2	1.01	2.38E-04			
wj_4	176	19	0.6	0.2	11.5	8.04E-04			
					2				
wj_5	331	12	1.7	0.2	5.06	6.05E-04			
wj_6	104	28	0.5	0.2	4.23	3.25E-04			
wj_7	50	15	1.3	0.3	1.9	1.75E-03			
wj_8	339	42	0.2	0.1	19.1	2.63E-04			
					2				
wj_9	115	38	0.5	0.2	2.62	6.06E-04			
wj_10	336	9	0.9	0.1	2.03	3.71E-04			
wj_11	103	38	0.4	0.1	2.74	1.37E-04			
wj_12	184	49	0.3	0	315.	4.17E-04			
					51				
wj_13	100	8	1.2	0.1	0.63	3.10E-04			
wj_15	41	21	0.6	0.2	4.61	6.09E-04			
wj_16	53	7	3.8	0.3	0.24	2.30E-03			
wj_19	333	15	0.2	0	4.67	4.42E-05			
wj_20	278	8	2.8	0.3	0.48	9.37E-04			
wj_21	234	21	0.3	0.1	7.05	1.31E-04			
wj_22	50	28	0.2	0.1	2.78	9.27E-05			

Measurement	Strike	Error strike	Dip	Error dip	Std resid	Collinearity	Dip_dir	Alpha	Dir_slope
wj_23	247	8	0.8	0.1	0.84	1.12E-04			
wj_24	238	5	0.3	0	1.28	1.08E-05			
wj_25	251	8	0.4	0	1.27	1.70E-05			
wj_26	192	17	0.4	0.1	6.96	1.45E-04			
wj_28	354	22	0.3	0.3	12.3	1.16E-03			
					2				
wj_29	1	2	1	0.1	1.1	3.02E-04			
wj_34	345	5	1.1	0.2	1.09	4.97E-04			
wj_35	305	4	1.9	0.1	0.29	2.09E-04			
wj_36	310	7	1.3	0.1	0.58	3.15E-04			
wj_37	308	19	0.7	0.2	6.44	4.71E-04			
wj_38	338	46	0.1	0.1	8.19	4.94E-05			
wj_39	173	3	0.7	0.2	0.54	2.72E-04			
wj_41	52	30	0.8	0.2	6.06	6.16E-04			
wj_42	26	15	1.1	0.4	2.21	1.62E-03			
wj_43	84	46	0.4	0.1	2.06	1.03E-04			
wj_44	73	34	0.4	0.2	4.12	4.82E-04			
wj_45	334	3	0.4	0	1.78	9.96E-06			
wj_47	203	8	0.6	0.2	4.61	3.04E-04			
wj_48	7	7	1.2	0.2	3.58	3.50E-04			
wj_49	349	25	0.2	0.1	7.75	2.41E-04			
wj_50	323	39	0.3	0.1	13.8	4.24E-04			
					9				
wj_51	284	33	1.4	0.6	0.89	3.07E-03			
wj_52	120	19	1.5	0.4	1.73	1.47E-03			
wj_53	172	21	0.4	0.1	9.13	3.29E-04			
wj_55	41	35	0.2	0.1	10.4	1.81E-04			
					7				
wj_56	140	34	0.3	0.1	4.39	2.48E-04			
wj_57	240	24	0.9	0.3	4.36	9.45E-04			
wj_58	211	22	0.8	0.2	6.17	1.43E-03			
wj_59	205	12	1.5	0.4	1.53	1.54E-03			
wj_64	182	6	0.5	0.1	3.94	3.91E-05			
wj_65	108	28	0.6	0.2	5.72	5.60E-04			
wj_66	144	22	1.2	0.3	5.54	1.68E-03			
wj_67	104	22	0.9	0.3	2.37	5.20E-04			
wj_68	203	8	0.7	0.1	3.28	1.18E-04			
wj_69	209	5	0.5	0	1.38	3.15E-05			
wj_71	222	13	0.6	0.1	4.63	2.62E-04			
wj_72	234	47	0.4	0.3	8.13	9.24E-04			
wj_73	297	7	1.5	0.1	1.89	7.99E-05			
wj_74	188	11	0.4	0.1	4.8	5.16E-05			
wj_76	253	39	1	0.1	4.36	3.78E-04			
wj_77	142	9	0.6	0.1	2.29	1.19E-04			
wj_78	52	8	1	0.1	1.89	1.15E-04			
wj_79	172	42	0.4	0.1	315.	8.95E-04			
					34				
wj_80	227	39	0.6	0.3	4.99	7.43E-04			
wj_81	199	10	0.8	0.2	2.45	2.87E-04			
wj_82	204	12	1.7	0.4	1.58	1.19E-03			
wj_83	235	33	1.1	0.3	2.82	2.00E-03			

Measurement	Strike	Error strike	Dip	Error dip	Std resid	Collinearity	Dip_dir	Alpha	Dir_slope
wj_84	248	11	2.4	0.2	0.85	7.55E-04			
wj_85	47	8	0.9	0.1	1.02	8.53E-05			
wj_88	132	35	0.7	0.3	5.2	1.62E-03			
wj_89	214	8	1.2	0.1	1.43	2.54E-04			
wj_90	165	2	1.1	0.1	0.86	7.88E-05			
wj_91	150	23	0.6	0.3	7.3	9.18E-04			
wj_94	260	41	1	0.1	3.96	2.59E-04			
wj_97	346	3	2.5	0.4	1.5	9.80E-04			
wj_98	177	7	0.3	0.1	6.07	2.27E-04			
wj_99	309	20	0.3	0.1	7.72	1.29E-04			
argyre_1	347	4	1.6	0.3	2.90	1.26E-03			
argyre_2	347	1	3.3	0.2	0.24	4.51E-04			
argyre_3	333	5	2.2	0.3	1.39	1.39E-03			
argyre_16	354	4	2.0	0.7	0.93	4.13E-03			
argyre_19	334	27	0.7	0.6	5.69	3.43E-03			
average	347 ± 6		2.0 ± 0.2				77 ± 6	0 ± 6	same
athabasca_0	200	23	0.1	0	9.1	4.48E-05			
athabasca_1	285	41	0.1	0.1	4.56	3.61E-05			
athabasca_2	80	27	0.7	0.1	1.99	1.56E-04			
athabasca_4	28	16	0.2	0	7.35	4.40E-05			
athabasca_5	148	12	0.4	0.1	3.63	5.42E-05			
athabasca_7	17	25	1.4	0.3	11.4	2.21E-03			
					7				
athabasca_1	179	28	0.2	0.1	335.	9.91E-05			
0					53				
athabasca_1	137	7	0.3	0	1.32	1.39E-05			
1									
athabasca_1	40	15	0.3	0.1	5.47	1.00E-04			
3									
athabasca_1	212	25	0.5	0.2	8.78	3.94E-04			
5									
becquerel_3	59	22	2.3	0.3	3.86	2.89E-03			
5									
becquerel_3	50	4	2.1	0.1	0.43	3.53E-04			
8									
becquerel_3	46	4	2.2	0.1	0.66	2.44E-04			
9									
becquerel_4	52	16	1.9	0.3	2.61	2.64E-03			
0									
becquerel_4	56	27	2.4	0.5	4.58	4.17E-03			
1									
becquerel_4	36	5	3.5	0.2	0.33	1.70E-03			
9									
becquerel_5	34	4	4	0.3	0.23	9.80E-04			
0									
becquerel_5	36	2	4.3	0.1	0.25	4.72E-04			
1									
becquerel_5	53	4	2.6	0.1	0.78	4.55E-04			
2									
becquerel_5	46	3	3.5	0.1	0.31	4.79E-04			

Measurement	Strike	Error strike	Dip	Error dip	Std resid	Collinearity	Dip_dir	Alpha	Dir_slope
3									
becquerel_5	65	29	0.7	0.1	6.99	3.62E-04			
5									
average	49 ± 4		2.7 ± 0.1				139 ± 4	0 ± 4	opposite
candor2_0	150	2	9.7	0.2	1.07	1.39E-03			
candor2_1	126	2	11.6	0.3	0.62	1.42E-03			
candor2_5	105	7	8.6	0.4	1.09	2.86E-03			
candor2_7	103	5	8.7	0.4	0.65	1.81E-03			
average	121 ± 2		9.7 ± 0.2				211 ± 2	66 ± 2	opposite
candor1_9	179	3	1.2	0.1	1.81	9.50E-05			
candor1_15	192	2	2.1	0.1	0.83	1.82E-04			
average	186 ± 2		2.0 ± 0.1				276 ± 2	0 ± 2	same
cross_2	291	9	2	0.2	1.4	4.75E-04			
cross_10	236	6	3.7	0.2	0.62	1.11E-03			
average	264 ± 6		2.9 ± 0.1				354 ± 6	0 ± 6	same
eberswalde	104	20	0.9	0.1	2.64	1.22E-04			
_0									
eberswalde	212	7	0.8	0.1	1.91	1.88E-04			
_1									
eberswalde	40	21	0.9	0.3	1.94	2.49E-03			
_2									
eberswalde	243	47	0.4	0.1	11.0	2.74E-04			
_5									
eberswalde	152	32	0.4	0.2	3.72	4.51E-04			
_8									
eberswalde	22	3	3.3	0.2	0.34	6.42E-04			
_11									
eberswalde	63	6	2.1	0.2	0.47	2.77E-04			
_12									
eberswalde	193	5	1.4	0.2	1.69	5.50E-04			
_14									
eberswalde	129	12	1.8	0.3	0.88	8.37E-04			
_15									
eberswalde	189	41	0.6	0.4	49.5	1.19E-03			
_16									
eberswalde	349	23	1.2	0.4	9.45	2.76E-03			
_17									
eberswalde	319	16	2	0.4	2.45	3.34E-03			
_19									
eberswalde	305	21	1.2	0.2	3.16	1.17E-03			
_20									
GLM1_0	189	2	1.7	0	0.68	7.20E-05			
GLM1_1	202	5	1.5	0.1	1.24	3.64E-04			
GLM1_2	188	9	1.4	0.2	3.54	1.90E-03			
GLM1_3	217	10	1.8	0.2	1.64	2.18E-03			
GLM1_4	180	4	1.2	0	356.	7.54E-05			
						47			
GLM1_5	166	5	0.8	0	2.76	9.24E-05			
GLM1_6	207	30	0.8	0.2	13.3	9.56E-04			
						1			
GLM1_7	192	2	3.1	0.1	1.1	1.51E-04			

Measurement	Strike	Error strike	Dip	Error dip	Std resid	Collinearity	Dip_dir	Alpha	Dir_slope
average	193 ± 4		1.5 ± 0.1				283 ± 4	57, 40, 89, 70, 72, 62 (± 4)	same
GLM2_0	220	3	12.3	0.4	0.38	3.13E-03			
GLM2_2	203	3	6	0.5	0.57	3.71E-03			
GLM2_3	221	1	11.6	0.1	0.17	1.82E-04			
GLM2_5	234	2	12.2	0.3	0.4	1.12E-03			
GLM2_9	229	7	5.1	0.4	0.63	4.88E-03			
GLM2_10	234	1	11.7	0.2	0.1	6.80E-04			
GLM2_11	222	6	5.1	0.3	1.1	2.21E-03			
GLM2_12	209	7	3.1	0.2	2.45	2.00E-03			
GLM2_13	243	2	12	0.3	0.28	7.26E-04			
GLM2_16	233	10	2.7	0.2	2.18	1.23E-03			
GLM2_20	211	2	5	0.3	0.61	1.12E-03			
average	224 ± 1		7.9 ± 0.1				314 ± 1	21 ± 1	same
GMM1_45	256	36	2.3	0.3	3	2.87E-03			
GMM1_46	254	11	2.8	0.1	0.85	5.89E-04			
GMM1_47	255	7	4.4	0.4	1.05	1.15E-03			
GMM1_49	235	8	2.3	0.2	0.46	7.63E-04			
GMM1_53	219	3	6.8	0.3	0.54	7.40E-04			
GMM1_54	254	2	3.6	0.1	0.23	1.35E-04			
GMM1_56	259	2	4	0.1	0.17	1.29E-04			
GMM1_57	264	47	1.4	0.3	1.5	1.47E-03			
GMM1_60	233	18	2.1	0.4	0.99	3.09E-03			
GMM1_71	236	11	3	0.3	1.89	1.52E-03			
GMM1_72	253	8	3.5	0.2	0.55	8.75E-04			
average	247 ± 6		3.3 ± 0.1				337 ± 6	7 ± 6	same
GMM2_37	241	3	3.4	0.2	0.38	4.96E-04			
GMM2_38	235	8	4.3	0.4	0.54	1.97E-03			
GMM2_39	250	6	6.9	0.4	0.14	2.46E-03			
GMM2_40	248	5	3.9	0.3	0.39	8.39E-04			
GMM2_41	242	3	6.1	0.2	0.22	8.97E-04			
GMM2_42	246	13	6	0.6	1.22	3.31E-03			
GMM2_43	230	6	6.2	0.5	1.15	3.85E-03			
GMM2_45	273	21	8.3	0.3	0.67	9.88E-04			
GMM2_46	280	4	6.2	0.2	0.41	5.81E-04			
GMM2_49	294	5	1.9	0.1	1.18	3.41E-04			
average	254 ± 3		5.0 ± 0.1				344 ± 3	6 ± 3	same
GMM3_32	253 ± 6	6	5.6 ± 0.2	0.2	0.59	4.92E-04	343 ± 6	0 ± 6	same
GUM1_74	239	2	5.4	0.2	0.56	4.91E-04			
GUM1_75	258	2	8	0.3	0.21	1.16E-03			
GUM1_78	263	20	3.9	0.3	0.85	8.38E-04			
GUM1_80	260	3	4.5	0.1	0.23	1.71E-04			
average	255 ± 5		5.5 ± 0.1				345 ± 5	$5, 3 (\pm 5)$	same
GUM1_83	220	4	2.9	0.1	1.67	2.68E-04			
GUM1_84	227	2	3.6	0.1	0.53	1.43E-04			
GUM1_85	222	5	3.4	0.2	1.99	1.11E-03			
GUM1_86	226	6	2.4	0.2	1.01	4.86E-04			

Measurement	Strike	Error strike	Dip	Error dip	Std resid	Collinearity	Dip_dir	Alpha	Dir_slope
danielson_3 7	121	1	29.3	0.5	0.2	2.36E-03			
danielson_3 8	118	1	30.5	0.5	0.19	1.84E-03			
danielson_3 9	117	2	31.7	0.8	0.24	3.51E-03			
danielson_4 0	118	1	26.7	0.4	0.14	9.15E-04			
danielson_4 7	135	2	11.4	0.3	0.49	1.32E-03			
danielson_4 8	138	4	9.4	0.5	0.47	3.71E-03			
danielson_4 9	141	2	16	0.4	0.28	3.50E-03			
danielson_5 0	132	2	15.3	0.4	0.39	2.93E-03			
danielson_5 1	125	3	13.2	0.6	0.66	3.66E-03			
danielson_5 2	128	2	12.3	0.3	0.37	9.39E-04			
danielson_5 3	129	3	16.8	0.6	0.4	4.52E-03			
danielson_5 4	123	1	22.2	0.1	0.22	4.29E-04			
danielson_5 6	105	10	18.7	0.3	1.05	2.95E-03			
danielson_5 8	118	1	21	0.2	0.25	7.14E-04			
danielson_6 2	119	3	15.7	0.5	0.43	2.85E-03			
average	124 ± 1		18.9 ± 0.1				214 ± 1	0 ± 1	variable

Table A2. 1 m orthoimage thinning and thickening results

location	slope	p-value	trend
H1	0.046	0.0000	thickening
H2	-0.013	0.0001	thinning
H3	-0.015	0.0645	-
H4	0.006	0.3554	-
H5	0.002	0.8577	-
H6	0.031	0.0000	thickening
H7	0.009	0.0684	-
H8	0.033	0.0018	thickening
H9	-0.012	0.0009	thinning
H10	0.014	0.0008	thickening
WJ1	-0.001	0.6424	-
WJ2	0.000	0.9593	-
WJ3	0.002	0.0483	thickening
WJ4	0.004	0.0867	-
WJ5	0.007	0.0010	thickening
WJ6	0.020	0.0007	thickening
WJ7	0.014	0.4676	-
WJ8	0.004	0.0362	thickening
WJ9	0.013	0.1075	-
WJ10	0.007	0.1357	-
GLM1	-0.005	0.2638	-
GLM2	-0.041	0.0199	thinning
GMM1	0.026	0.0000	thickening
GMM2	-0.003	0.9119	-
GMM3	0.000	0.9908	-
GUM1	0.000	0.8010	-
GUM2	-0.002	0.0140	thinning
GUM3	0.004	0.0000	thickening
Argyre	0.015	0.1423	-
Athabasca	-0.029	0.3183	-
Becquerel	-0.003	0.0658	-
Candor1	0.008	0.5138	-
Candor2	0.009	0.7460	-
Cross	-0.192	0.0750	-
Danielson	0.048	0.1767	-
Eberswalde	0.039	0.0266	thickening

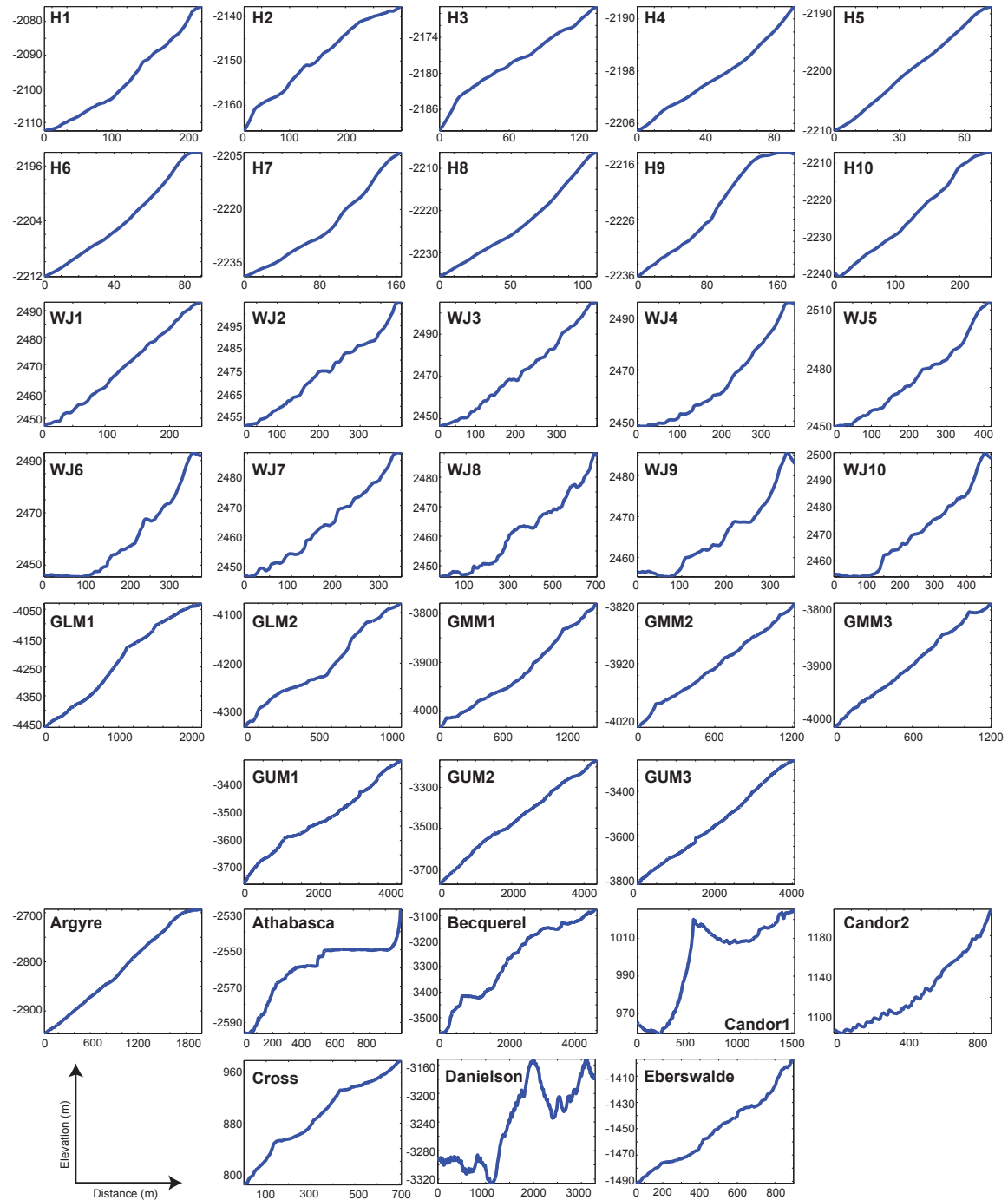


Figure A1

APPENDIX B

Auxiliary material for Chapter 5
 Diagenetic Origin of Nodules and Hollow Nodules of the Sheepbed Member, Yellowknife
 Bay, Gale Crater, Mars

Introduction

The auxiliary materials include Figure B1 which shows the manual traces of solid, hollow, and filled nodules, and pebbles performed in ArcGIS using 21 MAHLI images. Also included in this appendix are the image identification numbers for Mastcam mosaics used in this analysis.

Figure B1. MAHLI images containing traces of solid nodules, hollow nodules, and filled nodules. Yellow traces = solid nodules, red traces = hollow nodules, green traces = filled nodules, purple traces = pebbles. Scale bars = 5 mm. (a) Target Ekwir_1, sol 150, MAHLI image 0150MH0001630000101432R00. (b) Target Persillon, sol 154, MAHLI image 0154MH0001710000101524R00. (c) Target Mavor, sol 158, MAHLI image 0158MH0001850000101699R00. (d) Target Twitya, sol 159, MAHLI image 0159MH0000900000101730R00. (e) Target Yukon, sol 161, MAHLI image 0161MH0001630000101918R00. (f) Target Bonnet_Plume_1, sol 161, MAHLI image 0161MH0001920000101908R00. (g) Target Bonnet_Plume_2, sol 161, MAHLI image 0161MH0001920000101910R00. (h) Target Hudson_Bay, sol 161, MAHLI image 0161MH0001630000101922R00. (i) Target Hay_Creek, sol 162, MAHLI image 0162MH0001930000101964R00. (j) Target Drill_RP, sol 168, MAHLI image 0168MH0001630000102166R00. (k) Target Brock_Inlier, sol 169, MAHLI image 0169MH0001630000102240R00. (l) Target Autridge, sol 173, MAHLI image 0173MH0002270000102318R00. (m) Target Wernecke_3, sol 173, MAHLI image 0173MH0002270000102314R00. (n) Target Divot, sol 174, MAHLI image 0174MH0001460010102325E01. (o) Target Mini Drill Hole, sol 178, MAHLI image 0178MH0002110000102475R00. (p) Target Fort Confidence, sol 179, MAHLI image 0179MH0002020000102510R00. (q) Target McNaughton, sol 181, MAHLI image 0181MH0001630000102614R00. (r) Target McLeary, sol 181, MAHLI image 0181MH0001630000102620R00. (s) Target Cumberland_New, sol 275, MAHLI image 0275MH0002580000102991R00. (t) Target Cumberland_DRT, sol 291, MAHLI image 0291MH0002770010103392C00.

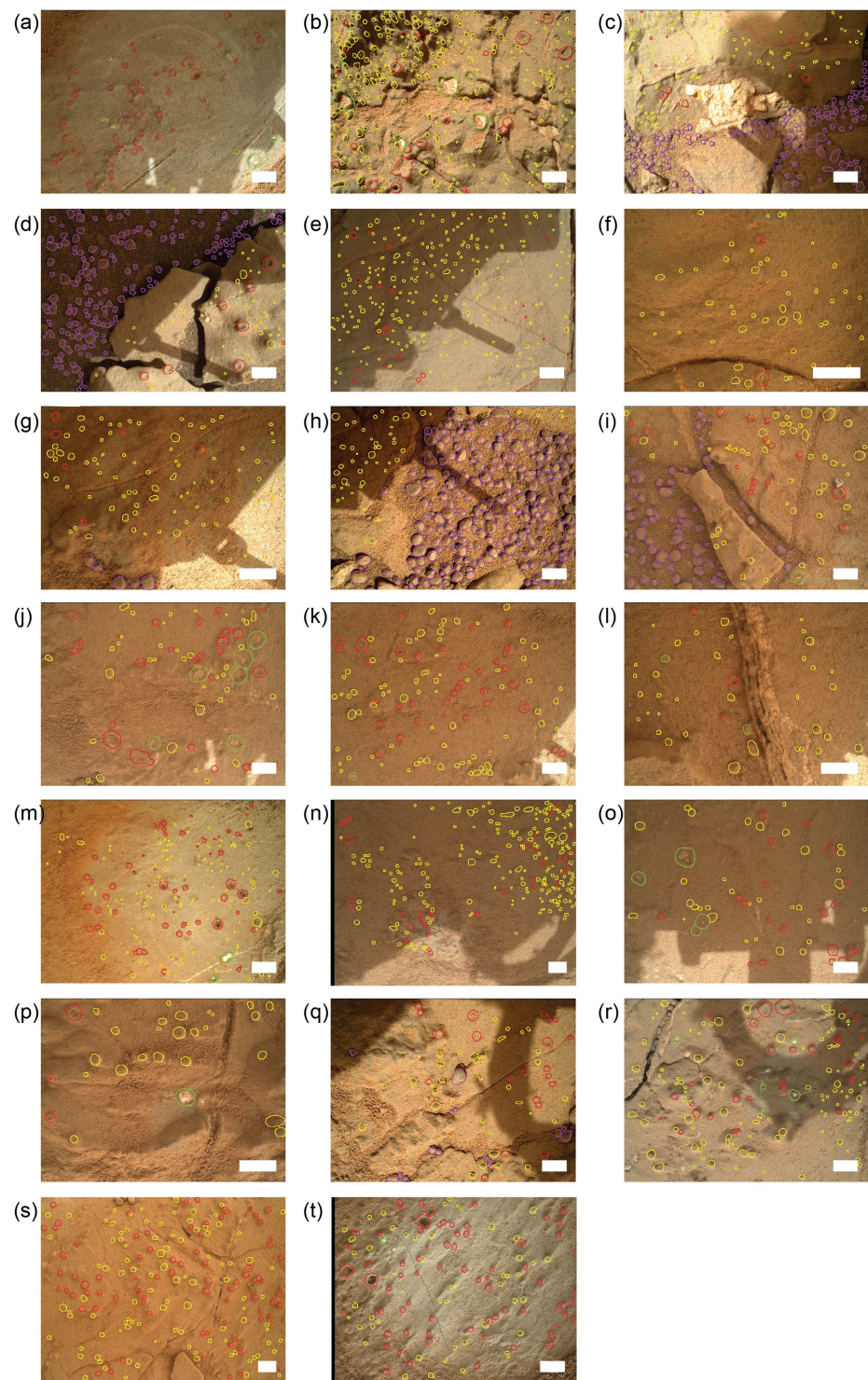


Figure B1

Mastcam Image Identification Numbers

John Klein Mosaic, M-100 camera, sol 166:

0166MR0008880000201629E01
 0166MR0008880010201630E01
 0166MR0008880020201631E01
 0166MR0008880030201632E01
 0166MR0008880040201633E01
 0166MR0008880050201634E01
 0166MR0008880060201635E01
 0166MR0008880070201636E01
 0166MR0008880080201637E01
 0166MR0008880090201638E01
 0166MR0008880100201639E01
 0166MR0008880110201640E01
 0166MR0008880120201641E01
 0166MR0008880130201642E01
 0166MR0008880140201643E01
 0166MR0008880150201644E01
 0166MR0008880160201645E01
 0166MR0008880170201646E01
 0166MR0008880180201647E01
 0166MR0008880190201648E01
 0166MR0008880200201649E01
 0166MR0008880210201650E01
 0166MR0008880220201651E01
 0166MR0008880230201652E01
 0166MR0008880240201653E01
 0166MR0008880250201654E01

Cumberland 1 Mosaic, M-100 camera, sol 185:

0185MR0010050000202232E01
 0185MR0010050030202235E01
 0185MR0010050060202238E01
 0185MR0010050090202241E01
 0185MR0010050120202244E01
 0185MR0010050150202247E01
 0185MR0010050180202250E01
 0185MR0010050210202253E01
 0185MR0010050240202256E01

Cumberland 2 Mosaic, M-100 camera, sol 275:

0275MR0011960000203446E01
 0275MR0011960010203447E01
 0275MR0011960020203448E01
 0275MR0011960030203449E01

Raised Ridge Mosaic, M-100 camera, sol 164:

0164MR0008830070201519E01
 0164MR0008830140201526E02
 0164MR0008830210201533E01
 0164MR0008830280201540E01
 0164MR0008830350201547E01
 0164MR0008830420201554E01
 0164MR0008830490201561E01
 0164MR0008830560201568E01
 0164MR0008830630201575E01

Selwyn Mosaic, M-100 camera, sol 159:

0159MR0008640000201355E01
 0159MR0008640010201356E01
 0159MR0008640020201357E01
 0159MR0008640030201358E01
 0159MR0008640040201359E01
 0159MR0008640050201360E01
 0159MR0008640060201361E01
 0159MR0008640070201362E01
 0159MR0008640080201363E01
 0159MR0008640090201364E01
 0159MR0008640100201365E01
 0159MR0008640110201366E01
 0159MR0008640120201367E01
 0159MR0008640130201368E01
 0159MR0008640140201369E01
 0159MR0008640150201370E01
 0159MR0008640160201371E01
 0159MR0008640170201372E01
 0159MR0008640180201373E01
 0159MR0008640190201374E01
 0159MR0008640200201375E01
 0159MR0008640210201376E01

Yellowknife Egress Mosaic, M-100 camera, sol 298:

0298MR0012480000203678E01
 0298MR0012480050203683E01
 0298MR0012480060203684E02
 0298MR0012480110203689E01
 0298MR0012480120203690E01
 0298MR0012480170203695E01
 0298MR0012480180203696E01
 0298MR0012480230203701E01
 0298MR0012480240203702E01
 0298MR0012480290203707E01

0298MR0012480300203708E01	0137MR0008170370200970E01	
0298MR0012480350203713E01	0137MR0008170380200971E01	
0298MR0012480360203714E01	0137MR0008170390200972E01	
0298MR0012480410203719E01	0137MR0008170400200973E01	
0298MR0012480420203720E01	0137MR0008170410200974E01	
0298MR0012480470203725E01	0137MR0008170420200975E01	
0298MR0012480480203726E01	0137MR0008170430200976E01	
0298MR0012480530203731E01	0137MR0008170440200977E01	
0298MR0012480540203732E01	0137MR0008170450200978E01	
0298MR0012480590203737E01	0137MR0008170460200979E01	
M100 Mastcam mosaic acquired on sol 137:		
0137MR0008170000200933E01	0137MR0008170470200980E01	
0137MR0008170010200934E01	0137MR0008170480200981E01	
0137MR0008170020200935E01	0137MR0008170490200982E01	
0137MR0008170030200936E01	0137MR0008170500200983E01	
0137MR0008170040200937E01	0137MR0008170510200984E01	
0137MR0008170050200938E01	0137MR0008170520200985E02	
0137MR0008170060200939E01	0137MR0008170530200986E01	
0137MR0008170070200940E01	0137MR0008170540200987E01	
0137MR0008170080200941E01	0137MR0008170550200988E01	
0137MR0008170090200942E01	0137MR0008170560200989E01	
0137MR0008170100200943E02	0137MR0008170570200990E01	
0137MR0008170110200944E01	0137MR0008170580200991E01	
0137MR0008170120200945E01	0137MR0008170590200992E01	
0137MR0008170130200946E02	0137MR0008170600200993E01	
0137MR0008170140200947E01	0137MR0008170610200994E01	
0137MR0008170150200948E01	0137MR0008170620200995E01	
0137MR0008170160200949E01	0137MR0008170630200996E01	
0137MR0008170170200950E01	0137MR0008170640200997E01	
0137MR0008170180200951E01	0137MR0008170650200998E01	
0137MR0008170190200952E01	0137MR0008170660200999E01	
0137MR0008170200200953E01	0137MR0008170670201000E01	
0137MR0008170210200954E01	0137MR0008170680201001E01	
0137MR0008170220200955E01	0137MR0008170690201002E01	
0137MR0008170230200956E01	0137MR0008170700201003E01	
0137MR0008170240200957E01	0137MR0008170710201004E01	
0137MR0008170250200958E01	0137MR0008170720201005E01	
0137MR0008170260200959E01	0137MR0008170730201006E01	
0137MR0008170270200960E01	0137MR0008170740201007E01	
0137MR0008170280200961E01	0137MR0008170750201008E01	
0137MR0008170290200962E01	0137MR0008170760201009E01	
0137MR0008170300200963E01	M100 Mastcam mosaic acquired on sol 138:	
0137MR0008170310200964E02	0138MR0008190000201014E01	
0137MR0008170320200965E01	0138MR0008190010201015E01	
0137MR0008170330200966E01	i0138MR0008190020201016E01	
0137MR0008170340200967E01	0138MR0008190030201017E01	
0137MR0008170350200968E01	0138MR0008190040201018E01	
0137MR0008170360200969E01	0138MR0008190050201019E01	
	0138MR0008190060201020E01	

0138MR0008190070201021E01
0138MR0008190080201022E01
0138MR0008190090201023E01
0138MR0008190100201024E01
0138MR0008190110201025E01
0138MR0008190120201026E01
0138MR0008190130201027E01
0138MR0008190140201028E01
0138MR0008190150201029E01
0138MR0008190160201030E02
0138MR0008190170201031E01
0138MR0008190180201032E01
0138MR0008190190201033E01
0138MR0008190200201034E01
0138MR0008190210201035E01
0138MR0008190220201036E01
0138MR0008190230201037E01
0138MR0008190240201038E01
0138MR0008190250201039E01
0138MR0008190260201040E01
0138MR0008190270201041E01
0138MR0008190280201042E01
0138MR0008190290201043E01
0138MR0008190300201044E01
0138MR0008190310201045E01
0138MR0008190320201046E01
0138MR0008190330201047E01
0138MR0008190340201048E01
0138MR0008190350201049E01
0138MR0008190360201050E01
0138MR0008190370201051E01
0138MR0008190380201052E01
0138MR0008190390201053E01
0138MR0008190400201054E01
0138MR0008190410201055E01
0138MR0008190420201056E01
0138MR0008190430201057E01
0138MR0008190440201058E01
0138MR0008190450201059E01
0138MR0008190460201060E01
0138MR0008190470201061E01
0138MR0008190480201062E01
0138MR0008190490201063E01
0138MR0008190500201064E01
0138MR0008190510201065E01
0138MR0008190520201066E01
0138MR0008190530201067E01
0138MR0008190540201068E01
0138MR0008190550201069E01
0138MR0008190560201070E01
0138MR0008190570201071E01
0138MR0008190580201072E01
0138MR0008190590201073E01
0138MR0008190600201074E01
0138MR0008190610201075E01
0138MR0008190620201076E01
0138MR0008190630201077E01
0138MR0008190640201078E01
0138MR0008190650201079E01
0138MR0008190660201080E01
0138MR0008190670201081E01
0138MR0008190680201082E01
0138MR0008190690201083E01
0138MR0008190700201084E01
0138MR0008190710201085E01
0138MR0008190720201086E01
0138MR0008190730201087E01
0138MR0008190740201088E01
0138MR0008190750201089E01
0138MR0008190760201090E01